ABSTRACT

Title of dissertation: LONG TERM STABILITY AND
IMPLICATIONS FOR PERFORMANCE
OF HIGH STRENGTH FIBERS
USED IN BODY ARMOR

Amanda L. Forster, Doctor of Philosophy, 2012

Dissertation directed by: Professor Mohamad Al-Sheikhly
Department of Materials Science and Engineering

The objective of this work is to examine the relationship between structure (both molecular and morphological structure) and properties of high strength fiber. The superior performance of the high strength fibers is predicated on the development of a highly aligned molecular structure that allows the polymer to exhibit a superior strength in the axial direction of the fiber. Armor manufacturers have exploited the inherent strength of these materials to develop body armor that continues to defeat ever-increasing threats. However, even an ideal molecular structure will be subjected to a potentially hydrolytic or oxidative environment during use, which can reduce the high strength of these fibers, and impact their ability to protect the wearer. The effect of the wear environment on the molecular structure, which is responsible for the high strength of these fibers, has not been well understood by the scientific community. In this work, the chemical mechanisms of degradation were investigated at the molecular level to understand the effect of the environmental conditions on crystallinity, orientation, and molecular weight. The chemical mech-

anism and kinetics elucidated from these measurements are used to understand the reduction in strength of these materials after degradation. Hydrolysis was found to be the predominant mechanism of degradation for polybenzobisoxazole and goes to irreversible chain scission. Hydrolysis is also the primary mechanism of degradation for aramid fibers. Ultra-high molecular weight polyethylene (UHMWPE) fibers undergo an oxidative mechanism of degradation, and the activation energy for this mechanism was calculated. Additionally, the release of acids from aramid copolymer fibers, and the performance of these fibers in hydrolytic and thermooxidative environments were studied to determine that hydrolytic degradation is the predominant degradation mechanism for these fibers.

Exploratory research was also performed in an effort to improve the stability of UHMWPE fibers by using radiation to crosslink the UHMWPE fibers and increase the temperature of their alpha relaxation. However, this radiation treatment was still found to reduce the overall tensile strength of these fibers. In summary, the wear environment and vulnerabilities of a material to degradation are essential when selecting materials or developing new materials for use in body armor.

LONG TERM STABILITY AND IMPLICATIONS FOR PERFORMANCE OF HIGH STRENGTH FIBERS USED IN BODY ARMOR

by

Amanda L. Forster

Dissertation submitted to the Faculty of the Graduate School of the
University of Maryland, College Park in partial fulfillment
of the requirements for the degree of
Doctor of Philosophy
2012

Advisory Committee:
Professor Mohamad Al-Sheikhly, Chair/Advisor
Professor Robert Briber
Professor Lourdes Salmanca-Riba
Professor Emeritus Joseph Silverman
Professor Michael Coplan

Dedication

This thesis is dedicated in loving memory of my mother, Martha Lattam, and my grandmother, Martha Weisner. You were my first, and most memorable teachers. Without your love and support this would have never been possible. I only wish that you could have both been here to see it.

Acknowledgments

I owe my gratitude to all the people who have made this work possible.

First, I would like to thank my advisor, Professor Mohamad Al-Sheikhly for supporting me, encouraging me, and giving me an invaluable opportunity to work on challenging and extremely interesting projects over the past four years. He is a truly dedicated teacher and mentor, and it has been a pleasure to work with and learn from such an extraordinary individual.

I would also like to thank my supervisor at NIST, Kirk Rice. Without his support, encouragement, and technical assistance, this thesis would have never been possible. Thanks are due to Professor Michael Coplan, Professor Robert Briber, Professor Lourdes Salamanca-Riba, and Professor Emeritis Joseph Silverman for agreeing to serve on my thesis committee and for sparing their invaluable time reviewing the manuscript.

My colleagues at NIST have provided immeasurable and invaluable assistance to me over the many years of work leading to this thesis. Dr. Mike Riley helped me immeasurably in the laboratory by lending his expertise with design and implementation of the tumbling apparatus, without which the conditioning experiments and conditioning protocol would not have been possible. Dr. Riley also deserves special mention for all of his technical assistance in teaching me to use LaTeX for document preparation. Without his help, this document would not have been possible. I owe a tremendous amount of gratitude to Dr. Joannie Chin, Dr. Gale Holmes, Dr. Fred Bateman, Dr. Stephanie Watson, and Mr. Dennis Leber at NIST for

Table of Contents

List of Figures

xiii

Chapter 1

Aramid and Oxazole Fibers Used in Body Armor

1.1 Chapter Overview

In this chapter, aramid and oxazole fibers used in body armor are introduced. A brief history of the use of these fibers in body armor and issues with their long term performance is provided. A method of accelerated degradation for these materials is described. The relationship between the molecular structure and the physical properties of these fibers is investigated. A mechanism of hydrolysis for oxazole fibers is proposed.

1.2 Aramids

1.2.0.1 History of Aramid Development

Aramid is defined by the US Federal Trade Commission [1] as a generic term for *a manufactured fiber in which the fiber-forming substance is a long chain synthetic polyamide in which at least 85 % of the aramid linkages are attached directly to two aromatic rings.* This definitaion distingushies aramids from nylons (which do not have this aromatic character). It encompasses several different fibers, including Kevlar, Nomex, and Twaron. *Para*-oriented aromatic polyamides were first synthesized in 1965 by Stephanie Kwolek, a DuPont research scientist, in an effort

to develop a fiber with a super-rigid molecular chain and a high modulus. While this new fiber showed promise, considerable challenges had to be overcome in order to commercialize it. All of the monomers needed had to be synthesized, and the polymer would not melt, causing processing problems [1].

Experimental fibers spun using a conventional wet-spinning process showed commercial promise. Their tensile modulus was stiffer than glass on a specific weight basis, and later experiments increased the fiber modulus to 2.5 times that of fiberglass. This initial breakthrough lead to greater understanding of the polymer solution behavior, and the discovery that solutions of this polymer exhibited the anisotropic behavior of liquid crystalline solutions, which are discussed in the next section. Another major breakthrough came in the early 1970s, when a modified dry jet spinning process for polyaramid was developed. Fibers produced using this process were almost twice as strong as those from the wet spinning experiments, and the spinning speed was quadrupled. These developments led DuPont to commercialize the fiber [1].

1.2.0.2 Liquid Crystals

A very brief introduction to liquid crystals is given here to better explain the behavior of solutions of PPTA and other rigid rod molecules that exhibit liquid crystalline behavior at certain concentrations. Typically one thinks of three well-known states of matter–*solid, liquid, and gas*. These phases differ from each other because the molecules in each state exhibit different amounts of order. Solids are

rigid arrangements of molecules in which molecules are constrained to occupy certain positions- in a crystal these are very ordered, but the positions can be random in an amorphous solid. In liquids, the molecules neither occupy a specific position, on average, nor maintain a particular orientation. They are free to diffuse around, interact with other molecules, and abruptly change their direction of motion. Attractive forces between the molecules keep the liquid together. The amount of order in a liquid is less than that in a solid. In a gas, the motion of the molecules becomes more chaotic, and the attractive force between the molecules is insufficient to hold the molecules together, as in the liquid state. Liquids and gases are similar in that the molecules in both states exhibit random, disorganized motion, however they differ in that in a liquid, molecules maintain a specific average intermolecular distance, but in a gaseous state, the average intermolecular distance is dictated by the size and shape of the container [2].

A fourth phase can also exist for certain materials. This phase lies between the solid and liquid state. As discussed previously, a solid phase possesses *positional order*. Additionally, the orientation of the molecules with respect to each other is constrained, they can also be said to possess *orientational order*. When a solid melts to an ordinary liquid, both types of order are lost completely, the molecules move and tumble randomly. When a solid melts to a liquid crystal, the positional order may be lost, but the orientational order remains. The molecules in a liquid crystal phase are free to move about as in a liquid, but their orientation is preserved [2]. An order parameter, S may be defined to specify the amount of orientational order in a liquid crystal phase. The order parameter may be represented by Equation 1.1,

which is based on a solution to the Legendre equation [3]. The Legendre equation is a second order ordinary differential equation that is frequently encountered in physics.

$$S = \langle P_2 \left(\cos \theta \right) \rangle = \left\langle \frac{3}{2} \cos^2 \theta - \frac{1}{2} \right\rangle \tag{1.1}$$

Where θ is the angle of the molecule with respect to a unit vector $\hat{n}$, which is known as the director. In a simple liquid crystal phase, one molecular axis tends to point along a preferred direction, which is denoted by $\hat{n}$.

All liquid crystals are anisotropic- either their shape is such that one molecular axis is very different from the other two, or in some cases, different parts of the molecule may have different solubility properties. Intermolecular interactions promote orientational and sometimes positional organization in an otherwise fluid phase. The most common shape for a liquid crystal is a rod-like shape in which one axis of the molecule is much longer than the other two. This is called a *calamitic* liquid crystal. Disc-like molecules can also form liquid crystals called *discotic* liquid crystals [3].

The simplest liquid crystal phase of calamitic liquid crystals is the *nematic* phase, in which molecules maintain a preferred orientation as they diffuse through the sample. The vector describing this preferred orientation is the director. There is no positional order in this phase. Two other phases common to calamitic liquid crystals are the *smectic A* and *smectic C* phases. These phases have positional order- the centers of mass are aligned in layers. If the director is aligned perpendicular

to the layers, then it is a smectic A phase, if it is aligned in any other direction, it is a smectic C phase. Discotic liquid crystals having perpendicular alignment, like stacks of coins, are known as *columnar* discotic liquid crystal phases [3].

Both calamitic and discotic liquid crystals are also called thermotropic liquid crystals, because their liquid crystalline phase is stable over a certain range of temperatures. However, there is another type of liquid crystal called a *lyotropic* liquid crystal, in which the liquid crystal phase only forms when the molecule is in solution. In lyotropic liquid crystals, the concentration of the solution is equally important or more important than the temperature of the solution in determining the stability of the liquid crystalline phase. The elongated, or *rigid rod* shape of PPTA molecules dissolved at high concentrations in the solvent sulfuric acid helps this polymer molecule preferentially order and form a lyotropic liquid crystalline phase [3].

1.2.0.3 Structure and Properties

Aramids used in body armor, such as Kevlar, are based on the polycondensation of *p*-phenylene diamine and teraphthalic acid or terephthaloyl chloride in a dialkyl amide solvent [1, 4], as shown in Figure 1.1.

The resultant polymer is then spun into fibers from a concentrated acid solution, as depicted in Figure 1.2.

As previously mentioned, solutions of this polymer exhibit rod-like behavior due to the rigid covalent bonds in the aramid main chain, characterized by the
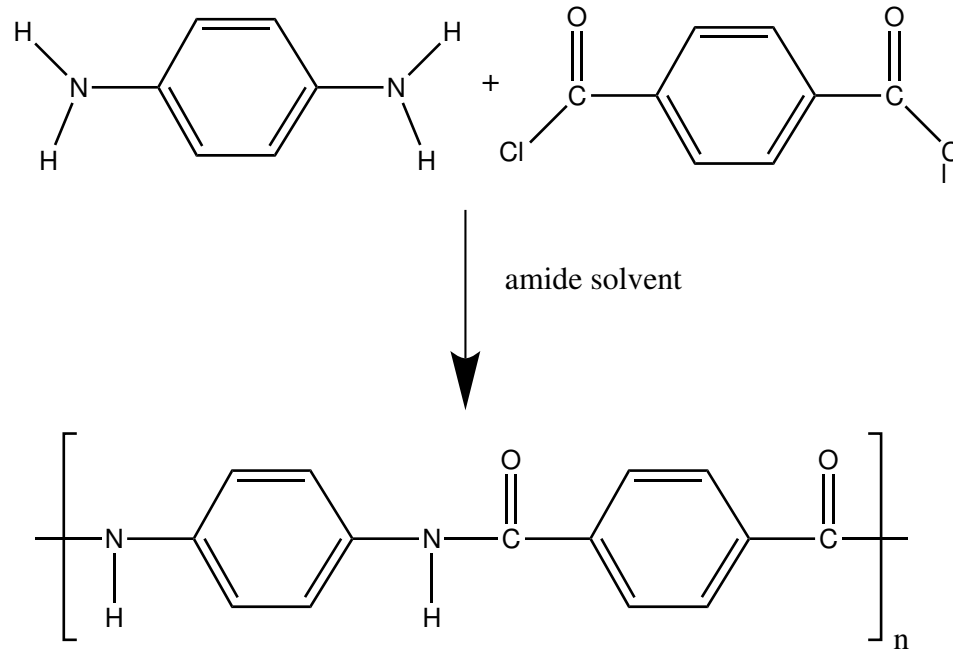
Figure 1.1: A reaction demonstrating the polycondensation of p-phenylene diamine and terephthaloyl chloride (could also use terephthalic acid) in a dialkyl amide solvent [1, 4] to form PPTA fiber.
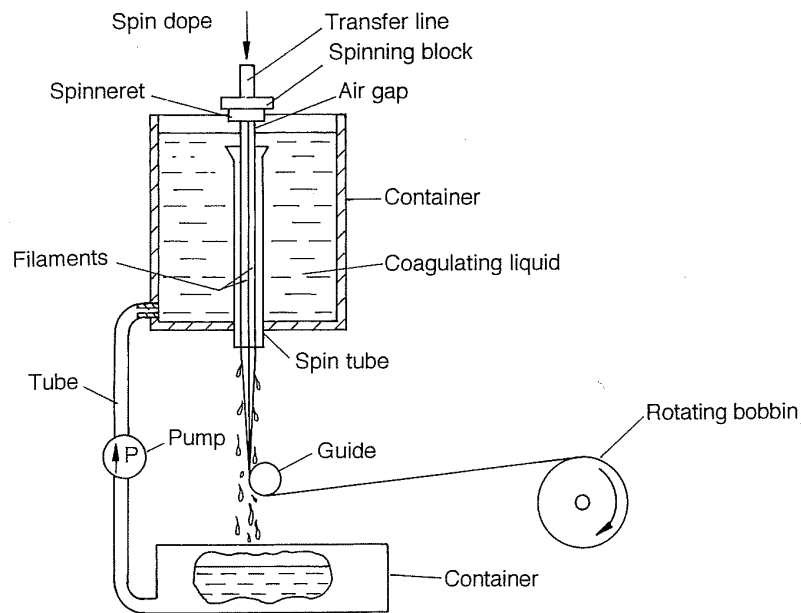
Figure 1.2: Schematic of dry-jet spinning technique used to make PPTA fiber [1]. A spin dope is forced through a spinneret at high speed. Filaments exit the spinneret into an air gap, then are drawn into a coagulating bath. The individual filaments are then drawn over a series of rotating bobbins to orient and align the fibers. The figure also shows recycling of the coagulation liquid.

120 ° bond angle between carbons in the chain [1]. At low concentrations, these solutions are randomly oriented, but as concentration is increased, the solutions become anisotropic and the polymer molecules adopt an ordered arrangement in small domains to increase their packing efficiency. Spinning from these liquid crystalline solutions contributes to the high strength and orientation of these fibers [1].

PPTA fibers have a highly ordered, crystalline molecular structure, which has been extensively studied by wide-angle X-ray diffraction. Based on these studies, PPTA fibers are assumed to have a pseudo-orthorhombic unit cell. The proposed crystal structure for PPTA fibers are shown in Figure 1.3.

Due to close proximity between NH and CO groups, intermolecular hydrogen bonds can form, which link the adjacent chains into hydrogen bonded sheets, as shown in Figure 1.3. These hydrogen bonded sheets fold within the fiber to form a radially pleated structure, as shown in Figure 1.4. The exact reason for the occurrence of this pleated structure is not completely understood. One prevailing theory is that this structure is formed during the coagulation of the fiber. The fiber skin forms first, and is subjected to most of the stress on the fiber during spinning. The coagulating solution at the core of the filament can then relax and form the uniform pleated periodicity during crystallization. This has also been seen in micrographs of the fiber, as shown in Figure 1.5 [5].

The physical properties of PPTA fibers are closely related to its physical structure, especially its highly ordered crystalline structure. In the idealized case of a fully extended PPTA molecule perfectly oriented with respect to the fiber axis, the fiber strength would be equal to the C-C covalent bond force 4.41×10^{-7} g, divided
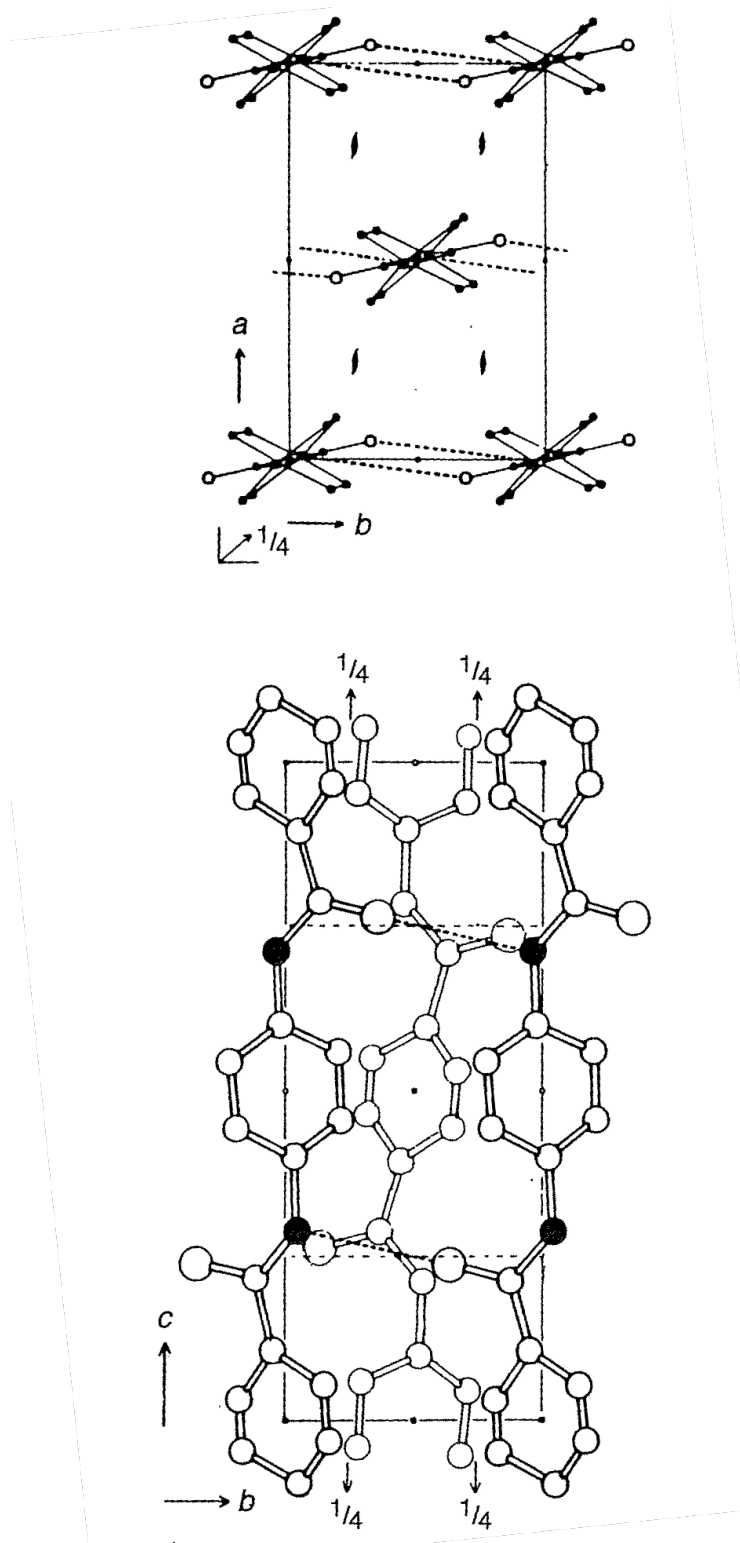
Figure 1.3: The crystalline structure of PPTA fiber is pseudo-orthorhombic unit cell crystal as shown in this schematic. [1].
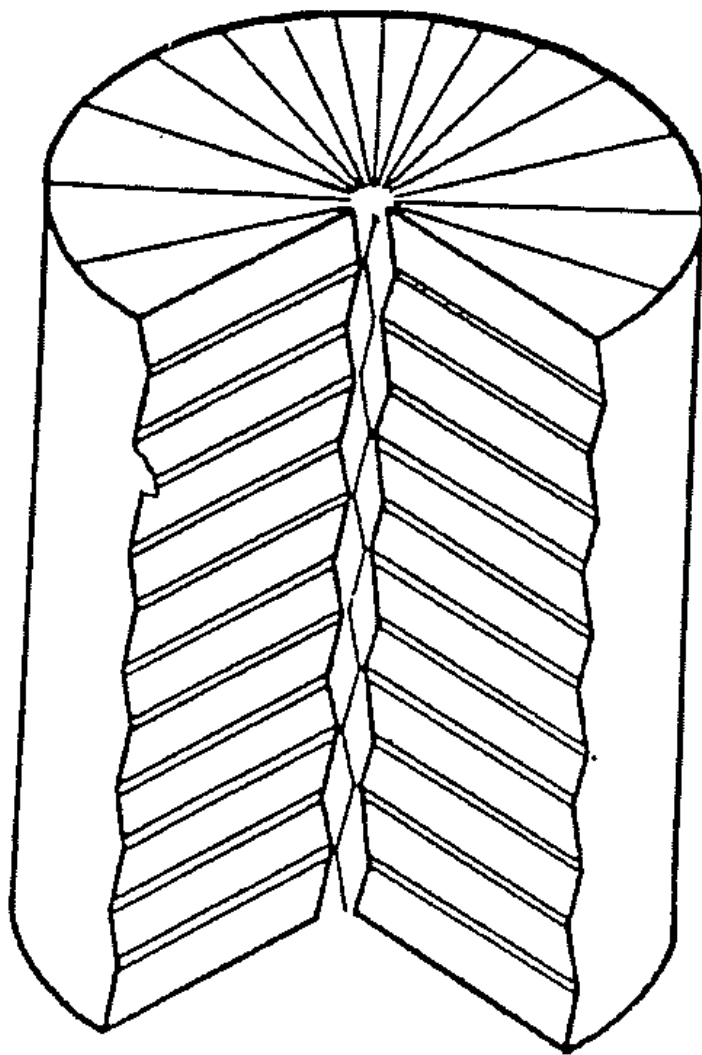
Figure 1.4: Hydrogen-bonding between NH and CO groups in PPTA fibers link adjacent chains into hydrogen bonded sheets. These sheets fold within the fiber, forming a radially pleated structure, as shown in this schematic [1].
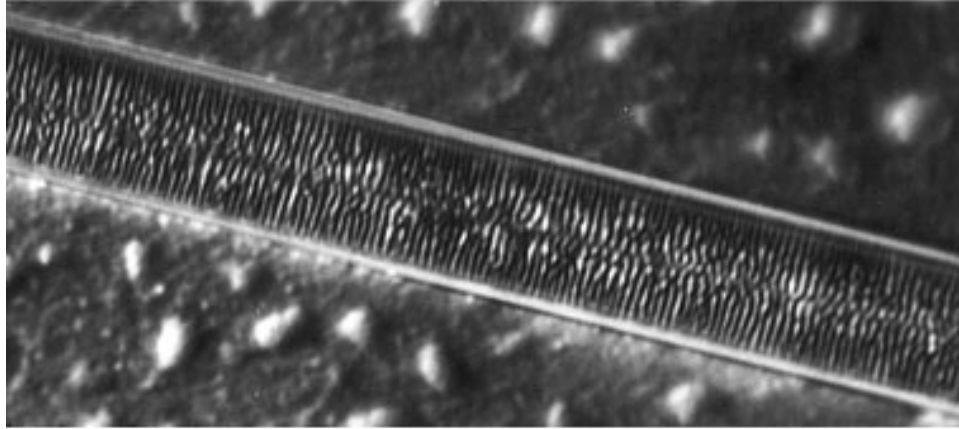
Figure 1.5: This SEM micrograph actually shows the pleated sheet structure of PPTA fiber. It is evident in the vertical lines shown through the middle of the fiber [5].

by the linear density of the chain, or 2.7 x 10^{-9}. This gives a theoretic microscopic tensile strength of 21.7 GPa. This is much larger than the actual measured strength of a PPTA fiber, which is 4 GPa (at very short gage lengths). Some of the difference in the theoretical and actual tensile strength can be ascribed to the simple assumptions used to make this estimate. Another attempt used a stochastic failure analysis on a microscopic scale to calculate an ultimate fiber strength of approximately 7.5 GPa. Overall, the discrepancies between the theoretical and actual tensile properties of PPTA can be attributed to several factors, including a relatively low upper limit on crystallinity due to processing conditions, crystal defects, and the skin-core gradient in crystalline orientation [1].

It is well known that PPTA fibers have excellent tensile properties, but its compressive and shear strength are relatively poor. There are three main modes of tensile failure in PPTA fibers. These are a pointed break, a fractured break, and a kink band break [1]. These can be identified using ordinary cross-polarized
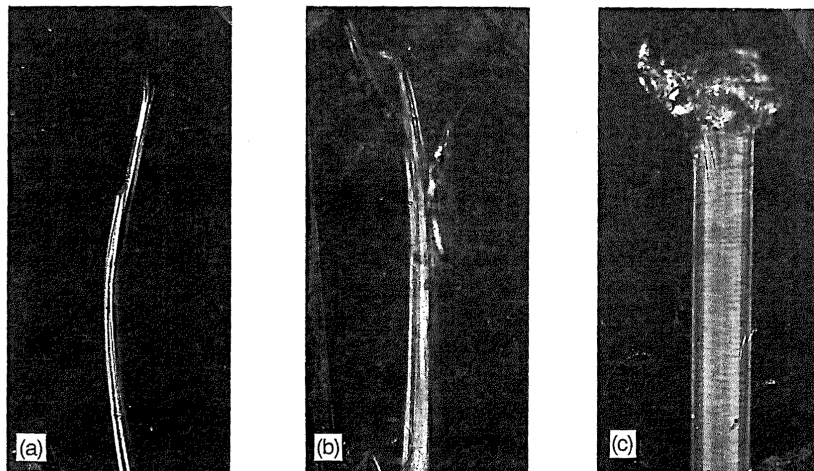
Figure 1.6: A micrograph showing the three different kinds of tensile failures in PPTA fiber- pointed break (a), fractured break (b), and kink band break (c) [1].

light microscopy, as shown in Figure 1.6. An SEM of a kink band is shown in Figure 1.7 [6].

These kink bands are formed when PPTA fibers are subjected to either severe bending or compression. Kink bands are characterized by a morphological deformation that appears as a series of successive bands at an angle of 50 to 60 ° to the fiber axis. Kink band formation has been visualized as being initiated as a plastic deformation that results in the appearance of several irregularly spaced single bands. This banding comprises a narrow, triangular, or wedge-shaped, region in which the orientation of the polymer chains is abruptly changed. As deformation increases, the kink bands propagate through the fiber to the axis and wedges become increasingly more kinked. Simultaneously, new kink bands form along the fiber. "Cross bands" form and intersect the original bands (Figure 1.8). With further increased compression, the outer region opposite the cross bands fracture under tension, forming a kink band break, as discussed previously [1].

11
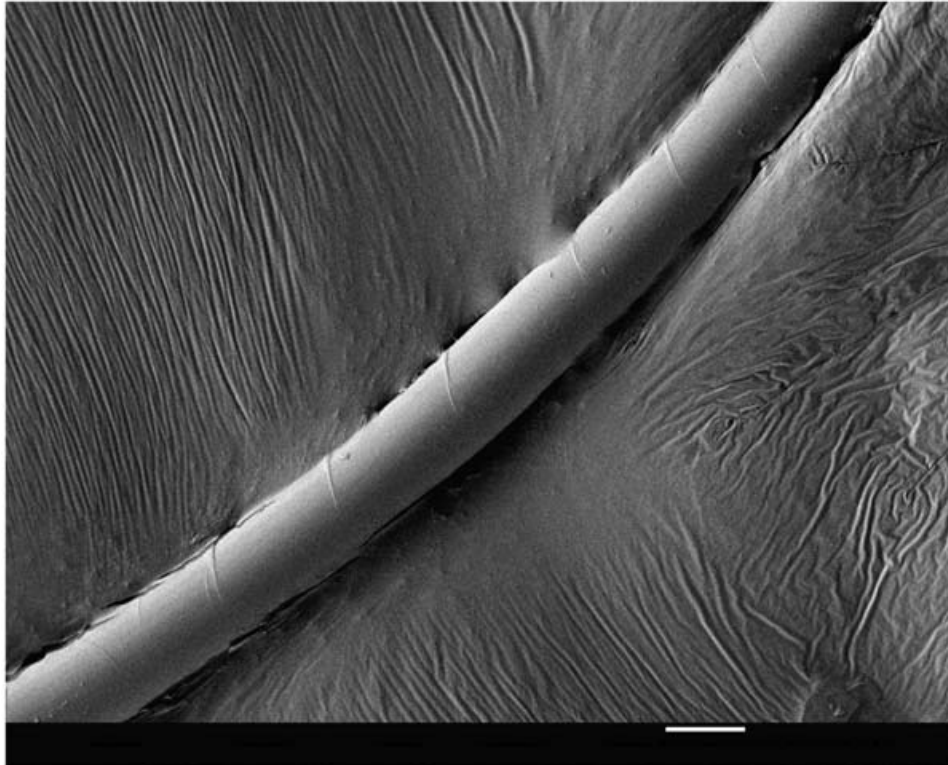
Figure 1.7: SEM image of single PPTA fiber showing the formation of kink bands as vertical lines in the compression side of the fiber after being looped [6].
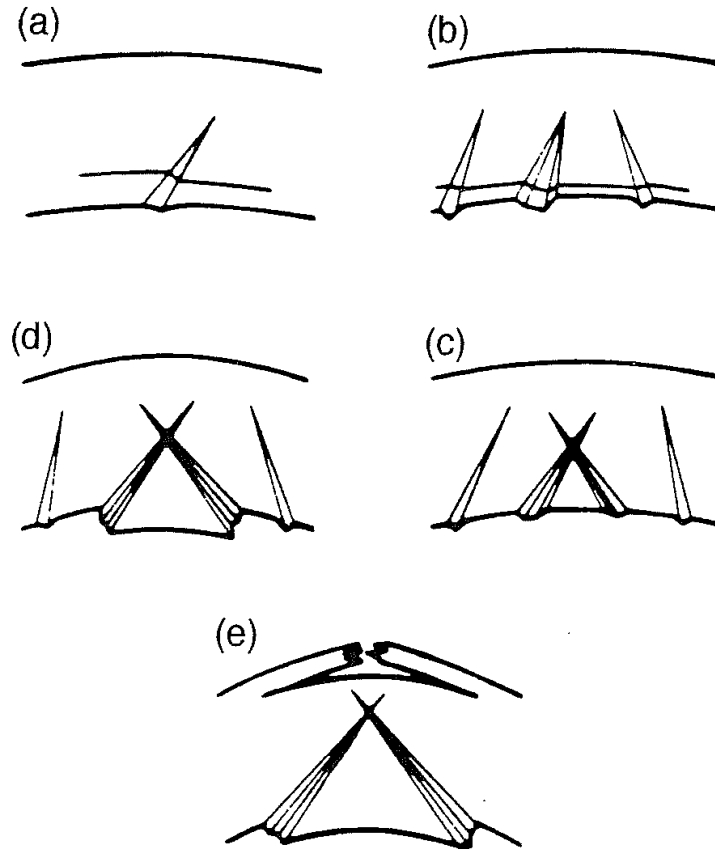
Figure 1.8: A micrograph showing the the process by which a kink band is formed-first a small region in which the chains are not oriented with respect to the fiber axis is formed under a compressive load, (a). Next, under increasing load, the deformation increases and begins to propagate through the fiber to the axis, (b), and wedges become increasingly more kinked. Simultaneously, new kinks begin to form along the fiber axis, and intersect the original bands, (c) and (d). With further increased compression, the outer region opposite the cross band fracture under tension as a kink band break (e) [1].

Kink bands represent the major drawback of PPTA's structural anisotropy. Essentially, the extended chain structure of PPTA fibers cannot support any appreciable amount of axial compression. This is further complicated by the fact that the only lateral bonding in the fiber is relatively weak Van der Waals forces and the hydrogen bonding between sheets of the chains. Thus, PPTA fibers require special consideration for compressive applications but have excellent tensile properties [1].

1.2.1   Polyazoles

1.2.1.1   History of Polyazole Development

After the discovery of aramids in the late 1960s, there has been a consistent search, especially at the Air Force Research Laboratory, for other chemistries to elicit similar rigid-rod polymers, especially given the practical limits in ultimate fiber tensile strength for aramids. Poly-[(benzo,2-d:4,5-d'bisthiazole-2,6-diyl)-1,4-phenylene] (PBZT), which is not discussed here, and poly(p-phenylene-2,6-benzobisoxazole), or PBO, are two polymers that were developed from this search [7]. PBO is produced by condensing 4,6-diamino-1,3-benzenediol dihydrochloride with terephthalic acid, as shown in Figure 1.9.

Typically, polyphosphoric acid, or PPA, is used as the solvent in the preparation of PBO fiber. PPA serves three functions in this process: solvent, catalyst, and dehydrating agent. This allows for the formation of polybenzobisoxazoles in solution, without the need for a separation process. Therefore, the polymerization solution is directly spinnable, eliminating the need for a separate dissolution step [7].
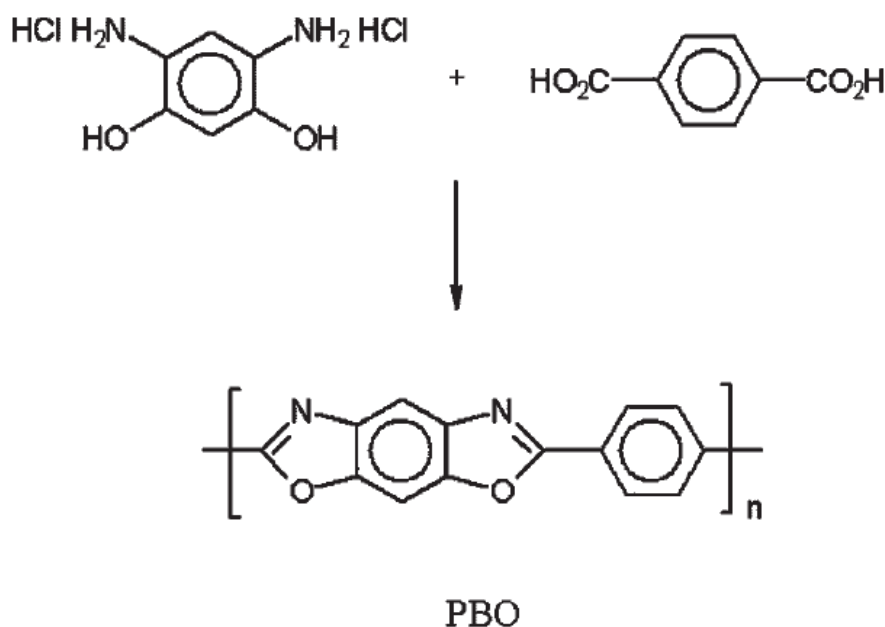
Figure 1.9: The synthesis of PBO fiber from the polycondensation of 4,6-diamino-1,3-benzenediol dihydrochloride with terephthalic acid [7].

Like PPTA, PBO forms liquid crystalline solutions at concentrations above a critical point, due to the rigid rod conformation of the polymer chains. Like other rigid rod polymers, PBO does not dissolve in aprotic organic solvents, but can be made to dissolve in certain solvents, such as nitroalkanes and nitrobenzenes with the addition of Lewis acids. Fiber spinning of nematic solutions of PBO is typically accomplished using a dry-jet wet spinning technique similar to that used to make PPTA fibers. Extrusion of the hot polymer solution occurs under pressure through a single or multi-hole spinneret to a narrow air gap, then the spinning filament is plunged into a non-solvent coagulating bath, where it transitions from a nematic solution to the solid state due to deprotonation of the polymer by the coagulant. The choice of the liquid in the non-solvent coagulating bath can affect the crystal

structure of the final fiber. The fiber is then stretched, washed and dried. Some fibers are also subsequently heat treated [7].

1.2.1.2   Structure and Properties

A common observation from most morphological studies on PBO fibers is that the crystallites are very well oriented, as one might expect for an oriented fiber. This observation is made from strong equatorial and multiple meridional reflections in wide angle X-ray diffraction patterns generated from these fibers [7]. Scanning electron microscopy (SEM) images of the failed surfaces heat-treated PBO fibers (both those that have been fractured via tensile testing or compressively peeled) show a fibrillar structure. A hierarchical structural model has been proposed for PBO, in which the fibers are made up of macrofibrils, fibrils, and microfibrils, with diameters of 5, 0.5, and 0.05 μm, respectively. Experimental studies have observed even smaller (7-10 nm) microfibrils than those proposed by this theory. SAXS patterns of PBO fibers show an equatorial streak which is attributed to the presence of voids or crystals elongated with respect to the fiber axis. These voids are typically attributed to the drastic volume reduction of the fiber due to removal of the solvent during coagulation [7].

A model of PBO fiber was proposed by Kitagawa in 1998. In this model, the fiber is formed from oriented microfibrils between 10-50 nm in diameter aligned with the axis of the fiber. The microfibrils contain many capillary-like microvoids that are generally considered to be areas of solvent that existed prior to coagulation. The

surface, or skin, of the fiber consists of a void-free region. This structural model is shown schematically in Figure 1.10, and has also been described as "a bundle of broom-straws" [8].

Like PPTA, PBO fibers have a very high thermal degradation temperature of over 600 °C, and are generally expected to decompose before melting or exhibiting a glass transition temperature [7]. The mechanical properties of PBO fibers are generally strong, tough, and very stiff. Their tensile strength is comparable to that of PPTA, UHMWPE, and carbon fibers. A typical tensile strength for PBO has been reported to be as high as 5.8 GPa, with a modulus of 180 GPa. However, the axial compressive strength of PBO is about 10 to 15 % of its tensile strength. The compression behavior of rigid rod polymers such as PBO has been extensively studied. Unlike carbon or glass fibers, organic fibers do not exhibit a catastrophic failure in compression, but rather undergo failure due to kinking, as discussed in the previous section on PPTA [7].

1.3   Brief History of Body Armor

Since 1972, the National Institute of Justice has sponsored research to develop lightweight, concealable body armor for use by police officers. This armor was primarily designed to protect officers from handgun threats. In 1975, 129 officers from federal, state, and local agencies were killed in the line of duty. Prior to this time, body armor was primarily developed for and used by the military. It was both heavy and conspicuous, typically made from steel, ceramics, or many layers of

The a-axis of crystal is radially oriented in a fiber.

cross-section

microfibril microvoid
surface

void-free region
$< 0.2 \ \mu$m

longitudinal-section

microfibril   microvoid

PBO molecules are highly oriented in the microfibril.
(orientation factor > 0.95)
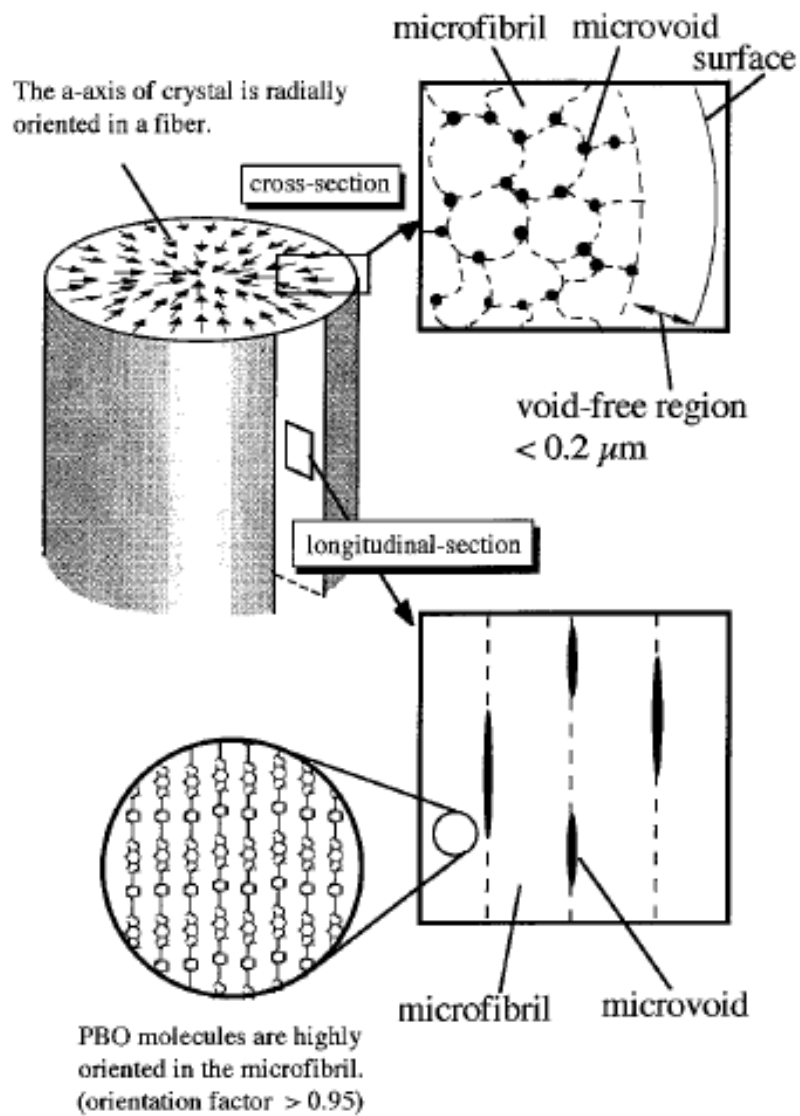
Figure 1.10: Structural model showing microfibrils, microvoids, and skin structure for PBO fiber [8]. Note the microvoids in the fiber, and its *bundle of broom straws* structure.

nylon. This type of armor was typically not worn by police officers unless a specific, immediate threat was perceived.

In 1973, a joint project between the Department of Justice and the Department of Defense was undertaken to develop a lightweight protective armor to be worn by key public officials. In the course of this testing, several new materials were tested for ballistic resistance and compared to nylon, which was the most common material used at that time for body armor. One new nylon-type material supplied by DuPont showed significant promise in these early trials. This material later became known as Kevlar-29, or poly(p-phenylene terephthalamide), or PPTA [1]. The development of this new ballistic material offered exciting possibilities to engineers interested in designing lightweight, concealable garments that could protect the wearer from injury due to handguns. Originally developed during a search for new tire cord materials, PPTA was first known as experimental fiber PRD-26 and then PRD-49-IV. It can easily be woven into a variety of different fabric constructions, making it ideal for ballistic-resistant garments [9].

Once PPTA's usefulness in the construction of body armor had been recognized, several questions related to evaluating various designs had to be solved, including what degree of threats should armor be expected to protect against, and what degree of injury was acceptable. Since common handguns dominated the available statistics for firearms that had been confiscated, used in assaults, and had caused injury or death in assaults, efforts were focused on developing armor to stop these threats. Velocities for the test rounds were established using test firings of weapons through a chronograph to measure projectile velocities. The next issue for

determining the degree of acceptable injury was more difficult. In the course of stopping a projectile, body armor undergoes a rapid deformation resulting in blunt force trauma injury to the wearer. The deflection of the armor while stopping a projectile is typically called either *backface deflection* or *backface signature* of the armor. The researchers involved convened a multidisciplinary panel to review all available data for blunt trauma injury on either animals or humans. Several conclusions were drawn from this work. First, the researchers acknowledged a general scarcity of empirical data relevant to non-penetrating projectiles and the evaluation of the effectiveness of body armor. Of the available data sets, none completely examined all of the parameters considered important for blunt trauma assessment. Further complicating matters, inconsistencies in the test methodologies between individual studies precluded broad data correlation between studies. Despite these challenges, predictive and experimental models were modified and developed during this effort, however the validation of these models were restricted. It was clear, however, that blunt trauma injuries behind armor were life-threatening, and the researchers recommended that criteria be developed to measure the backface signature and reduce it below a level that could cause "...serious injury or death" [9]. Eventually, correlations were drawn between injury to goats and humans that culminated in a backface signature criteria of less than 44 mm indentation in Roma Plastilina Type Number 1 clay, which is still used in modern body armor standards [10].

1.3.1 First Save

By 1975, a pilot program using vests designed in the 1973 study was initiated. Field testing involving 5000 police officers from 15 urban police departments began in the summer of 1975. On December 23, 1975, Officer Raymond T. Johnson, one of the officers in this pilot body armor program, was waiting to checkout at a local market that had been the target of frequent burglaries. A robber entered the store, brandished a weapon, and demanded money. Officer Johnson confronted the suspect and was shot twice in the torso during a violent struggle, but survived due to the protection of his experimental body armor. During the 1 year field test, an additional 16 officers were saved by their experimental body armor [11]. By the late 1970s, body armor was widely available for police officers, with wear rates increasing each year. To date, over 3000 officers have been saved by their body armor [12].

1.3.2 Attorney General's Safety Initiative

Twenty-eight years after the first save was recorded, the first failure of body armor against a threat it had been rated to stop occurred. On June 23, 2003, Forest Hills, PA police officer Edward Limbacher was performing surveillance against a drug suspect. Upon opening the door of his unmarked vehicle, the suspect fired, striking Officer Limbacher with .40 caliber rounds (which are used in body armor testing, and should have been stopped by his armor). A shot to the abdomen perforated the vest. Officer Limbacher survived but sustained serious injuries [11]. As previously mentioned, this was the first instance of an armor being perforated by a threat it

had been rated to stop. Focus within the law enforcement community immediately turned to the material the armor was made from- a new material called Zylon, or poly(p-phenylene-2,6-benzobisoxazole). Significant concern within the law enforcement and research communities about the safety of this material led then Attorney General John Ashcroft to announce a Body Armor Safety Initiative "...to address the reliability of body armor used by law enforcement personnel and to examine the future of bullet-resistant technology and testing." in November 2003 [13].

1.4   PBO Field Failure

In response to the Attorney General's initiative to examine failures of soft body armor containing the material poly(p-phenylene-2,6-benzobisoxazole), or PBO, the National Institute of Justice (NIJ) determined that a significant revision of the performance standard for ballistic body armor was required. One area that had not previously been examined was the long term, or field performance of body armor. Much research was conducted to investigate the issues with PBO in the field and several papers [14, 15, 16] and reports documenting the degradation of PBO fiber with exposure to elevated conditions of moisture and temperature were published. Once the issues with PBO fibers became clear, NIJ issued "NIJ Body Armor Standard Advisory Notice # 01-2005" to inform the community of body armor end users about the degradation issues with PBO. Concurrently, NIJ issued the "NIJ 2005 Interim Requirements for Bullet-Resistant Body Armor," requiring manufacturers to state that their armor did not contain any material listed on an NIJ

Standard Advisory Notice (e.g., PBO), and requiring that the armor "will maintain ballistic performance (consistent with its originally declared threat level) over its declared warranty period." Long-term performance of body armor was considered during the development of a revised performance standard for body armor. This new standard addresses a number of concerns, one of which was the ability of the armor to withstand environmental and wear conditions that an armor might see over its lifetime. This section describes my development of a soft armor conditioning protocol to help understand how armor may perform in the field.

Previous work has documented a detailed examination of Officer Limbacher's PBO armor in the field [17]. Two key observations from this study were that yarns extracted from the officer's armor showed a 32 % reduction in tensile strength when compared with yarns extracted from new armor, and that infrared spectroscopy analysis of yarns from the officer's vest showed evidence of degradation in the molecular structure of PBO. Further studies at NIST examined degradation of PBO armors under controlled laboratory conditions. A crucial finding from these studies was that PBO fibers degrade when exposed to elevated moisture and temperature, but are stable when exposed to elevated temperature in a dry environment [18]. Studies [19, 20] also showed that PBO yarns were vulnerable to degradation by mechanical wear, showing classical fatigue behavior. Findings from all of this fundamental research formed the basis of the theory behind the soft armor conditioning protocol.

The primary goals of the work are to develop a test protocol that, had it been in place prior to 2003, would catch the problems with PBO-based soft body armor before they appeared in the field. This protocol should neither under- nor over-

expose armor with respect to the environment that armor is expected to encounter during its lifetime. It quickly became clear that relating this protocol to an exact period of time in the field would be impossible. Body armor is made up of many different materials, all of which show different rates of degradation with exposure to a given set of conditions. To date, very little work has been published on artificial or accelerated aging of fibers used in body armor.

Work is currently underway to develop the relationship between exposure at conditions of low temperature to conditions at high temperature. However, mechanical wear still remains a challenge. The conditioning protocol does not predict the field service life for armor.

1.5   Previous Armor Service Life Prediction Efforts

Historically, there have been several efforts to assign an expected service life to body armor. Two studies are typically cited, one undertaken by DuPont in the mid-1980s [21] and one undertaken by NIST (then the National Bureau of Standards, NBS) published in 1986 [22]. The DuPont study indicated that a reduction in ballistic performance as measured by ballistic limit, or V_{50} testing, was seen after 3 to 5 years of use, but that a reduction in performance was better correlated to heavy use than to the age of the poly(p-phenylene terephthalamide), or PPTA, armor. As a result of this study, DuPont recommended that armor be replaced after 5 years, which caused some controversy in the law enforcement community [21, 23, 24, 25, 26, 27]. The NBS study examined 24 sets of 10 year old armor of the same 100 % woven

PPTA design, manufactured at the same time and distributed to various law enforcement agencies. The sample set of armors was distributed across various climates and saw various levels of wear, encompassing a range from never issued to heavily worn. The author concluded that armor stored under warehouse conditions maintained its full ballistic performance for at least 10 years, and perhaps indefinitely. The author also concluded that light to moderate wear may improve ballistic performance, and that heavy wear might slightly reduce ballistic performance. It is important to note that the limited sample size of this study makes it difficult to draw meaningful conclusions about the long term performance of armor in the field [22].

In more recent years, several body armor manufacturers have undertaken programs to examine the performance of fielded PBO armor by retrieving vests from the field, assigning a wear rating to the vests, and then conducting ballistic limit testing on the vests. Two reports, one from Armor Holdings Product Division [28] and one from DHB Armor Group [29] were both published in 2004. Both reports concluded that there was some loss in ballistic performance with both age and wear of the armor, although the methods used to report these data make it difficult to draw meaningful conclusions about the results. Both armor manufacturers indicated that they felt that used armor still had an adequate margin of safety. A study was also undertaken between 2001 and 2005 by the Technical Support Working Group (TSWG) to examine the effect of environmental conditions on armor performance by exposing shoot packs[1]of various ballistic materials to elevated conditions of moisture and temperature. TSWG operates as a program element under the Department of Defense Combating Terrorism Technical Support Office (CTTSO) and they serve

as "the national inter-agency research and development program for combating terrorism requirements at home and abroad." Due to problems with controlling the exposure conditions used in this study, the results were inconclusive. All materials in this study were severely degraded by the conditions chosen for the exposure. After reviewing the limited body of work that had been conducted on armor service life prediction, it was determined that there was little available to draw on for the development of the soft armor conditioning protocol.

1.6 Selection of Conditions for Accelerated Degradation Testing

1.6.1 Definition of Wear Environment

In an effort to better tailor a revision of NIJ Standard–0101.04 to the needs of the end user community, NIJ issued a Request for Information (RFI) to the armor community, including manufacturers and end users, in the fall of 2005. The RFI stated that *...NIJ is interested, though not exclusively, in operational requirements and testing methodologies that address: Validation of used armor performance; Non-destructive testing/monitoring methods for used armor to ensure ongoing performance; Improved requirements and testing protocols for new armor (e.g., blunt trauma, multi-shot impacts, contact shots); Numbers and sizes of sam-*

---

[1]Shoot packs are a simplified armor analog made by stacking and stitching layers of ballistic-resistant fabric in a construction similar to that that would be found in an armor. Shoot packs are typically square or rectangular, and do not have the protective coverings that would be found in body armor.

ples to be tested; Long-term performance of armor; Artificial armor aging protocols to replicate field use; Quality control and conformity assessments. . . In reviewing the responses to this request, several respondents were contacted. One of these, Mine Safety Appliance (MSA), had a long history in the production and service life prediction of other types of safety equipment. In January 2006, a meeting between was held with MSA to discuss armor aging, in which several approaches were discussed. In this discussion, it was suggested that armor should be robust enough to withstand conditions typically seen during wear and those seen during transit. Based on the previously published guidelines for armor replacement, a typical service life was defined as 5 years, and a typical wear environment was defined as near body temperature and humidities near 100 % humidity (due to perspiration of the wearer). If one defines a typical work schedule as 8 h per day, 5 d per week, 50 weeks per year, this works out to 2000 h of wear per year. If one then expects the typical lifetime of a vest to be 5 years, then that corresponds to 10,000 h of service at the wear conditions. These simple assumptions provided a starting point for the development of the protocol. To maintain the independence of federal government research, no further input was sought from MSA after these initial meetings in the protocol development [30].

A "rule of thumb" in chemical kinetics [31] often applied to accelerated aging of materials is *for every 10 °C increase in temperature, one can expect a doubling of the rate of reaction.* Application of this guideline to the defined wear temperature of 35 °C, results in 10,000 h of aging in approximately 8 weeks at 65 °C. It is important to note that this "rule of thumb" applies to certain reactions that occur

in solution and does not directly translate to reactions of degradation in the solid state. Additionally, body armor is made up of many different types of materials, all of which can be assumed to degrade at different rates. So, while the temperature 65 °C was chosen to accelerate degradation in the armor based on assumptions of a 5 year service life, it definitely cannot be said to predict armor service life because we do not yet know the exact relationship between temperature and degradation rate for ballistic materials.

When attempting to apply the "Rule of Thumb" to accelerated aging kinetics of materials, it is important to keep in mind that elevated temperatures may induce new mechanisms of degradation, rather than accelerating mechanisms of lower-temperature degradation. This is potentially what occurred in the study by TSWG that was discussed previously. For example, if temperature is increased to the point that a material will melt or burn, different chemical reactions will occur, and the results of the accelerated study will not be meaningful. To avoid this potential problem, dynamic mechanical thermal analysis (DMTA), a thermal analysis technique used to study the viscoelastic properties of polymers, was performed on representative fiber samples from the major material classes of body armor prior to temperature selection. DMTA is a technique to examine the A dynamic temperature ramp at a constant frequency of 1 Hz was performed on fiber samples of PPTA, PBO, and ultrahigh molecular weight polyethylene (UHMWPE). These results are presented in Figure 1.11.

This analysis revealed that temperatures exceeding 80 °C might be too high due to changes in the molecular structure of the UHMWPE fibers above this tem-
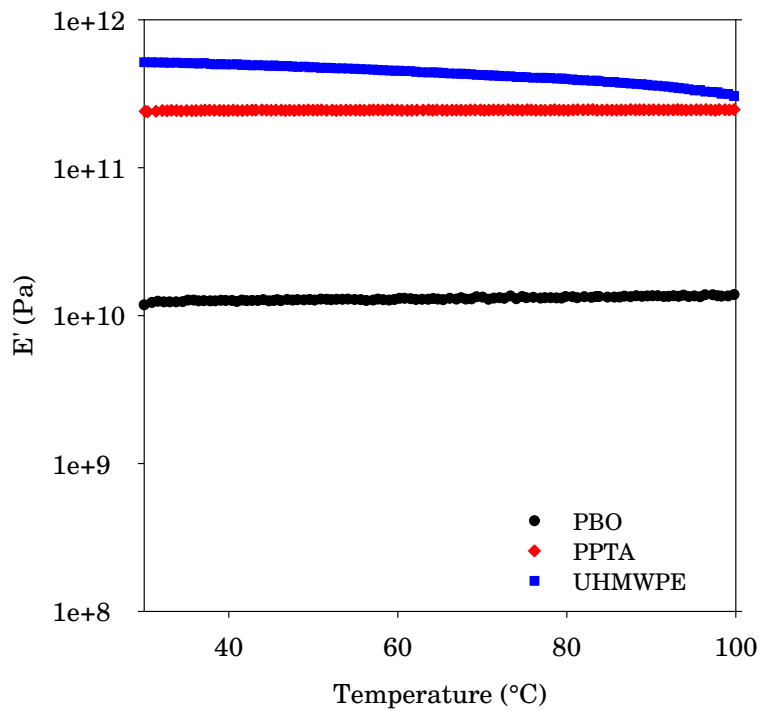
Figure 1.11: Dynamic Temperature Ramp Results for Common Ballistic Fibers. Note that PBO and PPTA are stable through the entire temperature range, but UHMWPE seems to be changing gradually, especially at the higher temperatures.

perature, however the PPTA and PBO fibers remain essentially unchanged in the temperature range studied. In the UHMWPE system, 80 °C is in the range of the α'-relaxation temperature, which is the temperature at which molecular motion within the polymer begins to increase, resulting in a decrease in the modulus of the polymer [32]. DSM Dyneema, a manufacturer of UHMWPE fiber for ballistic applications, published results of an artificial aging study in 2007 indicating that an Arrhenius relationship existed for UHMWPE fibers between 35 °C (the same as our reference base temperature) and 65 °C [33]. Therefore, it was determined that limiting our experiments to temperatures below 70 °C would allow us to avoid introducing new mechanisms of degradation in the fibers during our studies.

1.6.2 Selection of Temperature

Questions also arose regarding the exposure of armor to a temperature of 65 °C—(e.g., is this condition unreasonable in the environment in which body armor will be used?). Anecdotal evidence that officers commonly store armor in the trunks of their cars was frequently brought up during discussions of the armor wear environment. Additionally, armor is typically delivered across the country in trucks. However, the temperature and relative humidity inside a vehicle can vary widely depending on season, geographical region of the country, and location inside the vehicle. In order to answer this question, cooperation was sought from NIJ's Body Armor Technology Working Group (TWG), which is made up of law enforcement and corrections officers who have interest or expertise in ballistics and body

armor. Small, inexpensive universal serial bus (USB)-readable temperature and relative humidity data loggers were purchased and distributed to volunteers from the TWG from across the United States. These were placed inside actual police vehicles throughout different seasons and these data were examined periodically. The same data recorders were also placed inside OLES staff members' personal vehicles during the summer of 2006 in Maryland. A high temperature of 67 °C was obtained in July 2006 from the study of OLES staff member vehicles. Readings around 63 °C were also obtained in California and Illinois during the summer of 2007. An example of representative vehicle data collected during the summer of 2006 in Maryland are shown in Figure 1.12.

1.6.3   Selection of Relative Humidity

Another parameter that must be selected is the relative humidity used in the exposure conditions. One of the participants in the TWG vehicle conditions study, independent of this study, obtained permission to have officers wear an environmental sensor on the outside of their armor. Relative humidities and temperatures outside of the armor are probably close to, but possibly slightly lower than, those seen within the armor. The maximum temperature seen during this study was 41 °C and the maximum relative humidity seen was 76 %. Initially, the protocol was envisoned as a cyclical temperature and relative humidity exposure, with a low temperature condition of 35 °C, 90 % relative humidity. In an effort to maintain consistent conditions at an elevated temperature of 65 °C, high temperature relative
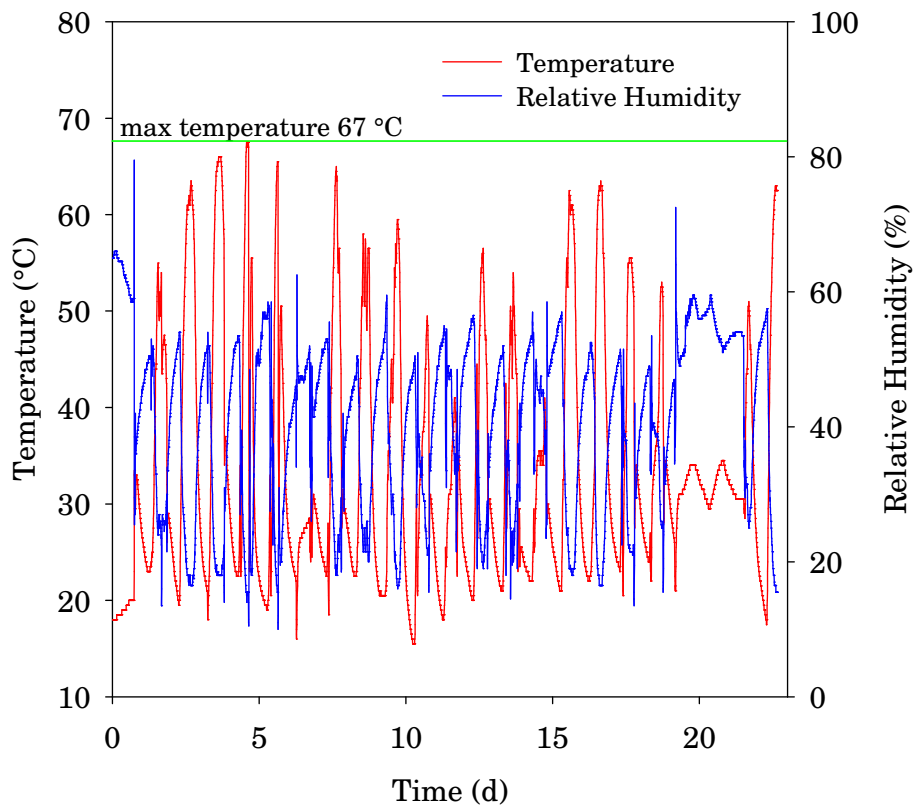
Figure 1.12: Representative Vehicle Temperature and Relative Humidity Data collected during the summer of 2006 in Maryland. Note the maximum temperature observed was approximately 67 °C.

humidities were envisoned as 21 %, which corresponds to the same quantity of water per gram of dry air (0.032 gram water per gram dry air). However, prior to beginning testing, a moisture sorption study was undertaken to examine the moisture uptake by the fiber at the two conditions of temperature and relative humidity. In changing conditions from 35 °C, 90 % relative humidity to 65 °C, 21 % relative humidity, a large desorption was observed in both PPTA (Fig. 1.13) and PBO (Fig. 1.14) fibers. This indicated that the moisture content in the air around the fiber was actually the wrong variable to control—it was more important to attempt to maintain a constant moisture content in the fiber, where the degradation reactions would occur. Fibers absorb and desorb water rapidly to remain in equilibrium with their environment. After examining several conditions, it was determined that 75 % relative humidity at both 35 °C and 65 °C would result in an approximately equal moisture content, as observed for PBO (Fig. 1.15) and PPTA (Fig. 1.16) fibers, so this relative humidity was selected for the initial trials.

1.6.4   Simulation of Mechanical Wear

Determination of the temperature and relative humidity conditions for the soft armor conditioning protocol was relatively straightforward. Defining the wear environment to simulate involved an analysis of possible conditions. However, environmental exposure only provides part of the solution. In the course of normal wear, armor is exposed to flexing, bending, and abrasion. All of these conditions could potentially cause degradation in the ballistic performance of armor. The combina-
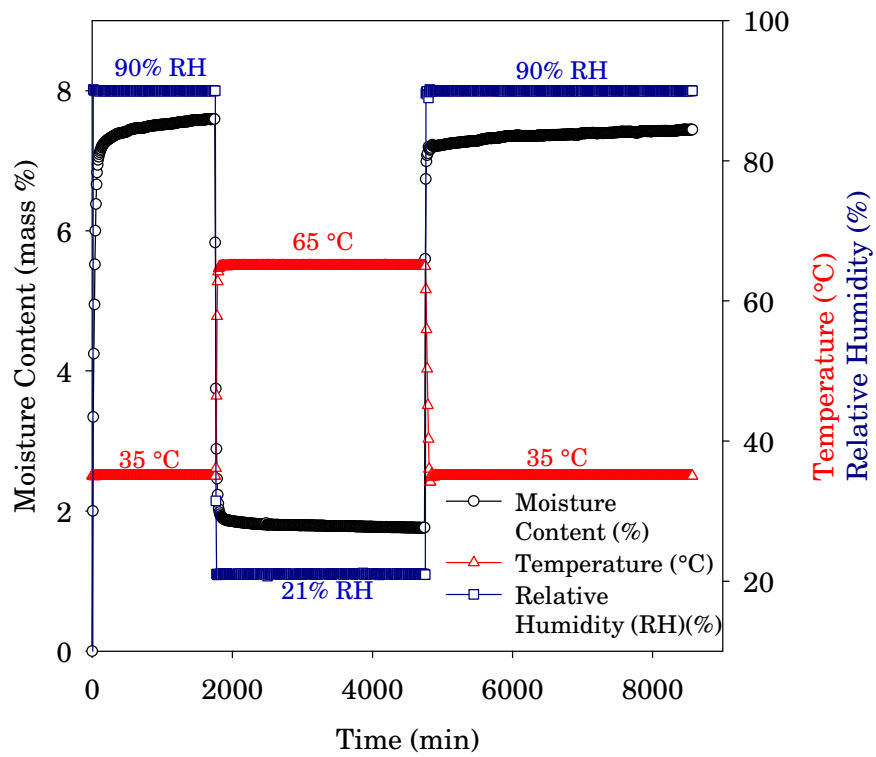
Figure 1.13: Moisture Sorption Data for PPTA (cyclic conditions). Note the large desorptions in the fiber at the higher temperatures.
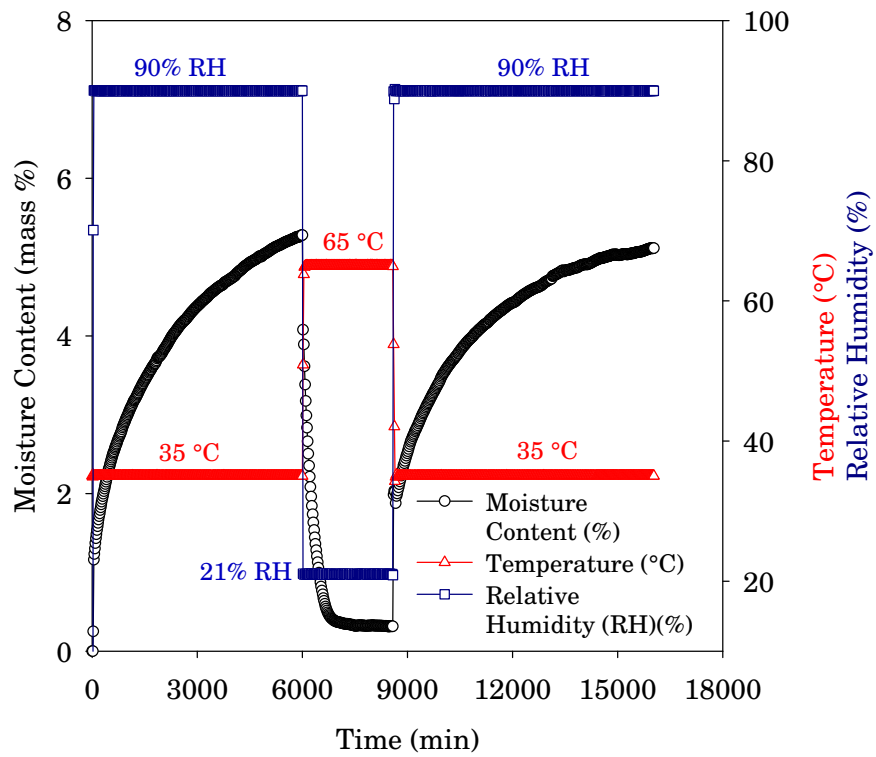
Figure 1.14: Moisture Sorption Data for PBO (cyclic conditions). Note the large desorptions in the fiber at the higher temperatures.
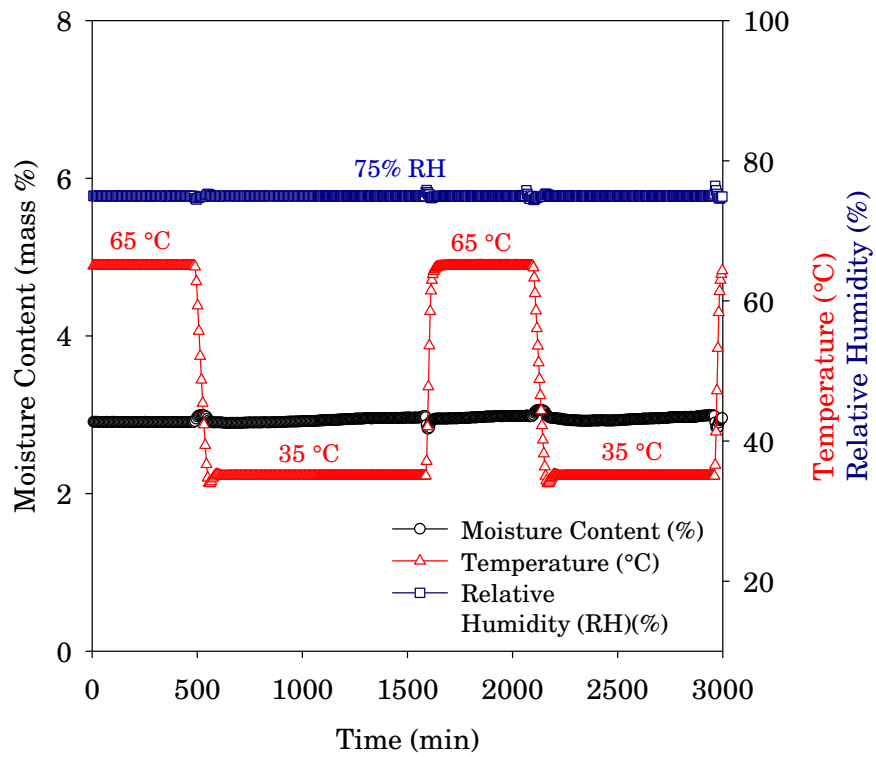
Figure 1.15: Moisture Sorption Data for PBO (constant conditions). Note the relatively steady moisture content of the fiber independent of temperature.
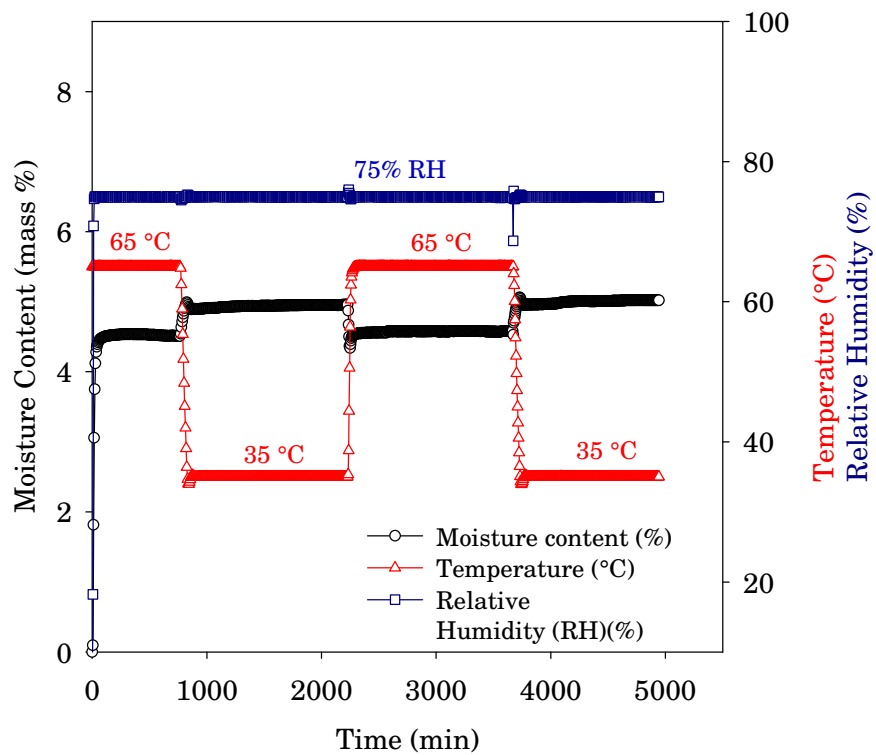
Figure 1.16: Moisture Sorption Data for PPTA (constant conditions). Note the relatively steady moisture content of the fiber, with a change of approximately 0.5 % or less.

tion of mechanical conditions with environmental exposure is the overall goal of the soft armor conditioning protocol. However, the definition of the mechanical wear environment is extremely challenging—tests which provide only abrasion ignore the potential fatigue aspects of folding and bending of the armor. A conservative analysis that a body armor user might bend over (e.g., when entering or exiting a vehicle) 4 times per hour, 40 h per week, 50 weeks per year could result in 8000 folding cycles per year, or 40,000 folding cycles over 5 years. Realistically, almost any movement a wearer makes results in some type of bend or fold in the armor, which could add up to many thousands of cycles per year [19]. Significant work has been devoted to this area by Holmes and co-workers [20]. Tests which create a single fold or bend in the armor create challenges in assessing the ballistic performance of armor, because very little area is available over which to conduct ballistic testing. This would require additional samples and drive up the cost of testing, and ignores the problem of abrasion, which is more difficult to quantify. The best solution to this challenge is to find a method of creating mechanical wear that roughly simulates the same types of wear seen in the field and provides a relatively uniform level of mechanical wear to the entire armor. Tumbling was selected as the solution that best combined simulating the desired damage with cost efficiency, both in terms of capital cost of equipment and quantities of samples. The goal of combining the tumbling with the environmental exposure was initially challenging, so early trials were done by removing armor panels from an environmental chamber, and tumbling periodically during the exposure period.

1.7 Experimental Techniques

A combination of analytical and ballistic characterization techniques were used throughout the development of the soft armor conditioning protocol in an effort to learn as much as possible from each trial. The two analytical techniques that were most commonly used were tensile testing and Fourier transform infrared analysis (FTIR) of yarns extracted from test armor panels. Other analytical techniques that were used include dynamic mechanical thermal analysis (DMTA) and moisture sorption analysis (MSA). Ballistic testing was limited to two techniques—perforation/backface signature (P-BFS) testing and ballistic limit (V_{50}) analysis.

1.7.1 Extracted Yarn Tensile Testing

To obtain yarn mechanical properties, tensile testing of yarns was carried out in accordance with ASTM D2256-02,"Standard Test Method for Tensile Properties of Yarn by the Single-Strand Method," using an Instron Model 4482 test frame equipped with a 91 kg (200 lb) load cell, and pneumatic yarn and cord grips (Instron model 2714-006). The jaw separation was 7.9 cm (3.1 in) and the cross-head speed was 2.3 cm/min (0.9 in/min). In this study, yarns were nominally 40.6 cm (16 in) long, and given 64 twists[2] on a custom-designed yarn twisting device. This level of twist was maintained on the yarns as they were inserted into the pneumatic yarn and chord grips. Strain measurements were made with an Instron non-contacting Type

---

[2]This twist level is within the range recommended by ASTM D2256-02, and was experimentally verified prior to beginning experiments.

3 video extensometer in conjunction with black foam markers placed approximately 2.5 cm apart in the gage section of the yarn. Ten to twelve replicates from each vest were tested to failure. The standard uncertainty of these measurements is typically 3 %, however the error bars generated for plots presented herein are based on the relative standard deviation of the yarn breaking strength, which is in some cases higher than 3 %.

1.7.2   Fourier Transform Infrared Analysis

Infrared analysis was carried out using a Nicolet Nexus Fourier Transform Infrared (FTIR) Spectrometer equipped with a mercury-cadmium-telluride (MCT) detector and a SensIR Durascope attenuated total reflectance (ATR) accessory or a Bruker Vertex 80 FTIR, also equipped with a Smiths Detection Durascope ATR accessory. Air dried by passage through a standard FTIR purge gas generator was used as the purge gas. Consistent tension on the yarns was applied using the force monitor on the Durascope. FTIR spectra were recorded at a resolution of 4 cm^{-1} between 4000 cm^{-1} and 700 cm^{-1} and averaged over 128 scans. Three different locations on each yarn were analyzed. Spectral analysis, including spectral subtraction, was carried out using a custom software program developed in the Building and Fire Research Laboratory's Polymeric Materials Group at NIST. All spectra were baseline corrected and normalized using the aromatic C-H deformation peak at 848 cm^{-1} for PBO and 820 cm^{-1} for PPTA. Standard uncertainties associated with this measurement are typically 4 cm^{-1} in wavenumber and 1 % in peak intensity.

1.7.3 Moisture Sorption Analysis

Moisture absorbed by the yarn specimens during the temperature/humidity exposure period was measured using a Hiden IGAsorp Moisture Sorption Analyzer. The IGAsorp software monitors the temporal changes in the mass of a specimen subjected to prescribed temperature and relative humidity conditions, and calculates equilibrium parameters via curve fitting. Specimens for sorption analysis were prepared by disassembling between 5 mg and 7 mg of yarn into individual filaments to prevent capillarity effects from dominating the sorption process. Specimens were dried in the moisture sorption analyzer at ≈ 0 % relative humidity and the prescribed temperature at which the sorption experiment would be carried out. Moisture uptake was measured at 50 °C and 60 % relative humidity as well as at 60 °C and 37 % relative humidity. The water sorption isotherm was generated using the isothermal mapper mode at 40 °C within a range of 0 % relative humidity to 95 % relative humidity. Results are the average of two specimens. The standard uncertainty of these measurements is typically 0.02 % mass fraction.

1.7.4 Dynamic Mechanical Thermal Analysis

Dynamic Mechanical Thermal Analysis (DMTA) was performed using a TA Instruments RSA III DMTA. Dynamic temperature ramp measurements were generated by loading a single fiber into film/fiber tension clamps, and applying a preload of approximately 1 g force to the sample. The measurement was performed in a strain controlled mode with a strain of 0.1 % at a frequency of 1 Hz. The tem-

perature was increased from 30 °C to 110 °C at a ramp rate of 3 °C/min. For the RSA III, the manufacturer-stated relative standard uncertainty [34] in the force measurement is typically ± 0.0002 g (0.2 mg), and the standard uncertainty in the temperature scale is typically ± 0.5 °C.

1.8   Conditioning Protocol Development

Multiple phases of development were conducted, all utilizing slightly different methods and equipment configurations. Each phase of development will be presented separately to better describe the development of the soft armor conditioning protocol.

1.8.1   Phase I

Initial experiments were performed using separate tumbling and environmental exposure steps. This allowed for "proof of concept" of tumbling as a mechanism to provide mechanical wear, and also allowed for exploration of potential environmental conditions.

1.8.1.1   Sample Description

Two types of test armors were used in the first phase of protocol development. One sample armor was constructed of 20 layers of plain woven 500 denier PBO, with 26 yarns per inch in the horizontal direction and 26 yarns per inch in the vertical direction. The layers of fabric were stitched together in two packs of 10 layers each

with a 2.54 cm (1 in) diagonal quilt stitch to form the ballistic package. This ballistic package was then encased in a stitched moisture-permeable fabric cover and inserted into a lightweight poly-cotton carrier to form an armor panel. The other sample armor was constructed of 25 layers of plain woven 500 denier PPTA, with 24 yarns in the horizontal direction and 24 yarns in the vertical direction. The layers of fabric were stitched together in one package with a 3.18 cm (1.25 in) diagonal quilt stitch to form the ballistic package. This ballistic package was then encased in a standard water-repellent treated nylon fabric cover and inserted into a medium-weight poly-cotton carrier to form an armor panel[3]. All armors were manufactured specifically for this study. The PBO armor samples were designed to be NIJ Standard–0101.04 Level IIA compliant. The PPTA armor samples were designed to be NIJ Standard–0101.04 Level II compliant [35]. Both armor samples were constructed to be the size required for NIJ Standard–0101.04 2005 Interim Requirements [36] compliance testing.

Both sample sets consisted of 13 armor panels. Of these 13 panels, 7 panels were exposed to all conditions and were designated for ballistic testing, 1 sample was exposed to all conditions and was used only for analytical testing, 2 panels were controls for heat and moisture and received no tumbling (one of these samples was designated for ballistic testing and one for analytical testing), 2 panels were tumbling controls and received no heat and moisture exposure (1 of these samples was designated for ballistic testing and 1 for analytical testing), and finally 1 con-

---

[3]The definitions of panel and armor panel used in this document are intended to be consistent with the definitions of these terms as described in Section 3 of NIJ Standard–0101.06 [10].
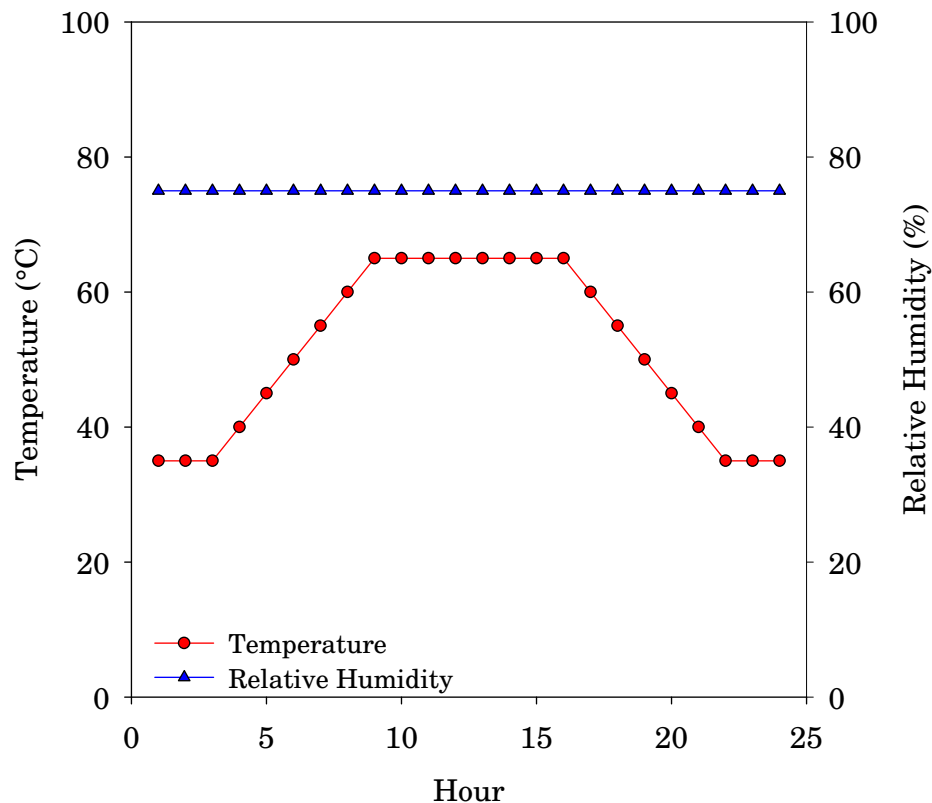
Figure 1.17: Phase I Protocol Cycle. Note that in this phase the relative humidity was held constant, and the temperature was increased from 35 to 65 °C once per 24 hour period.

trol sample received no heat, moisture, or tumbling exposure (was stored at room temperature and humidity of nominally 21 °C and 50 % relative humidity) and was used for analytical testing.

1.8.1.2 Exposure Conditions

As previously discussed, the temperature and relative humidity protocol originally consisted of a cyclical temperature profile between 35 °C and 65 °C, with a constant relative humidity of 75 %, as depicted in Figure 1.17.

Environmental exposures of the PPTA and PBO samples were conducted in

two separate chambers. Vests were hung vertically in the humidity chamber for the environmental portion of the exposures and removed at designated times for tumbling in a standard home clothes dryer (with the heating element disabled). The chamber was returned to room temperature and humidity before removing the armor for tumbling to avoid the formation of a condensing atmosphere in the chamber. Samples were extracted from armor designated for analytical testing after it was removed from the chamber for tumbling. Extractions were performed after the tumbling was completed. An estimate of the total number of revolutions of the armor for the first phase is 194,400 total revolutions, based on 3 h of tumbling, 3 d per week, for 9 weeks. The rotation speed of the standard home clothes dryer was measured at nominally 4.19 rad/s (40 revolutions per minute) using a laser tachometer.

1.8.1.3 Analytical Results

Relative tensile strengths of yarns extracted from the PBO armor panels are depicted in Figure 1.18. This figure shows the reduction of ultimate tensile strength, plotted as percent strength retention, of the PBO armor as a function of exposure time. After 9 weeks, armor exposed to heat, moisture, and tumbling had a tensile strength retention of approximately 62 %. This is comparable to the value that was observed in the back panel of a PBO armor that was defeated in the field, and the value that was ultimately reached after 6 months of aging in a previous study [17]. An interesting observation is that the armor panel that was exposed
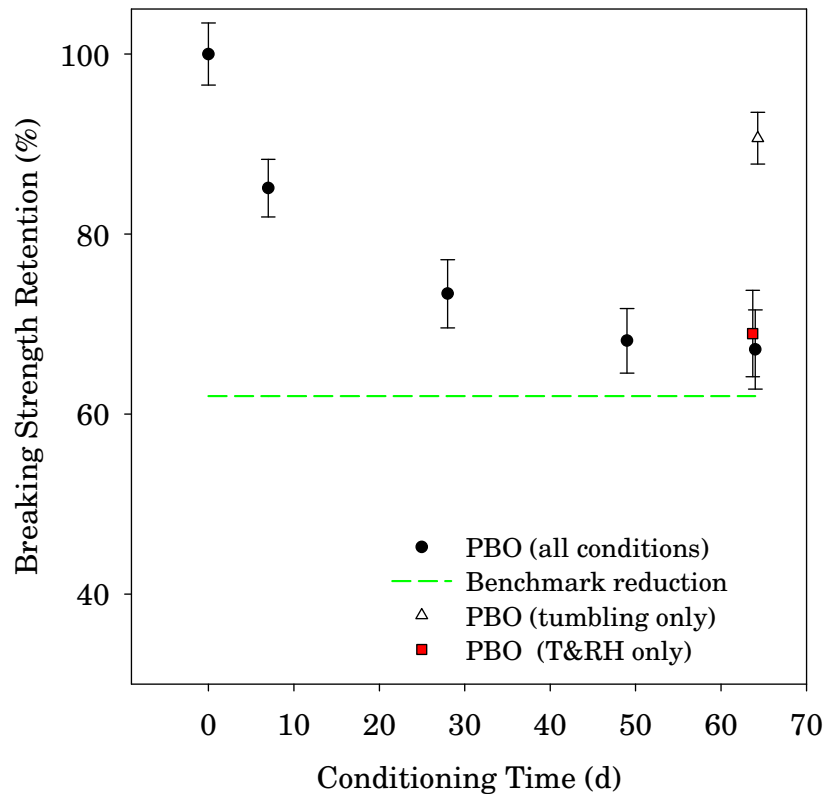
Figure 1.18: Phase I Breaking Strength Retention for PBO. Note the material's degradation when exposed to either the temperature, humidity, and tumbling as compared with temperature and humidity only. The sample that was only tumbled showed a reduction in tensile strength of less than 10 %. The error bars represent the relative standard deviation of the mean yarn breaking strength for 10 to 15 replicates. Points are offset horizontally for clarity.

to only heat and moisture had essentially the same tensile strength retention. The armor panel that was only exposed to tumbling had only a reduction in tensile strength of approximately 8 %. The tumbling used in this experiment did not produce enough mechanical damage to accelerate the effects of the heat and moisture exposure.

Relative tensile strengths of yarns extracted from the PPTA armor panels are depicted in Figure 1.19. This figure shows the reduction of ultimate tensile strength,
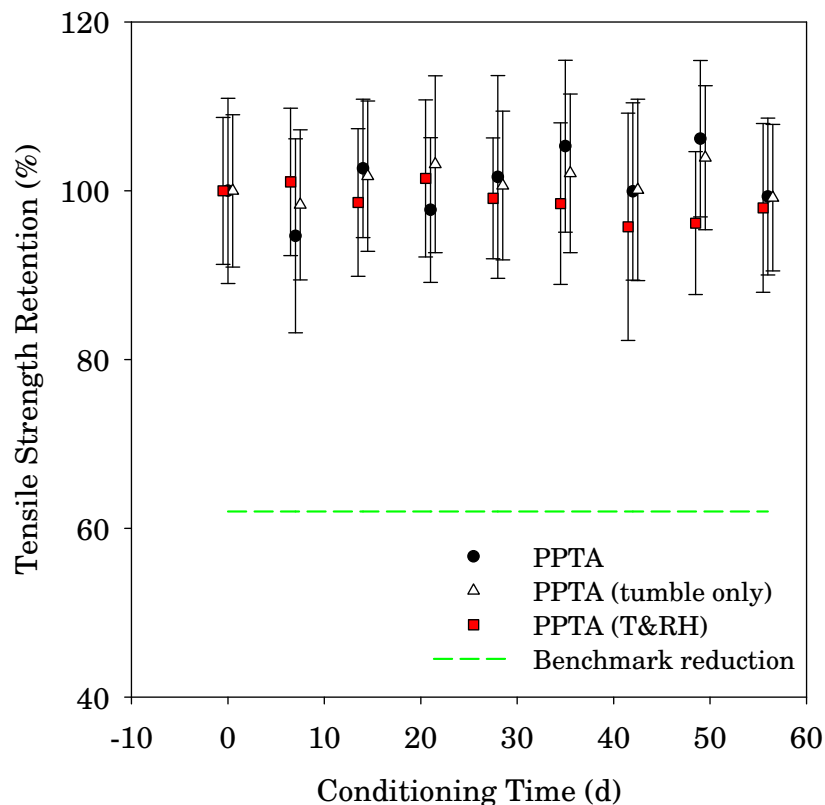
Figure 1.19: Phase I Breaking Strength Retention for PPTA. Note the that the material was apparently unaffected by the protocol. The error bars represent the relative standard deviation of the mean yarn breaking strength for 10 to 15 samples. Points are offset horizontally for clarity.

plotted as percent strength retention, of the PPTA armor as a function of exposure time. After 9 weeks, the armor exhibits essentially no change in tensile strength and was apparently unaffected by the exposure protocol.

In previous studies [17, 18], it has been shown that oxazole ring opening is a major indicator of hydrolysis in PBO. Figure 1.21 (full scale) and Figure 1.22 (expanded scale) show the infrared spectrum of new PBO fibers.

Infrared spectroscopy is a technique by which a sample is exposed to infrared radiation. This radiation is absorbed and converted by an organic molecule into
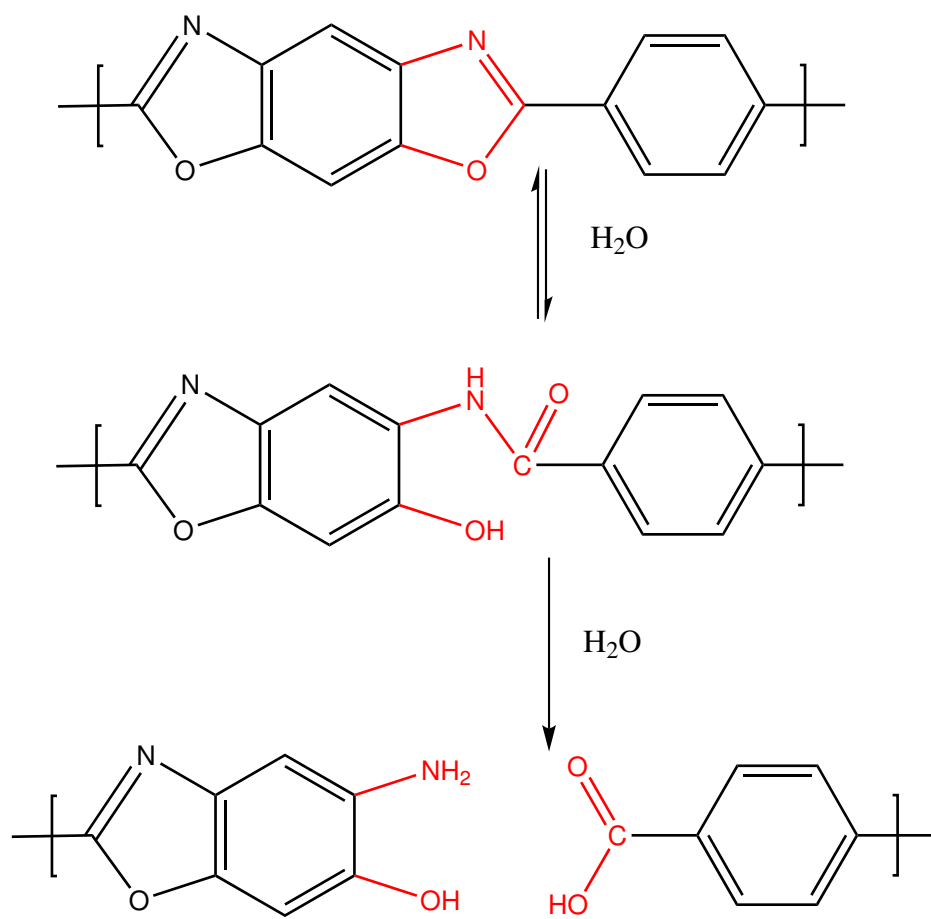
Figure 1.20: Proposed mechanism of hydrolysis for PBO with chain scission [17, 18, 37, 38, 39, 40, 41, 42, 43, 44, 45, 46, 47, 48, 49, 50]

.
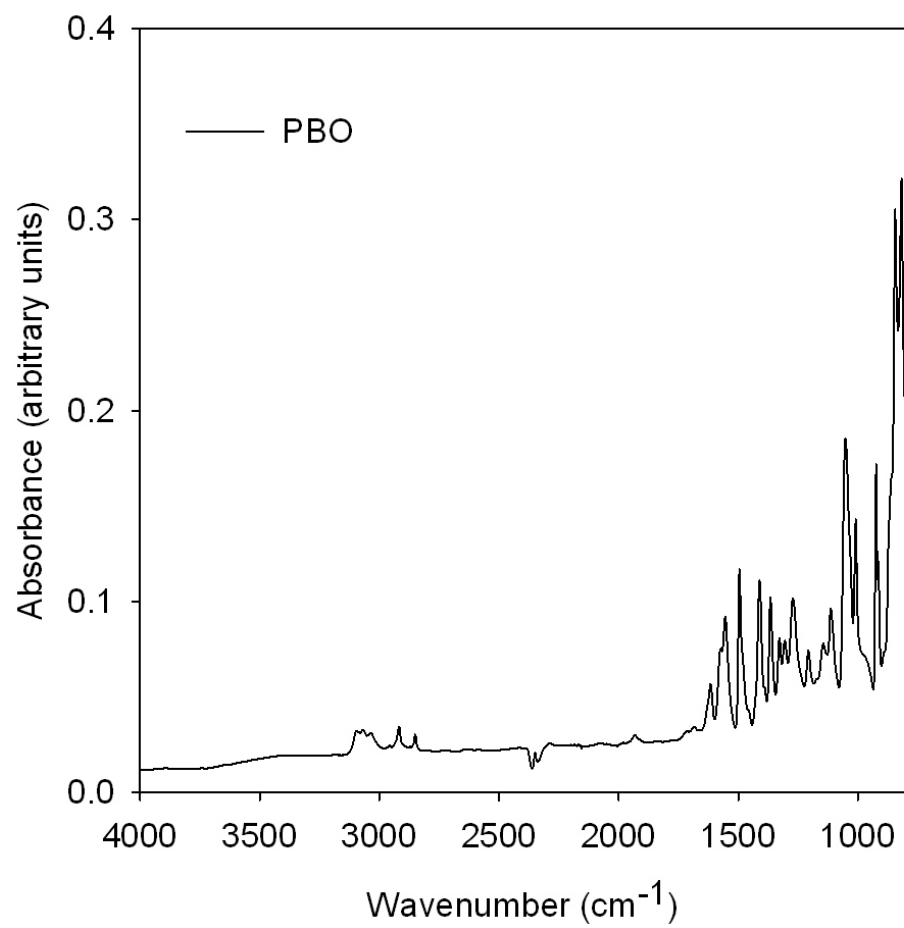
Figure 1.21: Infrared spectrum of new PBO fibers, full scale.
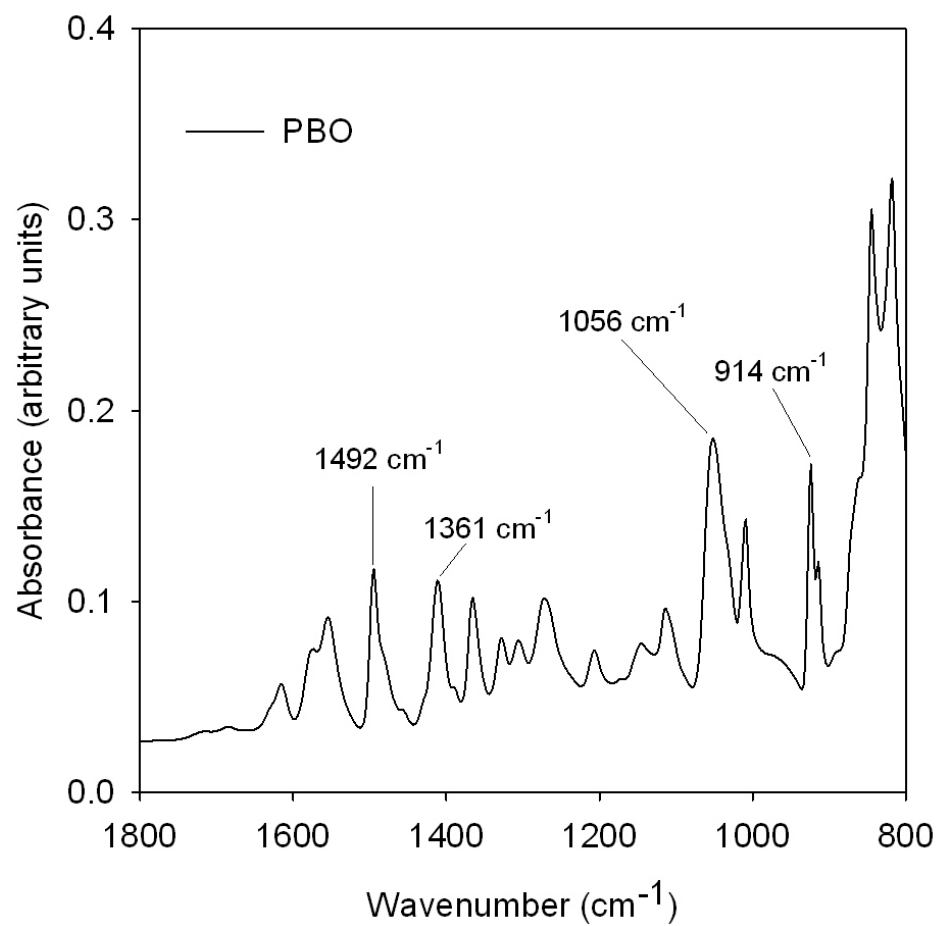
Figure 1.22: Infrared spectrum of new PBO fibers, scale expanded to show fingerprint region. Labeled peaks are attributed to the benzoxazole ring.

energy of molecular rotation or vibration. Certain groups of atoms give rise to absorption bands at or near the same frequency, regardless of the structure of the rest of the molecule. These characteristic absorption bands provide structural information about the molecule. The strength of this absorption is proportional to the amount of molecules present in the sample [51]. Through the use of difference spectra, where the infrared spectrum taken from the unconditioned sample (in this case, from a new vest) is subtracted from the spectra of yarns removed from the vest at different stages of environmental conditioning, the evolution of changes in the chemical structure can be studied [17, 18, 52, 53, 54]. Negative peaks in difference spectra are attributed to the loss of existing chemical structure, and positive peaks are indicative of the formation of new chemical structure [52, 53, 54]. Benzoxazole ring opening is identified by the loss of peaks attributed to the vibrations associated with the benzoxazole ring at 1496 cm^{-1}, 1362 cm^{-1}, 1056 cm^{-1}, and 914 cm^{-1}, and by the formation of a peak at 1650 cm^{-1} attributed to a carbonyl from amide or carboxylic acid, which are potential products of oxazole ring opening [18]. Hydrolysis due to opening of the benzoxazole ring results in losses in these peaks and the formation of a peak at 1650 cm^{-1} attributed to an amide carbonyl or carboxylic acid, which are potential products of oxazole ring opening. This data supports the degradation mechanism given in Figure 1.20. Infrared difference spectra of PBO taken over the course of the exposure study are shown in Figure 1.23.

The difference spectra show marked reductions in the peaks at 1492 cm^{-1}, 1361 cm^{-1}, 1056 cm^{-1}, and 914 cm^{-1}, all of which are attributed to oxazole ring opening. As previously mentioned, standard uncertainties associated with this mea-
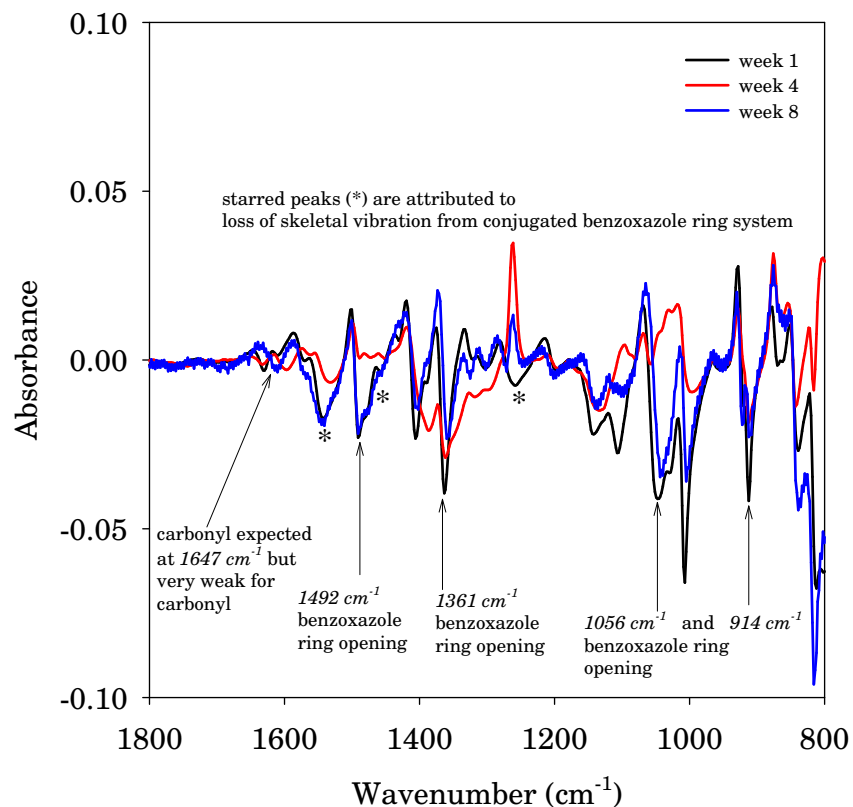
Figure 1.23: FTIR Difference Spectra for PBO exposed to temperature and relative humidity protocol consisting of a cyclical temperature profile between 35 °C and 65 °C, with a constant relative humidity of 75 %, as depicted in Figure 1.17. Spectra were generated by subtracting unexposed sample from exposed samples to look for loss of existing peaks or the formation of new peaks. Note the reduction in peaks associated with benzoxazole ring opening at 1492, 1361, 1056, and 914 cm^{-1}. The carbonyl expected at 1647 cm^{-1} is weaker than expected.

surement are typically $\pm$ 4 cm^{-1} in wavenumber and $\pm$ 1 % in peak intensity, so the slight shift in wavenumbers for the difference spectra may be due to variations in the individual spectra used to create the difference spectrum. However, a large peak at 1650 cm^{-1} to indicate the formation of an amide carbonyl or carboxylic acid as expected by the proposed mechanism is not observed. Detection of this peak using surface-sensitive ATR-FTIR may be reduced because of the abrasion of the yarn due to tumbling causing increased surface roughness.

52
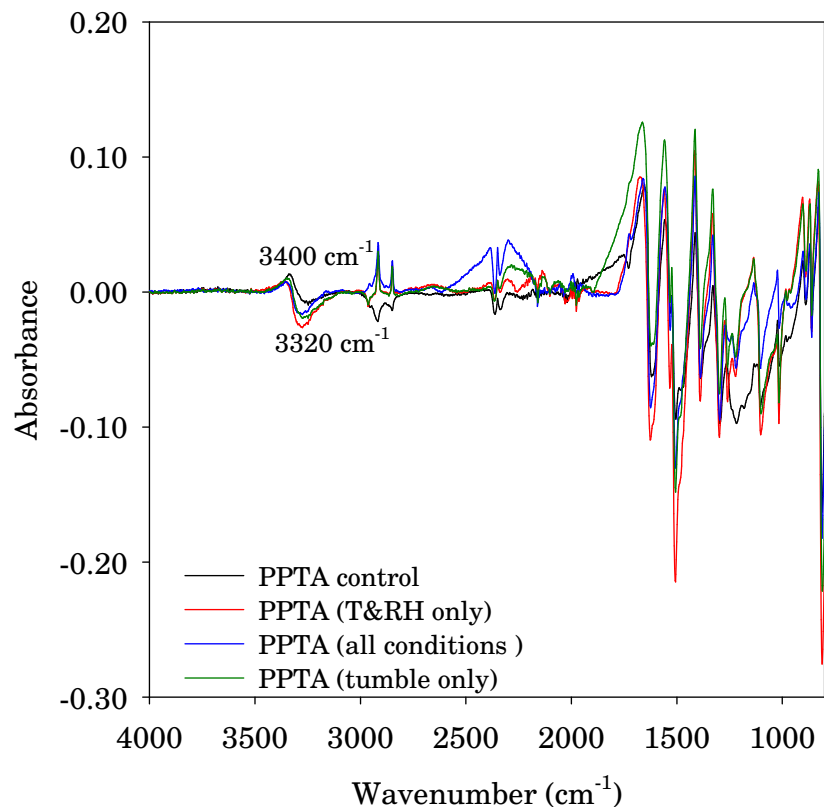
Figure 1.24: FTIR Difference Spectra for PPTA exposed to temperature and relative humidity protocol consisting of a cyclical temperature profile between 35 °C and 65 °C, with a constant relative humidity of 75 %, as depicted in Figure 1.17. The control sample is shown because it was kept sealed and measured over the same time period as the aged samples. The figure is shown at full scale, peaks of interest are labeled.

The difference infrared spectra of PPTA yarns extracted from body armor panels following environmental exposure are shown in Figure 1.24 and Figure 1.25. The body armor panels were divided into four groups–one group was subjected to tumbling alone, one to temperature/moisture exposure alone, one to temperature/moisture combined with tumbling (designated as "all"), and one group was sealed in plastic bags at room temperature of nominally 22 °C to serve as controls.

Infrared analysis and spectral subtraction revealed that all of the conditions, even the control conditions, resulted in some degree of PPTA hydrolysis. A proposed
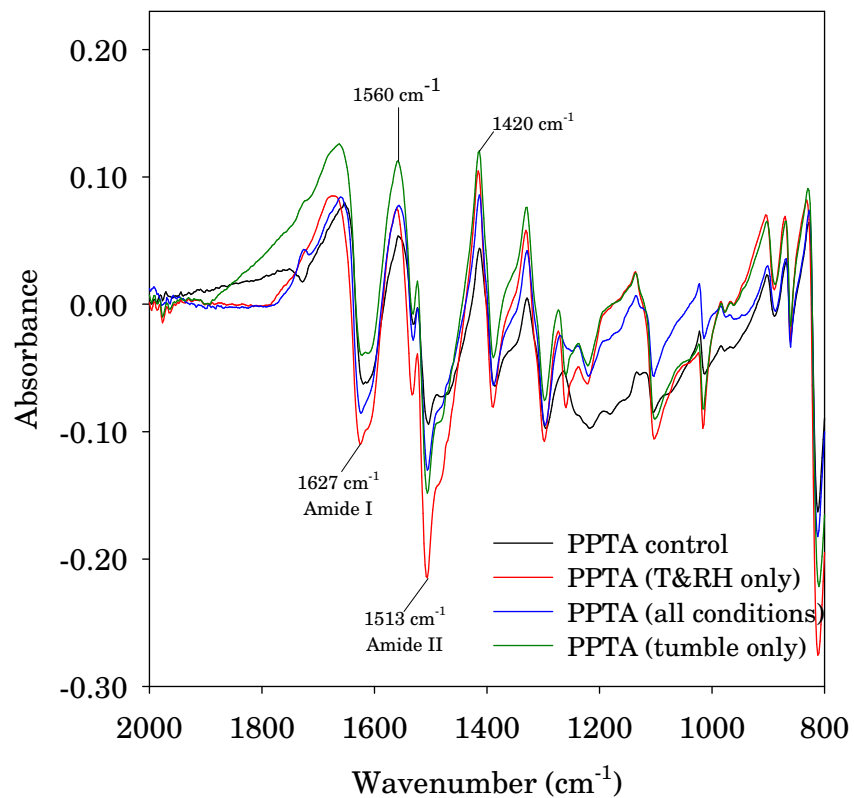
Figure 1.25: FTIR Difference Spectra for PPTA exposed to temperature and relative humidity protocol consisting of a cyclical temperature profile between 35 °C and 65 °C, with a constant relative humidity of 75 %, as depicted in Figure 1.17. Spectra is shown at an expanded scale, and peaks of interest in the fingerprint region are labeled.
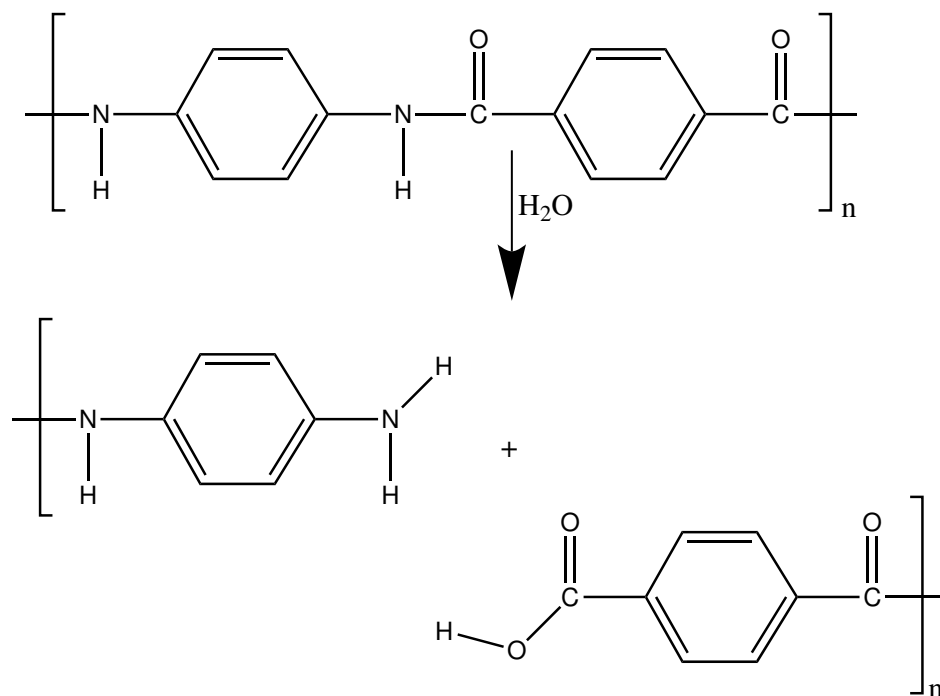
Figure 1.26: Proposed mechanism of hydrolysis for PPTA [55, 49, 50].

mechanism for PPTA hydrolysis is shown in Figure 1.26. The difference spectra in Figure 1.24 and Figure 1.25 shows negative peaks with positions corresponding to the original amide I peak at 1640 cm^{-1} and amide II peak at 1513 cm^{-1} . A new (positive) broad peak is observed at 3400 cm^{-1}, which is attributed to a combination of amine N-H stretching and carboxylic acid OH stretching. New peaks are also observed at 1570 cm^{-1} and 1420 cm^{-1} that are attributed to carboxylate ion stretching. This evidence points to the hydrolysis of the main chain amide group to amine and carboxylic acid.

The control panels that were not subjected to any environmental stresses also underwent hydrolysis. It is likely that as long as moisture is present, hydrolytic reactions in the PPTAs can occur.

To determine the treatment that caused the most hydrolytic damage, intensi-

Infrared Band (cm^{-1})	All	T&RH Only	Tumble Only	Control
3320	3	1	2	4
1627	2	1	4	3
1513	3	1	2	4
1560	2	2	1	3
1420	2	3	1	3

Table 1.1: Rank ordering of PPTA infrared bands; 1=greatest change; 3/4=least change. In some instances the change was the same- in that case both peaks were given the same ranking.

ties of the difference bands were examined and rank-ordered. A tabulation of the major difference bands (except for the bands at 3400 cm^{-1} which were too close to distinguish) and their intensity rankings is given in Table 1.1 below.

No clear or consistent pattern can be found in the above table; the intensity rank order differs for each infrared band. Since the tensile strengths of the yarns extracted from the environmentally conditioned panels did not exhibit any changes over the course of the conditioning treatments, it is possible that these chemical changes are beneath the threshold necessary to influence mechanical properties and may fall within the uncertainties of the infrared measurements.

1.8.1.4 Phase I Summary

This phase of development showed that it was possible to develop a protocol of elevated temperature and relative humidity that would cause damage to PBO armor after 9 weeks of exposure, but would not cause similar damage in PPTA

armor in this time period. However, the 8 week exposure time was deemed too long for practical implementation in the new NIJ Standard–0101.06. After this first phase, reduction of the time required to complete the protocol was the primary goal for Phase II.

1.8.2   Phase II

As was the case in Phase I, in order to meet the timetable for development of the conditioning protocol, initial exposures were performed using separate tumbling and environmental exposure for Phase II. This allowed for "proof of concept" of tumbling as a mechanism to provide mechanical wear, and also allowed for further exploration of potential environmental conditions.

1.8.2.1   Sample Description

Three sets of armors were used in the second phase of protocol development. Two woven armors were the same as those discussed in the Phase I testing. The additional armor was a nonwoven armor, constructed of 30 sheets of unidirectional (UD) laminated UHMWPE fibers. In a UD layer, all fibers are laid parallel, in the same plane. In this study, the sheets of UHMWPE armors were made of 4 layers of fibers, with the orientation of fibers in each layer at 90 ° to the direction of the fibers in the adjacent layers (0 °, 90 °, 0 °, 90 °). The sheets of UHMWPE were stitched together in three places at the top of the vest and one place at the bottom of the vest. Phase II also used two chambers and two sample sets. Chamber 1 contained

15 panels of PBO armor and 6 panels of UHMWPE armor. The PBO panels were tested as follows—in chamber 1, one of the PBO samples was a control and was not exposed to any heat, humidity, or tumbling exposure. Three panels were exposed to only tumbling (two of these were for ballistic testing and one was for analytical testing), two panels were exposed to only temperature and relative humidity (one of these was used for ballistic testing and one for analytical testing), 8 panels were exposed to all conditions and were designated for ballistic testing, and 1 sample was exposed to all conditions and was only tested analytically.

Chamber 2 consisted of 15 panels of PPTA armor and 5 panels of UHMWPE armor. The PPTA panels were used as follows—in chamber 2, one of the PPTA samples was a control and was not exposed to any heat, humidity, or tumbling exposure. Three panels were exposed to only tumbling (two of these were for ballistic testing and one was for analytical testing), two panels were exposed to only temperature and relative humidity (one of these was for ballistic testing and one was for analytical testing), 8 panels were exposed to all conditions and were designated for ballistic testing, and 1 sample was exposed to all conditions and was used only for analytical testing. All five of the UHMWPE panels were for ballistic testing.

1.8.2.2 Exposure Conditions

To shorten the time required to achieve the target degradation from Phase I, the temperature and relative humidity protocol was adjusted to allow for two cycles within a 24 h time period with a temperature profile between 35 °C and 65 °C,

at constant relative humidity of 75 % except on the cooling parts of the cycle to avoid condensation, where the relative humidity was dropped to 65 % as depicted in Figure 1.27.

Environmental exposures of the PPTA and PBO samples were conducted in two separate chambers. Vests were hung vertically in the humidity chamber for the environmental portion of the exposures and removed periodically for tumbling in a standard home clothes dryer (with the heating element disabled). The chamber was returned to room temperature and humidity before removing armor for tumbling to avoid the formation of a condensing atmosphere in the chamber. Samples were extracted from armor designated for analytical testing when it was removed from the chamber for tumbling. An estimate of the total number of revolutions of the armor for the first phase is 115,200 total revolutions, based on 2 h of tumbling, 2 d per week, for 6 weeks. The rotation speed of the standard home clothes dryer was measured at nominally 4.19 rad/s (40 rpm) using a laser tachometer. The load in each individual tumbler was increased in an effort to increase mechanical damage caused by tumbling.

1.8.2.3   Analytical Results

Tensile strength testing of yarns extracted from the armor panels are shown in Figures 1.28 through 1.30. Figure 1.28 shows the reduction of tensile strength, plotted as a percent strength retention, of the PBO armor and PPTA armor as a function of exposure time. After 6 weeks, the PBO sample which was exposed to
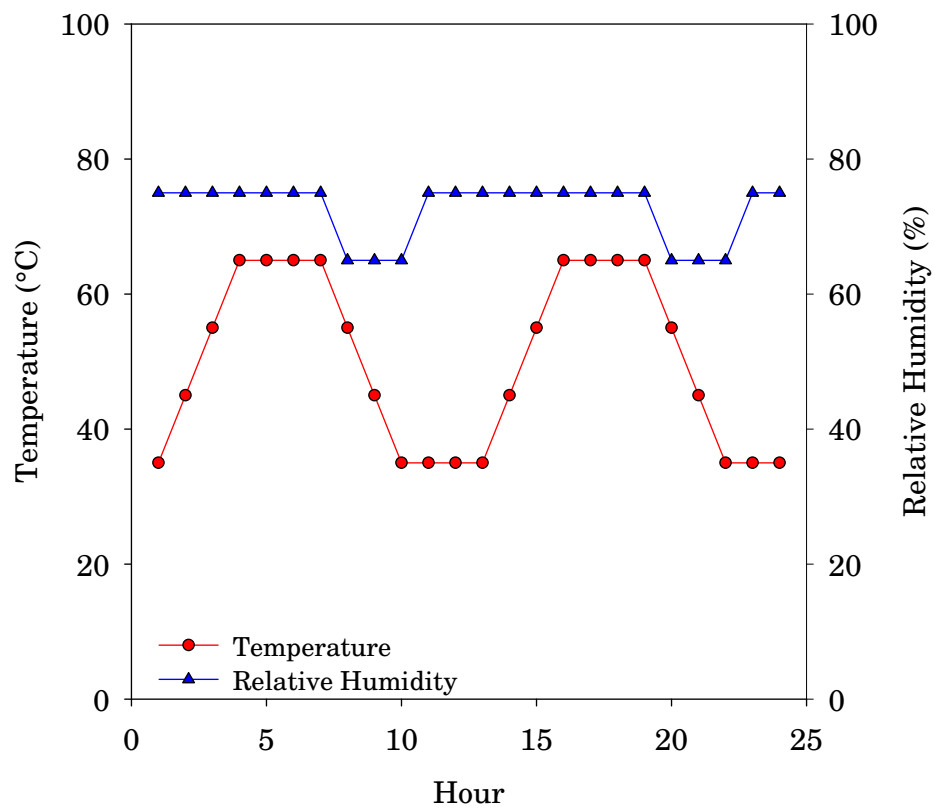
Figure 1.27: Phase II Protocol Cycle. In this protocol, the temperature is ramped twice over a 24 hour period from 35 to 65 °C.

the conditions of heat, moisture, and tumbling had a tensile strength retention of approximately 58 %. This is slightly lower than the target value established by previous studies. By comparison, the PPTA armor showed no reduction in tensile strength in this time. Figure 1.29 shows the results of testing on yarns that had been extracted from vests that were only exposed to temperature and relative humidity. The PBO yarns had an approximate tensile strength retention of 80 %, as compared to no strength reduction in the PPTA armor panels. Figure 1.30 shows tensile strength reduction data for armors that were tumbled at room temperature and humidity. Once again, the PBO armor had an approximate tensile strength reduction of 80 %, but the PPTA armor was essentially unaffected. It is important to note that for the PBO armors, the panels exposed to only temperature and relative humidity and the panels that were exposed to only tumbling had approximately equal strength retentions. This indicates that the contribution of each mechanism (environmental vs. mechanical) to overall degradation in this study was approximately equal, and that the combination of the two mechanisms had a synergistic effect. Infrared results indicated similar trends to those observed in the previous study and are not included here for brevity.

1.8.2.4   Phase II Summary

In this phase of development, the time per cycle was compressed so that two temperature and humidity cycles were completed in a 24 h period, and the armor was taken out and tumbled 3 times per week instead of 2. However, the protocol was only
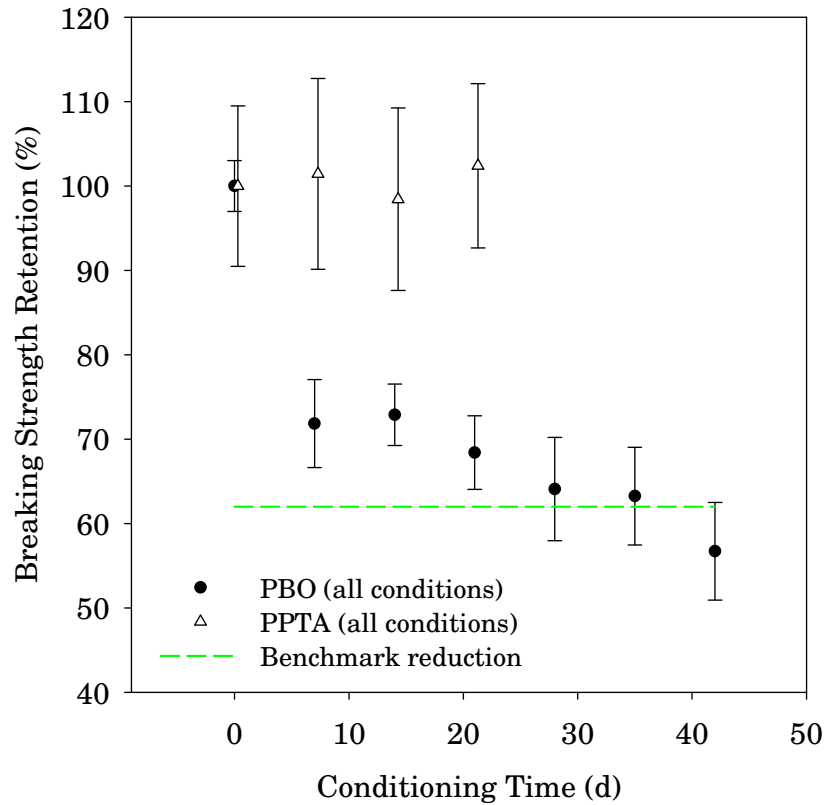
Figure 1.28: Phase II Breaking Strength Retention for PPTA and PBO (all conditions). The error bars represent the relative standard deviation of the mean yarn breaking strength for 10 to 15 samples. Note the difference in behavior between the two materials- PBO degrades much faster than PPTA. This degradation is due to hydrolysis, as shown in Figure1.20. PPTA points are offset horizontally for clarity.
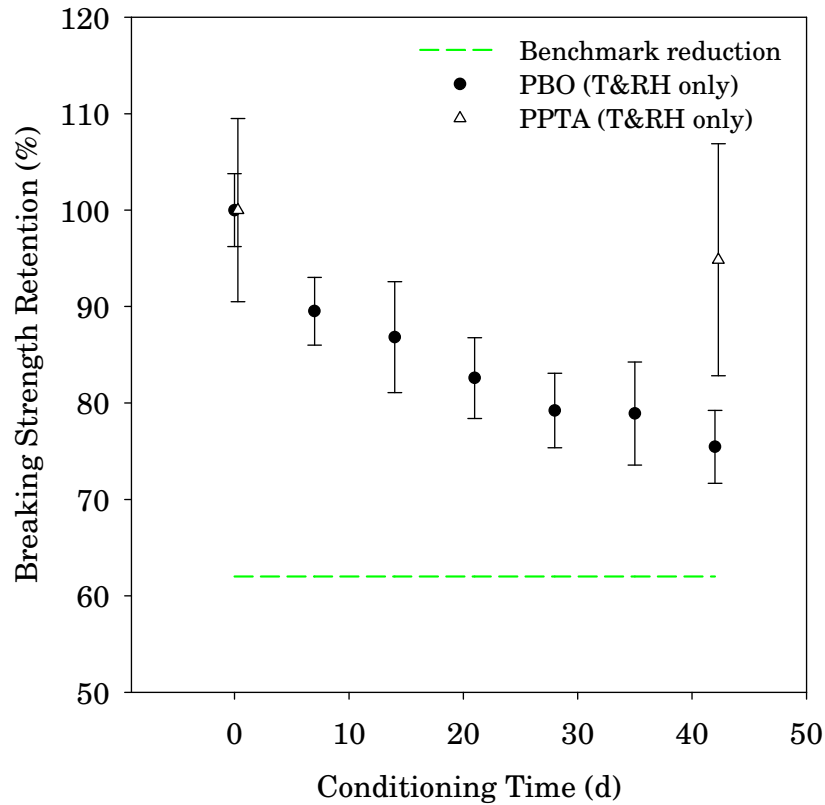
Figure 1.29: Phase II Breaking Strength Retention for PPTA and PBO (T & RH only). The error bars represent the relative standard deviation of the mean yarn breaking strength for 10 to 15 replicates. Note the difference in behavior between the two materials- PBO is degrading faster than PPTA. This degradation is due to hydrolysis, as shown in Figure1.20. PPTA points are offset horizontally for clarity.
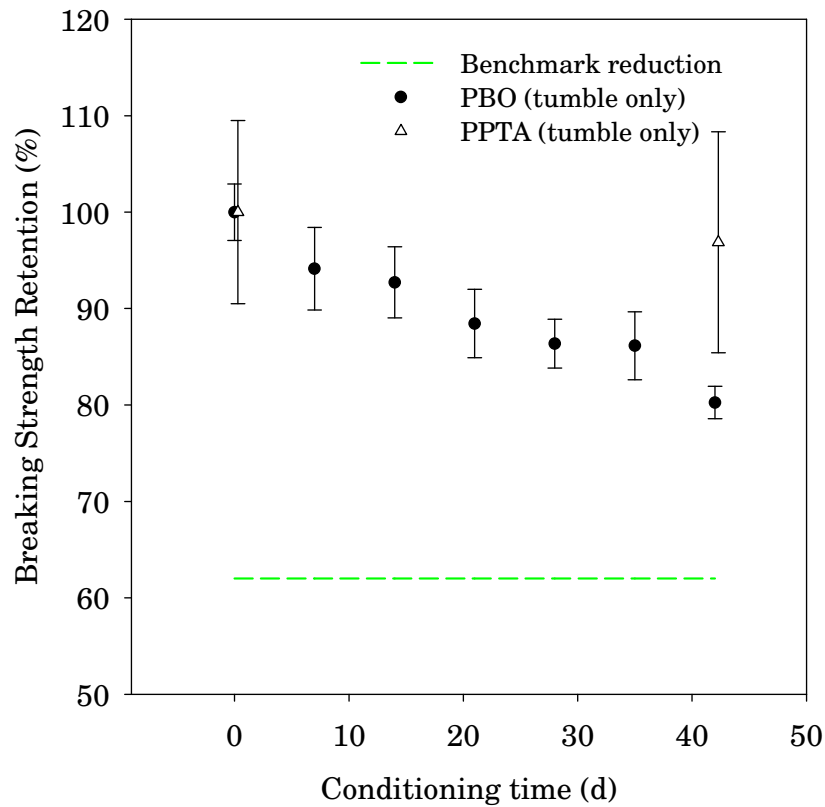
Figure 1.30: Phase II Breaking Strength Retention for PPTA and PBO (tumbling only). The error bars represent the relative standard deviation of the mean yarn breaking strength for 10 to 15 replicates. Note the difference in behavior between the two materials PBO is degrading faster than PPTA. This degradation is due to hydrolysis, as shown in Figure1.20. PPTA points are offset horizontally for clarity.

shortened from 9 weeks to 6 weeks with these changes. The 6 week exposure time was still deemed too long for practical implementation in the new NIJ Standard–0101.06. Therefore, major changes were planned for Phase III in order to further reduce the duration of the test.

1.8.3 Phase III

Phase III is a very significant phase in the development of Soft Armor Conditioning Protocols because it represents the first phase in which mechanical conditioning was combined with environmental conditioning in one test. Details and specifications of the device are availabe in reference [56].

1.8.3.1 Exposure Conditions

In an effort to accelerate the degradation achieved in Phases I and II, the temperature and relative humidity protocol were adjusted to a constant condition of 70 °C and 90 % relative humidity. The rationale behind this change was to shorten the test protocol by performing all of the testing at the high heat, high relative humidity condition instead of cycling between two conditions. Based on the necessary sample sizes for ballistic testing, 16 armor panels were tumbled at a time. Tumbling was performed at 0.523 rad/s (5 rpm) continuously throughout the exposure. A specific time interval for exposure was not set at the beginning of the study, the intention was to track the chemical and physical degradation of the armor to determine when the target reduction in tensile strength had been obtained.

1.8.3.2   Sample Description

Three types of armors were used in the third phase of protocol development. The two woven sample armors were the same as those discussed in the Phase I and Phase II testing. A new set of armor was obtained for Phase III, also constructed of 30 sheets of UD laminated UHMWPE fibers, as described previously. There was no stitching of the sheets of UHMWPE. After ballistic testing was completed, it was discovered that these samples had been fabricated incorrectly. Instead of cutting each sheet of the material separately in order to achieve the correct 0°, 90°, 0°, 90° orientation, the material was rolled out in a back and forth direction and all layers were cut out at once. Additionally, the layers were not aligned properly and portions of layers were missing from all of the armor panels that were manufactured in this way. This construction problem was determined to affect the ballistic properties of the material that were measured after conditioning.

One environmental chamber in which a tumbler had been installed was used in Phase III with two sets of samples. The first sample set consisted of 6 PBO armor panels, 7 UHMWPE armor panels, and 6 PPTA armor panels. One of each type of armor panel was exposed to only temperature and relative humidity and used for analytical testing. One of the PBO armor panels and one of the PPTA armor panels that were exposed to all conditions were used for analytical testing. The remaining armor panels (4 PBO, 4 PPTA, and 6 UHMWPE) were designated for ballistic testing. The chamber was programmed at constant conditions of 70 °C and 90 % relative humidity, with a constant tumbling speed of 0.52 rad/s (5 rpm). A separate

second set of testing was performed to obtain armors that had only been exposed to mechanical conditioning. In this test, 5 PBO panels, 6 UHMWPE panels, and 5 PPTA panels were tumbled at room temperature and humidity at 0.52 rad/s (5 rpm).

1.8.3.3   Analytical Results

Tensile breaking strength testing of yarns extracted from the PBO and PPTA armor panels are depicted in Figure 1.31 through Figure 1.33. Figure 1.31 shows the reduction of ultimate tensile strength, plotted as a percent strength retention, of the PBO and PPTA armors exposed to all conditions as a function of exposure time. After 10 d, the PBO sample that was exposed to the conditions of heat, moisture, and tumbling had a tensile strength retention of approximately 62 %, though we continued the test until day 13. In this phase, for the first time, there was an indication of strength loss in the PPTA armor. Samples that were exposed to all conditions had a tensile strength retention of approximately 88 % after 13 days of exposure. Figure 1.32 compares the PBO and PPTA armor panels that were exposed to only temperature and relative humidity. The PBO armor panels had a tensile strength retention of approximately 77 % and the PPTA armor panels had a tensile strength retention of 90 %. Figure 1.33 shows panels that were exposed to only tumbling. The PBO armor panels had a tensile strength retention of approximately 78 % and the PPTA armor panels showed no reduction in tensile strength. There are a few conclusions that can be drawn from these results. The first is that for PBO,

the test combining environmental exposure and tumbling still had approximately equal contributions of each mechanisms (environmental vs. mechanical) to overall degradation of the material. In the case of the PPTA armor, it is puzzling that there was a slight reduction in tensile strength in the samples that were only exposed to temperature and relative humidity. A possible explanation is that the armor could have been more sensitive to the slightly higher temperature and relative humidity in this study, which could have also been responsible for the slight reduction in strength observed in the armor exposed to all conditions.

Results from infrared analysis of yarns extracted from the PBO armor panels are depicted in Figure 1.34. This figure shows the change in absorbance as a function of aging time for specific infrared bands in PBO. Similar to the infrared analysis presented in Phases I and II of the study, these results show an overall reduction in the peak absorbance at 1606 cm^{-1}, 1302 cm^{-1}, 1257 cm^{-1}, 1136 cm^{-1}, 1036 cm^{-1}, and 909 cm^{-1}, which are typically associated with the benzoxazole and an increase in the peak absorbance at 1635 cm^{-1}, which is associated with carbonyl formation after opening of the benzoxazole ring. These two trends, taken together, indicate that hydrolysis was achieved in the PBO samples. This issue will be further explored later on in this chapter. One may note in Figure 1.34 that there is not a trend indicating a steady decline in absorbance for the benzoxazole ring. There is a sharp decline between day 0 and day 3, then at day 8, there was an apparent increase in the absorbance of the benzoxazole peak. This may be attributed to differences in the samples removed from the armor for testing on the different days, or may be due to the continual mechanical damage occurring in the system due to tumbling.
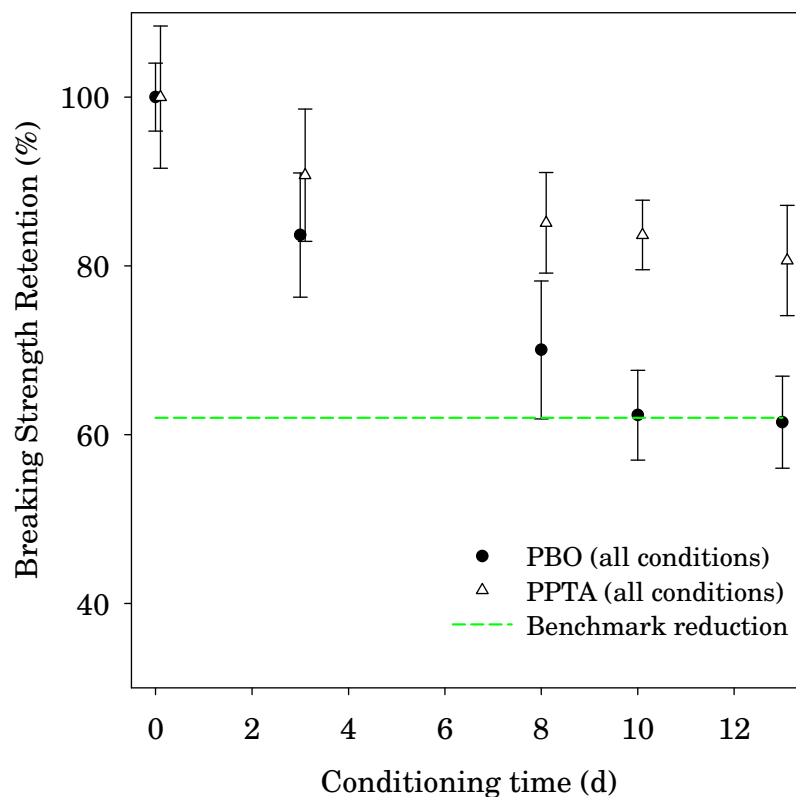
Figure 1.31: Phase III Breaking Strength Retention for PPTA and PBO (all conditions). The error bars represent the relative standard deviation of the mean yarn breaking strength for 10 to 15 samples. PPTA points are offset horizontally for clarity. Note that PPTA appears to be degrading more quickly than in previous studies, and that PBO slightly exceeded the benchmark degradation by the end of the test. The mechanism for PPTA hydrolysis is given by Figure 1.26, and the mechanism for PBO hydrolysis is given by Figure 1.20.
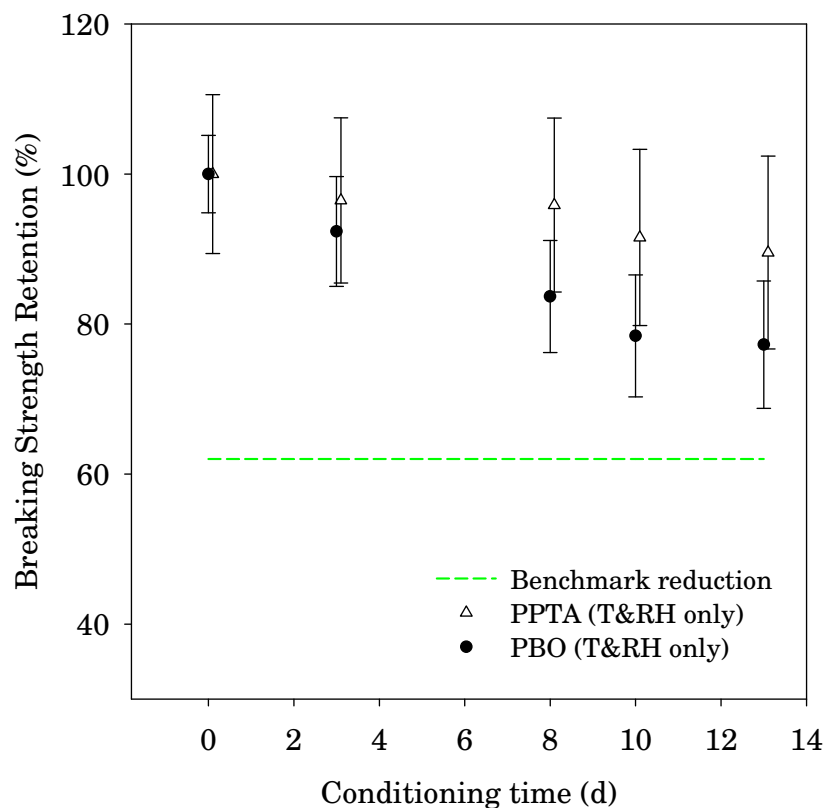
Figure 1.32: Phase III Breaking Strength Retention for PPTA and PBO (T & RH only). The error bars represent the relative standard deviation of the mean yarn breaking strength for 10 to 15 replicates. Note that PPTA appears to be degrading more quickly than in previous studies. PPTA points are offset horizontally for clarity. The mechanism for PPTA hydrolysis is given by Figure 1.26, and the mechanism for PBO hydrolysis is given by Figure 1.20.
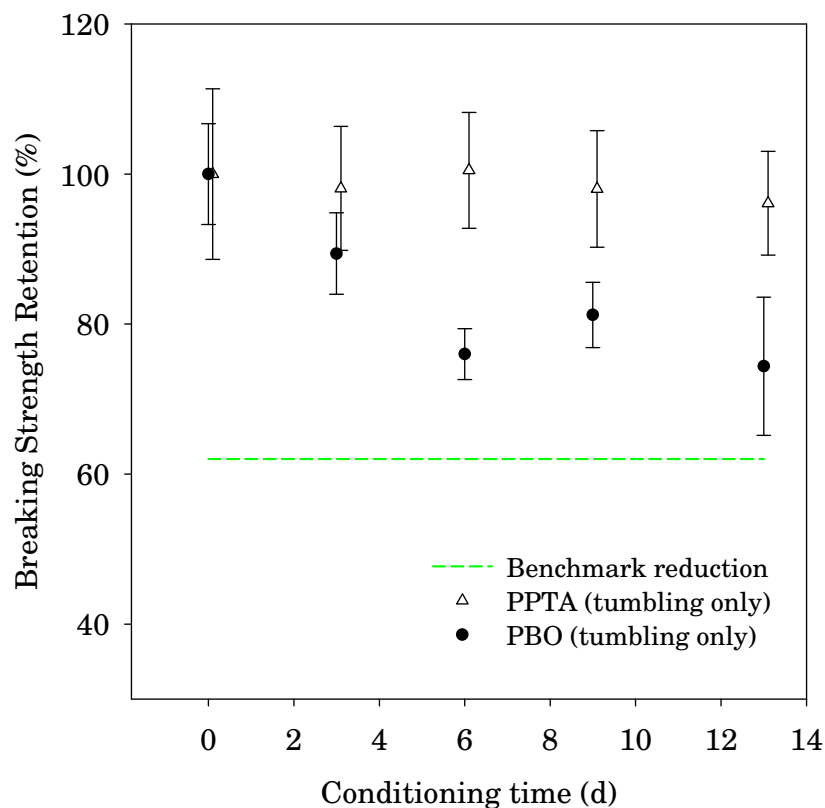
Figure 1.33: Phase III Breaking Strength Retention for PPTA and PBO (tumbling only). Note that PPTA appears to be degrading more quickly than in previous studies. The error bars represent the relative standard deviation of the mean yarn breaking strength for 10 to 15 replicates. The mechanism for PPTA hydrolysis is given by Figure 1.26, and the mechanism for PBO hydrolysis is given by Figure 1.20. PPTA points are offset horizontally for clarity.

This tumbling may abrade the degraded layer of material and expose fresh material underneath, which would lead to an apparent increase in the absorbance of the benzoxazole peak as referenced to data obtained on day 3. Analysis of the PPTA samples indicated similar trends to those seen in previous phases of the study.

1.8.3.4 Phase III Summary

Major changes to the protocol occurred in Phase III. The concept of cyclical conditions of temperature and relative humidity exposure were abandoned in favor of a constant high heat, high relative humidity condition. The tumbling and environmental exposure were combined into one test with the development of a custom-built tumbler inside of the humidity chamber. This tumbler is specified in NIJ Standard–0101.06, and described in Appendix A for reference. While the test presented in Phase III ran for 13 days, the target degradation was achieved before the end of the test. Therefore, it was determined that the changes made in Phase III allowed the exposure time to be reduced to a much more practical 10 days. The 10 d test was deemed acceptable for practical implementation into NIJ Standard–0101.06.

1.8.4 Phase IV

The Phase IV study was designed to verify the conditions selected in Phase III, and verify that 10 d was the appropriate period of time for the test. Conditions of exposure remained the same in this phase as in Phase III.
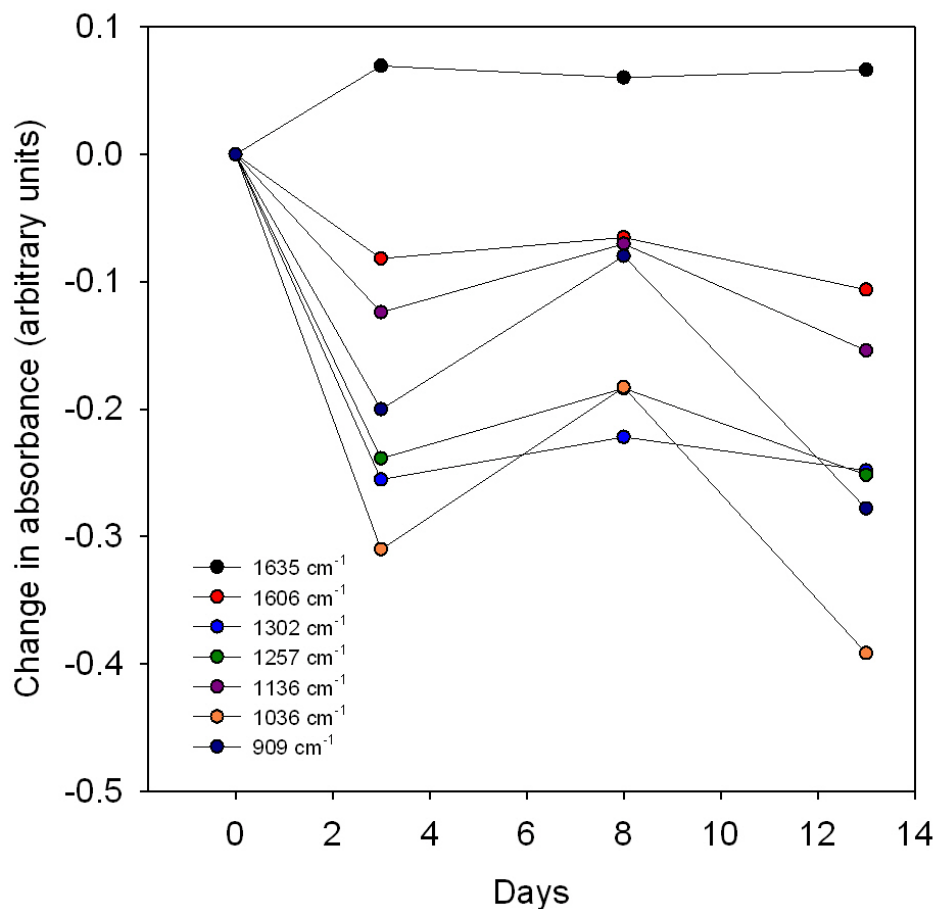
Figure 1.34: Changes in key infrared bands that indicate hydrolysis for PBO fibers as a function of aging time. Hydrolysis occurs via ring opening of the benzoxazole ring at 1606 cm^{-1}, 1302 cm^{-1}, 1257 cm^{-1}, 1136 cm^{-1}, 1036 cm^{-1}, and 909 cm^{-1}. The slight increase in absorbance at 1635 cm^{-1}, is associated with carbonyl formation after opening of the benzoxazole ring. Fibers were exposed to constant tumbling at 5 rpm in a chamber controlled at 70 °C and 90 % RH for 10 days. The standard error in the absorbance of these FTIR measurements is ± 4 %.

1.8.4.1 Sample Description

Three sets of armor samples were used in the fourth phase of protocol development. Two of the armors were the same woven armors as those discussed in the Phase I, Phase II, and Phase III testing. A new set of armor was obtained for Phase IV. This armor model consisted of 18 layers of four plies each of UD PPTA fiber, cross-plied at 0°, 90°, 0°, 90° sandwiched between thermoplastic film inside of a nylon armor panel cover. The panel cover seams were heat-sealed and the interior surface of the panel covers were coated for water repellency. There was no stitching of the sheets of UD PPTA. Phase IV used one environmental chamber in which a tumbler had been installed, and one sample set. This sample set consisted of 5 PBO armor panels, 6 UD PPTA armor panels, and 5 woven PPTA armor panels. One of the PBO armor panels and one of the PPTA armor panels which were exposed to all conditions were used for analytical testing. The remaining armor panels (4 PBO, 4 woven PPTA, and 6 UD PPTA) were used for ballistic testing. The chamber was maintained at constant conditions of 70 °C and 90 % relative humidity, with a constant tumbling speed of 0.52 rad/s (5 rpm).

1.8.4.2 Analytical Results

Tensile breaking strengths of yarns extracted from PPTA and PBO armor panels are depicted in Figure 1.35. As discussed in previous trials, this figure shows the reduction of ultimate tensile strength, plotted as a percent strength retention of both types of armor as a function of exposure time. After 10 d, the PBO sample
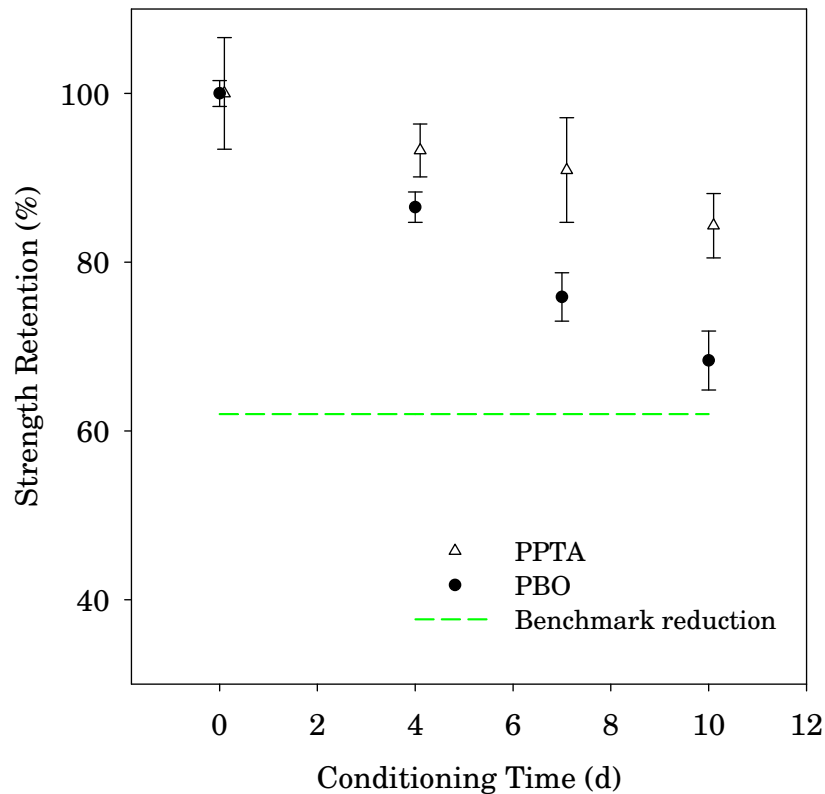
Figure 1.35: Phase IV Breaking Strength Retention for PPTA and PBO (all conditions). The error bars represent the relative standard deviation of the mean yarn breaking strength for 10 to 15 replicates. As in previous studies, PBO degrades much faster than PPTA. PPTA points are offset horizontally for clarity.

that was exposed to all of the conditions of heat, moisture, and tumbling had a tensile strength retention of approximately 68 %. The PPTA sample exposed to all of these conditions had a tensile strength retention of approximately 85 %. This strength loss in the PPTA armor was greater than that observed in previous studies.

Infrared analysis of yarns extracted from both the PBO and PPTA armors was performed, but analysis of this data did not provide any additional information beyond what has already been discussed herein.

1.8.4.3 Phase IV Summary

Minor adjustments to the protocol occurred in Phase IV. The environmental conditions were adjusted to prevent problems with condensation during minor, allowable excursions in conditions of temperature and relative humidity. The protocol used during this phase was adopted as Section 5, the Flexible Armor Conditioning Protocol in NIJ Standard–0101.06.

1.9 Hydrolysis of PBO and PPTA

The work to develop the conditioning protocol, combined with all the previous studies on PBO and Officer Limbacher's vest made it very clear that PBO was susceptible to hydrolysis [17]. Key observations from these study were that yarns extracted from the officer's armor showed a 32 % reduction in tensile strength when compared with yarns extracted from a new armor, and that infrared analysis of yarns from the officer's vest showed evidence of degradation in the molecular structure of PBO (Fig. 1.36). Further studies examined the degradation of PBO armors under controlled laboratory conditions [18]. A crucial finding from these studies was that PBO fibers degrade when exposed to elevated conditions of moisture and temperature (50 °C, 60% RH), but are stable when exposed to elevated temperature (55 °C) in a dry environment. This work resulted in a proposed mechanism of PBO hydrolysis, supported by previous work on hydrolysis of benzoxazoles and oxazoles [37, 38, 39, 40, 41, 42, 43, 44, 45, 46, 47, 48], which could lead to chain scission, and a subsequent molar mass reduction, as depicted in Figure 1.38 [18]. To further

investigate this mechanism, a study was designed to examine hydrolytic changes in the tensile strength and molar mass of PBO and poly(p-phenylene terephthalamide), or PPTA (Fig. 1.37). A proposed mechanism for the hydrolysis leading to chain scission of PPTA is given in Figure 1.39 [55, 57]. The main purpose of this study is to ascertain whether or not the degradation of PBO due to environmental conditioning results in complete (leading to chain scission, **3**) or partial hydrolysis (ceasing at the ring opening step, **2**). This study involved controlled exposures of both PPTA and PBO fibers to hydrolytic conditions as described in Phase III and Phase IV of the conditioning protocol development above. Samples were taken periodically and analyzed using tensile testing to determine their residual tensile strength, molecular spectroscopy for evidence of hydrolysis, and viscometry for a qualitative analysis of changes in molar mass. Confocal microscopy was performed on unexposed and exposed fibers to look for obvious changes in the fiber surface.
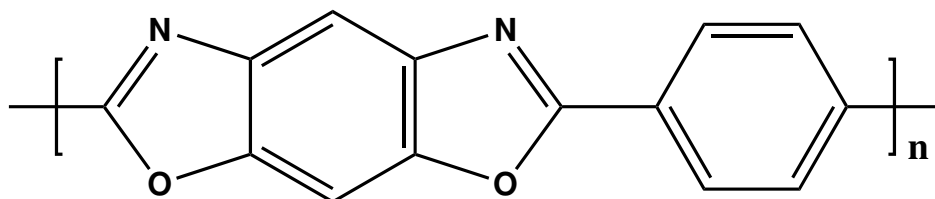
Figure 1.36: Chemical structure of PBO, for reference [17, 4].
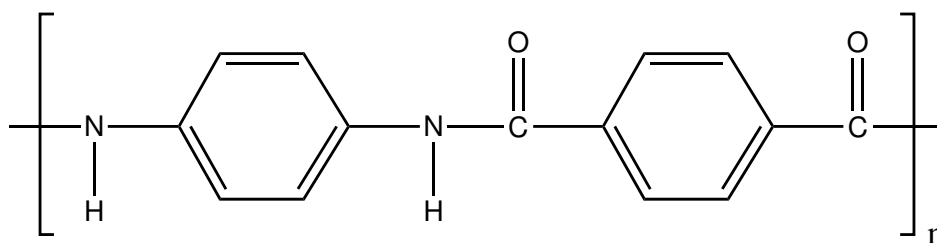
Figure 1.37: Chemical structure of PPTA, for reference [55, 4, 1].
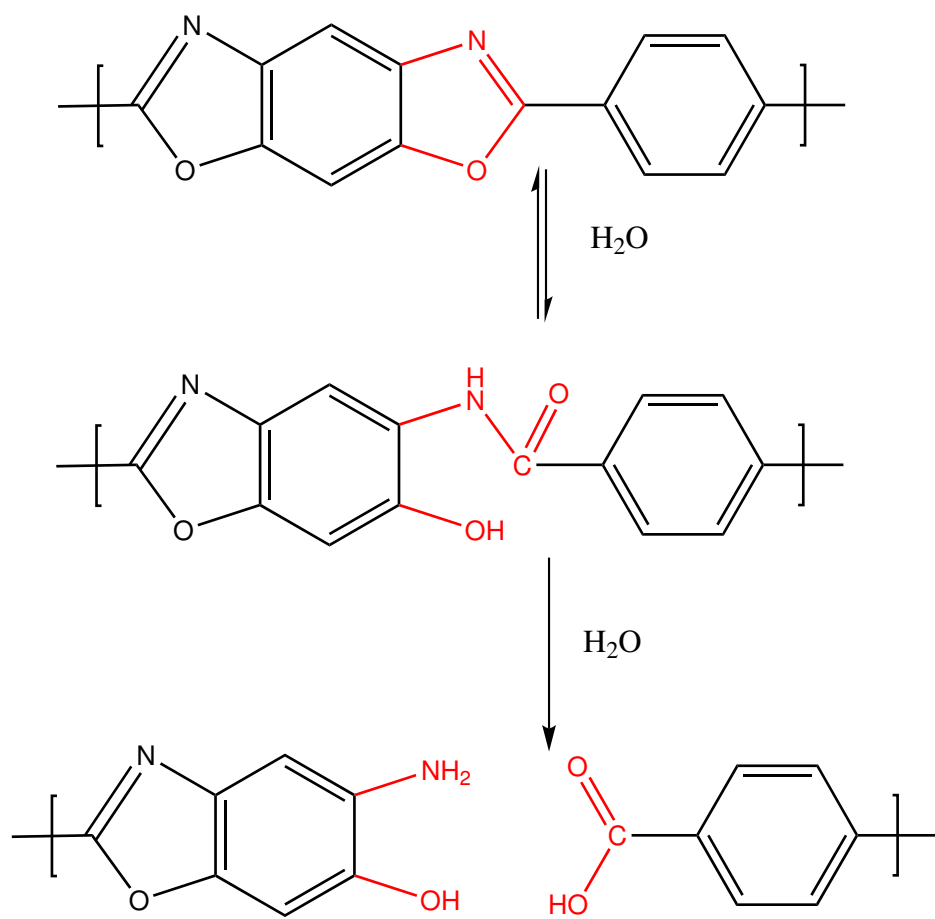
Figure 1.38: Proposed mechanism of hydrolysis for PBO with chain scission [17, 18, 37, 38, 39, 40, 41, 42, 43, 44, 45, 46, 47, 48, 49, 50]

.
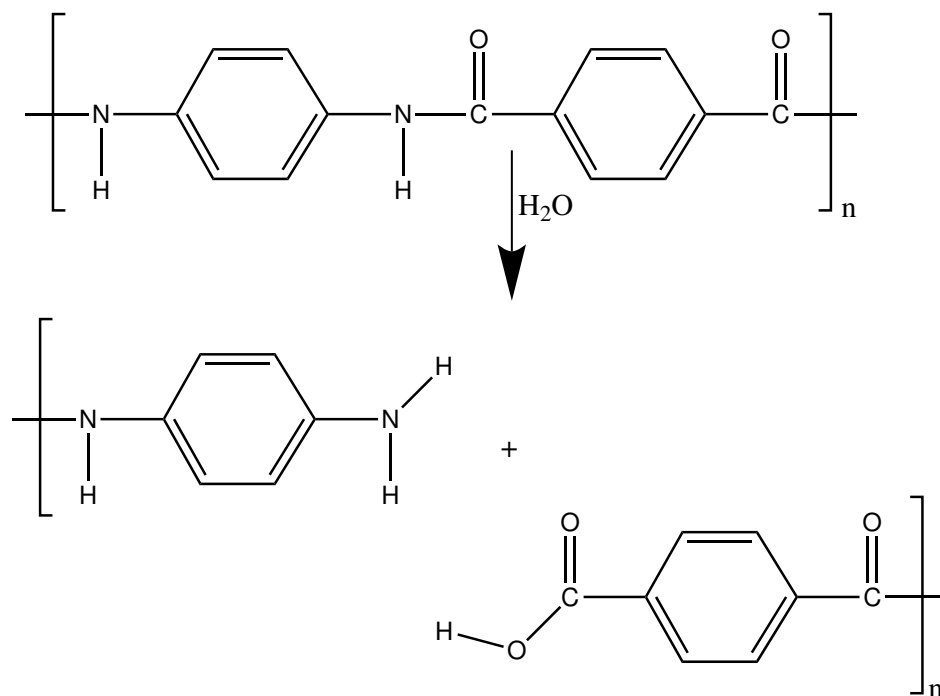
Figure 1.39: Proposed mechanism of hydrolysis for PPTA [55, 49, 50].

1.9.1 Dilute Solution Viscometry

PBO is only soluble in strong anhydrous acids such as sulfuric acid (SA), chlorosulfonic acid (CSA), and methanesulfonic acid (MSA) [7]. Previous viscometry work has been published using MSA as a solvent for PBO, so this solvent was selected for the purposes of this study to compare with literature values [7, 58, 59, 60, 61, 62]. All acid solvents were purchased in their anhydrous form and were used as received. All glassware and fibers were dried using a flow of dry nitrogen, placed in an oven at 35 °C for several hours, and stored in a dessicator filled with dry silica gel prior to use to minimize contamination of the samples with water. For the PBO, a stock solution was prepared at a concentration of 1 mg/mL, from which dilutions were made to obtain samples at concentrations of 0.01 g/dL, 0.03 g/dL, 0.05 g/dL, 0.07 g/dL, and 0.1 g/dL. For PPTA, a stock solution was prepared at

a concentration of 2 mg/mL, from which dilutions were made to obtain samples at concentrations of 0.02 g/dL, 0.10 g/dL, and 0.20 g/dL. All sample solutions were purged with dry nitrogen during dissolution. PBO solutions were prepared at 150 °C on a stirring hot plate and the PPTA solutions were prepared at room temperature on a stirring hotplate. All solutions were prepared and used in the same day to reduce the potential for contamination with water. Prepared solutions were purged with dry nitrogen and stored in a dessicator when not in use. Kinematic viscosities were measured using Cannon capillary viscometers in a thermostatic bath (Koehler K23376) at 25 °C $\pm$ 0.05 °C. The viscometer elution times were in the range of 241 s to 471 s. The standard deviation of the viscometer elution times is approximately 3 %. Standard error for this measurements is generally reported as 1.5 %.

1.9.2   Laser Scanning Confocal Microscopy

A Zeiss Model LSM510 reflection laser scanning confocal microscope (LSCM) was employed to characterize the surface morphology. The incident laser wavelength was 543 nm. By moving the focal plane in the z-direction, a series of single images (optical slices) can be stacked and digitally summed over the z-direction to obtain a 3-D image. All images were collected using the 150x objective and a z-direction step size of 0.1 μm to form a collection of images of different objective planes. These were digitally summed using the software package provided with the microscope. All images shown here are 2D projections created with the microscope software package.

1.10 Evaluation of Extent of Hydrolysis in PBO and PPTA

The molecular spectroscopy shown previously indicated that losses in bands associated with the benzoxazole ring. Previous studies [17, 18] have shown that oxazole ring opening is a major indicator of hydrolysis in PBO. However, based on the molecular spectroscopy results, it is not possible to tell if PBO is undergoing complete hydrolysis which leads to chain scission. A measurement of changes in the molar mass of degraded PBO would indicate whether or not chain scission was occurring.

Previous work has provided a detailed analysis of the application of the Mark-Houwink equation to polymers such as PBO and PPTA [1, 7, 58, 59, 60, 61, 62, 63]. Several papers have focused on the effect of ionic strength (varied by the addition of water and salts such as CH_3SO_3Na, LiF_3CSO_3, or Li_2SO_4) on the solution properties of these polymers [58, 60, 62]. Roitman has shown for low polymer solution concentrations (less than 0.01 g/dL), small amounts of ionizable solutes (such as water) in concentrations of less than 0.1 M can cause anomalous viscosity behavior [58]. In an effort to avoid this problem in this study, the minimum polymer concentration used was 0.01 g/dL.

A discussion of the necessary calculations to perform intrinsic viscosity analysis of polymer solutions to estimate molar mass can be found in many basic polymer science textbooks [64, 65, 66]. Best practices dictate that a researcher interested in molar mass of a polymer also be concerned with molar mass distribution. The presence of low and high molar mass components can affect the viscosity of the

polymer, however in this case such analysis is not performed. PBO and PPTA are only soluble in strong acids, and cannot be readily measured using size exclusion chromatography, as these solvents would cause damage to the equipment necessary to make this measurement. Two other options, light scattering and shear rheology, were also considered, but once again, the use of strong acid solvents in the instruments was not possible. For completeness of this work, a brief discussion of the equations used in this analysis is given here.

The efflux time of each polymer solution in the viscometer, t, was compared to the efflux time of the pure solvent, t_0, to obtain the relative viscosity, η_{rel}, Equation 1.2 and the specific viscosity, η_{sp}, Equation 1.3 [64, 65].

$$\eta_{rel} = \frac{t}{t_0} \tag{1.2}$$

$$\eta_{sp} = \frac{t - t_0}{t_0} \tag{1.3}$$

The reduced viscosity, η_{red}, is the ratio of the specific viscosity, η_{sp}, to concentration of the polymer solution, c, Equation 1.4 [64, 65].

$$\eta_{red} = \frac{\eta_{sp}}{c} \tag{1.4}$$

The inherent viscosity, η_{inh}, is the ratio of the natural log of the relative viscosity, η_{rel}, to the concentration of the polymer solution, c, given by Equation 1.5 [64, 65].

Environmental Conditioning (d)	PBO $[\eta]$ est. by η_{red}	PBO $[\eta]$ est. by η_{inh}	PPTA $[\eta]$ est. by η_{red}	PPTA $[\eta]$ est. by η_{inh}
0	18.78 ± 0.21	20.31 ± 0.31	8.62 ± 0.09	9.01 ± 0.11
4	15.73 ± 0.23	15.84 ± 0.32	7.47 ± 0.06	7.60 ± 0.07
7	11.41 ± 0.08	11.79 ± 0.10	5.95 ± 0.07	6.01 ± 0.08
10	7.60 ± 0.45	7.64 ± 0.49	4.96 ± 0.08	4.96 ± 0.09

Table 1.2: Estimation of intrinsic viscosity with η_{red} and η_{inh} for PBO and PPTA.

$$\eta_{inh} = \frac{\ln \eta_{rel}}{c} \tag{1.5}$$

The reduced viscosity, η_{red}, was plotted as a function of concentration and the y-intercept of this plot is taken as the intrinsic viscosity, $[\eta]$, which can be used to estimate molar mass. This process was repeated with the inherent viscosity, η_{inh}, to obtain two different estimates for intrinsic viscosity, $[\eta]$. The values of the y-intercepts were taken as the intrinsic viscosities as shown by Equation 1.6 and Equation 1.7 [64, 65].

$$[\eta_{red}] = k^{'}[\eta]^2 c + [\eta] \tag{1.6}$$

$$[\eta_{inh}] = k^{''}[\eta]^2 c + [\eta]^2 c + [\eta] \tag{1.7}$$

Estimates of the intrinsic viscosity via these two methods agreed to within 0.4 dL/g, except for the undegraded PBO sample, which only had agreement to within 1.5 dL/g. Values of the intrinsic viscosity estimated by each equation are presented in Table 1.2 for PBO and PPTA.

Figure 1.40 show representative viscosity data obtained for PBO which had

been environmentally conditioned for 4 d and Figure 1.41 shows representative data

for PPTA which had been environmentally conditioned for 10 d.
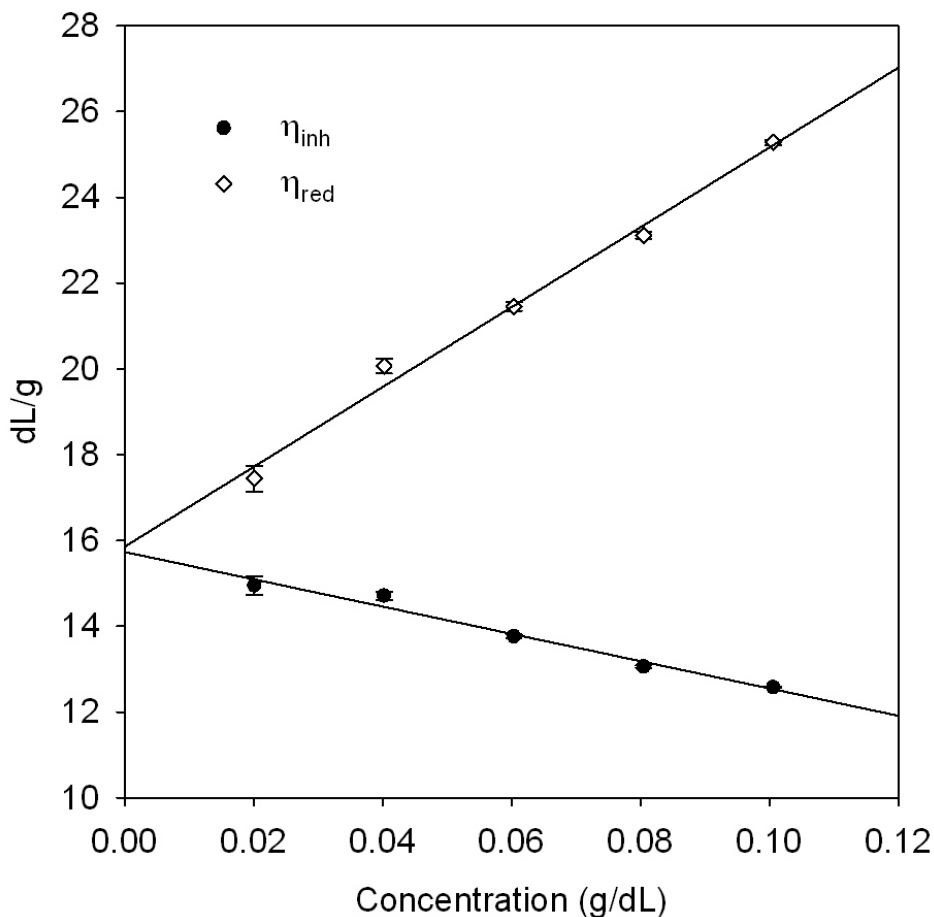
Figure 1.40: Representative viscosity data for PBO which had been environmentally conditioned for 4 d.

For PBO, the highly conjugated structure of the polymer chain from the extended delocalization of π electrons over the benzobisoxazole and phenyl rings results in a very rigid molecular structure [7]. The only possible conformational flexibility is attributed to rotation of bonds between the phenyl ring and oxazole ring [7]. The high degree of orientation of PPTA and PBO fibers is typically ascribed to the formation of a nematic phase at sufficient concentration, that allows the rod-like

84
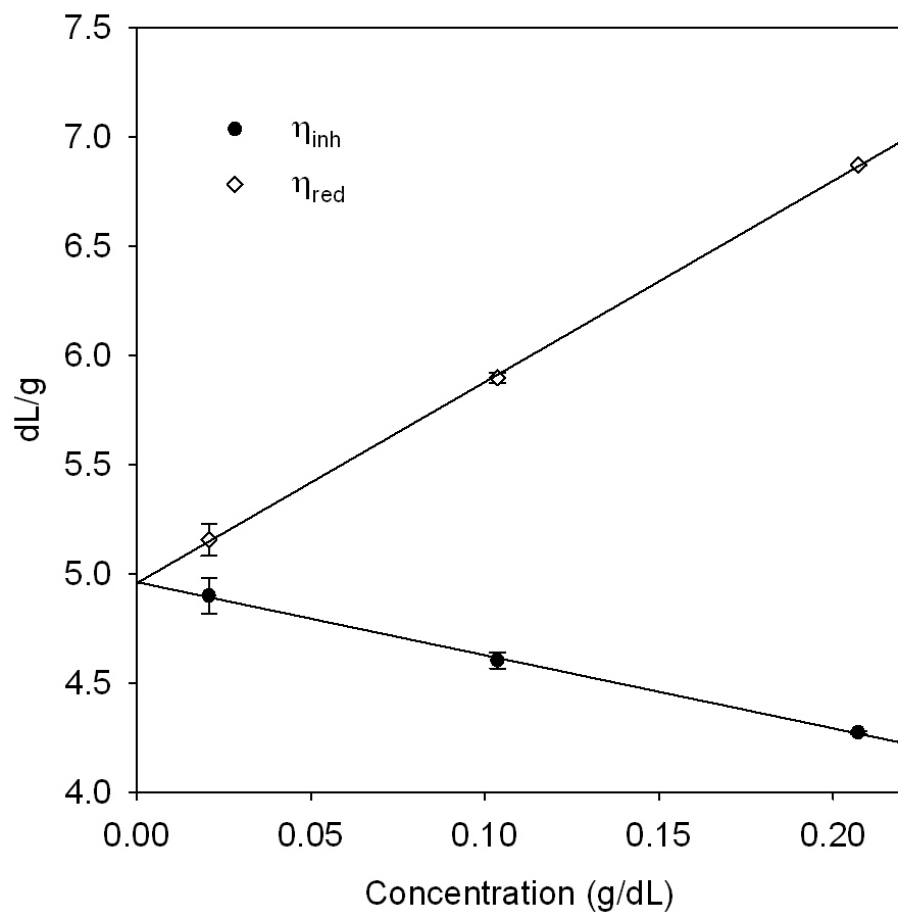
Figure 1.41: Representative viscosity data for PPTA which had been environmentally conditioned for 10 d. Standard error for this measurements is 1.5 %.

molecules to orient themselves with respect to the fiber axis during fiber formation [58, 67, 2, 3]. The average of the two intrinsic viscosities calculated was used to estimate the weight average molar mass using the Mark-Houwink equation for PBO, Equation 1.8 [7, 62], and PPTA, Equation 1.9 [62, 63].

$$[\eta] = 2.27 \ \times \ 10^{-7} \ \overline{M}_w^{1.8} \tag{1.8}$$

The Mark-Houwink exponent of 1.8 is an indication of the high molecular rigidity of PBO. For comparison, this exponent is 1.0 for semi-rigid polymers, and for an ideal random coil polymer under θ conditions it is 0.5. The value of 1.09 for Kevlar reflects its slightly more flexible molecular structure [7].

$$[\eta] = 8.0 \ \times \ 10^{-5} \ \overline{M}_w^{1.09} \tag{1.9}$$

Equations 1.8 and 1.9 were used to calculate an estimated weight average molar mass for samples extracted from both armors during the environmental conditioning experiment. The baseline (undegraded) PBO sample has a molar mass of approximately 26,000 g/mol, which is comparable to the 28,650 g/mol previously reported by Gupta [61]. The goal of this study was to examine the relative changes in molar mass during environmental conditioning instead of attempting to make an absolute measurement of molar mass, so it was determined that this estimate was acceptable for this qualitative technique. Over the course of the environmental conditioning, the PBO sample degraded to an approximate molar mass of 15,000 g/mol. The baseline (undegraded) PPTA sample molar mass was calculated to be approx-

Environmental Conditioning (d)	PBO (g/mol)	Standard Deviation (%)	PPTA (g/mol)	Standard Deviation (%)
0	26,157	1.37	42,241	1.02
4	22,746	0.95	36,579	1.03
7	19,161	0.42	29,595	1.22
10	15,169	3.39	24,926	1.48

Table 1.3: Estimation of the reduction of weight average molar mass for PBO and PPTA with environmental conditioning.

imately 42,000 g/mol. This value was verified by a PPTA manufacturer [68] to be reasonable, but is considerably higher than that reported in the literature [1]. After 10 d of environmental conditioning, the molar mass of the PPTA sample was reduced to approximately 25,000 g/mol. Full details of these results are presented in Table 1.3.

1.10.1 Comparison of Changes in Molar Mass Reduction with Changes in Tensile Strength

After 10 d of environmental conditioning, the PBO sample had a tensile strength retention of approximately 68 %. The PPTA sample tumbled in the environmental conditioning environment had a tensile strength retention of approximately 85 %. This strength loss in the PPTA armor was greater than that observed in previous studies [69]. Error bars represent the relative standard deviations.

In an effort to more readily compare the estimated reduction in molar mass with the extracted yarn tensile testing results for PBO and PPTA the molar masses were also converted to a percentage of the original value. This conversion of these

data allowed for the determination of the the percent residual tensile strength and the percent residual molar mass, which are plotted as a function of environmental conditioning time in Figure 1.42 and Figure 1.43. This approach revealed a correlation between the reduction in molar mass and the reduction in tensile strength with increased environmental conditioning time. To further examine this phenomenon, for PBO, residual tensile strength was plotted against residual molar mass, and a least squared linear fit yielded an R^2 value of 0.97 and a slope of $a=0.75$, suggesting a correspondence between residual tensile strength and residual molar mass. The reduction in molar mass, which would be indicative of chain scission, may support the hypothesis that PBO fully undergoes chain scission during exposure to elevated conditions of temperature, moisture, and mechanical damage, as opposed to simply undergoing the benzoxazole ring opening step of the hydrolysis reaction as shown in structure (2) of Figure 1.20, which would give a fiber with a structure similar to PPTA. While the overall downward trend is supported with this same analysis for PPTA, when a linear fit was applied to these data, the R^2 value was 0.94 and the slope was a=0.35, again indicating a correlation between the reduction in molar mass and the reduction in tensile strength. However, the sensitivity of this relationship is different for PPTA. Future work will separate the mechanical and environmental degradation conditions in an effort to better understand their individual roles in the environmental conditioning of PBO and PPTA fibers and to fully answer the question of how hydrolysis progresses in PBO.
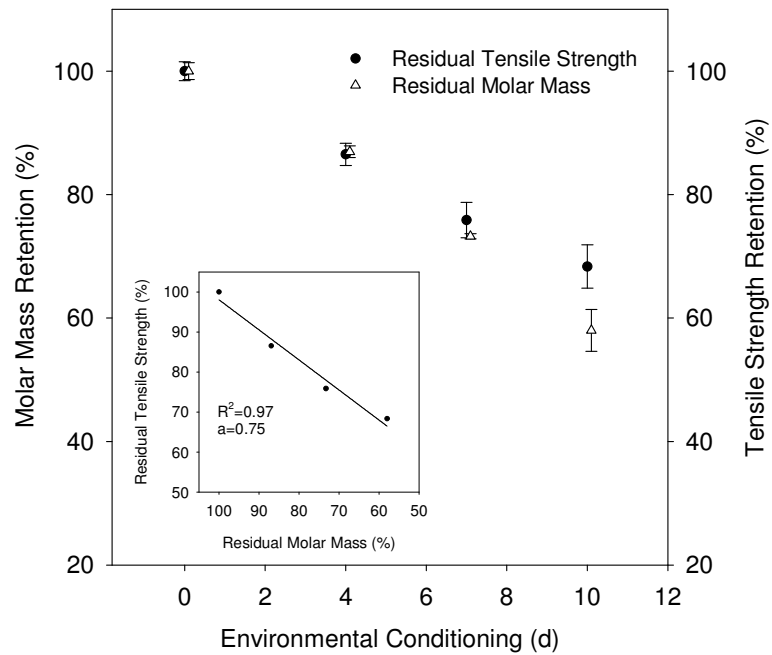
Figure 1.42: Comparison of residual tensile strength with residual molar mass for PBO. The error bars represent the relative standard deviation of the mean yarn breaking strength or mean molar mass. Note the correspondence between reduction in tensile strength and reduction in molar mass. Residual molar mass points are offset horizontally for clarity of presentation.
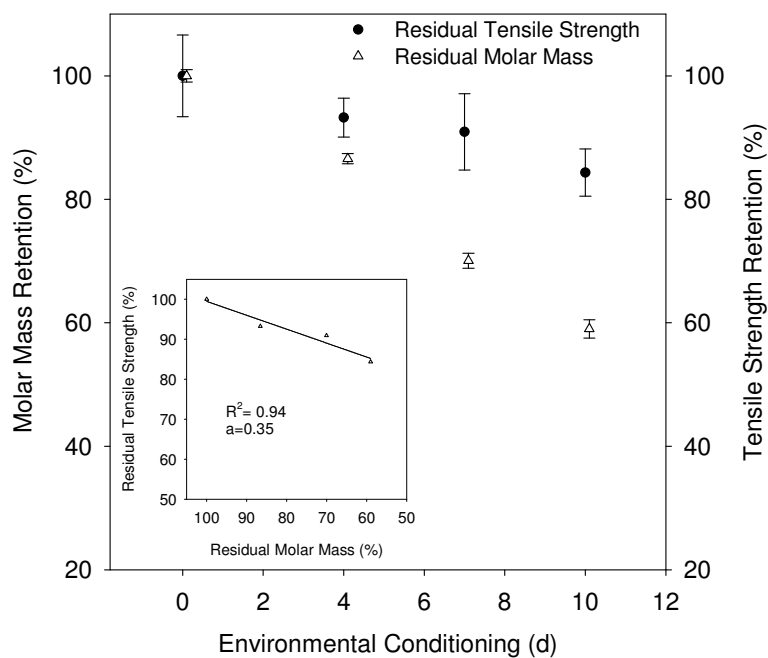
Figure 1.43: Comparison of residual tensile strength with residual molar mass for PPTA. The error bars represent the relative standard deviation of the mean yarn breaking strength or mean molar mass. Note that while there is still a correspondence between a reduction in tensile strength and a reduction in molar mass, the sensitivity of this correspondence is different than for PBO. Residual molar mass points are offset horizontally for clarity of presentation.

1.10.2 Microscopic Examination of Fiber Surface

It is possible that the observed reduction in molar mass and tensile strength can be attributed to the polymer being abraded away from the body armor fabric during tumbling. To minimize this possibility, the yarns used in testing were removed from the inner layers of the body armors. This practice, combined with the fact that the armor was tumbled inside of two protective layers (the carrier and the armor panel cover), and stitched together to minimize layer-to-layer friction, should reduce the effect of abrasion on the results. In order to further examine the effect of abrasion, confocal microscopy was used to examine fibers before and after degradation (Fig. 1.44 and Fig. 1.45). There is some evidence of additional formation of pits and kink-bands on the surface of the degraded samples. Similar confocal images were obtained in a previous study and these changes were attributed to hydrolysis and chemical exposure [70]. Confocal images of PPTA before and after degradation (Fig. 1.46 and Fig. 1.47) show an increase in surface smoothness (possibly due to abrasion) after environmental conditioning, similar to that seen in other studies where fibers were intentionally abraded [19]. Images observed in previous microscopy studies on PPTA fibers after exposure to artificial sweat and cleaning chemicals are also similar [70].
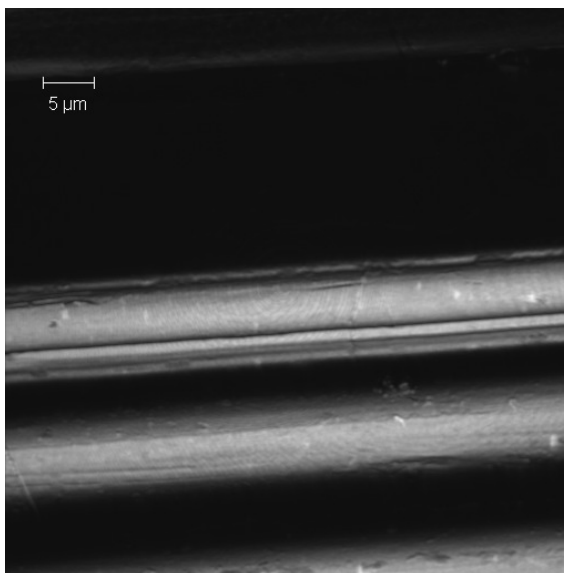
Figure 1.44: Confocal 2D projection of undegraded PBO fiber. Note the overall smooth surface of the fiber. The long horizontal groove in the fiber is likely attributed to processing.
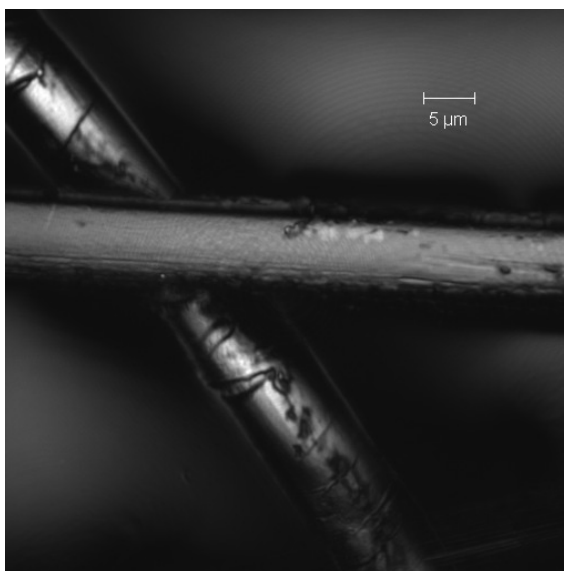
Figure 1.45: Confocal 2D projection of PBO fiber environmentally conditioned for 10 d. Note the kink bands in the lower fiber and the pitting in the upper fiber.
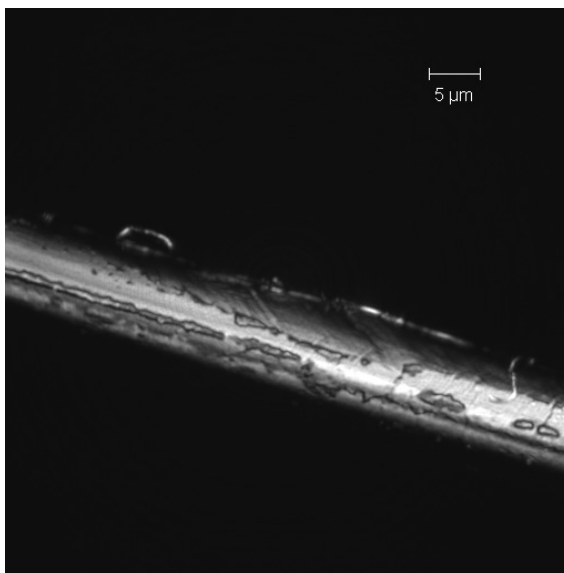
Figure 1.46: Confocal 2D projection of undegraded PPTA fiber. Note the the shiny, reflective surface of the smooth undegraded fiber. Darker spots on the image are likely due to lubricants from processing.
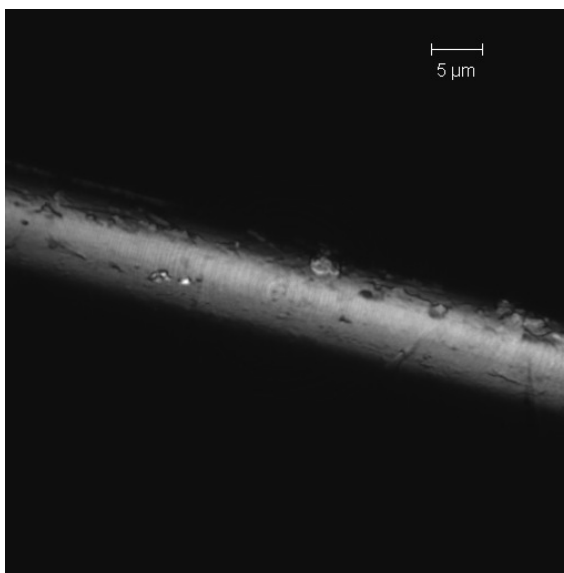
Figure 1.47: Confocal 2D projection of PPTA fiber environmentally conditioned for 10 d. Note the dull surface of the degraded fiber. Darker spots are indicative of pitting in the surface.

Chapter 2

Copolymer Aramid Fibers Used in Body Armor

2.1 Chapter Overview

In this chapter, copolymer aramid fibers used in body armor are introduced. The release of acid from these materials when exposed to water is evaluated. The stability of the physical properties of these materials after exposure to an accelerated degradation environment is investigated and related to changes in the molecular structure of these fibers.

2.2 Copolymer Aramid Fiber Introduction

As discussed in Chapter 1, modern body armor utilizes a wide range of polymers to provide the level of performance required for these applications. The materials most commonly used in body armor are poly(p-phenylene terephthalamide) (PPTA) and ultra-high molecular weight polyethylene (UHMWPE); however, in an effort to expand consumer choices, several additional fibers have been recently introduced into the United States body armor marketplace. These fibers were developed in the former USSR in the late 1970s, and are based on several starting monomers [71]. Several of these fibers were investigated in this study, including Artec[1], Rusar, SVM, and Armos. PPTA and poly-(p-phenylenebenzobisoxazole)

(PBO) fibers were used as comparison fibers. Artec, Rusar, and Armos all have the same basic chemical composition, as depicted in Figure 2.1, and are formed by polycondensation reaction of two diamines, p-phenylene diamine and 5-amino-2-(p-aminophenyl)-benzimidazole with terephthalic acid or terephthaloyl chloride.

PPTA fibers are manufactured by polycondensation of p-phenylenediamine with terephthalic acid. The structure of PPTA fibers is shown in Figure 2.2. For the purposes of this work, linkages between terephthalic acid and 5-amino-2-(p-aminophenyl)-benzimidazole will be referred to as benzimidazole linkages and linkages between p-phenylene diamine and terephthalic acid will be referred to as PPTA linkages.

PBO is a member of the benzazole polymer family and is characterized by the heterocyclic benzobisoxazole group in its main chain structure, as shown in Figure 2.3. The conjugated benzobisoxazole and phenyl rings in the PBO repeat unit contribute to extended π electron delocalization and molecular rigidity, which provides high thermal stability and outstanding mechanical properties to this class of polymers.

The main difference between the aramid copolymer fibers is the ratio of benzimidazole linkages to PPTA linkages [72]. While specific information on these ratios is difficult to obtain, one weaver of these fibers supplied information indicating that in the case of Artec, the ratio of PPTA to benzimidazole linkages was 2:1, and in the case of Rusar, the ratio of diamine to benzimidazole linkages was 1:1. Additionally, Rusar is made with raw materials sourced from Eastern Europe, and Artec is made with raw materials sourced from the United States [73]. Late in the course of the

completion of the study, it was discovered that Rusar and Artec fibers may actually be the same [74]. Since no official data were published to confirm that these two fibers were similar, it was then decided to keep considering them as two different materials.

Another fiber that was investigated in this study is sold under the trade name SVM. This homopolymer fiber is manufactured by direct polycondensation of 5--amino-2-(p-aminophenyl)-benzimidazole with terephthalic acid [75]. The structure of SVM fiber is shown in Figure 2.4.

In a communication to the body armor community released in January 2006, there was an allegation by a competing fiber manufacturer that copolymer fibers based on 5-amino-2-(p-aminophenyl)-benzimidazole can release hydrochloric acid (a byproduct of manufacturing which may remain on the fibers), which could potentially be detrimental to other fibers that might come in contact with these materials [76]. Despite the fact that these allegations came from a competing manufacturer, due to the well-publicized issues with PBO hydrolysis in field use, it was decided that this allegation should be investigated to determine whether it presented a officer safety issue.

---

[1]Certain commercial equipment, instruments, or materials are identified in this paper in order to specify the experimental procedure adequately. Such identification is not intended to imply recommendation or endorsement by the National Institute of Standards and Technology, nor is it intended to imply that the materials or equipment identified are necessarily the best available for this purpose.
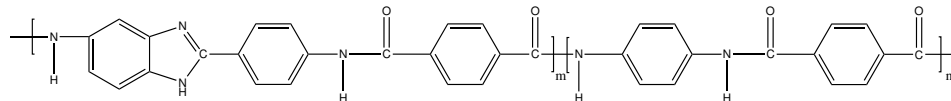
Figure 2.1: Basic chemical structure of the copolymer fibers (Armos, Rusar, and Artec).
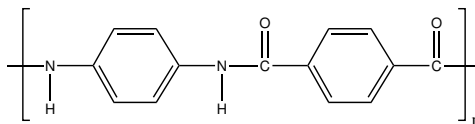
Figure 2.2: For reference, the basic chemical structure of PPTA fibers.

2.3 Fiber Manufacture

While details of the specific processes by which these fibers are made is difficult to find in the literature, a general idea of the fabrication of Armos fiber can be determined from a paper published by Machalaba *et al.*, in 2000 [77]. One can readily assume that the general processing steps would apply to the other fibers as well. The homopolymer (SVM) or copolymer (Armos, Rusar, Artec) is manufactured by polycondensation of terephthaloyl chloride and some combination of para-aromatic diamines (p-phenylene diamine or 5-amino-2-(*p*-aminophenyl)-benzimidazole) in an amide-salt solvent system (specified as dimethylacetamide and lithium chloride in the Machalaba paper) [77]. The polymer formed from this reaction is then filtered and degassed prior to being spun into a filament yarn. This yarn is then drawn and heat treated to form the final finished product.
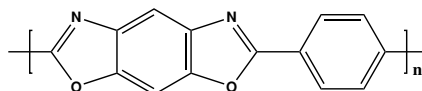
Figure 2.3: For reference, the basic chemical structure of PBO fibers.
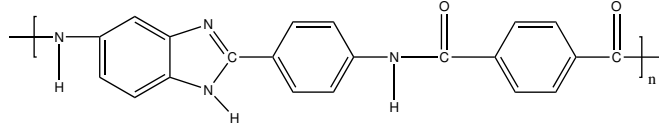
Figure 2.4: Basic chemical structure of SVM fibers.

2.4 Structure, Moisture Sorption, and Other Properties

Slugin *et al.* published two papers in 2006 related to the use of Rusar fibers for composites and ballistic protection applications. Additional information is given regarding the rationale for use of the co-monomer 5-amino-2-(*p*-aminophenyl)--benzimidazole. A paper published by Perepelkin in 2001 compares the properties of Armos and SVM with commercial polyamide yarns. The primary difference between these fibers is in their structural properties. Polyamide fibers have a fibrillar structure with stretched chains and three-dimensional order. SVM fibers also have a fibrillar structure with stretched chains, but only one-dimensional crystalline order. The Armos fiber has a fibrillar structure with stretched chains, but no crystalline order. The strength at break of the Armos fiber is reported at 4.5 GPa to 5.5 GPa as compared to 2.7 GPa to 3.5 GPa for the polyamide fibers, leading the authors to conclude that crystallinity is not a prerequisite for preparing fibers with good mechanical properties [78]. It appears that the Armos fiber has been investigated for use in composite applications due to its unique transverse mechanical properties. A paper by Leal *et al.*, from 2007 attributes the lack of three-dimensional organization in the Armos fibers to the ability to achieve greater draw ratios, better molecular orientation, and improved mechanical properties. Additionally, Armos develops intermolecular hydrogen bonds that allow for stress transfer between adjacent chains.

This improves the compressive properties of the fiber and makes it attractive for use in composite applications [72, 79]. Studies on the moisture sorption properties of several fibers as compared to PPTA have shown that Rusar has very similar sorption isotherms to PPTA. Differences in the sorption properties of these materials are attributed to the lower crystallinity of SVM and Rusar as compared with PPTA. As previously discussed, the benzimidazole linkages in these polymers do not crystallize as readily as the more linear polyamide linkages do [80, 81].

Much work [82, 83, 84, 85] has been performed to investigate the thermal stability of these fibers for use in high-temperature environments and fire applications. These materials are chemically similar to other fibers used in fire-resistant applications, such as para-aramid and meta-aramid fibers, so interest in their thermal properties is not surprising. The decomposition temperatures in air for Armos showed that it was stable to oxidation and onset of degradation to approximately 400 °C [15]. A separate study on the thermal stability of PPTA, SVM, Rusar, and Armos fibers in which the fibers were exposed to 250 °C for up to 100 h showed that the mechanical properties of the SVM fibers decreased the most rapidly, and that there was little difference in the thermal stability of the other fibers examined [82].

2.4.1   Suitability for Ballistic Applications

Slugin *et al.* [86] present V_{50} data on ballistic packages manufactured from two different linear densities of Rusar yarn to demonstrate the appropriateness of this material for ballistic applications. The authors report a V_{50} of 640 m/s and 550 m/s

for packages made from microfilament yarn fibers with linear densities of 29.4 tex (264.6 denier) and 58.8 tex (529.2 denier), respectively [86]. However, important details regarding the construction of the ballistic packages were omitted, making it difficult to draw conclusions from these results. Much work [87] has been focused on the establishment of a theoretical link between mechanical properties and ballistic performance for high strength yarns. While this work has not yet been successfully extended to deformable projectiles, other empirical data, such as that generated in many studies of PBO degradation, indicate that there is a correlation between changes in mechanical properties and reductions in ballistic performance [16].

2.4.2 Acid Release

A paper published by Shchetinin *et al.* in 2006 attempted to address the allegations raised by the competitive fiber manufacturer about the evolution of acid from these fibers. In this paper, it is revealed that hydrochloric acid is a by-product in the synthesis of the polymer, as shown in Figure 2.5 but most of the acid is removed when the fiber is washed after spinning and heat treatment [88]. The acidity of the finished fiber is also discussed in a paper from 1995 by Kotomin *et al.*, which indicated that the pH of the fibers varied between pH 3.5 and pH 6.6 with heat treatment conditions, as determined by titration of an aqueous extract of the fiber [79]. There is a residual amount of acid (0.1 % to 2.5 % of the fiber's mass) chemically bound to the amide and imidazole groups in the fibers. This amount of bound acid is greatest for the SVM fibers, indicating that it is a by-product of

synthesis with the 5-amino-2-(p-aminophenyl)-benzimidazole and the terephthalic acid or anhydrate. The authors used SVM yarns for their study, and in the paper indicate that the amounts of bound HCl in the Armos and Rusar copolymer fibers are less than 0.2 %. SVM fiber samples with an initial hydrochloric acid content of 1.5 % were stored in sealed flasks with deionized water at a ratio of 1 part fiber to 10 parts water, and the pH of the water was periodically evaluated after storage at 15 °C to 25 °C. The pH of the water decreased from 6.4 initially to 4.8 after 360 d of storage under these conditions. The authors conclude that this is an insignificant change in the pH of the water over this period of time. This paper also indicates that since the acid content of the Rusar/Artek (in this paper they use Rusar and Artec/Artek interchangeably, leading to the deduction that these fibers are chemically very similar) and Armos are so low, that this is not an issue for these fibers; however, no data are offered to support this conclusion [88].

2.5   Experimental

2.5.1   Description of the Study

In an effort to evaluate many of the environmental conditions that fibers used as ballistic material might encounter during their lifetime, this study has been performed in three different phases. During the first phase of the study, fiber samples of Armos, Artec[2], Rusar, SVM, PBO and PPTA were immersed in deionized water for 10 days, and the pH and chloride ion content of the water were measured over time using ion-selective electrodes. Infrared analysis was performed on both exposed
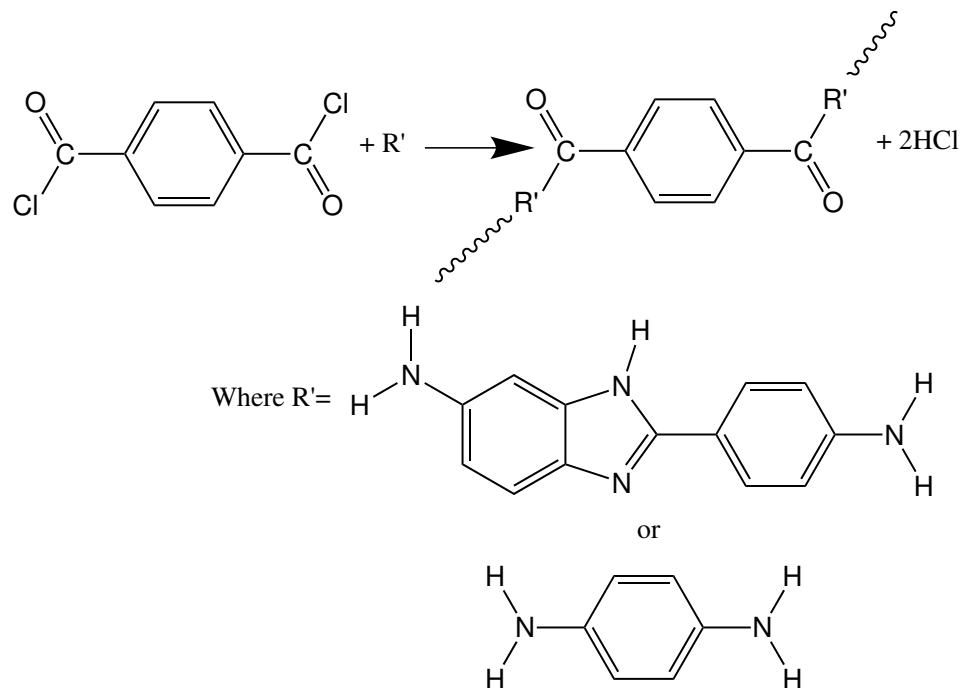
Figure 2.5: General schematic for the synthesis of aramid copolymer fibers, showing the release of HCl during the process [88].

and unexposed fibers to evaluate the effect of exposure to water on their chemical structure. In a second phase, fiber samples of Armos, Artec, Rusar, SVM and PBO were wound on perforated bobbins and exposed in an environmental chamber to high temperature (65 °C) and relative humidity (80 %) for 50 days. Test samples were taken from the conditioned materials after 10 d, 15 d, 20 d and 50 d of exposure. As in the first phase, pH and chloride ion content were monitored using ion-selective electrodes. Additionally, single fiber tensile testing was performed on extracted fibers to assess the effect of the environmental exposure on the yarn's mechanical properties. Infrared analysis was also performed on both exposed and unexposed fibers to track changes in some characteristic chemical bindings. In a third phase, fiber samples of Armos, Artec, Rusar, SVM and PBO were wound on

perforated bobbins and exposed in an environmental chamber to high temperature only (65 °C), and, as in the previous phases, pH and chloride ion content were measured. Infrared analysis and tensile testing were also performed on each of the extracted samples.

2.5.2   Analytical Methods

2.5.2.1   pH and Chloride Ion Content Analysis

As previously mentioned, during the first phase of this study chloride ion elution and pH were monitored by ion-selective electrodes as a function of time under controlled conditions on fibers submerged in deionized water. Fiber samples weighing 5 g, were immersed in 500 mL of deionized water for 10 days, and measurements were performed periodically *in situ*. Previous studies in our laboratory had shown that, after 10 d, no further changes in pH or chloride emission were observed. The beakers were kept tightly sealed with paraffin wax film except when measurements were being made. The total volume of water was kept constant in the beakers by addition of deionized water, if necessary, over the course of the experiment. The release of chloride ions into solution and solution pH were monitored using a Fisher Scientific Accumet Excel XL50 multichannel meter with a chloride combination ion-selective electrode (ISE) and a pH electrode. The standard uncertainty for the pH

---

[2]Due to limited sample availability, all Artec samples in the study were removed from a fabric swatch. This swatch appeared to have been treated with a water-repellent finish, which may have affected the results presented herein.

electrode is $\pm$ 0.1 pH units, and the relative standard uncertainty is $\pm$ 2 % for the ion-selective electrode [89]. During the second and third phase of the study, 5 g of each fiber sample were immersed into 500 mL of deionized water. Once stabilization was reached, the pH and chloride ion concentration were recorded using the same equipment as the one described above.

2.5.2.2 Fourier Transform Infrared Analysis

Infrared analysis was carried out using a Bruker Vertex 80 Fourier Transform Infrared Spectrascope (FTIR), equipped with a Smiths Detection Durascope Attenuated Total Reflectance (ATR) accessory. Air, dried by passage through a standard FTIR purge gas generator, was used as the purge gas. Consistent tension on the yarns was applied using the force monitor on the Durascope. FTIR spectra were recorded at a resolution of 4 cm^{-1} between 4000 cm^{-1} and 600 cm^{-1} and averaged over 128 scans. Three different locations on each yarn were analyzed. Spectral analysis, including baseline correction, was carried out using OPUS 6.5 software from Bruker. Standard uncertainties associated with this measurement are typically $\pm$ 4 cm^{-1} in wavenumber and 1 % in peak intensity [90].

2.5.2.3 Yarn Tensile Testing

To obtain yarn mechanical properties, tensile testing was performed in accordance with ASTM D2256-02: "Standard Test Method for Tensile Properties of Yarn by the Single-Strand Method" using an Instron Model 4482 test frame equipped with

a 1 kN load cell, and pneumatic yarn and cord grips. The jaw separation was 7.9 cm and the cross-head speed was 2.3 cm/min. Each yarn was nominally 40.64 cm long, and was twisted to 60 turns on a custom designed yarn twisting device. The twist was maintained on each yarn during insertion into pneumatic grips. Strain measurements were made with an Instron non-contacting Type 3 video extensometer, in conjunction with black foam markers placed approximately 2.5 cm apart in the gage section of the yarn. Fifteen replicates from each extracted samples were tested to failure. The standard uncertainty of these measurements is typically $\pm$ 3 %; however, the error bars generated for plots presented herein represent the relative standard deviation of the yarn breaking strength, which is in some cases higher than 3 %.

2.5.2.4 Elemental Analysis

Samples of Armos, Artec, Rusar, SVM, PBO, and PPTA were analyzed for elemental content using Fundamental Parameters X-ray Fluorescence Spectrometry, or FP-XRF, for the purpose of detecting elements present and determining the approximate mass fractions of those elements other than H, C, O, and N. FP-XRF methods are designed to be interactive and are implemented as sophisticated computer programs. The investigator can specify to the computer program all *a priori* knowledge of the chemical and physical properties of each specimen.

The FP-XRF program used in this work was the IQ+ method from PANalytical, Inc (Almelo, The Netherlands), which was running in the SuperQ operating

system, version 4.0d, of a model PW2404 wavelength-dispersive spectrometer, also from PANalytical, Inc. The IQ+ method was calibrated using a set of glass and briquette standards provided by the vendor, which was bolstered by a number of National Institute of Standards and Technology Standard Reference Materials. This calibration scales the calculations to the actual performance of the spectrometer. The program was originally calibrated in 2001 and has been maintained by implementing drift correction updates since that time. All measurements were made in scanning mode, in vacuum for solids, with the Rh anode X-ray tube operated at 3 kW. All specimens were weighed into sample cells, and an estimate of the viewed area was made. These values were entered into the program to help scale the expected X-ray count rates calculated from the FP equations. The cells were 37 mm polyethylene (TechRef, Anaheim, CA) with 6 μm polypropylene window material (Somar, Las Vegas, NV).

Armos, Rusar, Zylon, SVM, PBO and PPTA fibers were cut to lengths of 10 mm to 40 mm. The loose fibers were packed into the sample cups so that the fibers were closely packed and covered the film as uniformly as possible. During the measurements, the plastic films burst under pressure from the fibers and heating in the spectrometer. All fibers remained in place, but were exposed directly to the X-ray beam as the support films curled back from the center. All specimens (a specimen in this case is considered a collection of chopped fibers) were weighed to the nearest 0.01 g and their diameters were measured to the nearest 1 mm. An empty sample cell was measured to identify elements present in the cell. Calculations were based on the known molecular formula of the polymers.

The potential bias of the IQ+ method was tested by measuring specimens of SRM 1632c Trace Elements in Coal (Bituminous). One sample of SRM 1632c was prepared by pressing 3 g in a 31 mm steel die at 20 tons for 20 s. This specimen was measured using the same IQ+ program as used for the fiber samples. For this coal, the certified value for C was expressed as CH_2 and set as a fixed, known quantity in the FP calculations. The certified value for N was also set as a fixed value, and the Sum = 100 constraint was set. Then, the measured elements were calculated. The found and certified values for SRM 1632c are shown with the results for the other fibers.

2.6   Results and Discussion

2.6.1   Fibers Exposed to Liquid Water

2.6.1.1   Chloride Ion Concentration and pH Measurements

Representative pH and chloride ion concentration measurements as a function of time are shown in Figure 2.6 and Figure 2.7. The most rapid changes in both pH and chloride ion concentration occur in the first three days of liquid water exposure. Assuming that HCl is present, when the fibers are immersed in water, H^+ Cl^- ions will disassociate and be released through the surface of the fiber.

The change in pH was greatest for the SVM yarn, which is expected due to the high content of HCl this yarn due to processing, as previously reported [88]. The change in pH as a function of immersion time is shown in Figure 2.6. SVM

107

fibers showed a pH decrease from approximately pH 6.0 to approximately pH 3.0. Rusar fibers showed a decrease from approximately pH 5.5 to pH 4.0. The pH of PPTA fibers remained steady over the course of the study. Armos fibers showed a small decrease in pH from approximately pH 6.0 to pH 5.0. PBO fibers showed a slight increase from approximately pH 6.5 to approximately pH 7.5. Artec showed the smallest change in pH as a function of time, with a reduction to approximately pH 5.5 in 10 d, however these results may have been affected by a treatment on the fabric. Later in the course of the study, a manufacturer provided us with samples of woven fabric of Rusar treated for water repellency and woven fabric of untreated Rusar. The study was repeated with these two materials, and Rusar fibers that were treated for water repellency showed similar pH changes to the Artec fibers. It was later verified by a manufacturer of this material that these two materials are the same.

As could be expected from the pH results, SVM showed the greatest increase in overall chloride ion concentration, as shown in Figure 2.7. The overall increase was from almost 0 mg/L chloride in solution up to 112 mg/L chloride in solution for the SVM yarn. The chloride ion concentration increased from almost 0 mg/L to approximately 6 mg/L for Rusar fibers, indicating that another species may be responsible for its drop in pH. None of the other fibers investigated exhibited a significant change in the chloride ion concentration.

Usually DI water is slightly acidic due to the absorption of carbon dioxide in pure water, producing very low concentrations of carbonic acid [91], as depicted in Figure 2.8. The water deionizer source used for these experiments stores the

deionized water in a large reservoir as it is made, so the water is exposed to air and carbon dioxide prior to use. One can surmise that the source of the chloride ion may be attributed to residual ammonium chloride formed from the reaction of terephthaloyl chloride and the primary or secondary amines to form the polymers studied herein via a Schotten Baumann reaction [92], as shown in the previous chapter. The polycondensation reaction of the amine and the acid chloride to form the amide bond will result in the small molecule by-product HCl. This product may remain in the polymer after washing, or become polymerized into the chain at the end groups. The nitrogen in the amide bond has a lone pair of electrons that could react with the HCl to form the ammonium chloride ion pair. Traces of this salt may remain after thorough washing of the fibers, and when the polymer is immersed in water for these studies, small amounts of chloride ion may migrate to the surface of the fiber, where they will encounter ample concentrations of H^+ counter-ions. The chloride ion concentration measurements were made over 10 days to ensure that all available chloride ions diffused out of the fiber and into solution. Figure 2.7 shows that SVM only reaches an equilibrium chloride ion concentration after approximately 8 days, indicating that chloride ions are likely migrating from within the fiber to the surface.

In Figure 2.6 and Figure 2.7, HCl is the anticipated source of the H^+ ions being measured in the pH portion of the experiment, however to verify that HCl is correctly identified as this source, the counterion Cl^- is also measured. Due to the large difference in the concentration of chloride ions released, SVM is shown only in the inset plot in this Figure. To further illustrate this observation, the change in
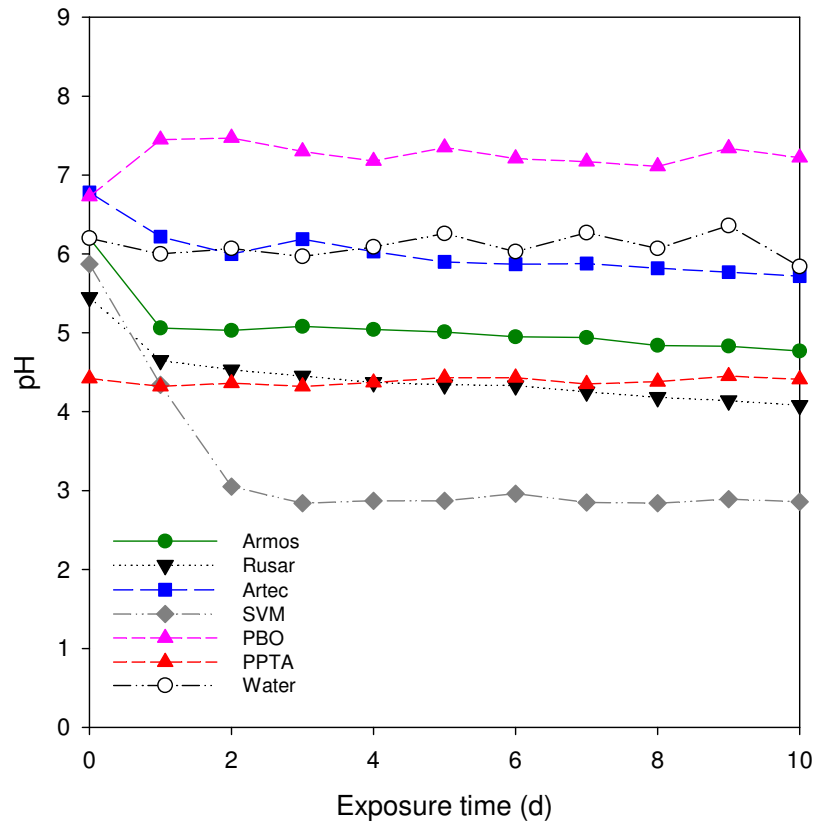
Figure 2.6: Change in pH of the DI water in which all fibers were immersed over time. All of these fibers are spun from acid solutions, and most fibers show a pH lower than that of the DI water control, except PBO. This could be due to the neutralization process used in the manufacture of this polymer.
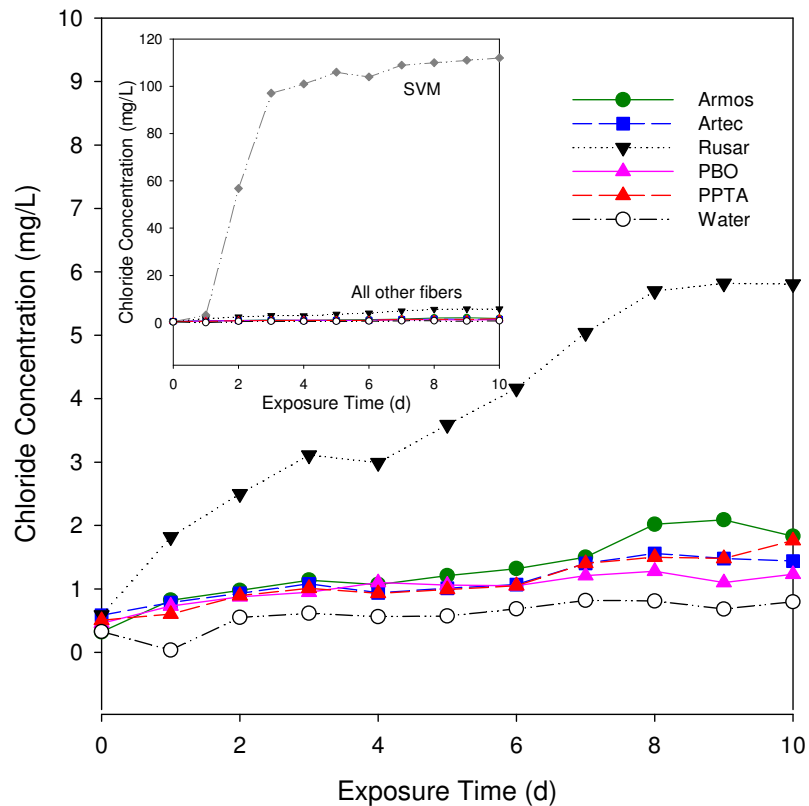
Figure 2.7: Chloride ion release following immersion in deionized (DI) water for all fibers. HCl is the anticipated source of the H^+ ions being measured in the pH portion of the experiment, however to verify that HCl is correctly identified as this source, the counterion Cl^- is also measured. Due to the large difference in the concentration of chloride ions released, SVM is shown in the inset plot. It is evident from this graph that HCl is only the source of the reduction in pH for the SVM fiber.

CO_2 (g)	⇌	CO_2 (aq)	(a)
CO_2 (aq)	⇌	H_2CO_3 (aq)	(b)
H_2CO_3 (aq)	⇌	H^+ (aq) + HCO_3^-(aq)	(c)
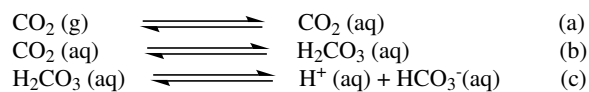
Figure 2.8: Scheme for formation of carbonic acid in deionized water [91].
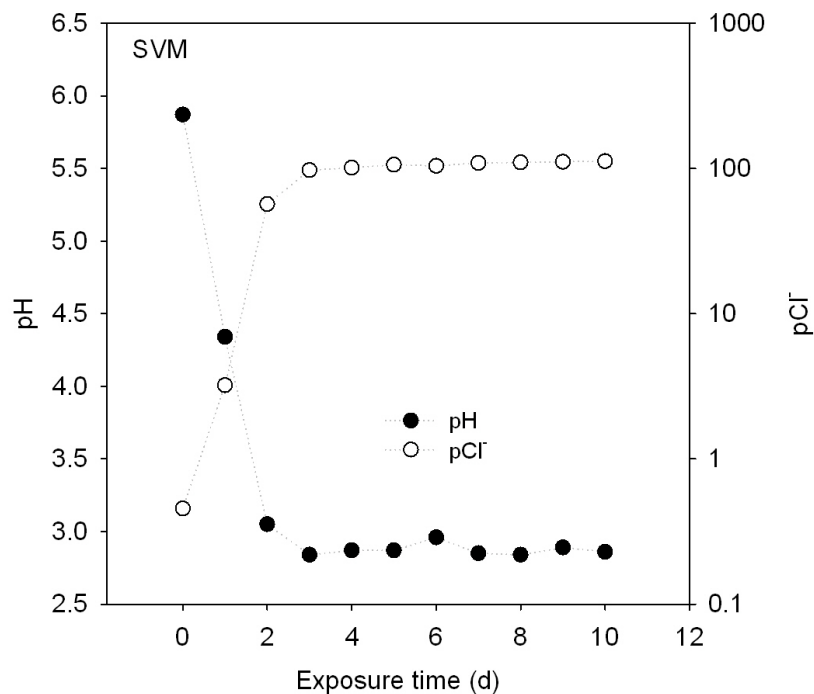
Figure 2.9: he change in pH over time is plotted with the change in chloride ion concentration over time while immersed in water for SVM. It is evident from this graph that HCl is only the source of the reduction in pH for the SVM fiber. As more Cl$^-$ counter ions are liberated from the fiber (their concentration increases), the pH of the solution decreases, indicating the presence of H$^+$ ions in this system.

pH over time is plotted with the change in chloride ion concentration over time in Figure 2.9. It is evident from this graph that HCl is only the source of the reduction in pH for the SVM fiber.

2.6.1.2   Analysis of Chemical Structure

Due to the lack of available literature regarding the infrared analysis of the chemical structures of the copolymer fibers utilized in this study, a separate ef-

fort was undertaken to investigate their spectra. Peak assignments were generated through the review of several references on PPTA fibers [93],[94], general infrared spectroscopy [95, 51, 96], and benzimidazole spectroscopy [97, 98]. As expected, the spectra of the copolymer fibers show characteristics found in the spectra of the two homopolymers. A typical ATR FT-IR spectrum of SVM is shown in Figure 2.10. To further investigate the validity of the peak assignments shown in Table 2.1, two benzimidazole-containing model compounds, 2-phenylbenzimidazole, Figure 2.11, which will be referred to as MC1 in this paper, and 2-(2-aminophenyl)-1H-benzmidazole, Figure 2.12, which will be referred to as MC2 in this paper, were purchased and analyzed in their neat form using ATR-FTIR spectoscopy. The spectra of MC1 and MC2 are shown in Figure 2.13 and Figure 2.14 respectively. MC1 has peaks attributed to benzimidazole at 1591 cm^{-1}, 1462 cm^{-1}, 1444 cm^{-1}, and 1187 cm^{-1}. MC2 has peaks attributed to benzimidazole at 1491 cm^{-1}, 1460 cm^{-1}, 1441 cm^{-1}, 1106 cm^{-1}, and 955 cm^{-1}. These peaks correspond to peaks attributed to benzimidazole in the spectra of the copolymer fibers and SVM fiber as shown in Table 2.1, which reinforces the validity of these peak assignments.

2.6.2 Fibers Exposed to High Temperatures and Humidity Conditions

Fibers in the study were exposed to conditions of high temperature and humidity to better simulate the wear environment, then the pH and chloride ion concentration measurements were repeated.
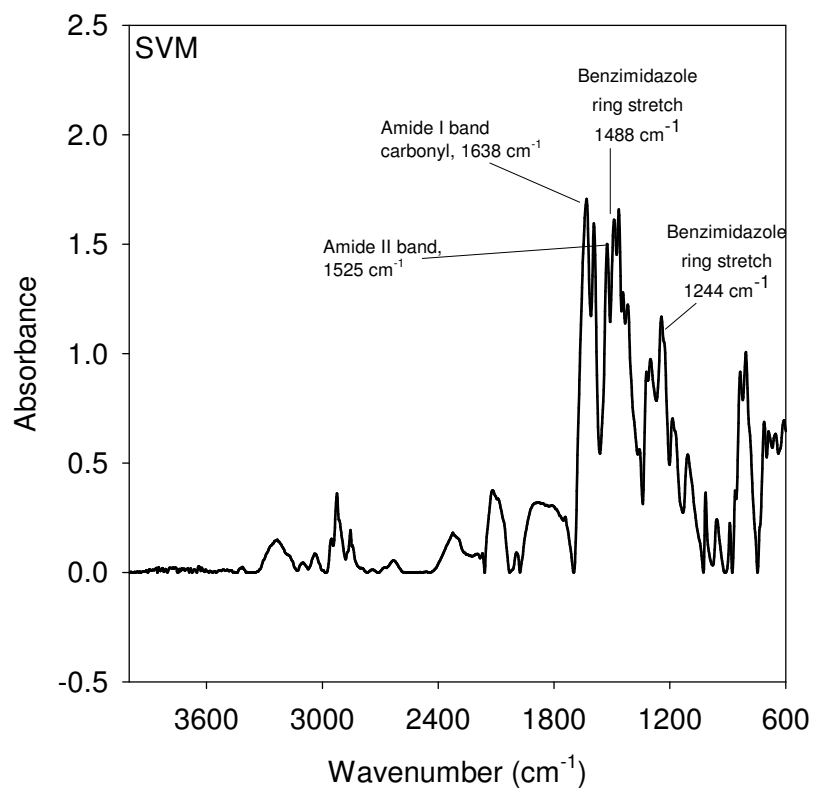
Figure 2.10: ATR FT-IR spectrum of virgin SVM fiber. Characteristic peaks are labeled.
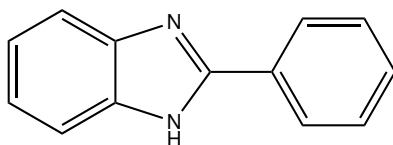
Figure 2.11: 2-phenylbenzimidazole, adapted from published structure [100].
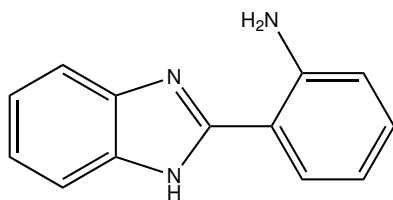
Figure 2.12: 2-(2-aminophenyl)-1H-benzmidazole, adapted from published structure [100].

Table 2.1: Infrared Peak Assignments for Artec, Armos, Rusar, SVM and PPTA fibers [99].

Artec cm^{-1}	Armos cm^{-1}	Rusar cm^{-1}	SVM cm^{-1}	PPTA cm^{-1}	Note	General Assignment
				3309	Broad	NH Stretch [94]
3271	3271	3271			Broad	Imidazole N-H hydrogen bonding to H$_2$O or imine [97]
1638	1639	1638	1632	1638	Strong	Amide I band carbonyl [93]
1596	1596	1596	1593		Shoulder	Benzimidazole NH in-plane bend [98]
1513	1512	1513	1525	1510	Sharp Shoulder	Amide II band carbonyl [93]
1487	1486	1488	1488		Shoulder	Benzimidazole ring stretch [98]
	1467		1464		Shoulder	Benzimidazole ring stretch [98]
1443	1443	1443	1443		Shoulder	Benzimidazole [98]
			1417		Shoulder	Benzimidazole ring stretch [98]
1406	1406	1406		1394	Shoulder	Primary amine salts [51]
1305	1304	1304	1300	1303	Shoulder	CN stretch; Amide III group motion [94]
1244	1245	1247	1244		Shoulder	Benzimidazole ring stretch [98]
1187	1186	1186	1186		Medium	Benzimidazole in-plane CH bend [98]
1108	1107	1108	1106	1107	Medium	Benzimidazole in-plane CH bend [97]
1016	1016	1016	1015	1017	Medium	CH out of plane bend [94]
957	957	955	957		Weak	Imidazole in-plane bend [98]
890	889	890	889	893	Weak	CH out of plane [93]
				820	Strong	CH out of plane [94]
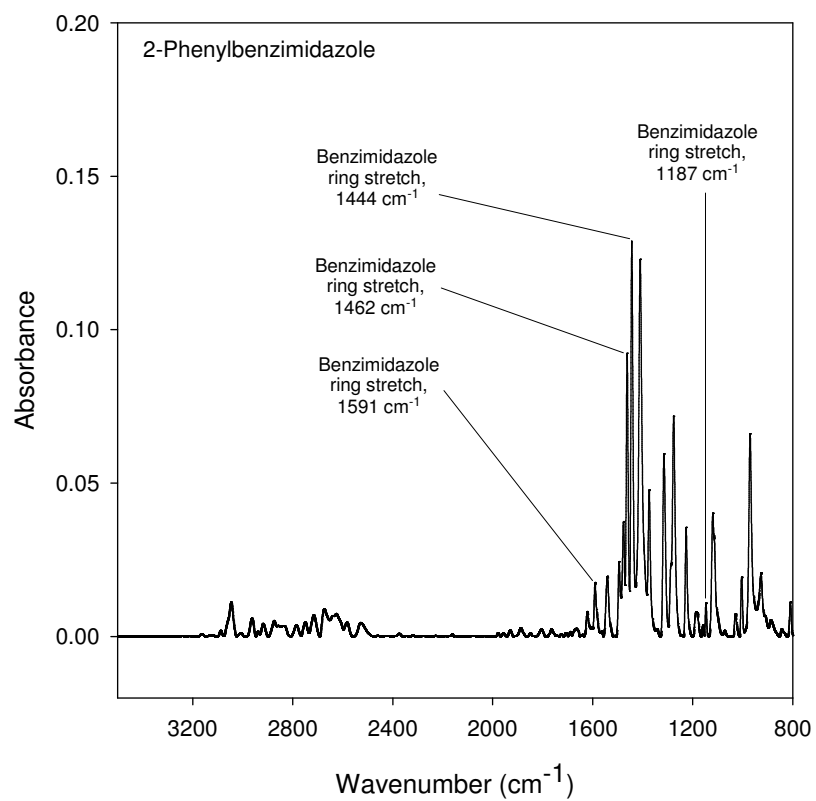
Figure 2.13: 2-phenylbenzimidazole ATR-FTIR spectra. Characteristic peaks are labeled.
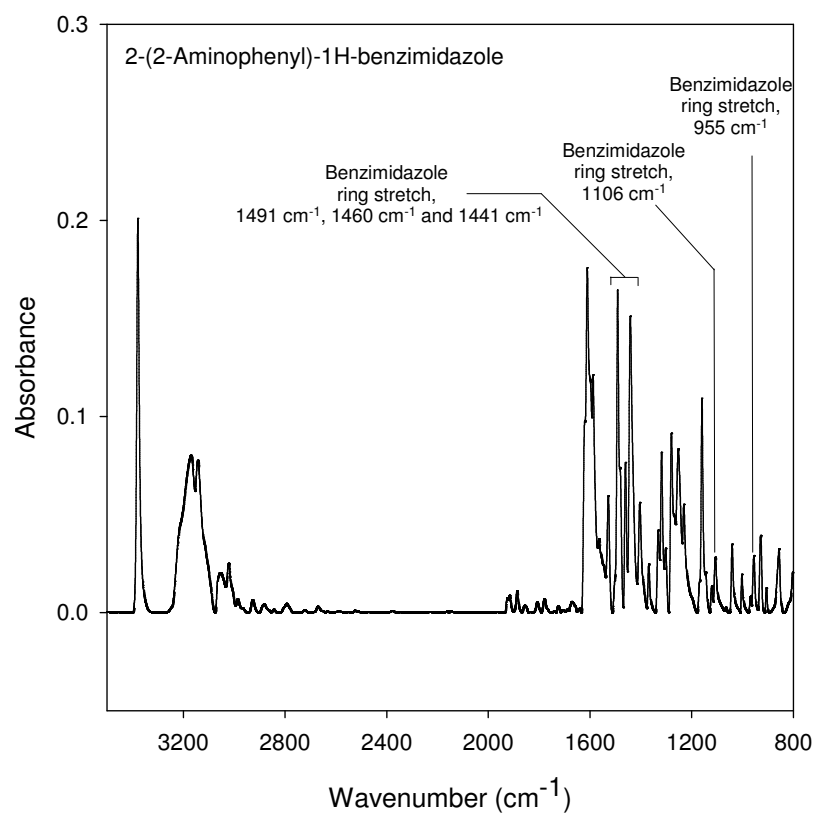
Figure 2.14: 2-(2-aminophenyl)-1H-benzmidazole ATR-FTIR spectra. Characteristic peaks are labeled.

2.6.2.1 Chloride Ion Concentration and pH Measurements

Representative pH and chloride ion concentration measurements as a function of time are shown in Figure 2.15 and Figure 2.16. Note that the pH decrease observed in the liquid water exposure study is not reproduced with exposure to high temperature and relative humidity. There is a decrease in pH for SVM and Rusar samples, but this decrease is smaller than in the first part of the study. The pH of these samples drops from pH 6.0 to around pH 5.0 within 10 d of exposure, as compared to a decrease from pH 6.0 to almost pH 3.0 for SVM fibers when immersed in liquid water. Armos and Artec show similar behavior as in the first phase of the study. The chloride ion results observed for SVM in the first phase were significantly lower in this phase, a puzzling result which will be the subject of future investigation, and no noticeable increases in chloride ion content were observed for any samples in the second phase of the study.

2.6.2.2 Chemical Properties

PPTA fibers are known to be susceptible to acid catalyzed amide hydrolysis as depicted in Figure 2.17. Given the similarities in the chemical structure of the fibers considered in this study to PPTA, one might anticipate that these fibers could also be vulnerable to a similar hydrolysis mechanism.

Through the use of difference spectra, where the infrared spectra taken from the unconditioned sample is subtracted from the spectra of fibers which have been subjected to environmental conditioning in the humidity chamber, the evolution of
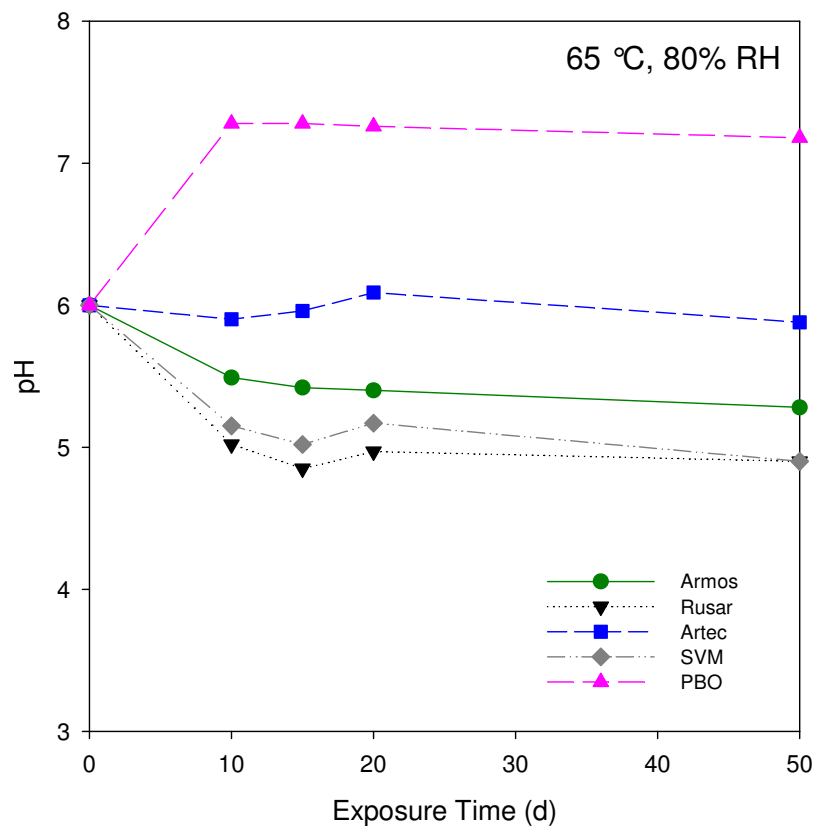
Figure 2.15: Change in pH following exposure to 65 °C, 80 % RH. This experiment was performed to better simulate the wear environment and determine whether there was a risk to the end user of being exposed to acids from the body armor. The standard uncertainty in these measurements is ± 0.1 pH units.
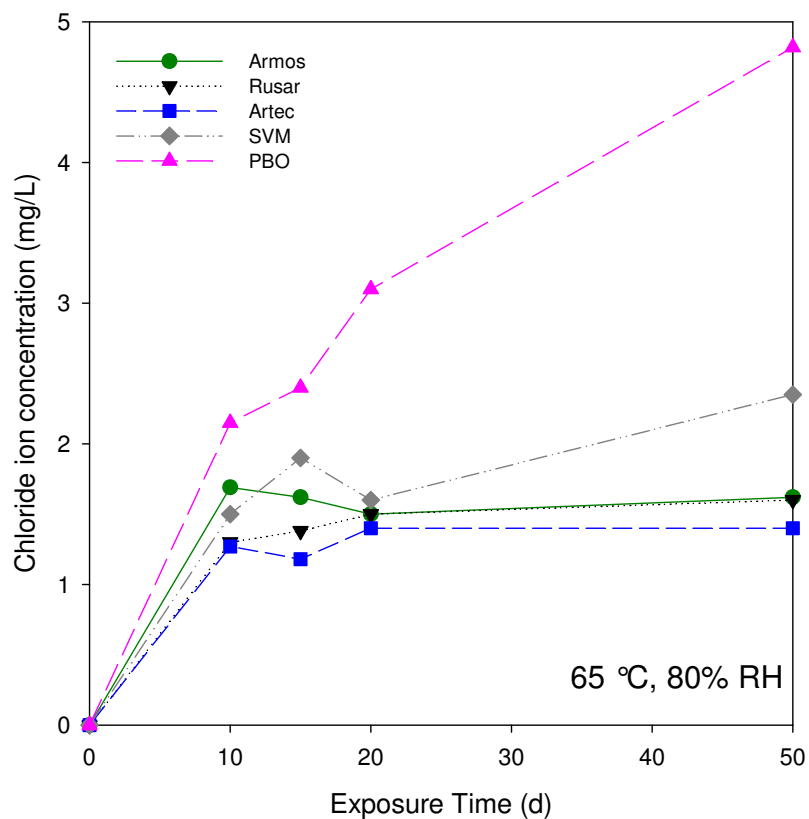
Figure 2.16: Change in chloride ion release following exposure to 65 °C, 80 % RH. This experiment was performed to better simulate the wear environment and determine whether there was a risk to the end user of being exposed to acids from the body armor, and if acids were released, if they were due to HCl. The standard uncertainty in these measurements is ± 2 %.
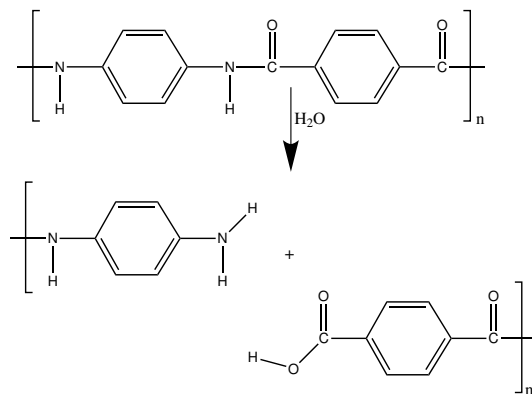
Figure 2.17: Scheme for amide hydrolysis for PPTA fibers.

changes in the chemical structure can be studied [101, 102, 52, 53, 54]. Negative peaks in difference spectra are attributed to the loss of existing chemical structure, and positive peaks are indicative of the formation of new chemical structure [52, 53, 54].

Previous work examining the hydrolysis of PPTA fibers [103] via difference spectra techniques showed losses in the Amide I and Amide II peaks, and increases in both the NH/OH peaks and carboxylate ion peaks. Similar characteristics were found in the difference spectra of the fibers studied in this work. Difference spectra for Artec, Armos, Rusar, and SVM were generated by subtracting the spectrum of the unexposed sample of each fiber from the spectra of the sample which had been environmentally conditioned for 50 d. These data are presented in Figure 2.18 and Figure 2.19.

Figure 2.18 shows the low wavenumber region of the IR spectrum. Note the losses in Amide I peaks for all of the fibers between 1630 cm^{-1} and 1618 cm^{-1}, and Amide II peaks at 1532 cm^{-1} (Artec) and 1520 cm^{-1} (SVM). Carboxylate ion formation is observed at 1452 cm^{-1} (Armos) and 1457 cm^{-1} (Artec), but losses in this general region are observed for Rusar and SVM. Peaks in this region can also be associated with benzimidazole [99], so losses in these regions could be attributed to chain scission and loss of benzimidazole sections of the chain backbone.

Figure 2.19 shows changes in the IR spectrum at wavenumbers above 3000 cm^{-1}. A new peak at 3255 cm^{-1} for SVM fibers is attributed to the formation of NH and OH typically seen in amide hydrolysis. The negative peak at approximately 3350 cm^{-1} for Artec is obviously due to a loss in NH or OH, possibly due to hydrolysis
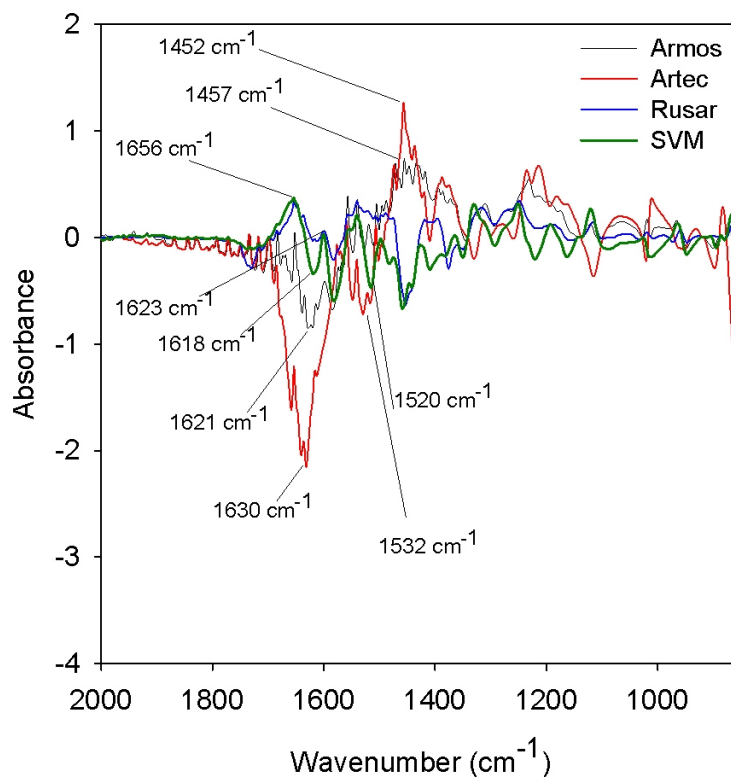
Figure 2.18: ATR FT-IR difference spectra of fibers from 65 °C, 80 % RH study, fingerprint region. Note the losses in Amide I peaks for all of the fibers between 1630 cm^{-1} and 1618 cm^{-1}, and Amide II peaks at 1532 cm^{-1} (Artec) and 1520 cm^{-1} (SVM). Carboxylate ion formation is observed at 1452 cm^{-1} (Armos) and 1457 cm^{-1} (Artec), but losses in this general region are observed for Rusar and SVM. Peaks in this region can also be associated with benzimidazole [99], so losses in these regions could be attributed to chain scission and loss of benzimidazole sections of the chain backbone.
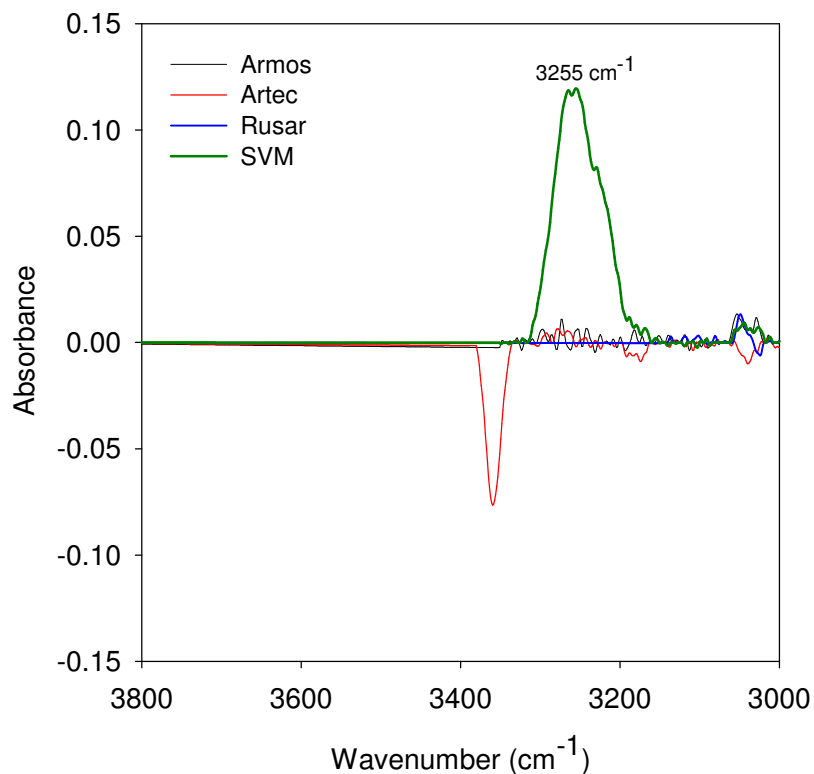
Figure 2.19: ATR FT-IR difference spectra of fibers from 65 °C, 80 % RH study, scaled above 3000 cm^{-1}. The new peak at 3255^{-1} for SVM is attributed to the formation of NH and OH typically seen in amide hydrolysis. The negative peak at approximately 3350 cm^{-1} for Artec is obviously due to a loss in NH or OH, possibly due to hydrolysis of this material. This is supported by losses for Artec in the Amide I and II bands, as shown in the previous figure.

of this material. There are slight changes in the spectra of Armos, but the spectrum of Rusar is unchanged in this region. While the difference IR spectra of these fibers do not exactly match previously observed results for amide hydrolysis, there are general similarities in the IR results that indicate that these fibers are changing with exposure to water.

2.6.2.3 Physical Properties

Figure 2.20 shows the tensile strength retention of fibers exposed to conditions of high temperature and relative humidity. Both Rusar and SVM show measurable decreases in their tensile properties. Extensive studies have already established that PBO is sensitive to hydrolysis when in high humidity environments, which was confirmed by this study. Armos and Artec, which have similar chemical structures, seem to be the most stable under these conditions, with losses of approximately 3 % and 7 %, respectively, of their tensile strengths over the course of a 50 d exposure to the high heat and relative humidity conditions. As previously mentioned, PPTA is sensitive to acid-catalyzed hydrolysis of amide linkages in the chain backbone [103]. Because all of the fibers studied herein contain amide linkages, it is possible that the extractable acid (as evidenced by the reduction in pH in these two samples) may catalyze amide hydrolysis in Rusar and SVM, leading to a greater reduction in their respective tensile strengths.

2.6.3 Fibers Exposed to High Temperature Conditions

2.6.3.1 Chloride Ion Concentration and pH Measurements

Figure 2.21 and Figure 2.22 show representative pH and chloride ion concentration measurements as a function of time for all fibers. All samples show similar behaviors to those observed in the second phase of the study with an increase for PBO, slight decreases for Armos and Artec, and more significant decreases for Rusar and SVM with drops from pH 6 to pH 5 and pH 4.5 respectively. Note that there
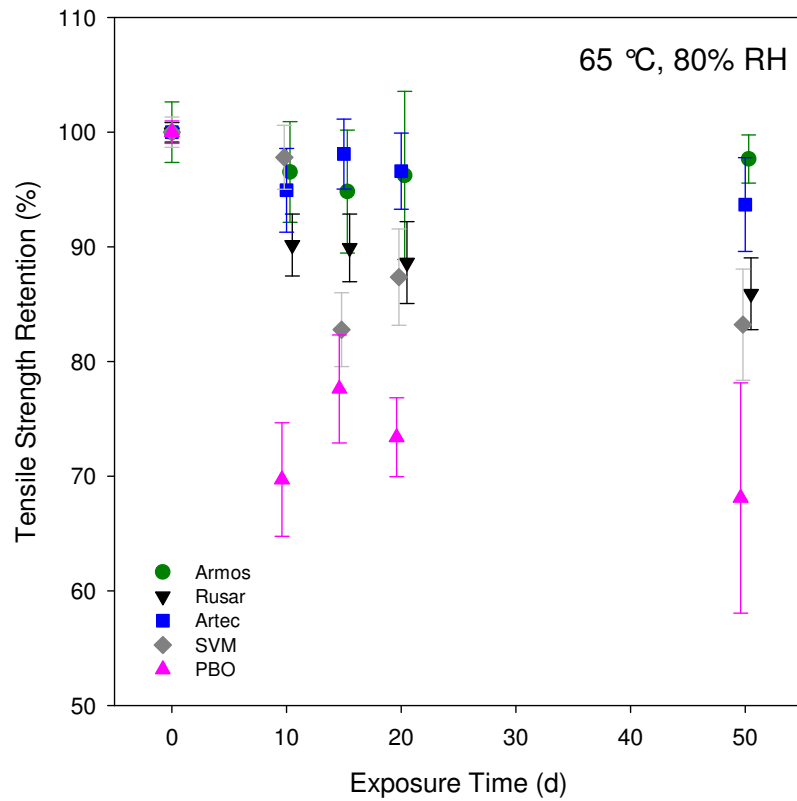
Figure 2.20: Tensile strength retention following exposure to 65 °C, 80 % RH. Note that the tensile strength retention for all fibers is considerably greater than that of PBO, which is known to undergo hydrolysis under these conditions. Rusar and SVM showed the largest reduction in tensile strength in this study when PBO is excluded.
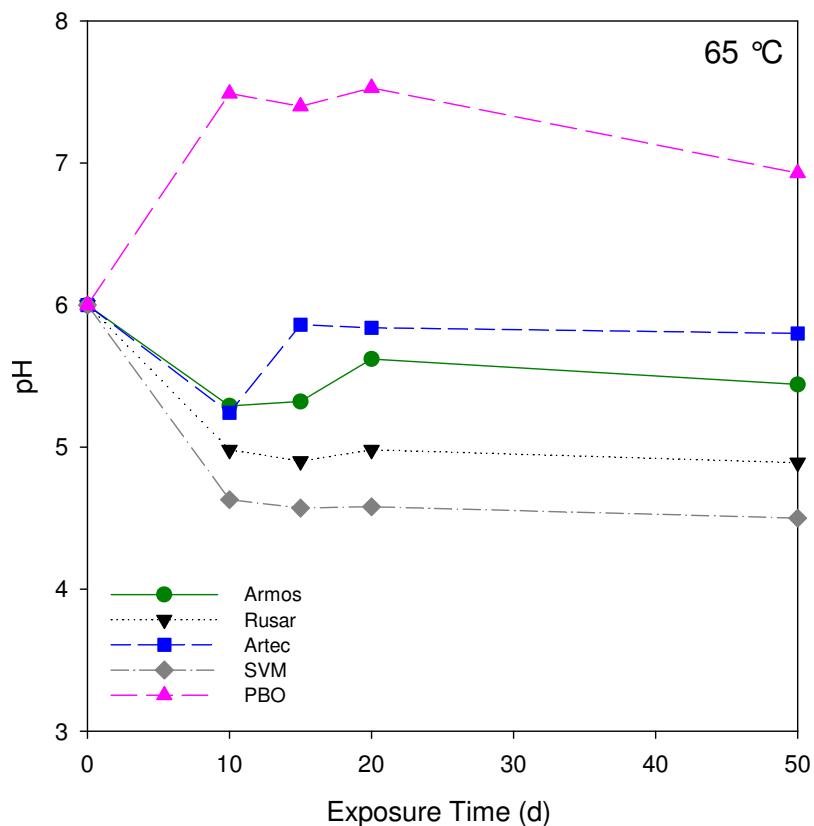
Figure 2.21: Change in pH following exposure to 65 °C oven. This experiment was performed to better simulate the storage environment (e.g., the trunk of a car) and determine if there was a risk to the end user of being exposed to acids from the body armor.

are almost no changes in the pH between 10 d and 50 d, meaning that any changes occur within the first 10 d of exposure. The chloride ion results observed for SVM in the first phase were not repeated in this phase, and no noticeable increases in chloride ion content were observed for any samples in the second phase of the study.

2.6.3.2 Chemical and Mechanical Properties Analysis

Figure 2.23 shows the tensile strength retention of the fibers exposed to high temperature without humidity. The tensile strengths of the fibers studied were maintained over the course of high temperature exposure. ATR-FTIR analysis showed
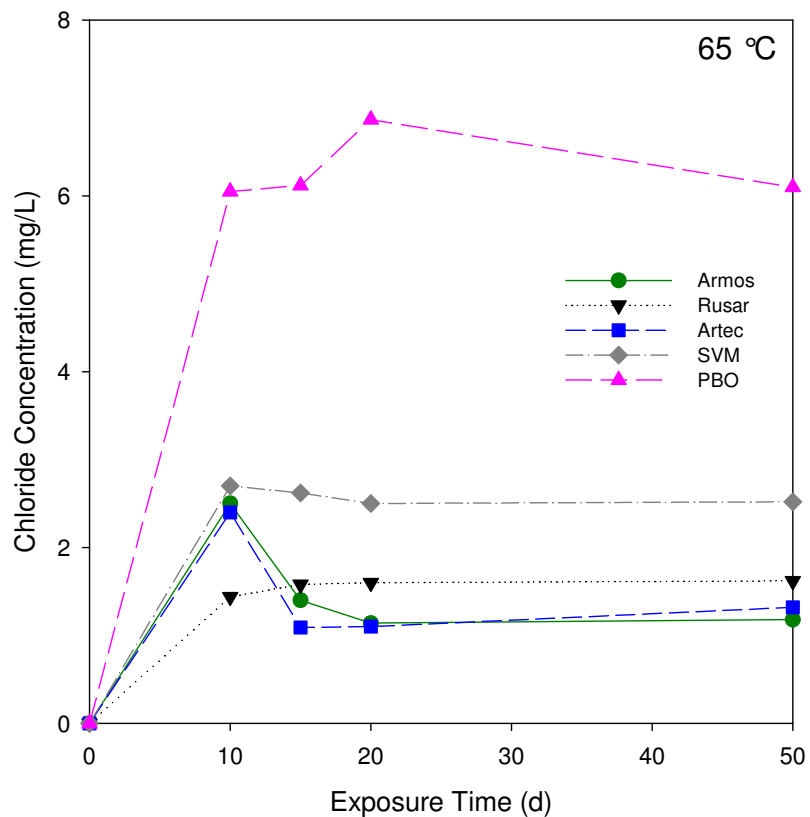
Figure 2.22: Change in chloride ion release following exposure to 65 °C oven. This experiment was performed to better simulate the storage environment (e.g., the trunk of a car) and determine if there was a risk to the end user of being exposed to acids from the body armor, and if acids were released, if they were due to HCl.
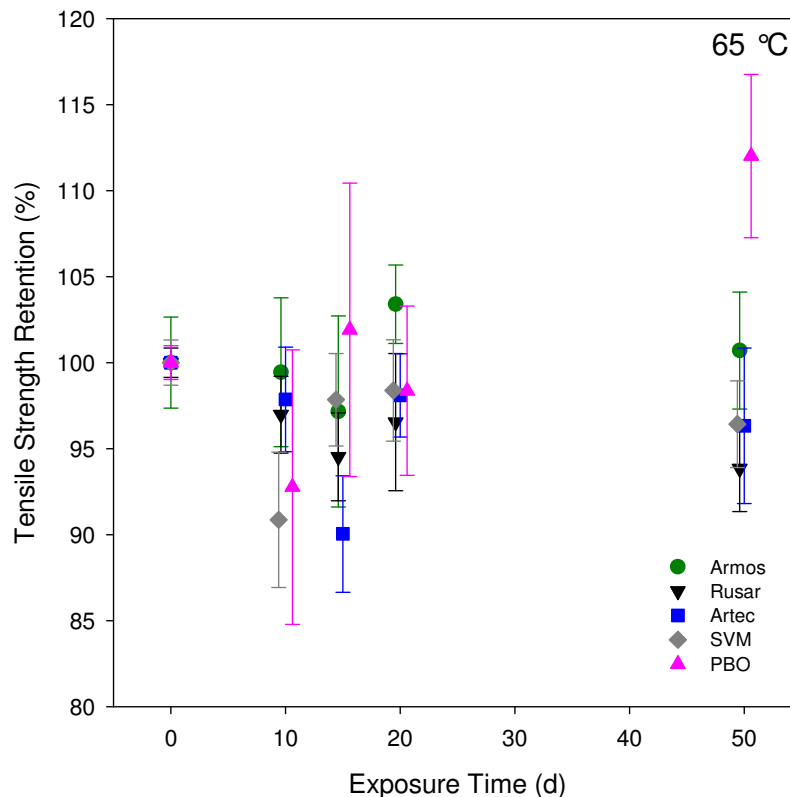
Figure 2.23: Tensile strength retention following exposure to a 65 °C oven for all samples. Note that there is little change in tensile strength after this exposure, and some samples even appear to become stronger.

no changes in the spectra of the fibers studied.

2.6.4 Elemental Analysis

Elemental analysis was performed using FP-XRF on the following fibers: Rusar, Armos, Artec (removed from fabric sample), SVM, PBO and PPTA (removed from fabric sample). Results of the analysis are shown in Table 2.2. The elements H, C, O, and N were calculated from the polymer molecular formulas from the repeat units rather than from measured data. For S in PPTA and P in PBO, there were clear evidence that the S and P are bound to oxygen atoms. This is shown by the presence of a satellite peak on the shoulder of the K-M peak in the collected spectra.

All of the fibers except PBO and PPTA contain measurable amounts of chloride. This indicates that these fibers may be manufactured using the diacyl chloride of terephthalic acid in a Schotten-Baumann process [92]. Despite the higher concentration chloride ions in the SVM sample that was immersed in water, the chloride content of this fiber was similar to that of the other fibers studied at 2.6 % by mass. The Artec sample had the highest percentage of chloride at 2.9 % by mass.

2.7 Conclusion and Future Work

All fibers studied herein, even PPTA, release some quantity of acid forming constituents when immersed in liquid water. However, the pH change for the fibers SVM and Rusar were greater than that observed for the other fibers. The theory that hydrochloric acid is responsible for this reduction in pH may only be true for the SVM fibers, as only these fibers exhibited a significant increase in chloride ion concentration to correspond to the reduction in pH. This leads to the conclusion that another type of acid must be responsible for the pH reduction in the Rusar sample. This acid could be attributed to residual processing chemicals, such as sulfuric acid, that remain in the fiber after washing. It could also be due to unreacted terephthalic acid from polymerization. When exposed to water vapor and then immersed in liquid water, a certain amount of acid was still released in the fibers based on 5-amino-2-(p-aminophenyl)-benzimidazole; however, this amount was considerably smaller than in the case of direct liquid water exposure, especially for SVM fibers. While the pH change of the fibers exposed to vapor water was not so significant as in the direct

Table 2.2: Elemental Analysis of Fibers Determined using Wavelength-Dispersive X-Ray Fluorescence Spectrometry and the Semiquantitative Fundamental Parameters Method IQ+

All Elements Expressed as Mass Fractions (%)				
Fiber Type:	**Armos**	**Artec**	**PPTA**	**Rusar**
Molecular Formula:	$C_{35}H_{24}N_6O_4$	$C_{35}H_{24}N_6O_4$	$C_{14}H_{10}N_2O_2$	$C_{35}H_{24}N_6O_4$
H	4.0	3.9	4.2	4.0
C	69.2	67.0	69.5	69.1
N	13.8	13.4	11.6	13.8
O	10.6	10.2	13.9	10.6
F	nd	2.6	nd	nd
Na	nd	0.012	0.52	nd
Al	0.002	0.002	0.003	0.003
Si	0.005	0.007	0.005	0.005
P	< 0.001	0.001	0.001	0.008
S	0.002	0.012	0.29	0.007
Cl	2.4	2.9	0.007	2.5
K	nd	nd	0.013	nd
Ca	nd	0.001	nd	nd

| **Fiber Type:** | **SVM** | **PBO** | **SRM 1632c Coal** | |
Molecular Formula:	$C_{21}H_{14}N_4O_2$	$C_{14}H_6N_2O_2$	Found	Certified
H	3.9	2.5	13.0	5.11
C	69.1	70.8	77.4	77.45
N	15.3	11.8	1.54	1.54
O	8.8	14.3	4.0	nd
F	nd	nd	nd	0.007
Na	nd	0.024	0.028	0.0299
Al	0.005	0.003	0.79	0.915
Si	0.005	0.005	1.25	1.654
P	0.015	0.34	0.013	nd
S	0.006	0.001	1.0	1.462
Cl	2.9	0.010	0.11	0.1139
K	nd	0.053	0.11	0.1139
Ca	nd	nd	0.12	0.145

water immersion part of the study, a loss in the fiber mechanical properties was observed, leading to the conclusion that exposing these fibers to humidity weakened them. Additionally, high temperature exposure does not appear to cause acid release or tensile strength loss.

Chapter 3

Ultrahigh Molecular Weight Polyethylene Fibers Used in Body

Armor

3.1 Chapter Overview

In this chapter, ultrahigh molecular weight polyethylene fibers are introduced. The relationship of the stability of the physical properties of this material to changes in the morphology and molecular structure of the material due to exposure to elevated temperatures is evaluated.

3.2 Polyethylene Background

Polyethylene is formed from chain polymerization of the monomer ethylene depicted in Figure 3.1, and is a very simple polymer in that it consists of only carbon and hydrogen atoms.

Polyethylene can be produced by free radical polymerization or by coordination catalysis. Free radical polymerization of ethylene results in branching of the
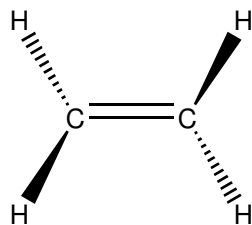
Figure 3.1: Chemical structure of the ethylene molecule.

132

polymer chain, by which monomeric units (in this case, ethylene molecules) can form long side chains, or branches. This polymer is known as low-density polyethylene (LDPE) and has crystallinity between 40 and 60 % and density between 0.91 and 0.93 g/cm^3. LDPE has a very low glass transition temperature (Tg) (approximately -120 °C), and moderately high crystallinity with a melting point of 105-115 °C [4]. Coordination catalysts, also known as Ziegler-Natta catalysts for the chemists credited with inventing them, prevent the branching that occurs in free radical polymerization of ethylene, and make the formation of linear polyethylene commercially possible. Generally, a Ziegler-Natta catalyst is the combination of a transition metal from groups IV to VIII and an organometallic compound of a metal from groups I to III of the periodic table. This catalyst guides the addition of the ethylene monomer in a stereospecific manner, and prevents the branching from occurring forming a linear chain [64]. Polyethylene formed in this manner is distinguished from branched LDPE by the term high-density polyethylene or HDPE. This mechanism is shown in Appendix B.

HDPE has crystallinity between 70 and 90 % and density between 0.94 and 0.96 g/cm^3, and an average molecular weight between 20,000 and 100,000 grams per mole [4]. It is generally accepted that an ethylene molecule is inserted between the transition metal atom and the terminal carbon atom in the growing chain. This leaves one unsaturation per chain in the final polymer (which has some significance in the radical chemistry that occurs during irradiation of the polymer) [64]. Ultrahigh molecular weight polyethylene (UHMWPE) is made in the same manner as HDPE (utilizing the Ziegler catalyst system). UHMWPE also has crystallinity between 70

133

and 90 % and density between 0.94 and 0.96 g/cm^3, although the chains formed are much longer than HDPE, having an average molecular weight between 3 and 5 million [71, 104, 105, 106].

3.3   Manufacture of UHMWPE Fibers

UHMWPE fibers are commercially manufactured by two companies DSM, headquartered in Holland, who markets their fiber as Dyneema, and Honeywell, headquartered in the United States, who markets their fiber as Spectra. UHMWPE fibers are commercially produced by a technique known as gel spinning. A solution of polyethylene with a molecular weight between 3 and 5 million is dissolved in a solvent at low concentration (approximately 1-2 % by weight) and elevated temperature, and this solution is extruded through a spinneret into a water bath. After cooling in the water bath, a gelatinous filament is obtained, which still contains a significant portion of solvent [107]. This gelled filament is comprised of a physical network of polyethylene chains and is sufficiently strong to be transported to an oven for drawing and solvent removal. The dilute solution is used to disentangle the chains and prepare them for orientation through a "superdrawing" process. This process involves extending the filaments 50 to 100 times their original length in order to make a highly-oriented, approximately 85 % crystalline fiber [71, 108]. A unique aspect of gel spinning is that filaments produced in this manner remain able to be "superdrawn" even after all of the solvent has been removed from the filament. Figure 3.2 is a schematic of this drawing process. While the exact identity of processing
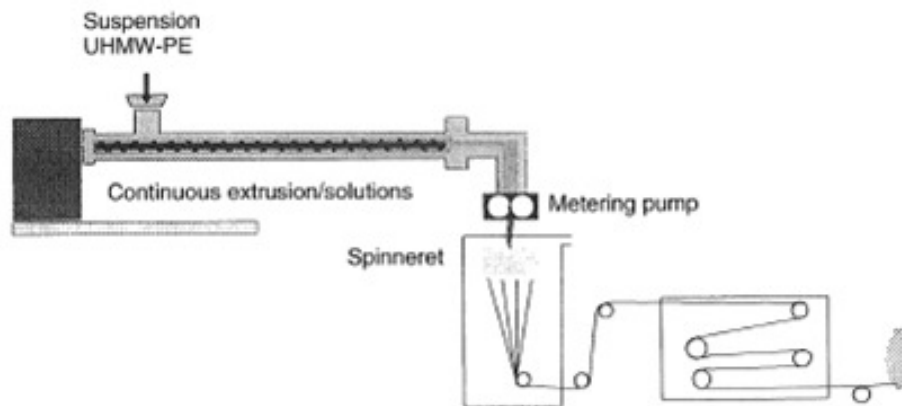
Figure 3.2: Schematic of the gel spinning process [71]. Superdrawing occurs where the formed fiber is stretched over a series of rollers as shown in the bottom right of the figure.

agents used in UHMWPE fibers is not exactly known, literature on other types of UHMWPE has indicated that we can expect the presence of antioxidants, such as Irganox, and slip agents, such as erucamide, in the fiber. As will be discussed later in this work, their presence is important to consider during irradiation of UHMWPE.

3.4 Structural Models of UHMWPE Fibers

Gel-spinning produces a rather unique molecular structure to the polymer chains within each of the filaments. There are a few general theories as to the structure of these fibers. The first of these is the *microfibrillar model*. In this model, each filament of UHMWPE is considered to consist of about 150 *macrofibrils*, that are highly extended chains forming crystalline *microfibrils*, each having a diameter between 15 and 20 nm. An alternative model is the continuous crystalline model, in which macrofibrils are comprised of a mostly continuous crystalline phase with rare, dispersed defects [109]. The primary difference between these two models is

135
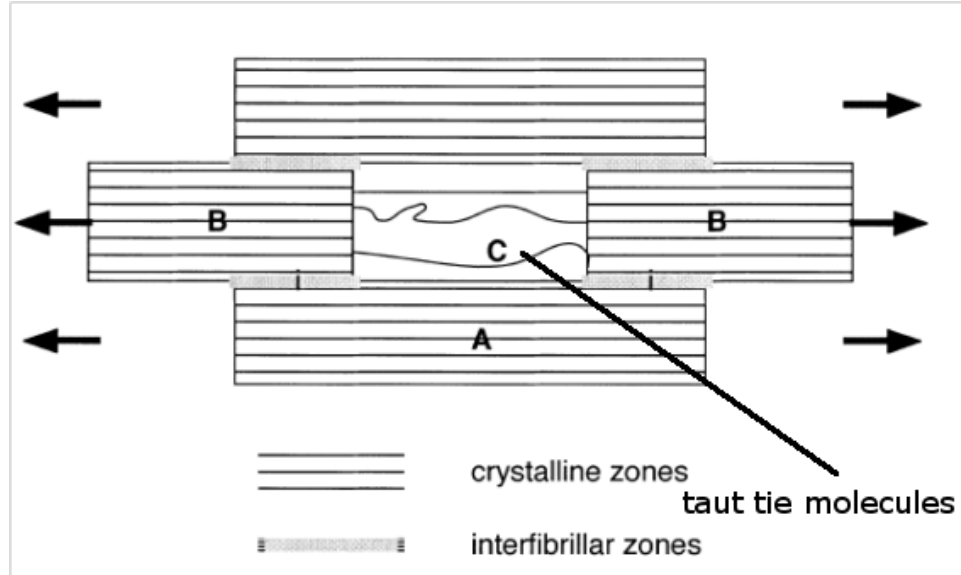
Figure 3.3: Schematic of the crystalline bridge model [110].

the way they treat the intensity of stress transfer between microfibrils. A third model, known as the *crystalline bridge model* combines aspects of the previous two, allowing for strong lateral interactions between crystalline regions across a microfibrillar interface, and much weaker interactions in the noncrystalline areas [110]. A schematic of the crystalline bridge model is shown in Figure 3.3, where regions A and B represent fully chain-extended crystalline regions, region C represents the fraction of disordered chain segments, which are noncrystalline, and the regions marked i are interfaces between the various areas. Region C is assumed to contain intra-microfibrillar tie-molecules under varying degrees of stress, called taut-tie molecules [110, 111]. These tie molecules are assumed to transmit axial stresses between the crystalline regions, and appear in some form in almost every model of the fiber structure [110].

A more detailed structural analysis and examination of structure-property re-
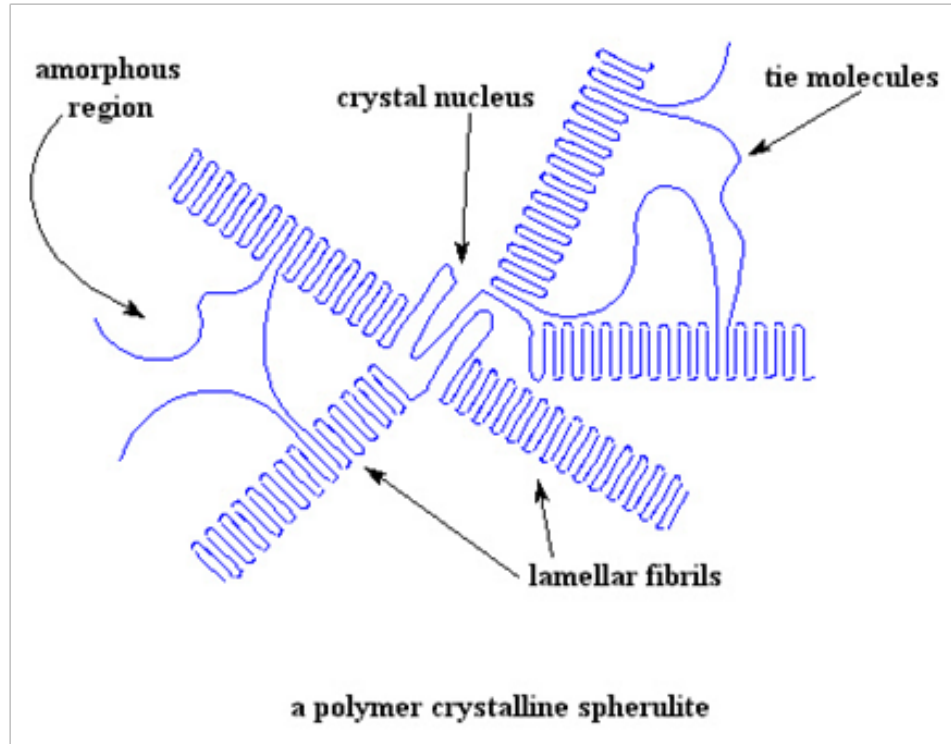
Figure 3.4: Another depiction of the taut tie molecules [110].

lationships for gel-spun UHMWPE fibers was undertaken by Fu, et. al. in 1996. This paper combined full-pattern, small angle, and powder X-ray diffraction with ^{13}C nuclear magnetic resonance, differential scanning calorimetry (DSC), and optical microscopy. The authors identified an orthorhombic and a monoclinic crystalline phase, as well as two noncrystalline phases, one being an amorphous phase and one being an intermediate phase. The crystalline regions of the fibers are primarily orthorhombic, with both a folded and an extended-chain conformation. High modulus fibers such as those studied are primarily comprised of crystals in the extended-chain conformation [112]. Another depiction of the taut-tie molecules are shown in Figure 3.4.

External stress applied to the fiber during the drawing process leads to a less

than perfect crystal [112]. One might assume that more perfect crystals would result in better mechanical properties; however this was not the case. Higher draw ratios appeared to produce better mechanical properties in the fibers [112]. Hu and Hsieh measured the average unit cell of the orthorhombic crystallites and found a and b to be equal to 7.40 0.03 Å and 4.94 0.03 Å, respectively. They also measured the average crystallite size normal to the $< 110 >$ planes to be in a range between 163 and 182 Å [112]. The fiber exhibited a much smaller fraction of monoclinic than orthorhombic crystallites. Thermal experiments indicate that the monoclinic crystal phase is not thermodynamically stable; as once it is destroyed by melting or annealing above 148 $°$ C, it cannot be recovered upon recrystallization. It is generally assumed that the monoclinic phase is transformed to the orthorhombic phase by chain rotation upon melting [112, 113, 114].

According to Fu, *et al.*, the intermediate phase of the UHMWPE fiber has several key characteristic structural features [112]. The chains involved in this phase are in the trans conformation and, due to the highly drawn nature of these filaments, are ordered preferentially with respect to the fiber axis. X-ray and NMR experiments indicate that these chains are collected together within domains, rather than as free chains throughout the structure. Chain mobility in this intermediate phase is between the low-mobility orthorhombic phase and the high-mobility amorphous phase. Interpretation of measurements of this phase can be difficult because, while it is not a crystalline phase, the separation between atoms on adjacent chains in this phase is similar to that of the $< 002 >$ diffraction of the crystalline phase, which can cause erroneous interpretations of diffraction results, however, the lateral separation

does not have crystalline periodicity. Fu's measured lateral orthorhombic crystallite sizes are smaller than those reported by other researchers due to the effect of this phase on the $< 002 >$ diffraction. Fu reports lateral sizes of 9.4 and 7.7 Å for two commercial samples of UHMWPE fibers [112]. The lateral size of the orthorhombic crystallite is important because it is generally believed to define the diameter of the crystalline microfibrils that make up the filament. Many models of UHMWPE fibers consider the role of *taut-tie molecules* (TTM) [111, 115], which are noncrystalline, highly strained chains in the *trans* conformation that are thought to form a *bridge* between crystallites along the fiber axis. These are also called *trans*-conformation tie molecules. Fu's concept of the intermediate phase is a more ordered version of the TTM concept. Fu states that individual TTMs would not contribute to the diffraction pattern observed for the fiber because they consist of individual chains with no correlations in position, however the diffraction pattern observed from the intermediate phase is attributed to lateral order. Fu attributes the tensile strength of the UHMWPE fibers to the high degree of orientation and order of the crystalline and intermediate, or ordered amorphous, phases [112]. A schematic of Fu's model is shown in Figure 3.5.

3.5 Theoretical Mechanical Properties of UHMWPE Fibers

The theoretical physical properties of UHMWPE fibers have long been a subject of much interest. The theoretical Young's modulus was calculated using bond energy information obtained from infrared spectroscopy to be 182 GPa by Treloar
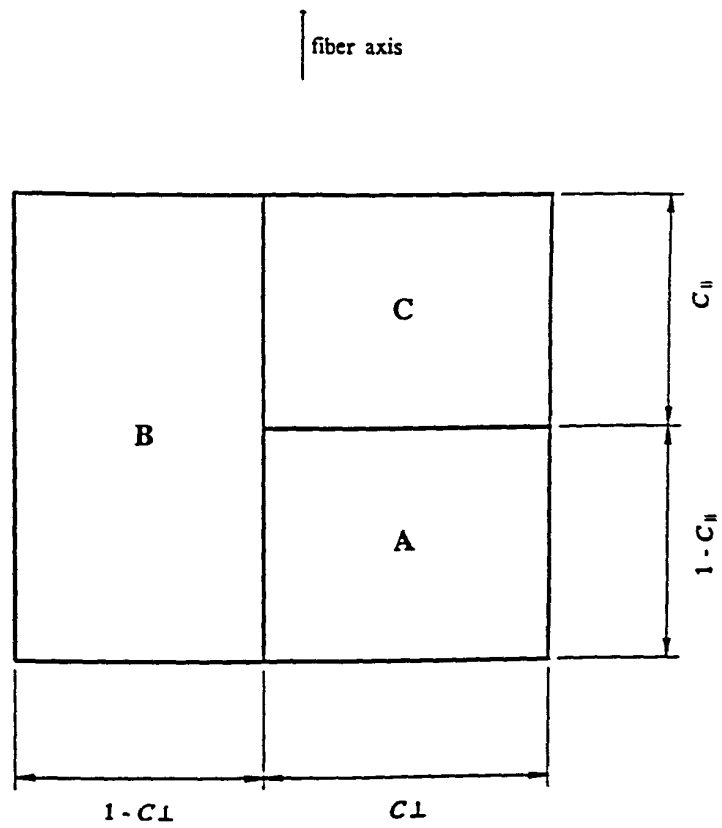
Figure 3.5: Schematic of Fu's model of an UHMWPE fiber. *A* is the amorphous area, *B* is an intermediate phase held in its metastable state by connections to the crystalline phase, *C* [112].

and others [116, 117]. The theoretical tensile strength of a single extended polyethylene chain has been calculated to be on the order of 20-60 GPa based on carbon-carbon bond energies, and is calculated by the product of the Young's modulus and the strain for which the energy of the bonds is maximized. Additionally, all chains are assumed to fracture simultaneously and this assumes a defect free, chain extended structure with infinite polymer chains [107, 118]. Obviously, these are not conditions attainable in the real world, making actual tensile strengths lower, approximately 3.7 GPa. However, given that tensile strengths obtained are only about 20 % of the theoretical maximum tensile strength, much work has been undertaken to find ways to improve the mechanical properties of UHMWPE fibers.

3.6   Limitations of UHMWPE fibers

Creep is defined as the time-dependent change in strain following a step change in stress [119]. Polymeric materials exhibit creep under static loading conditions, which is a problem for any polymer used in a load bearing design. One significant limitation of the use of UHMWPE fibers are the poor creep properties of this material. The creep is typically attributed to structural irregularities and poor cohesive energy density of the fiber [110]. The cohesive energy density in this case refers to the cohesive forces between molecules. A comparison of the cohesive energy density for various polymers is given in Figure 3.6 [120]. Representative creep data for oriented PE fibers are shown in Figure 3.7 at different stresses [121].

Creep data are presented in the form of a Sherby-Dorn plot, which presents
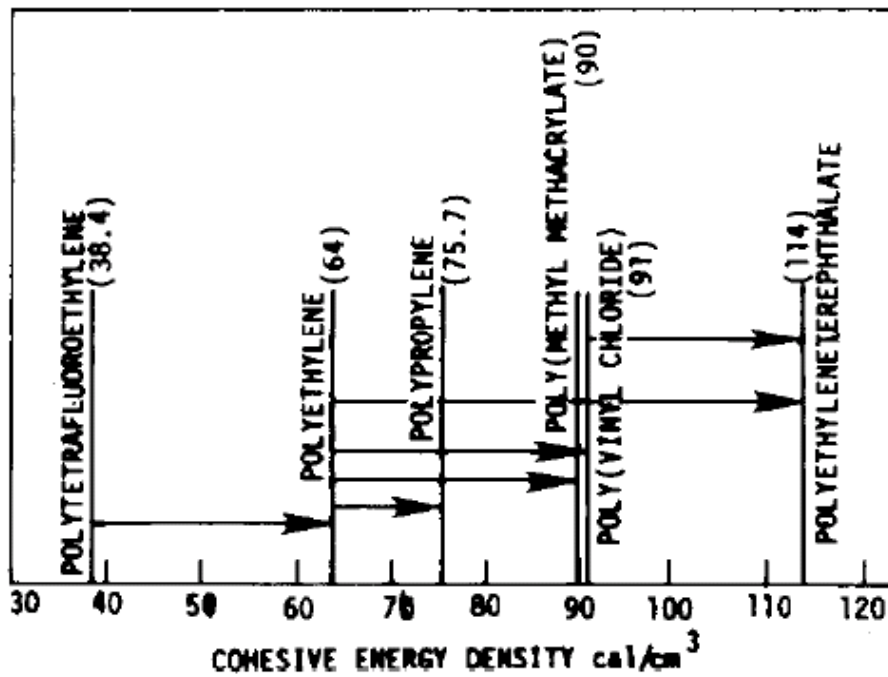
Figure 3.6: Cohesive energy density of polyethylene, as compared to other common polymers Note that polyethylene has one of the lowest cohesive energy densities of the polymers listed. This indicates that there is a low attractive force between the polymer chains in this material [120].
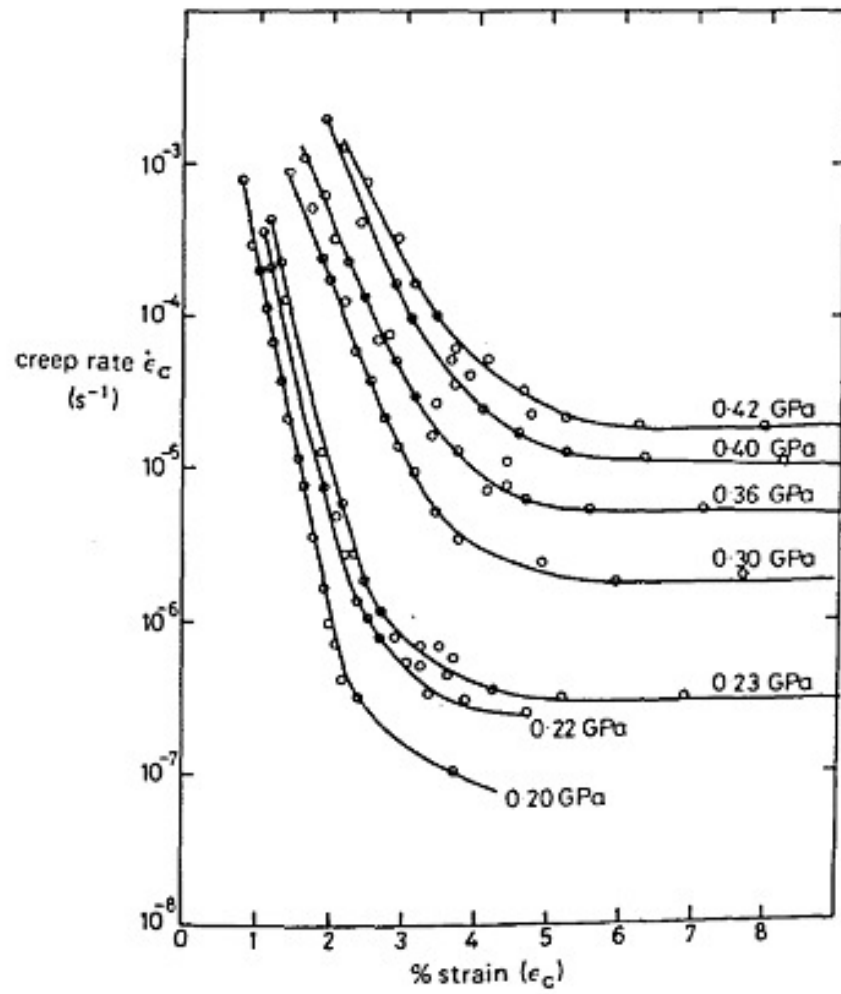
Figure 3.7: Representative Sherby Dorn plot demonstrating creep in oriented PE fibers [121].

creep as a function of strain rate versus stress. This allows for the combination of data obtained during creep testing (quasi-instantaneous application of load) and tensile testing (in which load is applied with varying rates). These data lie together on one master curve, underscoring the relationship between creep and yield behaviors in these polymers [121]. An example of a Sherby Dorn plot is shown in Figure 3.7. These plots depict two of the three regions of creep; initial creep, which is the initial rapid deformation of the polymer as a function of applied load, and plateau creep, which represents the increasing deformation or elongation of the polymer to increasing stress by configuration rearrangements, first by chain segments relatively close together and then by those further and further apart, requiring more time [122]. While creep is often studied when trying to optimize UHMWPE fiber behavior; the relationship between structure and creep in this material is not well understood. Ward describes creep behavior as two thermally activated processes acting in parallel: short time high stress process, which he attributes to a small activation energy of localized slip in the crystalline regions, and a long time, low stress process, which he attributes to the large activation energy of the network of chains in the fiber [121]. In order to better understand the role of bond interactions in creep deformation of polymers, much work has been undertaken to examine the stress-induced deformation of infrared absorption bands [123, 124]. Von Schmeling used this technique to assess stress at the molecular level in UHMWPE fibers. This work found that some chains in a typical UHMWPE fiber are very highly stressed (up to 10 GPa), which approaches estimates of the chain strength (20-60 GPa) [107, 118]. The authors verified that fiber deformation (such as during a creep event) occurs

by elastic stretching, alignment and straightening of the chain backbone, plasticity in the crystalline regions, and microfibrillar slippage due to the numerous defects in the highly oriented fiber structure. The authors recommend crosslinking or incorporation of side chains [125] as means to reduce the microfibrillar slippage in the fiber and improve its creep properties [121, 126].

3.7 Long Term Stability of UHMWPE

3.7.1 Prior Art

UHMWPE [127, 128, 129, 33] is one of the two main types of fibers currently used in ballistic-resistant body armor. Due to the previously discussed PBO hydrolysis of body armor, attention has been focused on studies to ensure the long-term stability of all fibers used in body armor. As previously mentioned, UHMWPE is a long-chain polyolefin with a molar mass between 3 and 5 million. Its tensile strength is reported to be approximately 40 % greater than PPTA fiber [130] due to its high crystallinity and highly oriented zig-zag sp^3 conformation. In addition, polyethylene has no functional groups, resulting in superior chemical resistance as compared to other materials [70]. Previous researchers have focused efforts on understanding the artificial aging of UHMWPE on bulk polymers typically used in orthopedic joint replacement applications [131]. A study published by Chabba, examined the artificial aging properties of UHMWPE fibers, focusing on oxygen uptake as a marker of degradation and calculating the activation energy of this process as being approximately 120 kJ/mol. The activation energy for oxidative chain scission in simple

alkanes such as methane, ethane, propane, n-butane, and isobutane have been previously published, mostly in regards to the selection of the most appropriate metal catalyst for this reaction. The activation energy for oxidative chain scission in simple alkanes was found to be between 13 and 32 kJ/mol. Methane had the highest activation energy, and isobutane had the lowest activation energy. This study focused on the effectiveness of different metals in the total oxidation of the small alkanes. The authors state that activation (of the metal catalyst) increased with chain size and to a lesser extent with branching [132]. Previous work on the thermal degradation of polypropylene determined an average activation energy of 123 kJ/mol for chain scission in polypropylene [133]. Iring and co-authors examined the thermo-oxidative degradation of polyethylene in the temperature range of 130 to 160 °C at 101 kPa oxygen pressure and calculated an activation energy for oxidative chain scission of approximately 140 kJ/mol [134]. In this study, aging temperatures of 43 and 65 °C were chosen to simulate the wear condition of near body temperature storage conditions, and 90 and 115 °C were used to accelerate degradation.

3.7.2 Experimental Determination of the Long-term Stability of UHMWPE Fibers

3.7.2.1 Samples

The UHMWPE fibers used in this study were supplied by DSM Dyneema and stored in dark ambient conditions. Fibers were wound onto perforated spools and placed into dry ovens at 43, 65, 90, and 115 °C for a predetermined period of time. A

series of relative temperature/relative humidity dataloggers (MicroDAQ) were used to monitor temperature during the exposure period.

3.7.2.2 Mechanical Properties Testing

The mechanical properties of the yarns were measured using established methods for measuring the ultimate tensile strength. An Instron Model 5582 test frame equipped with a 1 kN load cell and pneumatic yarn and cord grips (Instron model 2714-006) was used for these tests. The experiment was performed in accordance with ISO 2062 [135]. A 58.42 cm (23 in) Dyneema yarn was given 23 twists (1 twist per 2.54 cm) on a custom designed yarn-twisting device, and the level of twist was maintained while transferring the yarn to the pneumatic grips. The gage length was 25 cm and the crosshead speed was 250 mm/min. The strength at break was recorded and each data point represents the mean of at least 7 trials.

3.7.2.3 Oxidation Measurement

Oxidation of the fiber samples was measured using Fourier Transform Infrared Spectroscopy. A Nicolet Nexus 670 Fourier Transform Infrared Spectrometer (FTIR) equipped with a liquid nitrogen-cooled mercury cadmium telluride (MCT) detector and a SensIR Durascope (Smiths Detection) attenuated total reflectance (ATR) accessory was used in the oxidation measurement. Consistent pressure on the yarns was applied using the force monitor on the Durascope. Final scans represent the average of 128 individual scans with a resolution of 4 cm^{-1} between 650 and 4000 cm^{-1},

respectively. Spectra analysis, including spectral baseline correction and normalization was carried out using a custom software package developed in the Polymeric Materials Group at the National Institute of Standards and Technology to catalog and analyze multiple spectra. The spectra were baseline corrected and normalized using the peak at 1472 cm^{-1}, which was attributed to the CH_2 bending mode. Typical standard uncertainties for spectra measurement are 4 cm^{-1} in wavenumber and 1 % in peak intensity. For the purposes of evaluation the degree of oxidation, the overlapping peaks were deconvoluted using the wizards available in the Microsoft Origins software package between 1680 and 1740 cm^{-1}. This peak ratio was introduced as the oxidation index [136, 137, 138].

3.7.2.4 Crystallinity Determination

Differential scanning calorimetry was carried out using a TA Q2000 differential scanning calorimeter (DSC) (TA Instruments). After exposure at the specified temperature over a designated time interval, the UHMWPE fibers were cut into small segments and sealed in a hermetic sample pan. The typical weight of the sample was between 3 and 5 mg. Samples were held in at 25 °C for 5 min, then heated at 10 °C/min to 190 °C. Melting curves were resolved into three to four peaks, which can be assigned to the melting of different crystal phases. The melting points were characterized by the temperature of the peak maximum, and the heat of fusion was determined by integrating the area under the curve. Three replicates were prepared for each condition.

3.7.3 Experimental Results and Discussion

3.7.3.1 Mechanical Properties of Artificially Aged Fibers

Figure 3.8 and Figure 3.9 show the change in tensile strength as a function of aging at different temperatures. As anticipated, the reduction in tensile strength was lowest at the aging temperature of 43 °C. Only a slight decrease in the tensile (1.65 %) was observed after one week of aging, with a small additional decrease over the first month to 1.96 %. A slow, steady deterioration in the tensile strength was observed throughout the long term aging study. The study was ended at 102 weeks of aging, with a final tensile strength loss of 9 %.

The reduction in residual tensile strength was more evident at the aging temperature of 65 °C. The decrease in tensile strength after the first week was approximately 3 %, and in the first month it was 7.73 %. After 94 weeks of aging, the study was ended, with a final tensile strength loss of over 30 %.

As expected, the reduction in tensile strength was even more apparent at the higher temperatures. The UHMWPE fibers lost 28 % of their initial tensile strength at the aging temperature of 90 °C in the first week, and continuously decreased to 56 % after 17 weeks. Fibers exposed to the aging condition of 115 °C lost 42 % of their original tensile strength after 1 week. The study continued for 17 weeks, after which the fibers had lost 52 % of their original tensile strength. However, given the rapid and catastrophic loss of tensile strength in the fibers aged at 90 °C and 115 °C, it is likely that these fibers are undergoing shrinking and losing orientation during heating. Shrinkage of highly drawn and oriented polyethylene has been
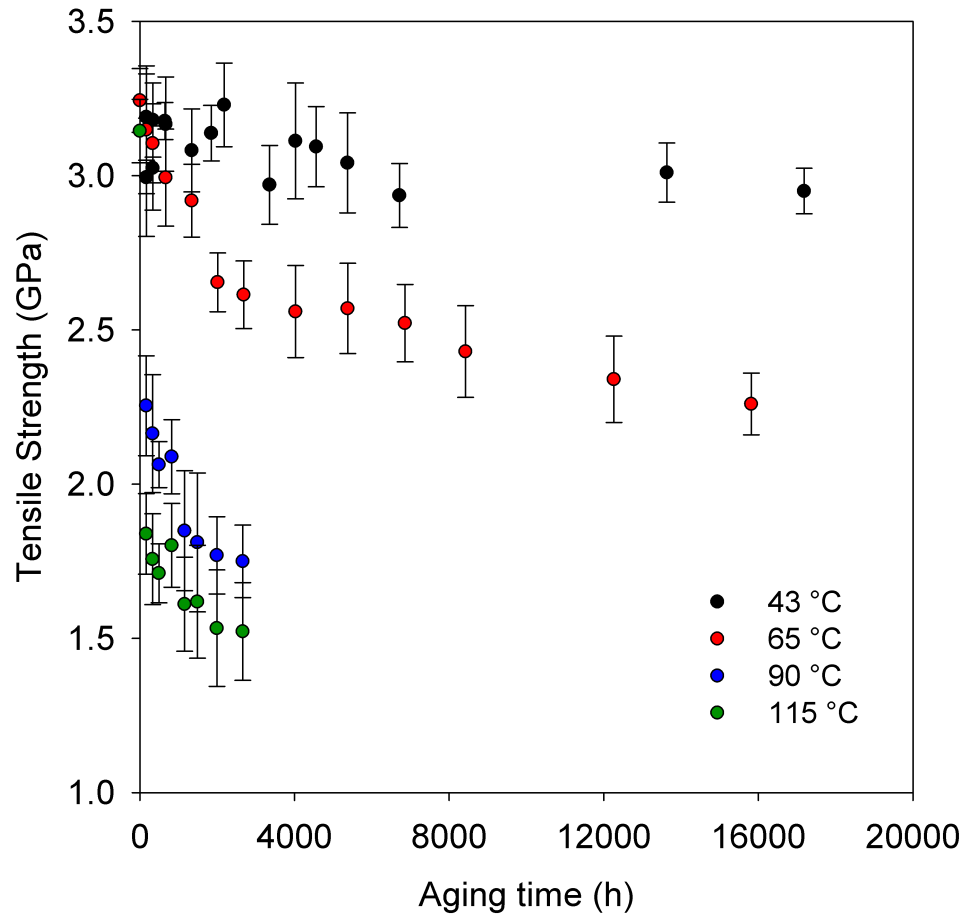
Figure 3.8: The decrease in tensile strength of artificially aged UHMWPE fibers at various temperatures over time. The 43 °C exposure was repeated to verify original data. Data for the second trial at 43 °C are designated as 43 °C new.
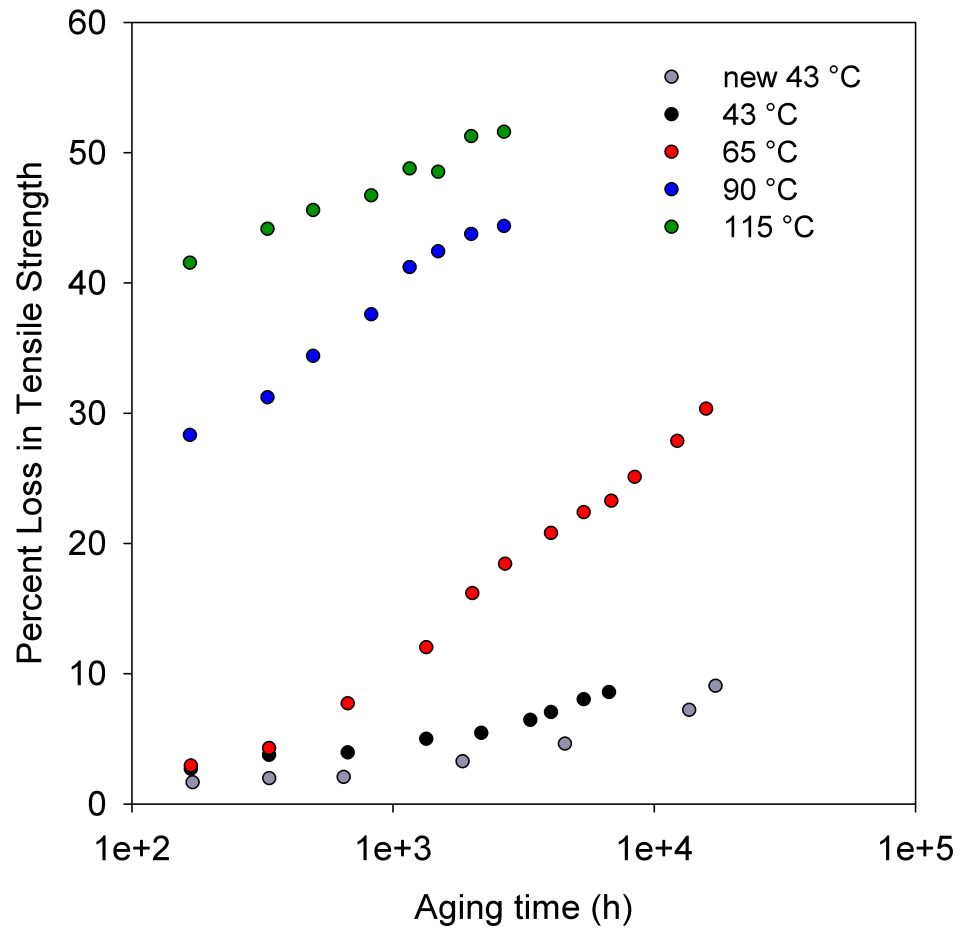
Figure 3.9: The decrease in residual tensile strength of artificially aged UHMWPE fibers at various temperatures over time (log scale).

widely reported [139, 140, 141]. The loss of orientation in the fiber is probably largely responsible for the rapid loss in tensile strength (especially at 1 week) in the fibers aged at 90 °C and 115 °C, rather than oxidative chain scission. It is likely that this loss in tensile strength occurred very quickly after exposure to the 90 °C and 115 °C ovens. Data collected at these temperatures will still be used in the activation energy calculation discussed below, but probably represents a different mechanism of tensile strength loss.

In order to assess the long term service life of UHMWPE fibers, the master curve at 43 °C, as shown in Figure 3.10. The lowest aging temperature represents the base use condition for the fibers (body temperature). A master curve was created by using 43 °C as the reference temperature, and then horizontally shifting the higher temperature aging data until they superimpose smoothly to form a single curve [33, 142, 143]. The amount that each curve must be shifted is called the *shift factor*, a_t, and is used in Equation 3.1 to determine the activation energy of the aging mechanism.

$$\ln a_t = \ln \frac{t_t}{t_0} = -\frac{E_a}{R} \left(\frac{1}{T_{ref}} - \frac{1}{T} \right) \qquad (3.1)$$

Where a_t is the shift factor, t_0 is the aging time of reference temperature, t_t is aging time after shifting, E_a is the activation energy, R is the universal gas constant, and T_{ref} is the reference temperature. The value of the activation energy as calculated by Equation 3.1 is found to be 140 kJ/mol, in agreement with previously published results [33].
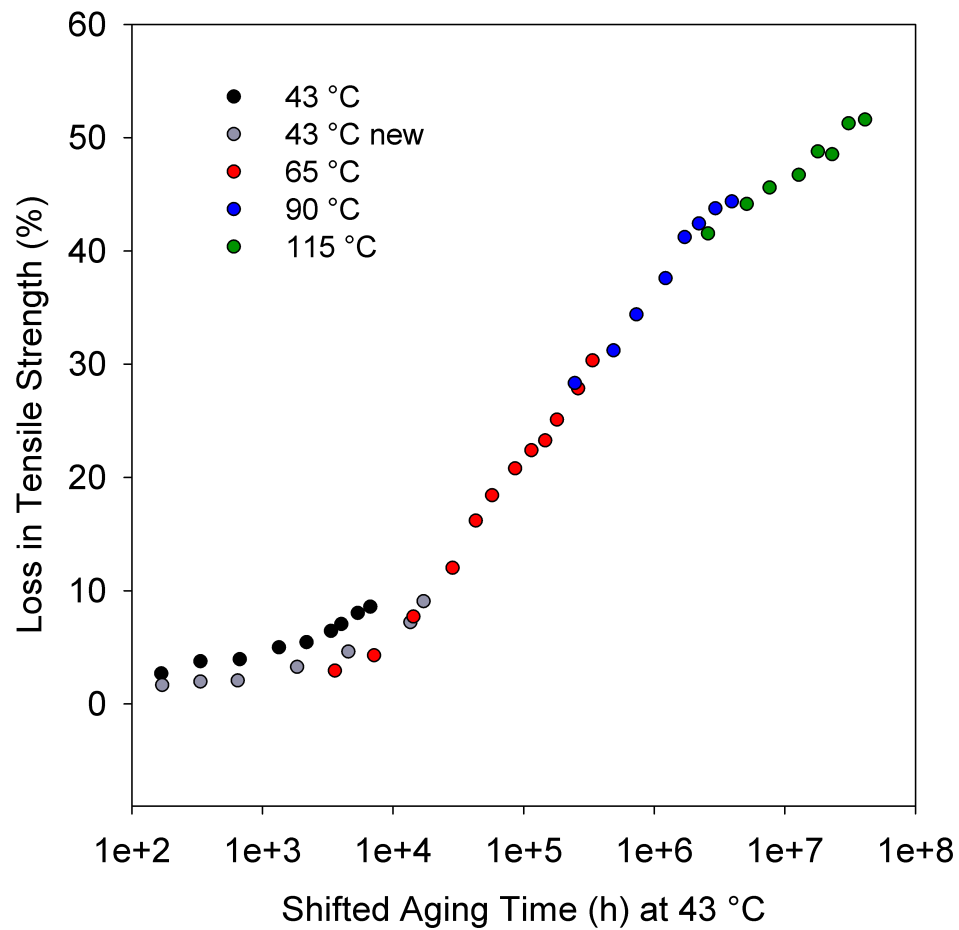
Figure 3.10: The decrease in residual tensile strength of artificially aged fibers at various temperatures over time (log scale).
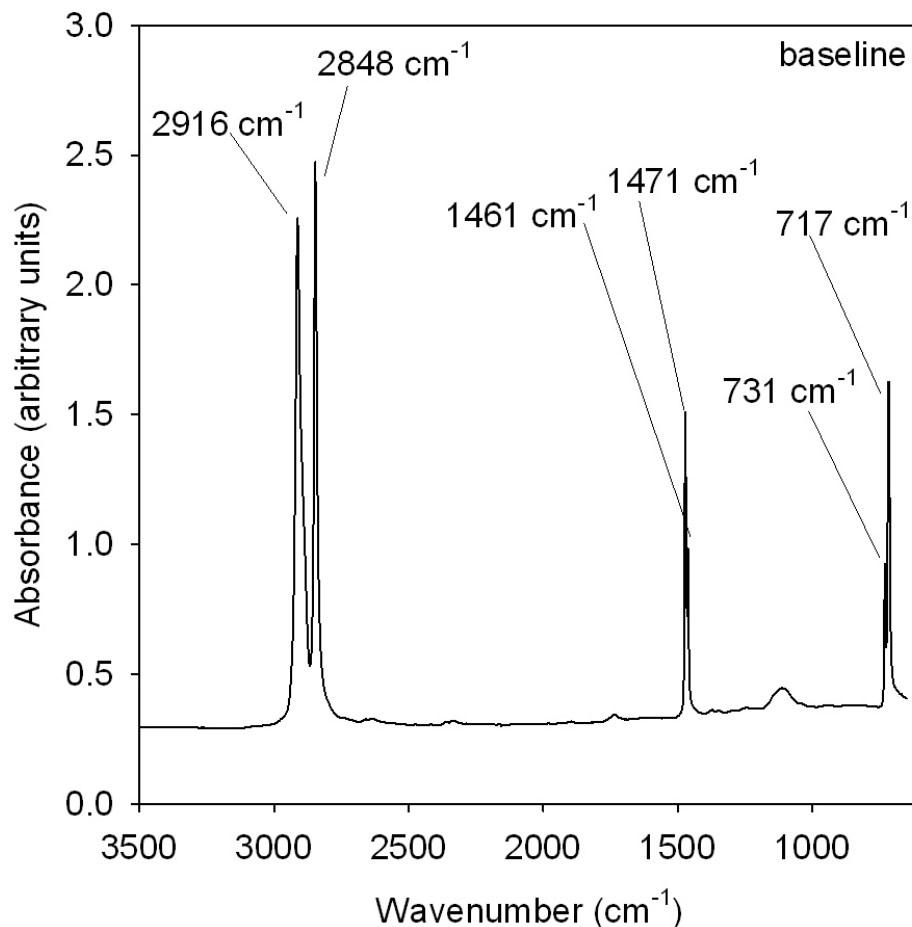
Figure 3.11: FTIR spectra of baseline, or unaged, UHMWPE fiber. The units of absorbance are arbitrary. The characteristic peaks at 2916 and 2848 cm^{-1} are identified as sp^3 C-H stretching, 1471 and 1461 cm^{-1} are assigned to C-H bending, 731 and 717 cm^{-1} are in-phase and out-of-phase C-H rocking, respectively. A small peak around 1125 cm^{-1} is unassigned.

3.7.3.2 Oxidation Analysis

A representative FTIR spectra of baseline, or unaged UHMWPE fibers is shown in Figures 3.11. The characteristic peaks at 2916 and 2848 cm^{-1} are identified as sp^3 C-H stretching, 1471 and 1461 cm^{-1} are assigned to C-H bending, 731 and 717 cm^{-1} are in-phase and out-of-phase C-H rocking, respectively. The FTIR spectra for all fibers are included for reference in Appendix B.

Oxidation increases with aging temperature and time, and is identified by the formation of a new peak at 1737 cm^{-1} which is assigned to an ester; and another shoulder peak is expected at 1713 cm^{-1}, which is identified as a ketone. At least two peaks are superimposed to form a complex FTIR spectrum. Both peaks were treated as Gaussian functions and fitted by OriginPro software as shown in Figure 3.12 through 3.14. The intensity of the ketone group intensified with increasing aging time at 43 °C. Thus, the degree of oxidation of UHMWPE fibers could potentially be quantified by introducing the oxidation index (OI), as used in other artificial aging applications for bulk UHMWPE [129, 138, 144]. For the purposes of this study, the peak at 1472 cm^{-1} was used as the reference peak, and the OI is the peak area at 1713 cm^{-1} divided by the peak area at 1472 cm^{-1}. Equation 3.2 gives the relationship between OI and aging time. Figures 3.15 and 3.16 show the increase in OI over time for all aging temperatures.

$$OI = \frac{A_{1713cm^{-1}}}{A_{1472cm^{-1}}} \tag{3.2}$$

The OI increased moderately at the lower aging temperatures. For the aging temperatures 43 °C and 65 °C, the OI increased from 0.0002 to 0.0243 and 0.0249, respectively, with a curve shape of concave-up. For the higher aging temperatures, the OI increased more rapidly. After 17 weeks of aging at 90 °C, the OI increased from 0.0002 to 0.0385, and for 17 weeks of aging at 115 °C, the OI increased from 0.0002 to 0.0471. Figure 3.17 shows the relationship between tensile strength and OI, the higher the aging temperature, the faster the drop in tensile strength, regardless
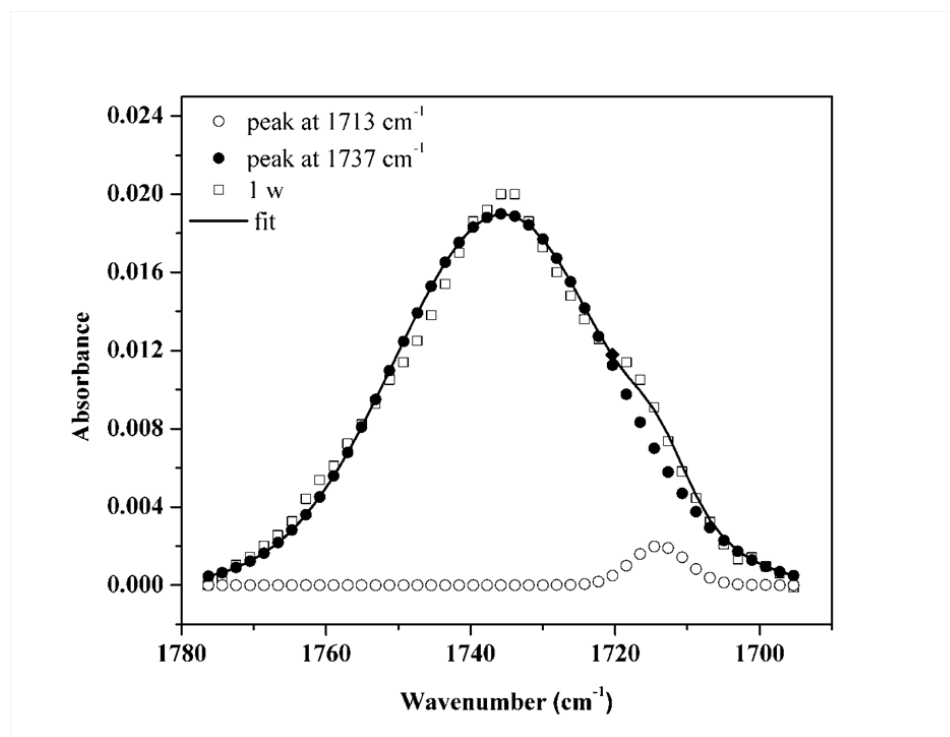
Figure 3.12: Resolved FTIR spectra of UHMWPE fiber aged at 43 °C for 1 week, scale enlarged to show 1680 to 1780 cm^{-1} region, where oxidation appears, more clearly. The units of absorbance are arbitrary. The shoulder of this peak is resolved using deconvolution software to elucidate the formation of a new peak around 1713 cm^{-1}.
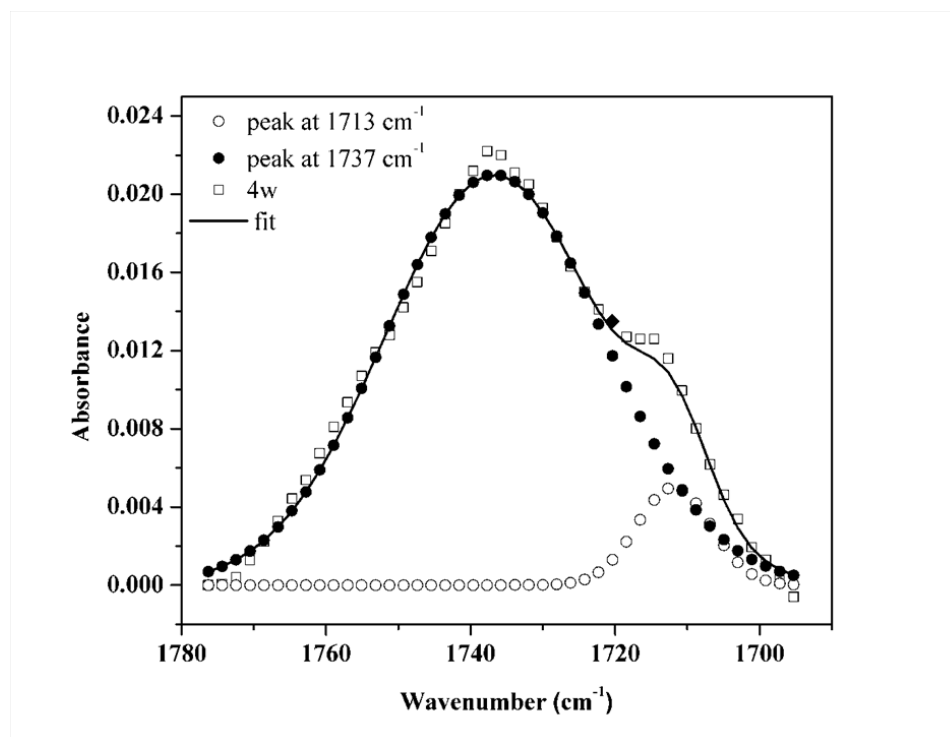
Figure 3.13: Resolved FTIR spectra of UHMWPE fiber aged at 43 °C for 4 weeks, scale enlarged to show 1680 to 1780 cm^{-1} region, where oxidation appears, more clearly. The units of absorbance are arbitrary. The shoulder of this peak is resolved using deconvolution software to elucidate the formation of a new peak around 1713 cm^{-1}.
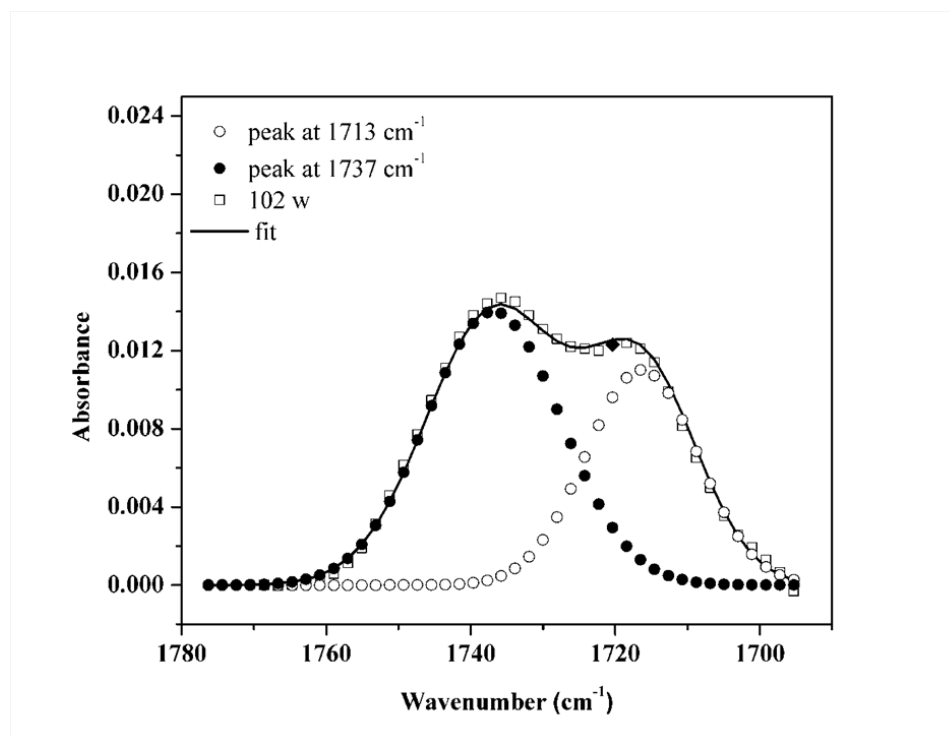
Figure 3.14: Resolved FTIR spectra of UHMWPE fiber aged at 43 °C for 102 weeks, scale enlarged to show 1680 to 1780 cm^{-1} region, where oxidation appears, more clearly. The units of absorbance are arbitrary. The shoulder of this peak is resolved using deconvolution software to elucidate the formation of a new peak around 1713 cm^{-1}.
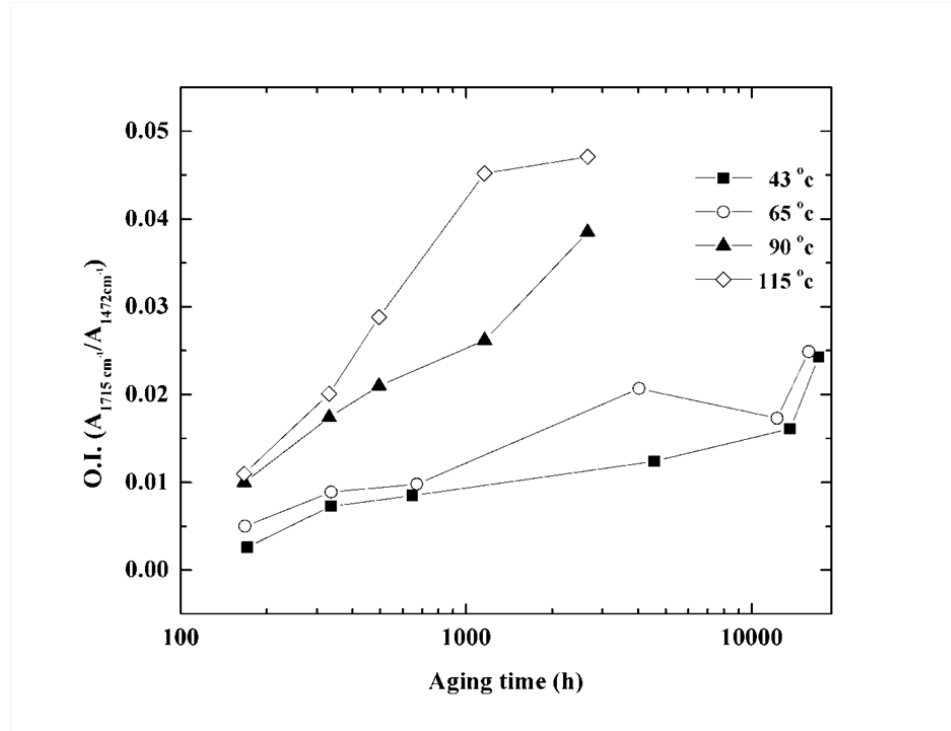
Figure 3.15: Changes in oxidation index (OI) for different aging temperatures as a function of time for UHMWPE fibers (log axis).

of the OI value.

3.7.3.3 Thermal Analysis and Crystallinity Determination

Representative DSC thermograms of UHMWPE fibers aged at various temperatures for 4 weeks are presented in Figure 3.18. Thermograms of UHMWPE fibers aged at all available combinations of temperature and time showed multiple broad melting peaks with overlapping regions between 139 and 158 °C. These melting peaks were assumed to be Gaussian, and OriginPro 8.0 was used to predefine four different melting peaks and adjust the ratio of these melting peaks. Typically, the calculation of percent crystallinity using a literature value from DSC data (243.4 J/g [129]) is an excellent way to assess relative changes between samples with aging.
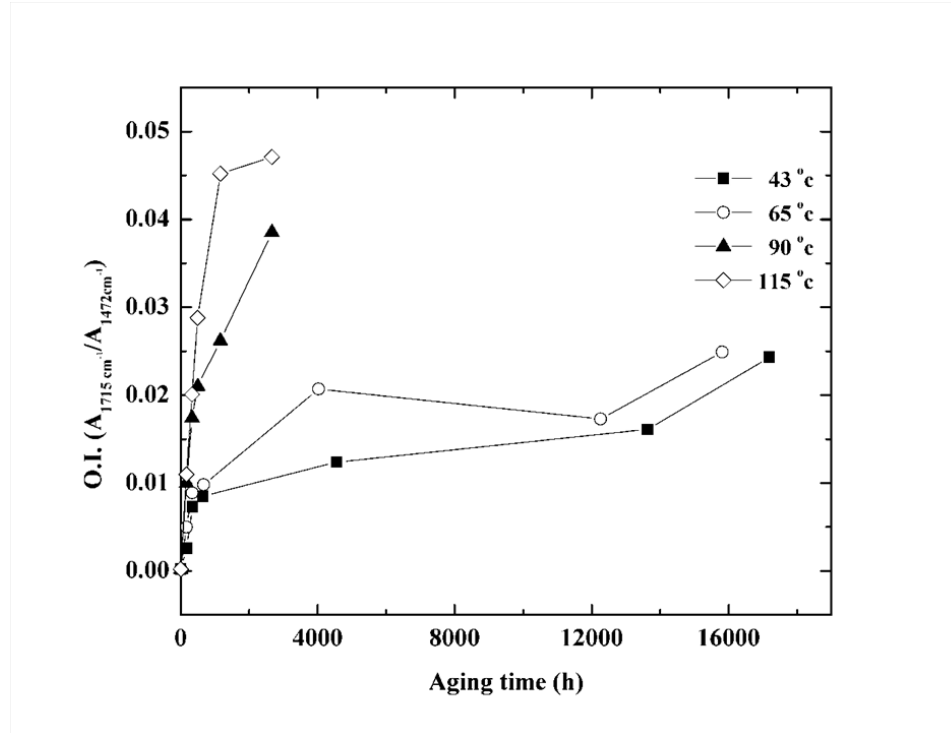
Figure 3.16: Changes in oxidation index (OI) for different aging temperatures as a function of time for UHMWPE fibers (linear axis).

However, for these UHMWPE fibers, the overall percent crystallinity of the fibers as calculated by this method was nearly unchanged, as shown by the Table 3.1. It was evident, however, that there were 4 different melting points superimposed on each other, and that the relative fraction of the sample melting at these different temperatures was changing. Therefore a different approach to this analysis was taken.

The effect of aging temperature on melting temperature and heat of fusion are shown in Figures 3.19 and 3.20. At least four endothermal peaks were deconvoluted for the aging temperatures below 90 °C, and three peaks for 115 °C. The lowest melting peak in the region of 139 °C is assigned as T_{m1}, which is relatively broad. This peak increased slightly with increasing aging temperature and is typically referred

160
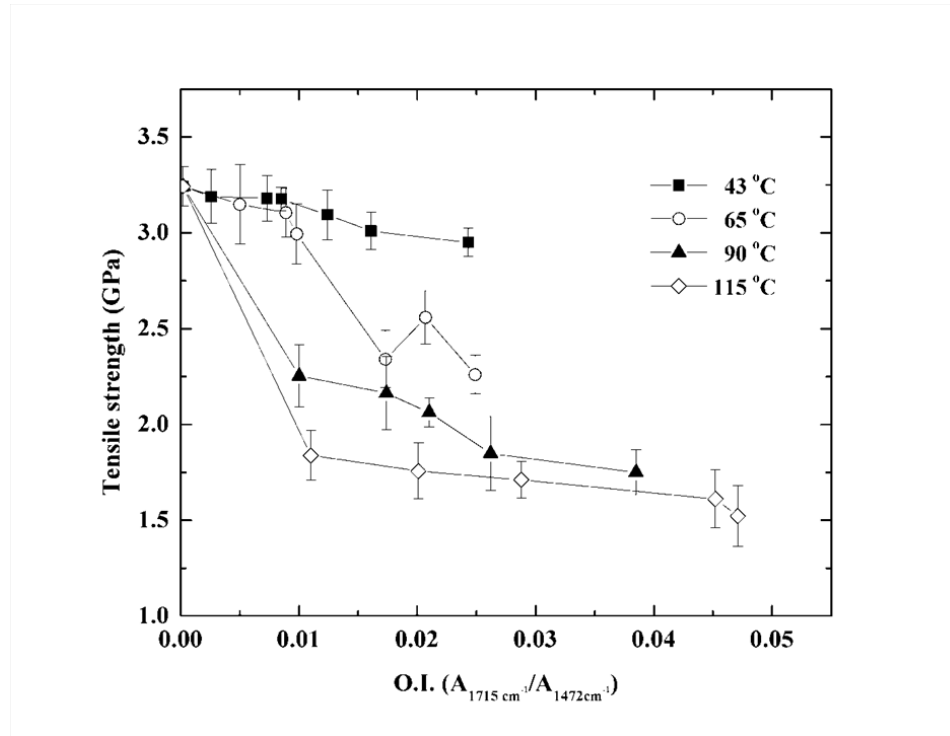
Figure 3.17: The relationship between tensile strength and oxidation index at different aging temperatures for UHMWPE fibers. In all cases, as the OI increases, tensile strength decreases.

Sample Condition	T_{m1} °C	T_{m2} °C	T_{m3} °C	T_{m4} °C	ΔH_f J/g	X_c %
Unaged	136.4	147.9	155.7	159.0	264.8	91
43 °C, 13 wks	137.9	148.4	155.0	-	263.9	90
65 °C, 16 wks	137.9	148.4	154.7	-	271.2	93
90 °C, 17 wks	138.4	148.7	154.9	-	259.2	89
115 °C, 17 wks	-	148.9	154.4	-	276.0	94

Table 3.1: Summary of melting points, heat of fusion, and crystallinity for UHMWPE aged at various temperatures for between 13 and 17 weeks. Note that the percent crystallinity is not greatly changed with aging, while the resolution of melting points is changed with aging. Standard uncertanties associated with the use of DSC in the measurement of these thermal properties is 5 %.
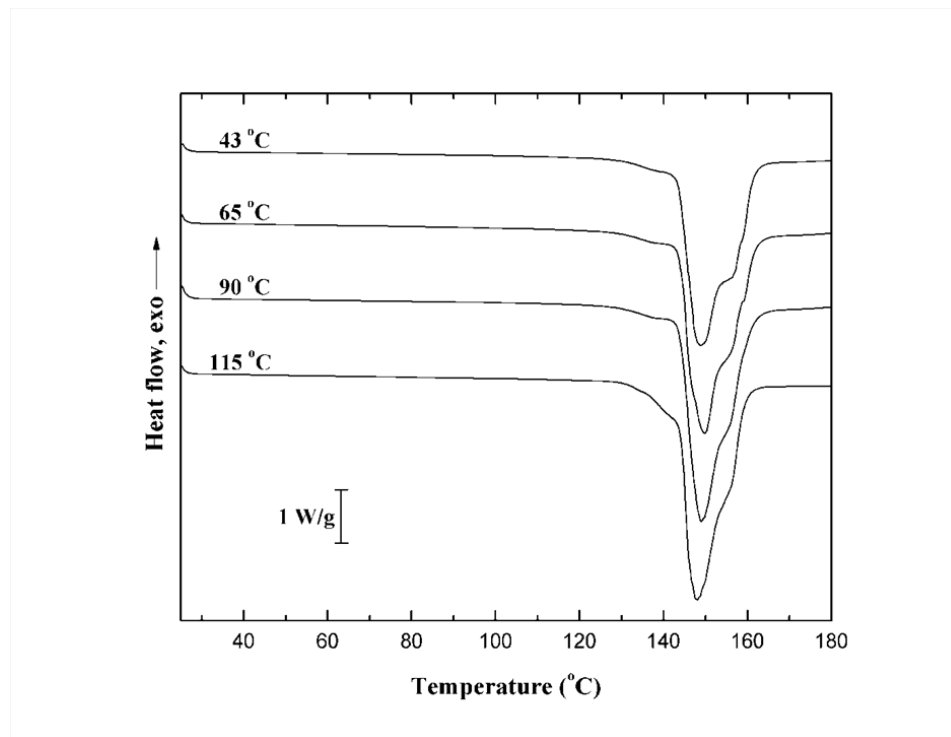
Figure 3.18: DSC thermograms of UHMWPE fibers, after 4 weeks of aging at various temperatures. Note the formation of a shoulder on the endothermic melting peak around 149 °C.

to as the melting of the folded lamellar crystal [129, 145, 146]. This increase in the melting temperature can be associated with increasing thickness of the lamella and alignment of the chains [129, 145, 146]. The heat of fusion (ΔH_m) of T_{m1} increases by about 7 % with the increase in aging temperature from 43 to 115 °C. The melting peak around the region of 149 °C is assigned as T_{m2}, which is the strongest signal in the melting thermogram. T_{m2} was attributed to melting of orthorhombic crystals to form pseudo-hexagonal crystals [129, 145, 146]. It did not show significant changes in melting temperature with increased aging time. However, the percentage of peak area for the heat of melting increased from 47.6 to 55.7 % with the increase in aging temperature from 43 to 90 °C, and then dropped to 46 % at 115 °C. T_{m3} is located at 154 °C which was attributed to the melting of the mesophase crystal, pseudo-hexagonal [129, 145, 146]. The (ΔH_m) of T_{m1} increases from 24.7 to 39.8 % when the aging temperature is increased from 43 to 115 °C. The fourth peak, T_{m4}, only appeared in the melting curves for fibers aged at lower temperatures, and may attributed to the melting of the monoclinic crystal phase [129, 145, 146].

To further investigate the effect of aging on crystallinty, the melting temperature and (ΔH_m) were plotted as a function of aging time. The melting points are plotted in Figures 3.21 to 3.24, and the percentage of peak area for the heat of melting were plotted in Figures 3.25 to 3.28. To calculate these areas, the melting endotherm was deconvoluted into four peaks to correspond with the four different melting points. These peaks were integrated to give four different areas, and then the percentage of the area of the total melting endotherm attributed to each individual peak was calculated. A representative example of the peak deconvolution is

163
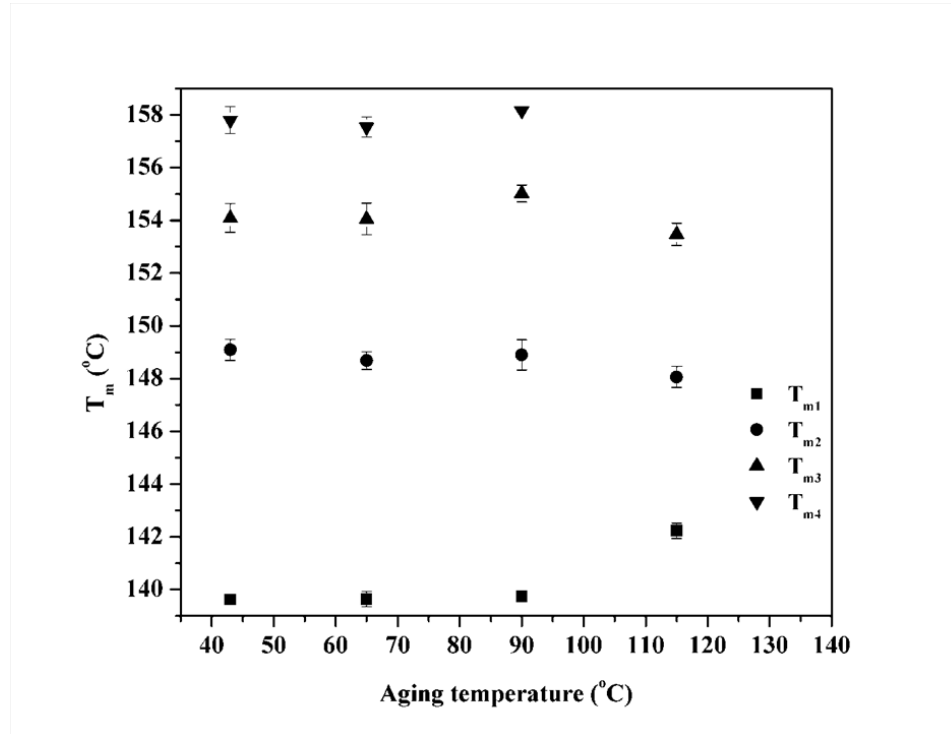
Figure 3.19: Change in melting points for four different peaks as a function of aging temperature for UHMWPE.
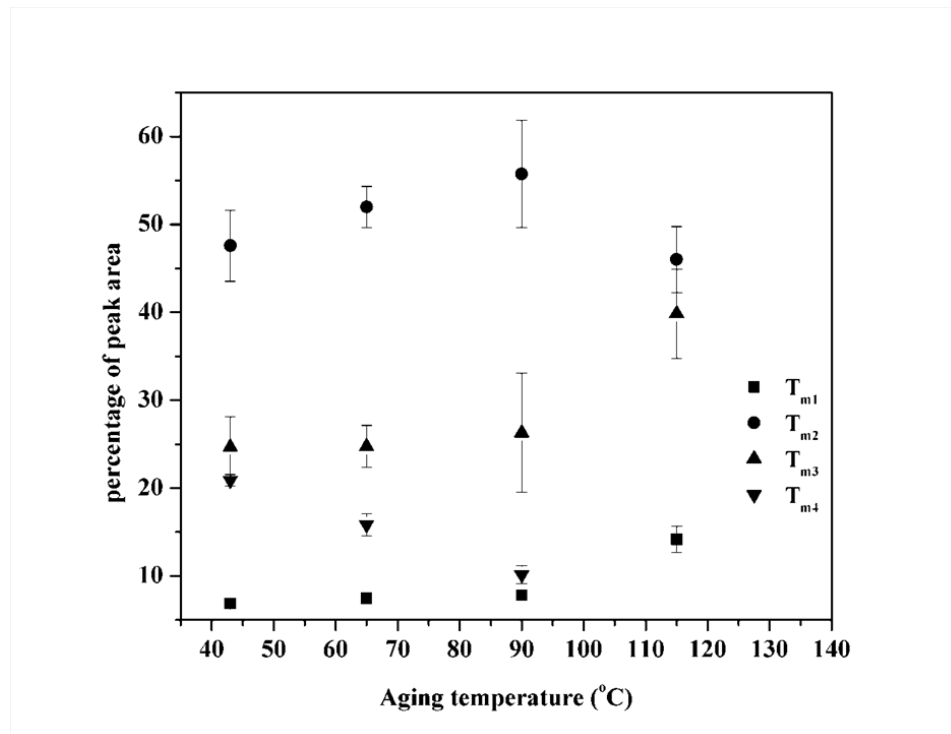
Figure 3.20: Change in heat of fusion as a function of aging temperature for UHMWPE.

given in Appendix B. For T_{m1}, T_{m2} and T_{m4}, there were only slight changes and no visible changes in melting temperature among the four different aging temperatures over the course of the aging experiment. However, T_{m3} increased slowly for aging at 43 and 65 °C after aging 102 and 94 weeks, respectively but showed no significant change after aging at 90 °C for 18 weeks. There was a faster increase for aging at 115 °C. Generally, the overall trend of (ΔH_m) for T_{m1}, T_{m2} and T_{m3} was an increase with increasing aging time, excluding minor fluctuations, except for T_{m1} aging at 115 °C. The percentage of peak area for T_{m4} decreased with increasing aging time, especially at higher aging temperature. However, T_{m4} can only be resolved under four weeks aging at 90 °C and cannot be observed at the aging temperature of 115 °C.

It is reasonable to expect that the tensile strength of UHMWPE fibers is associated with its thermal properties. The loss of tensile strength in the aged UHMWPE fibers may result from the growth of smaller crystallites during aging process or the vanishing of some crystals. In order to further investigate this theory, wide-angle X-ray scattering was performed on the fibers.

3.7.3.4   Characterization of Morphological Changes in Fiber Due to Aging

Wide angle X-ray scattering (WAXS) measurements were conducted using a laboratory-scale small-angle X-ray scattering instrument[1](Rigaku) with Mo Kα_1 radiation of wavelength 0.70926 Å in conventional pinhole geometry. The incident
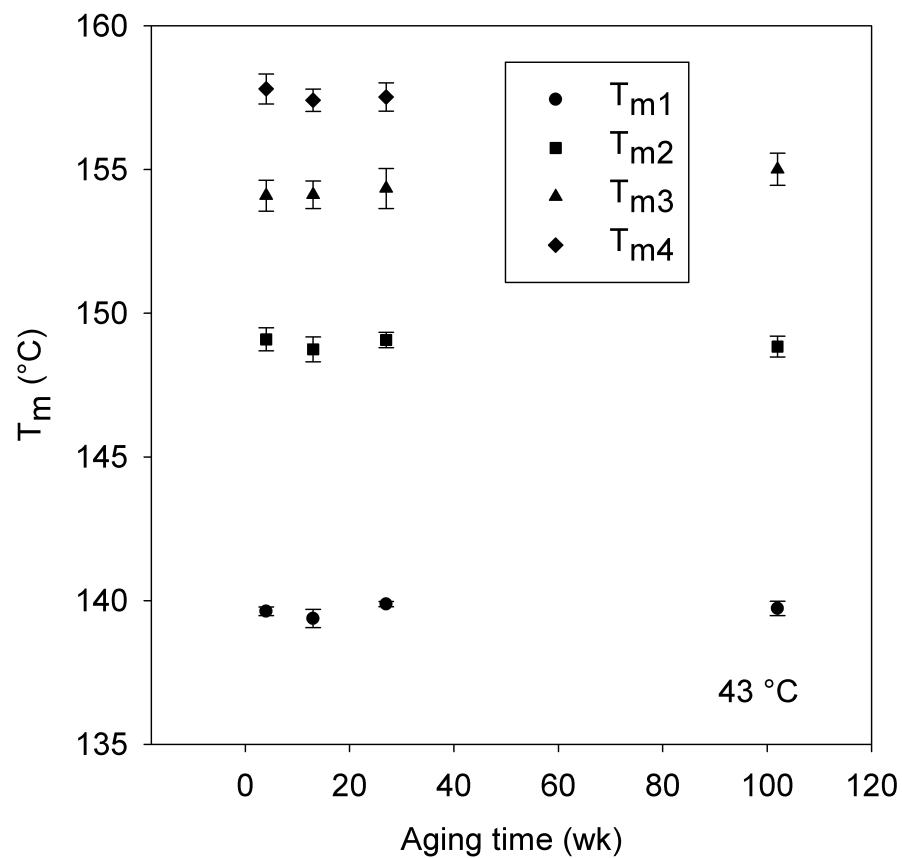
Figure 3.21: Melting points for four different peaks as a function of aging time for UHMWPE aged at 43 °C.
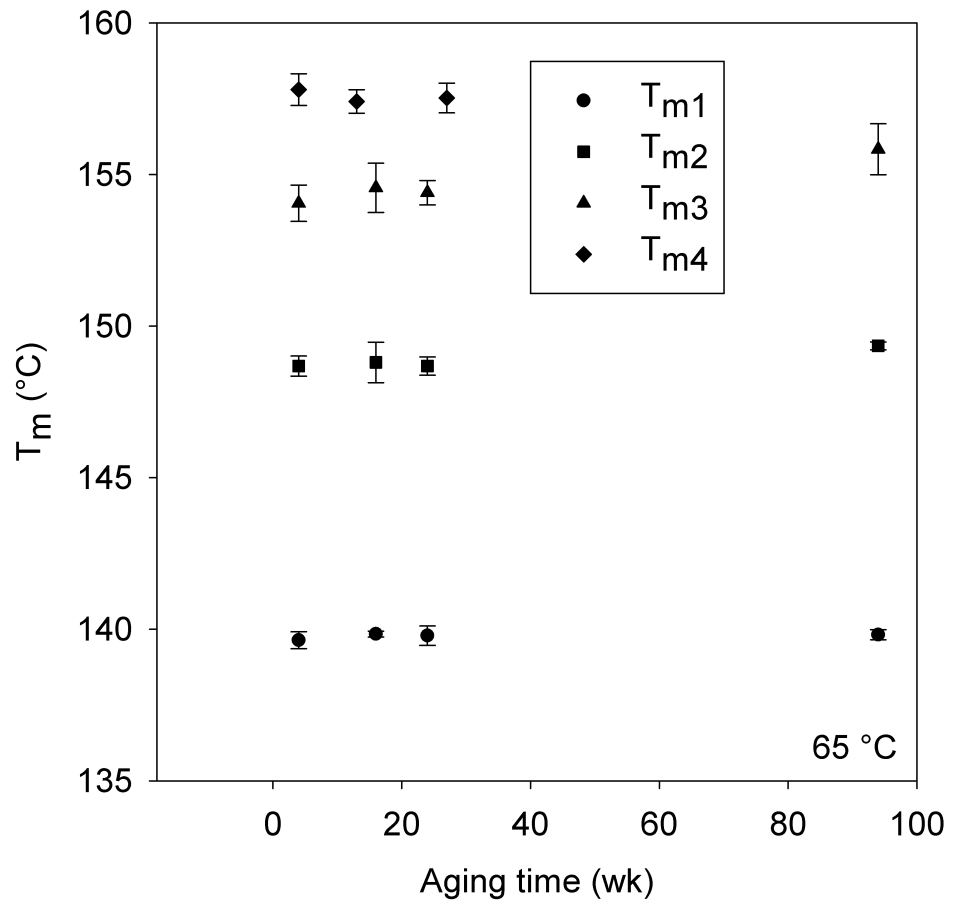
Figure 3.22: Melting points for four different peaks as a function of aging time for UHMWPE aged at 65 °C.
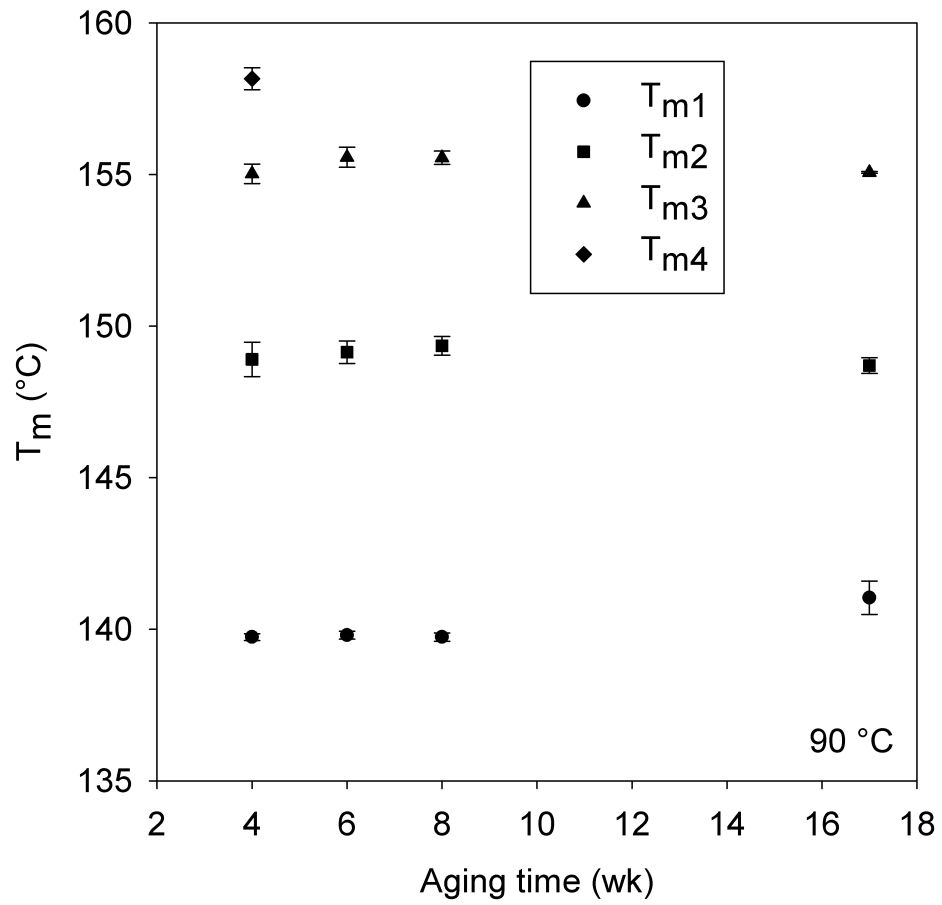
Figure 3.23: Melting points for four different peaks as a function of aging time for UHMWPE aged at 90 °C.
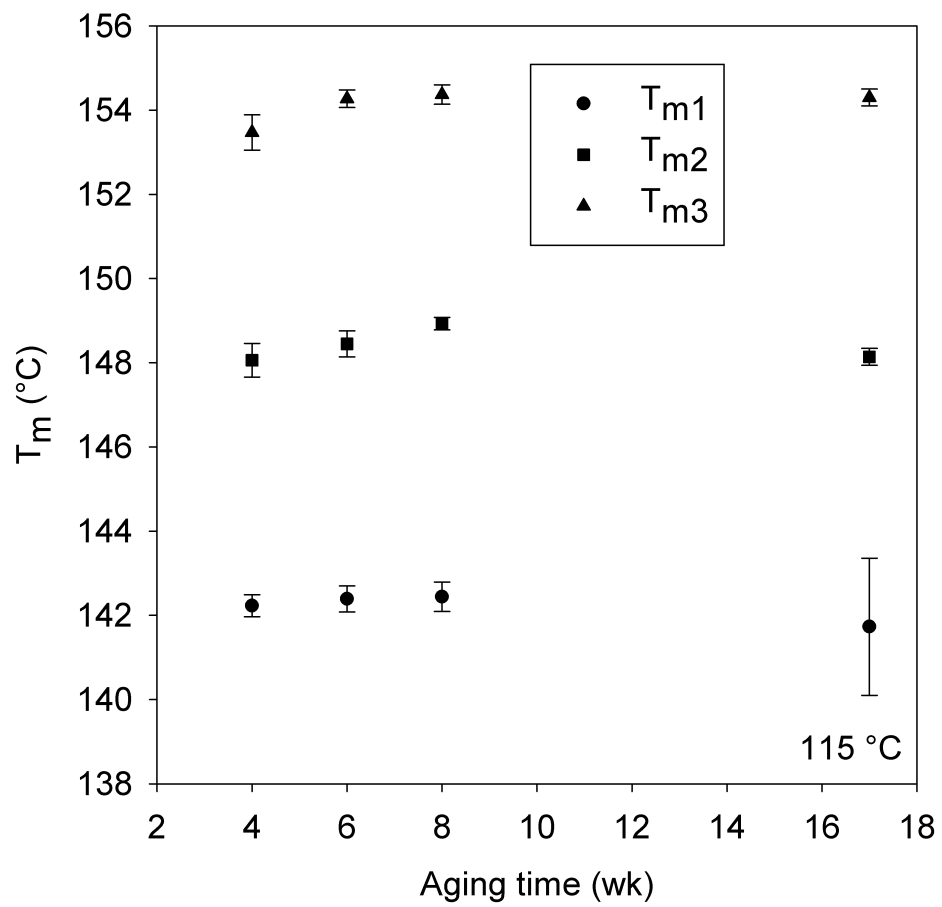
Figure 3.24: Melting points for four different peaks as a function of aging time for UHMWPE aged at 115 °C.
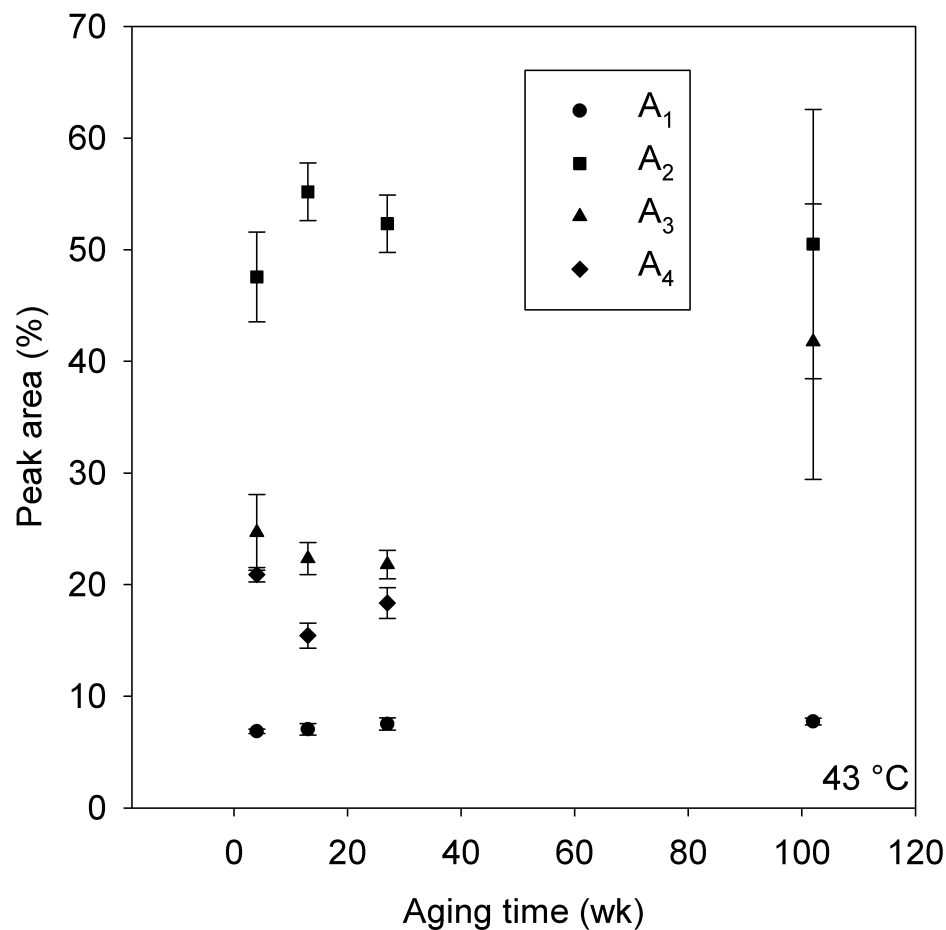
Figure 3.25: Percentage of peak area for the heat of melting as a function of aging time for UHMWPE aged at 43 °C. To calculate these areas,the melting endotherm was deconvoluted into four peaks to correspond with the four melting points as discussed previously. These peaks were integrated to give four different areas, and then the percentage of the area of the total melting endotherm attributed to each individual peak was calculated and plotted here. A representative example of the peak deconvolution is given in Appendix B.
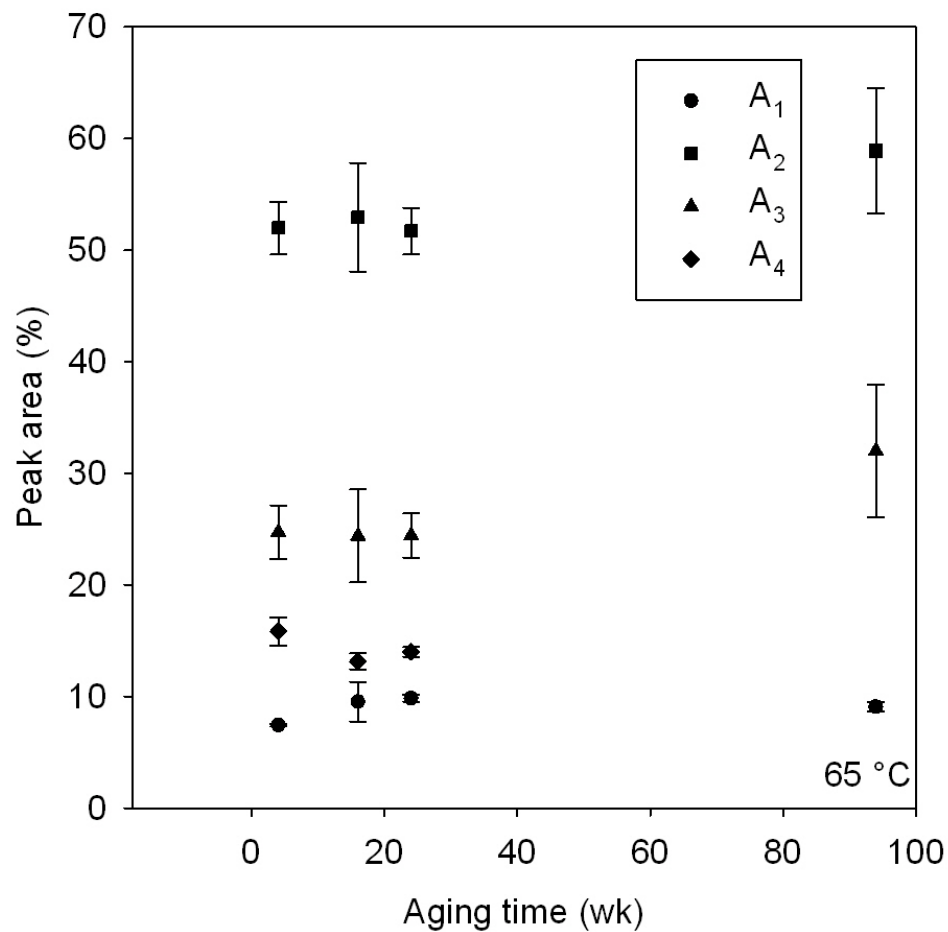
Figure 3.26: Percentage of peak area for the heat of melting as a function of aging time for UHMWPE aged at 65 °C. To calculate these areas, the melting endotherm was deconvoluted into four peaks to correspond with the four melting points as discussed previously. These peaks were integrated to give four different areas, and then the percentage of the area of the total melting endotherm attributed to each individual peak was calculated and plotted here. A representative example of the peak deconvolution is given in Appendix B.
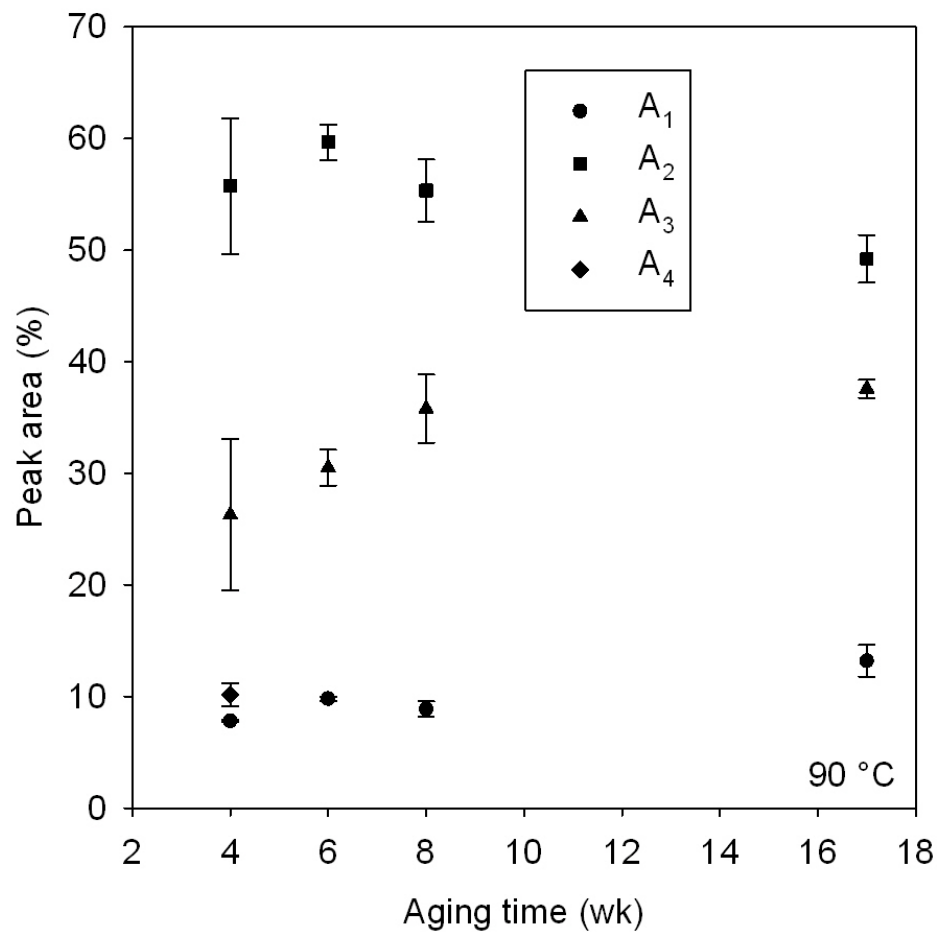
Figure 3.27: Percentage of peak area for the heat of melting as a function of aging time for UHMWPE aged at 90 °C. To calculate these areas,the melting endotherm was deconvoluted into four peaks to correspond with the four melting points as discussed previously. These peaks were integrated to give four different areas, and then the percentage of the area of the total melting endotherm attributed to each individual peak was calculated and plotted here. A representative example of the peak deconvolution is given in Appendix B.
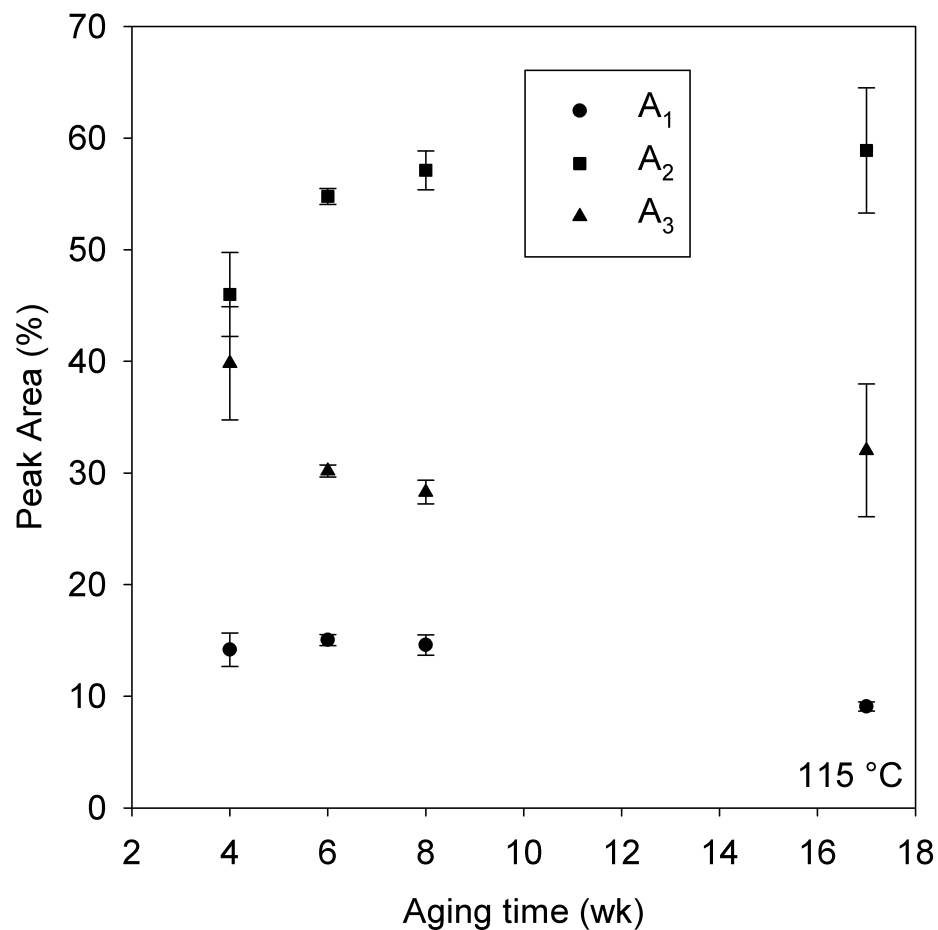
Figure 3.28: Percentage of peak area for the heat of melting as a function of aging time for UHMWPE aged at 115 °C. To calculate these areas,the melting endotherm was deconvoluted into four peaks to correspond with the four melting points as discussed previously. These peaks were integrated to give four different areas, and then the percentage of the area of the total melting endotherm attributed to each individual peak was calculated and plotted here. A representative example of the peak deconvolution is given in Appendix B.

beam, diffracted beam and sample chamber were under vacuum. An image plate was used to collect the two-dimensional scattering patterns. The fibers were mounted perpendicular to the direction of the beam [147].

X-rays are electromagnetic radiation occupying the spectrum from approximately 10^{-2} to 10^2 Å. WAXS studies on polymers are typically either performed using the $K\alpha$ characteristic radiation from a copper target tube with a wavelength of 1.5418 Å, or the wavelength 0.7107 Å from a molybdenum target tube. The X-ray wavelength of approximately 1 Å is approximately the same order of magnitude as the interatomic distances of interest in condensed matter, making X-rays a powerful tool for probing the arrangement of atoms in matter [147].

X-rays exhibit a particle-wave duality, therefore certain properties of X-rays are best considered when a beam of X-rays is considered as a stream of photons. Photons can be characterized by an energy E and a momentum p, while a wave is characterized by a wavelength λ and a frequency ν. These are related by the *de Broglie relationship*. There is no mass or charge associated with a photon, thus the shorter the wavelength, the higher the photon's energy. for $CuK\alpha$ and $MoK\alpha$, the photon energies are 8.04 and 17.44 keV, respectively [147].

The strength of a beam of radiation is characterized by its flux. If the beam is a plane wave, then the flux J is measured as the amount of energy transmitted per unit area per second. When the radiation is considered as a stream of particles, J is represented by the particle flux, or the number of photons passing through a unit

---

[4]The small-angle X-ray scattering instrument was reconfigured for WAXS by moving the detector to perform these measurements.

area per second. When the radiation is regarded as a wave J, is proportional to the square of the amplitude of the oscillating wave field. When a plane wave of flux J_0 irradiates a sample, a scattered spherical wave emanates in all directions. To obtain information about the structure of the sample, the flux of the scattered radiation, J must be interpreted as a function of the scattering direction, and will change in proportion to J_0. Therefore, the ratio J/J_0 as a function of the scattering direction is the information of interest. Given that J_0 is a plane wave and J is a spherical wave, the ratio J/J_0, which is also called the differential scattering cross section, has a dimension of area per solid angle. The differential scattering cross section can be integrated to give the total scattering cross section, which is the total number of particles scattered in all directions per second divided by the flux of the incident beam. The total scattering cross section has the dimension of area [147].

Diffraction of X-rays by matter results from scattering of X-rays by individual electrons in the sample and interference of the scattered waves. In a WAXS experiment, the flux is measured as a function of the scattering direction. These data are analyzed to obtain information about the relative location of atoms in the sample [147].

Figure 3.29 shows the geometry of the path length difference of a scattering experiment. $\mathbf{S_0}$ is the unit vector describing the direction of an incident plane wave, as shown in Figure 3.29. The incident wave, $\mathbf{S_0}$ is scattered by particles located at points O and P in the schematic. A detector is placed in the direction specified by unit vector $\mathbf{S}$ at a distance far from the scattering centers. As long as the scattering is coherent and does not result in a phase change, the phase difference $\Delta\phi$ between
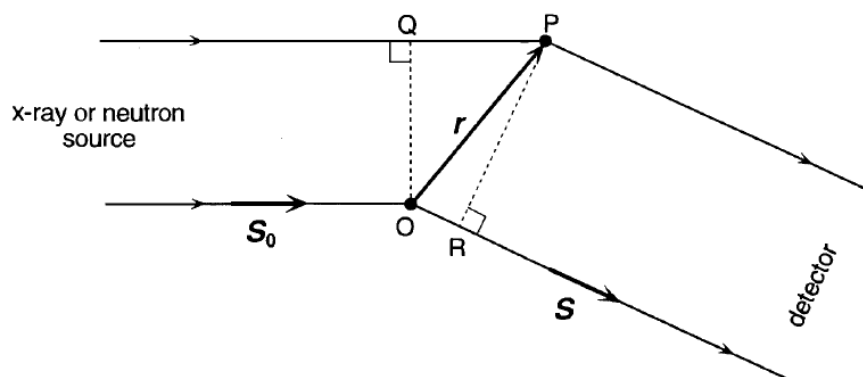
Figure 3.29: A schematic of a neutron or X-ray scattering experimental setup showing the path length difference between the radiation source, the scattering centers, O and D, being analyzed, and the detector [147].

the waves scattered at O and P arriving at the detector depends on the path length difference $\delta\phi$ between the two rays [147].

3.7.3.5 Results and Discussion of WAXS Analysis

Gel spun UHMWPE fibers are between 80 and 90 % crystalline, and considering their means of manufacture, the crystallites within the fiber are expected to be very highly oriented. An examination of the scattering intensity plots in Figure 3.30 shows that for the unaged UHMWPE sample in the upper left corner, the circumferential diffraction spots are grouped in narrow arcs. These broaden with increased aging time and temperature, as shown in the scattering intensity plots for the aged specimens. Thus, these samples lose orientation when exposed to elevated temperatures for long periods of time, likely due to shrinkage and relaxation of the fiber, as previously discussed. Some of the loss of orientation may also be due to the formation of a transient hexagonal "mobile" or "rotator" crystal phase [148, 149].

fiber axis direction
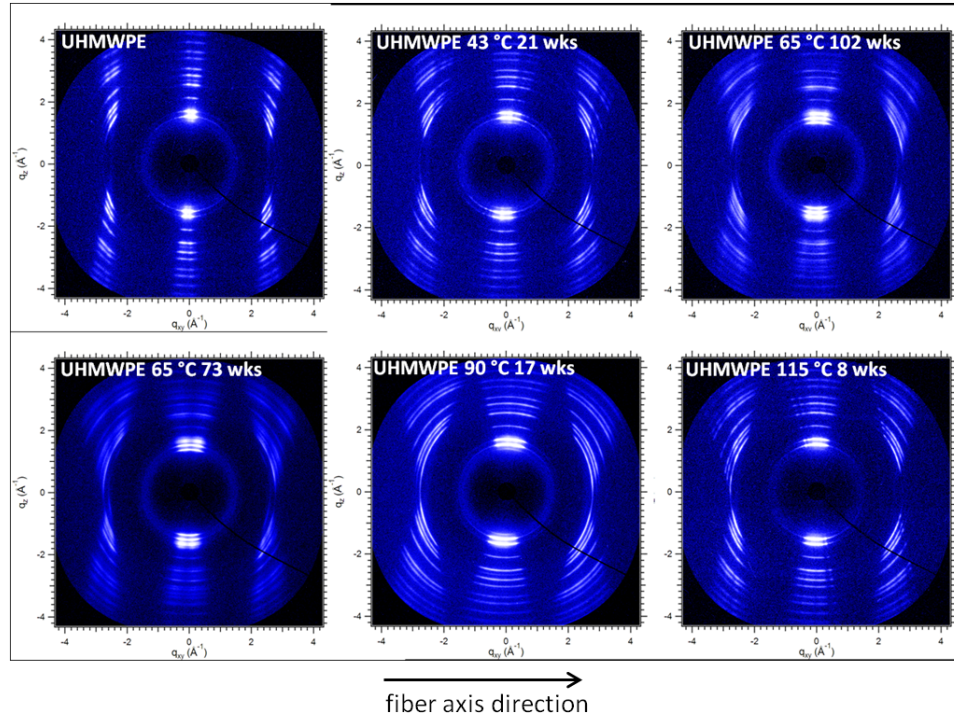
Figure 3.30: WAXS scattering intensity plots for aged and unaged UHMWPE fibers. The orientation of the fibers is decreased with exposure to elevated temperatures.

This phase has been observed to form with the stable orthorhombic phase at temperatures below the melting point of the orthorhombic phase [149].

Figure 3.31 shows equitorial wide angle X-ray scattering (WAXS) from UHMWPE fibers in various aging conditions, taken from 2D data in Figure 3.30. These conditions are unaged samples, samples aged at 43 °C for 21 weeks, samples aged at 65 °C for 102 weeks, samples aged at 65 °C for 73 weeks, samples aged at 90 °C for 17 weeks, and samples aged at 115 °C for 8 weeks.

The WAXS scattering was performed with the direction of the X-ray beam aligned perpendicular to the axis of the fiber (perpendicular to the direction of the fiber's orientation). The arrangement of chains in an orthorhombic unit cell of polyethylene is shown in Figure 3.32 for reference. The polyethylene orthorhombic
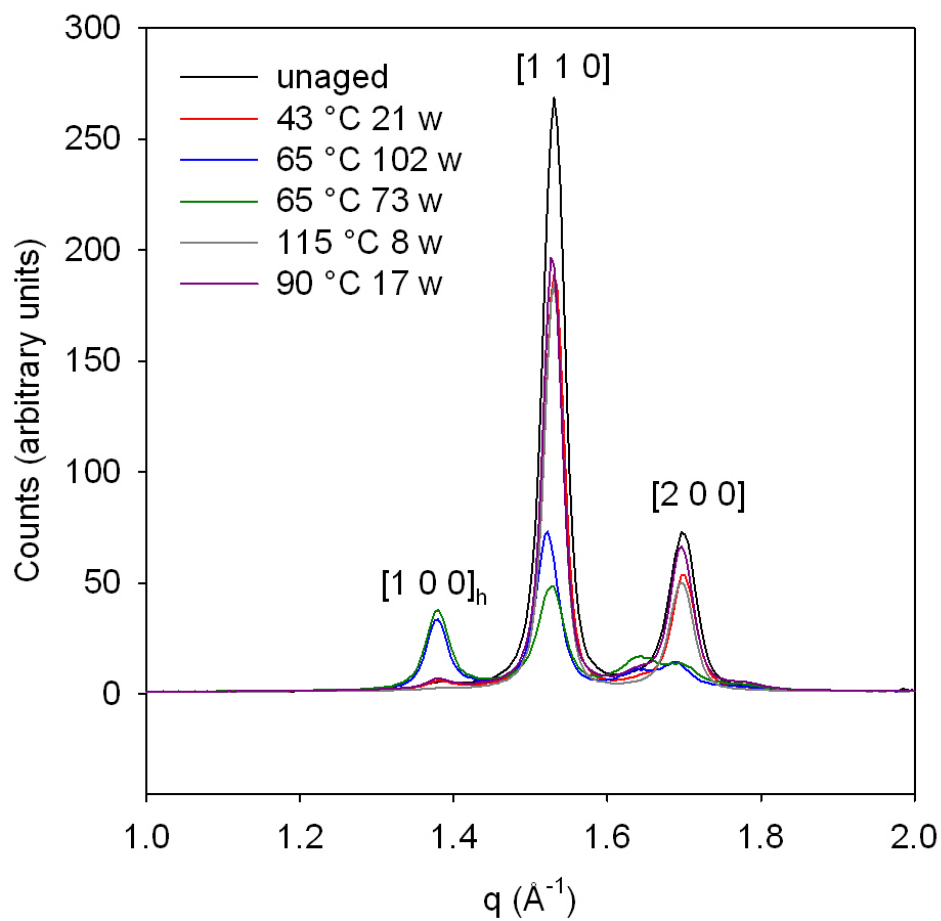
Figure 3.31: WAXS from UHMWPE fibers aged at various conditions for various times. These conditions are new, unaged samples, samples aged at 43 °C for 21 weeks, samples aged at 65 °C for 102 weeks, samples aged at 65 °C for 73 weeks, samples aged at 90 °C for 17 weeks, and samples aged at 115 °C for 8 weeks.

unit cell dimensions for orthorhombic are a = 0.741 nm, b = 0.494 nm, and c = 0.255 nm [150] and the polyethylene hexagonal unit cell dimensions are a = 0.842 nm, b = 0.456 nm, and c < 0.255 nm [148]. The two peaks in the WAXS data at q = 1.53 Å^{-1} and q = 1.70 Å^{-1} are indexed to the orthorhombic crystal structure of UHMWPE, while the peak at q = 1.39 Å^{-1} is indexed to the [1 0 0] reflection of the hexagonal phase [151]. Previous work was used to assign all peaks [152, 153, 154, 149, 148, 151].

Increases are seen in the scattering of the [1 0 0] hexagonal peak for fibers aged at 65 °C for 73 and 102 weeks, indicated by the blue and green curves in Figure 3.31. There are also corresponding decreases in the scattering intensity for the orthorhombic planes at [1 1 0] and [2 0 0], most likely due to the loss of orientation smearing the intensity out azimuthally. Previous work [149] has also shown the formation of a metastable hexagonal phase upon heating of solution-crystallized polyethylene samples, although it is unclear why this result is most pronounced for the fibers heated to 65 °C and not to higher temperatures.

Further examination of WAXS data show the formation of shoulders to the left and right of the [2 0 0] peak. These shoulders may be due to the formation of a second hexagonal peak. The peaks at [1 0 0]$_h$, [1 1 0], and [2 0 0] are very close together, so it is difficult to discern peak overlap from amorphous (which is typically seen as a broad, ill-defined peak in WAXS). There is likely a contribution from both the amorphous region and the overlap of these peaks that result in broad peaks that do not reach the baseline. The shoulder may also be due to the formation of small crystallites due to recrystallization of the sample after aging at the elevated temperatures, which is akin to annealing of these samples. Overall, the shapes of
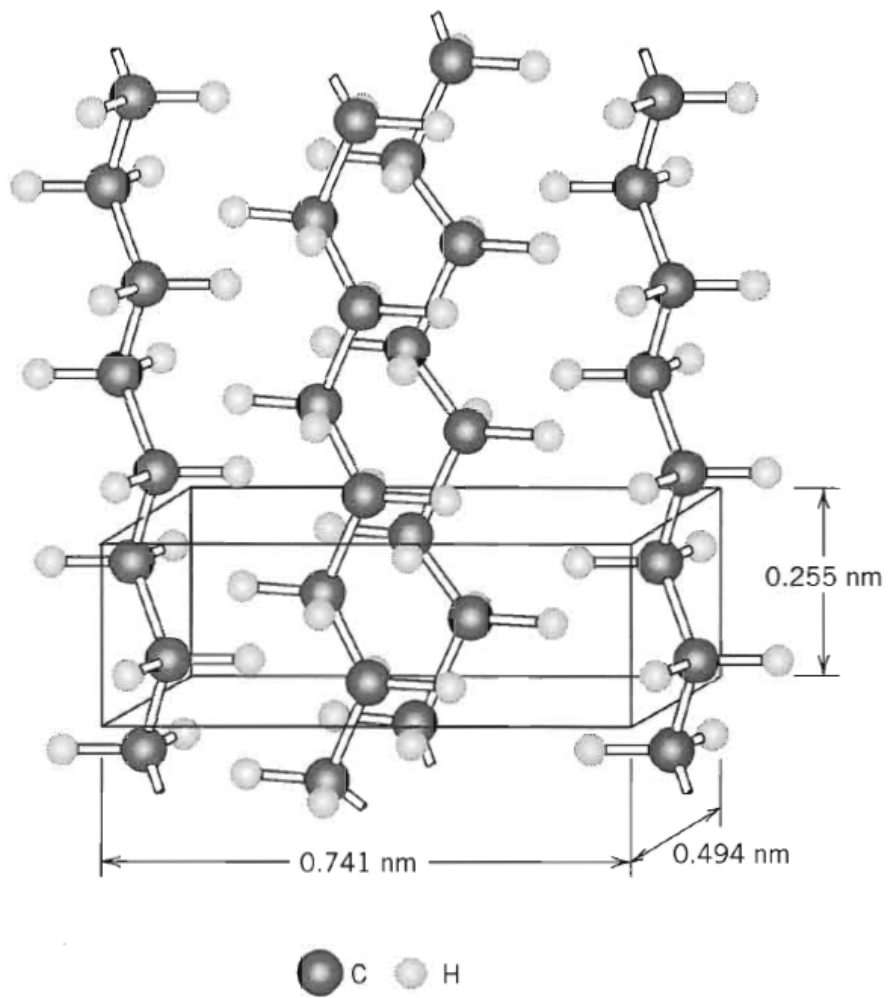
Figure 3.32: The arrangement of molecular chains for an orthorhombic unit cell for polyethylene [150].

the peaks appear to broaden and become less intense with increased aging time or temperature. Overall, the WAXS results verify that the UHMWPE fibers lose orientation due to aging, and that there is the possible formation of a hexagonal phase. Further experimental work is necessary to fully understand the changes in morphology in UHMWPE fibers due to elevated temperature aging.

3.8   Summary

In summary, when exposed to elevated temperatures for long periods of time, UHMWPE fibers lose tensile strength. Fibers exposed to 90 °C and 115 °C undergo shrinkage and loss of orientation, which causes a loss in tensile strength. Molecular spectroscopy verified that all samples were oxidized by the elevated temperature exposure. There are also changes in the morphology of the fibers. These factors should all be considered when using these fibers in conditions in which they might be exposed to elevated temperatures for long periods of time.

Chapter 4

Irradiation of UHMWPE Fibers

4.1   Chapter Overview

In this chapter, previous efforts to use ionizing radiation to crosslink UHMWPE fibers are described. Exploratory work performed to crosslink UHMWPE fibers using low overall dose, high dose rate, electron beam irradiation is discussed.

4.2   Irradiation of Bulk Polyethylene

Ionizing radiation has long been used to crosslink bulk polyethylene. When polyethylene is irradiated, ions and excited states are formed [155]. When polyethylene is subjected to ionizing radiation, alkyl free radicals, *trans*-vinylene unsaturations, diene unsaturations, and hydrogen gas are formed [156, 157, 158]. A schematic drawing of the (a) alkyl, (b) allyl, (c) dienyl, (d) trienyl, and (e) tetraenyl free radicals are depicted in Figure 4.1. Alkyl free radicals are unstable and quickly migrate via a hydrogen hopping mechanism, which will be discussed in a subsequent section. Alkyl free radicals can decay via one of three different mechanisms. In the first, intramolecular recombination, two alkyl radicals on the same polyethylene chain can combine, forming a *trans*-vinylene unsaturation. The next, intermolecular recombination, two alkyl radicals on adjacent chains combine, forming a crosslink.

The third possibility is that the alkyl radical migrates to an allylic position of an unsaturation, forming either an allyl free radical if it is a vinylene, or forming a polyenyl free radical if it is a polyene unsaturation [159].

While some alkyl free radicals form allyl free radicals in the crystalline region [160], most alkyl free radicals are expected to migrate to the crystal surface, where crosslinks, (bonds between two adjacent polymer chains) can be formed. Crosslinking in the crystalline region of the polymer is not favored because the spacing between the chains (4.1 Å) is longer than the carbon-carbon bond length (1.5 Å) [161].

Another process that can occur during the irradiation of polyethylene is chain scission. Chain scission results in a reduction of the average molar mass of a macromolecule [162]. Typically polyethylene will preferentially form crosslinks during radiation treatment, with the ratio between the number of main chain scissions and crosslinks not exceeding 0.1, assuming that irradiation is performed in an environment that excludes oxygen, so chain scission is not an issue [162, 163, 164]. Oxidation does occur in the irradiation of polyethylene when oxygen diffuses into the polymer during or after irradiation. Peroxyl radicals, hydroperoxides, and peroxides are all species that play an important role in the radiation induced oxidation of polyethylene. The primary product is a hydroperoxide, which decomposes to free-radicals that initiate the oxidation of the polymer to form ketone groups, which undergo chain scission, reducing the overall strength of the polymer [165].

One important mechanism for solid state radical migration, which was proposed by Dole, is a set of successive inter or intra-molecular hydrogen abstraction
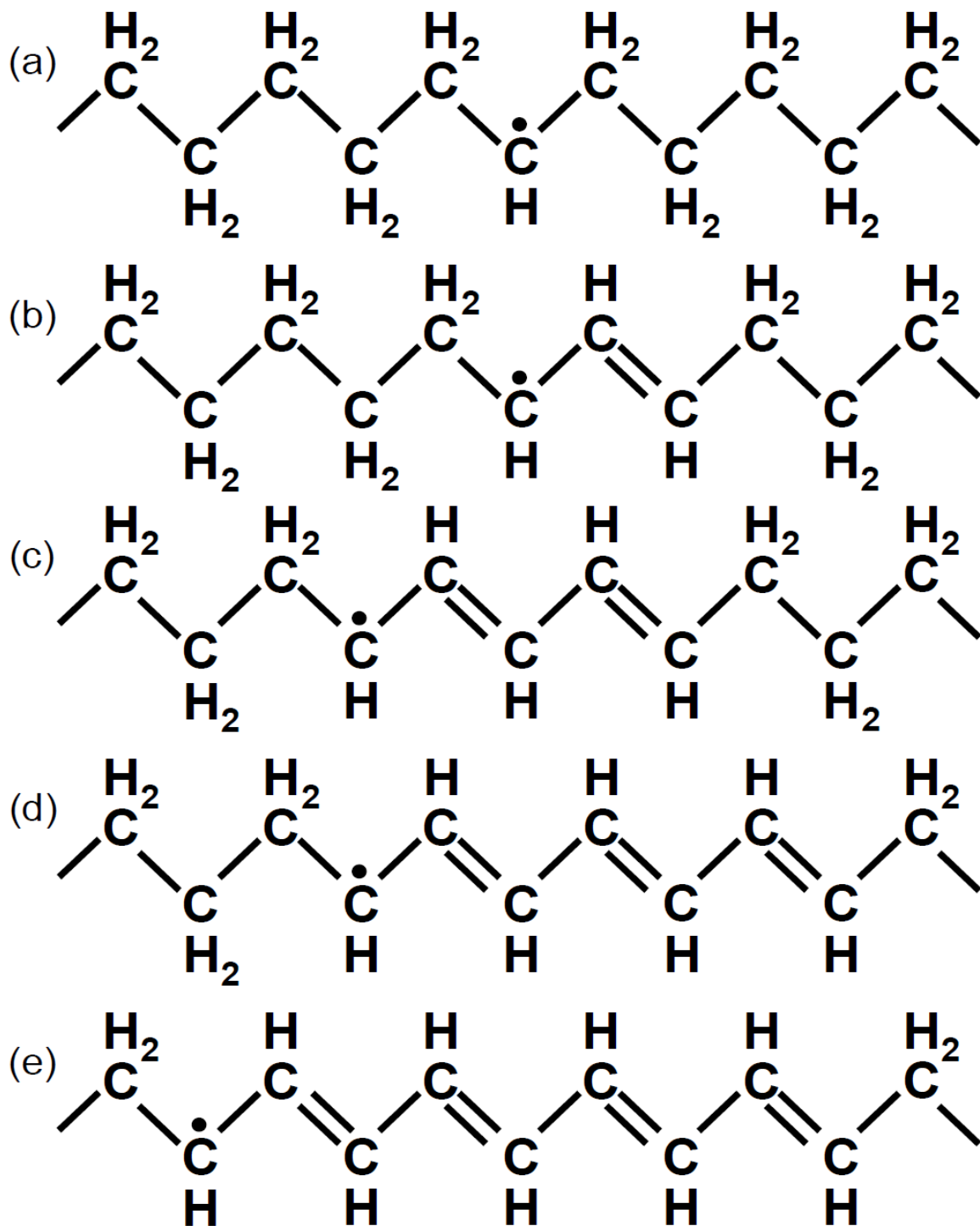
Figure 4.1: Free radicals expected from the irradiation of polyethylene. Schematic drawing of the (a) alkyl, (b) allyl, (c) dienyl, (d) trienyl, and (e) tetraenyl free radicals.
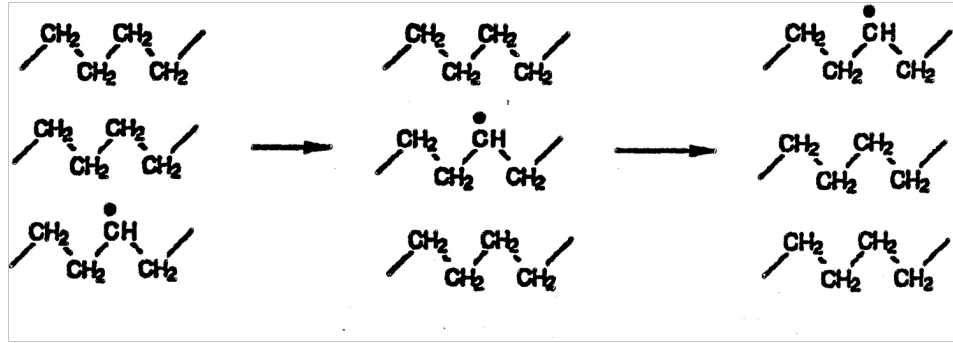
Figure 4.2: Hydrogen abstraction from one chain to another, and the simultaneous *hop* of the radical site [166].

reactions, which can also be called *hydrogen hopping.* In this reaction, a radical site on a macromolecule abstracts a hydrogen atom from an adjacent carbon atom (either on the same chain or a nearby chain), meaning that the radical site effectively moves to a new location. This process can repeat itself, another hydrogen can be abstracted, and the radical can move once again to a new location, and so on. Via this process, the radical undergoes a random walk throughout the solid polymer. Figure 4.2 shows the first step in this hydrogen hopping mechanism [166].

4.3 Irradiation of UHMWPE Fibers

In an effort to improve properties such as thermal conductivity [167], low temperature thermal strain [168], and creep resistance of UHMWPE fibers, many researchers have undertaken efforts to crosslink these fibers using high energy radiation [107, 115, 121, 125, 164, 167, 168, 169, 170, 171, 172, 173, 174, 175, 176], or some form of chemical or ultraviolet crosslinking [177, 178, 179, 180, 181, 182].

4.3.1 Low Dose Rate Irradiation

Several papers were published on the use of gamma irradiation in various doses to crosslink UHMWPE fibers [164, 169, 174, 175, 176]. In one such paper from 1981, deBoer and Pennings irradiated UHMWPE fibers with tensile strengths ranging from 1.6 to 3.5 GPa using ^{60}Co gamma radiation, with doses varying from 7 to 91 kGy. The authors were successful at crosslinking the fibers, as demonstrated by gel contents following irradiation of up to 85 %, however, they observed a marked decrease in tensile strength (up to 40 %) with increasing dose. The authors attributed this decrease in tensile strength to preferential chain scissioning of stressed chains (later called TTMs) in the fiber structure. In an effort to test this hypothesis, the authors annealed fibers with an initial tensile strength of 3.5 GPa prior to irradiation in an effort to relax these stressed chains and reduce the potential for their preferential scission during crosslinking. The annealing produced a slight decrease in tensile strength, to about 3.4 GPa. After 8 kGy of irradiation, the tensile strength was found to decrease only another 3 %, to 3.3 GPa. In addition, the authors note that the very presence of crosslinks may reduce the tensile strength of the fiber by causing a local increase in density and creating an area of stress concentration [176]. A further publication from the same authors was able to determine a crosslinking efficiency of 0.33 crosslink per 100 eV of absorbed energy for this experiment [169]. In 1996, Deng and coworkers revisited the topic of gamma irradiation of UHMWPE fibers. Samples were exposed to a nominal dose of 2.5 Mrad (25 kGy) in three environments: air, nitrogen, and acetylene using a ^{60}Co

source and a 0.25 Mrad/h (2.5 kGy/h) dose rate. Differential scanning calorimetry analysis was performed to study crystalline melting and thermal oxidation. Melting peak analysis indicated a dual melting peak, possibly due to a core-skin structure for the fibers. Changes were observed in the melting peaks of samples irradiated in air and in acetylene that were attributed to changes in the molecular structure due to chain scission and oxidation for the air irradiated samples, and crosslinking for the acetylene irradiated sample. Tensile testing was performed to assess the tensile strength of the fibers after irradiation, and was shown to vary according to irradiation environment. Results of Deng's study are puzzling because they show an increase in tensile strength immediately after irradiation for all samples except for those irradiated in air, but 160 days after irradiation, a major reduction in tensile strength was observed. This is probably due to the lack of annealing in this experiment, which would have eliminated long-lived radical species and prevented the detrimental oxidation of the polymer observed by this study.

The tensile strength (tenacity) of the fibers was decreased after irradiation slightly for samples in the acetylene environment, and significantly for samples in the air environment. The authors attribute this to crosslinking and oxidation, respectively. The tenacity of the samples irradiated in nitrogen and under vacuum was slightly improved. After 160 days of post-irradiation aging, all of the samples showed a decrease in tenacity, leading the authors to conclude that the tensile properties of UHMWPE fibers are reduced upon exposure to gamma irradiation [175]. Conversely, work on the irradiation of highly oriented HDPE polyethylene fibers indicates that the tensile properties of these fibers are enhanced by radiation treat-

ment [164, 174]. This indicates that a different mechanism exists for interaction of radiation with the UHMWPE fibers than for fibers of lower molecular weight, probably due to their unique structure.

4.3.2 Differences between High and Low Dose Rate Irradiation

The two main technologies commercially available for the irradiation of materials are gamma sources, typically ^{60}C sources, and electron beams, which generate beams of mono-energetic electrons and have a very high dose rate [162]. Gamma sources generate photons which are scattered during their interaction with matter by several processes to form electrons. These include the photoelectric effect, the Compton scattering, and pair production. The photoelectric effect, in which a photon ejects a single electron from an atom of the stopping material, and is described by Equation 4.1 is the principal interaction process at low photon energies [162].

$$E_e = E_0 - E_s \tag{4.1}$$

Where E_e is the energy of the ejected electron, E_0 is the energy of the incident photon, and E_s is the binding energy of the electron in the atom. Compton scattering occurs when a photon interacts with either a free or a bound electron, so that the electron is accelerated and the photon deflected with reduced energy, and is described by Equation 4.2 [162].

$$E_e = E_0 - E_\gamma \tag{4.2}$$

In which E_e is the energy of the recoil electron, E_0 is the energy of the incident photon, and E_γ is the energy of the scattered photon. Pair production involves the complete absorption of a photon in the vicinity of an atomic nucleus, or less frequently, an electron with the formation of two particles, an electron and a positron, and is described by Equation 4.3 [162].

$$E_0 = E_e + E_p + 2m_e c^2 \tag{4.3}$$

Where E_0 is the energy of the incident photon, E_e is the energy of the electron, E_p is the energy of the positron, and m_e is the rest mass of the electron, and c is the speed of light in a vacuum. The value for this term is the rest energy of the electron, or 0.511 MeV. The decay of the ^{60}Co isotope produces two gamma rays, one having an energy of 1.173 MeV and one having an energy of 1.333 MeV, as shown in Figure 4.3 [162].

Electron beam radiation interacts with matter through elastic and inelastic scattering, and the emission of electromagnetic radiation. Elastic scattering occurs when electrons are deflected by the electrostatic field of an atomic nucleus. Inelastic scattering occurs when electrons interact with the electrostatic field of atomic electrons so that the atomic electrons are either excited to a higher energy level or ionized. These processes are inelastic because they involve the transfer of energy from the incident electron to the atomic electron, which causes the incident electron to slow down. The energy loss per unit path length $-(dE/dl)_{col}$ due to inelastic collisions is known as the specific energy loss or stopping power. Mass collision stopping
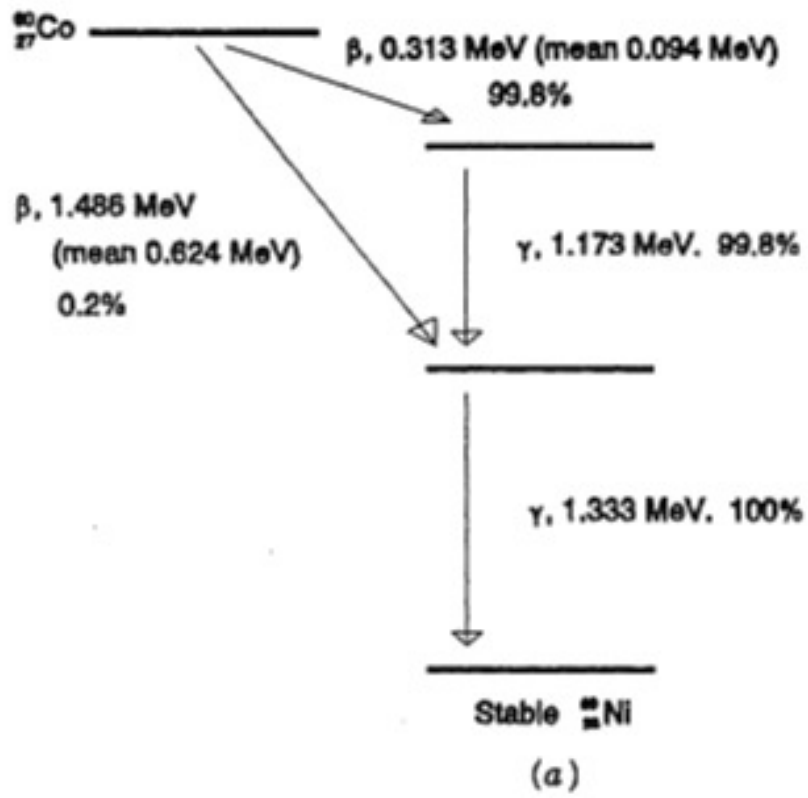
Figure 4.3: Decay of the ^{60}Co isotope.
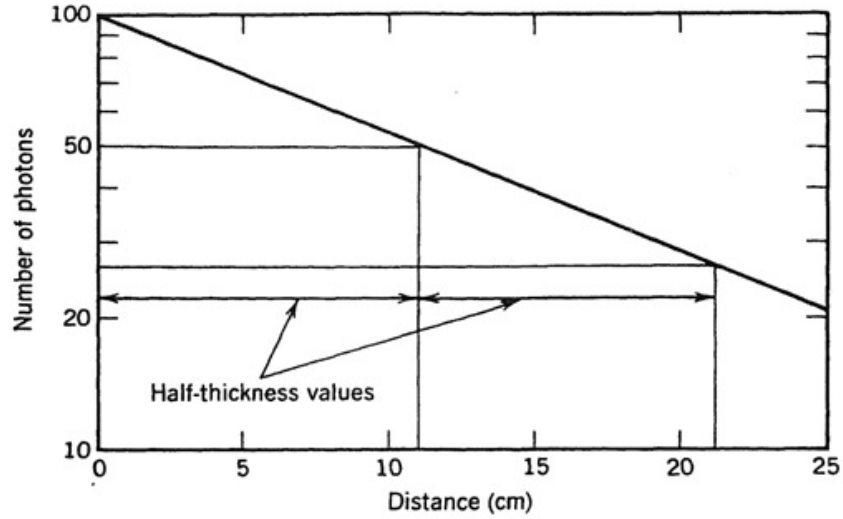
Figure 4.4: Number-distance curve for ^{60}Co gamma radiation absorbed in water [162].

power $(S/\rho)_{col}$ is more commonly calculated and is given by Equation 4.4 [162].

$$\left(\frac{S}{\rho}\right)_{col} = -\left(\frac{dE}{dl}\right)_{col}\left(\frac{1}{\rho}\right) \tag{4.4}$$

Where ρ is the density of the material. High speed charged particles passing close to the nucleus of an atom may be decelerated, and the energy loss emitted as electromagnetic radiation. This emitted radiation is known as bremsstralung radiation, or X-rays [162].

Linear energy transfer (LET) is defined as the linear rate loss of energy by an ionizing particle traversing in a material medium. In gamma irradiation, photons are generated first, and these interact with matter to form electrons. In electron beam irradiation, mono-energetic electrons are generated directly. For gamma irradiation, the number of photons transmitted per given thickness of water for a ^{60}Co source is shown in Figure 4.4 [162].
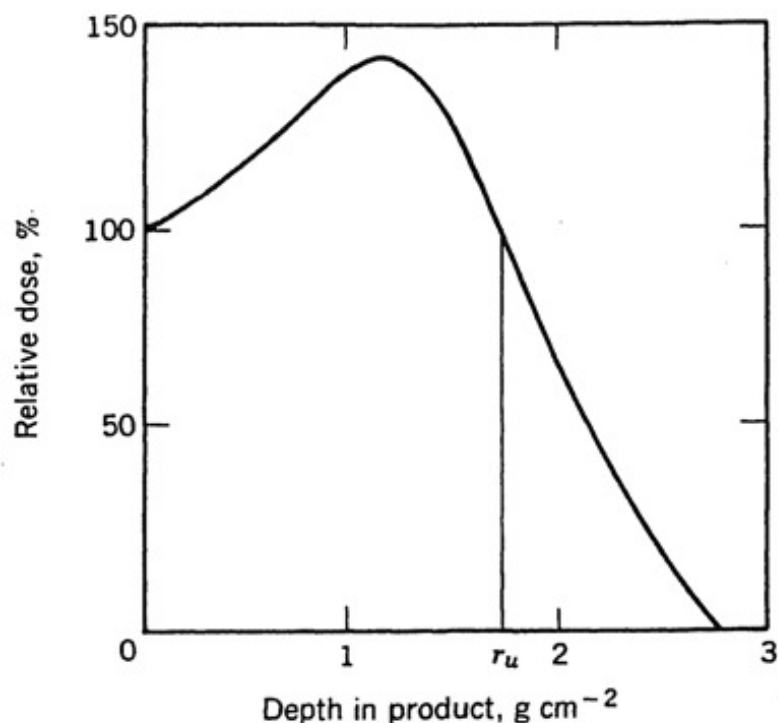
Figure 4.5: Depth-dose curve for 5 MeV electrons in water [162].

The penetration of the accelerated electron depends upon the kinetic energy of the electron. A depth-dose curve for 5 MeV electrons in water is shown in Figure 4.5 [162].

Another major distinction between the two sources is the dose rate. Typically, gamma irradiation is known as a low dose rate type of irradiation. Typical dose rates from a gamma irradiator are between 5 and 25 kGy/h, while electron accelerators can deliver dose rates thousands of times higher. This means that the same dose that takes hours in the gamma irradiation source will take only seconds or minutes in the electron accelerator. The high dose rate environment in the electron accelerator can also lead to significant thermal effects. Another issue to consider is the difference in the availability of oxygen diffusion and oxygen degradation during the exposure

time- materials irradiated for longer periods of time are more likely to undergo oxidation [183].

4.3.3   High Dose Rate Irradiation

Many researchers have examined high dose rate electron beam irradiation as a potential means of crosslinking UHMWPE fibers. Klein, *et al.* published a paper in 1987 examining the effectiveness of irradiation of UHMWPE fibers for crosslinking. They note that most crosslinking occurs in the amorphous regions of the polymer, meaning that samples of low crystallinity are more efficiently crosslinked than those of high crystallinity. Additionally, the authors note that the formation of crosslinks that link crystal layers are most important in forming a material with a high gel content (high crosslinking). Klein also notes that for the case of irradiation of UHMWPE gel spun fibers, chain scission is an important reaction [37], whereas in the case of bulk polyethylene, crosslinking is the dominant reaction and chain scission is relatively unimportant [162, 184, 185, 186, 187]. Samples of UHMWPE fibers were irradiated using either a 6 MeV, 1 kW pulsed electron beam unit, or a 2.9 MeV, continuous electron beam from a Van de Graaf generator. Samples were either irradiated in vacuum or in an acetylene environment. Experiments to measure the tensile creep, recovery and yield behavior of the irradiated fibers were conducted and found that the irradiated fibers had a lower creep rate at all stresses tested for both environments (air and acetylene) and also that the gel spun fiber was more sensitive to chain scission by irradiation than a lower molecular weight melt spun

fiber. Evidence of crystal chain scission was observed during tensile creep testing, which the authors attribute to the high molecular weight and morphology of the fiber.

Chain scission is more catastrophic in a high molecular weight system, and available crosslink sites are saturated at low dose due to the low amorphous content of these fibers. After the crosslink sites are saturated, chain scission becomes dominant in the fiber. This is further underscored by gel fraction data obtained by Klein showing gel fractions increasing in the UHMWPE fibers (indicating crosslinking) up to a dose of 0.13 Mrad (1.3 kGy), and after that point dropping significantly [172]. This is in direct contrast to polyethylene fibers of normal molecular weight, irradiated in an acetylene environment at doses up to 4.8 Mrad (48 kGy), also measured by Klein in a different publication, in which gel content was shown to increase almost linearly with dose and also resulted in an improvement in mechanical properties [173].

4.3.3.1 Role of Taut Tie Molecules

A conclusion that can be drawn from the work reviewed in the previous sections is that the irradiation of UHMWPE fibers to improve resistance to creep requires very carefully controlled experiments due to the tendency of these fibers to undergo chain scission as opposed to crosslinking. The fibers are extremely sensitive to chain scission by irradiation, which was explored further in a work by Dijkstra in 1988. This paper discusses the role of the taut tie molecules (TTMs) that were discussed

Figure 4.6: Schematic model of the gel-spun hot-drawn UHMPWE fiber, consisting of crystal blocks with length l_c and disordered domains with length l_a [115].

previously in the irradiation of UHMWPE fibers [115]. The tensile strength of the UHMWPE fiber depends on the TTM chains that connect crystal blocks in the fiber structure. Stresses in the microfibrils are transferred between crystals by the TTMs and the disordered region between crystals, making these two regions the weakest points in the microfibrils. The C-C bond strength is theoretically calculated to be about 25-30 GPa based on Morse potential calculations and infrared spectroscopy data. As discussed previously, actual strengths and elongations are much less than these theoretical values. The elongation at break (b) is determined by the sum of the length of the crystal block, the length of the disordered domain, and the tensile stress at break, as depicted in Figure 4.6 and shown by Equation 4.5.

$$\varepsilon_b = \frac{\Delta l}{l} = \left(\frac{\frac{\sigma_b}{E_c} l_c + 0.35 l_a}{l_c + l_a} \right) \tag{4.5}$$

Where l_a is the length of the disordered domains, l_c is the length of the crystalline domains, σ_b is the tensile stress at break, E_c is the crystalline modulus, and 0.35 represents the elongation at break of the disordered domain, estimated at about 35 %. The tensile modulus of the fiber is given by Equation 4.6.

$$E = \frac{\sigma}{\varepsilon} = \frac{1 + \frac{l_a}{l_b}}{1 + \left(\frac{1}{\beta} \cdot \frac{l_a}{l_c}\right)} \tag{4.6}$$

Where β is the fraction of load carrying TTMs in the disordered domain. Upon irradiation of the fiber and subsequent scission of the TTM, both ends of the TTM will immediately recoil due to the sudden release of stress in the chain. The two radicals will be separated over such a distance that the probability of their recombination, as would occur in the irradiation of most types of polyethylene, is not a likely event. This means that in the case of tensile testing, the stress must be transferred by the remaining TTMs, therefore the stress in these molecules is increased and the overall tensile strength of the fiber is lowered. This theory offers a reasonable explanation of the difficulty encountered in crosslinking UHMWPE fibers, though notably absent from discussions of this topic is the role of dose rate in chain scission or crosslinking of UHMWPE fibers [115].

4.3.3.2   Role of Acetylene in Crosslinking

Another important observation is that the experiments that have successfully crosslinked UHMWPE fibers using irradiation have all taken place in an acetylene environment. In 1993, Jones, Salmon, and Ward undertook an effort to better understand this phenomenon using high modulus (but not ultra-high molecular weight) polyethylene fibers and linear low density polyethylene films. These two forms of polyethylene were selected to aid in measuring the samples via electron spin resonance and ultraviolet-visible spectroscopy, respectively. Results from these

spectroscopic methods showed that samples irradiated in acetylene had a greater presence of polyenyl radicals than samples irradiated under vacuum. The authors postulate that radical pairs are crosslinked by polyene bridges, which simultaneously prevent disproportionation reactions that lead to chain scission in the polymer. The authors propose a mechanism for this reaction (Figure 4.7), in which dienyl, trienyl, and tetraenyl crosslinks can all be formed. One might ask why the reaction would preferentially form polyenyl crosslinks. This can be explained by a bond length argument. Two radicals must meet and form $R_1 - R_2$ crosslinks in an environment that excludes acetylene, with a bond length of c. 0.154 nm. In an acetylene containing environment, the radicals may form a crosslink with one molecule of acetylene per link, with a bond length of c. 0.288 nm. Both of these cases require a significant amount of conformational activation energy, but less energy is required to form a $R_1 - C = C - C - R_2$ crosslink with two molecules of acetylene per linkage, or even three or four acetylenes per linkage , so the acetylene basically acts as a very short polyethylene chain that can be used to bridge to adjacent chains within the fiber, forming a crosslink [188]. Thus, the use of acetylene in crosslinking polyethylene may mitigate some of the problems associated with chain scission in this reaction.

4.4   Motivation

Crosslinking has been used to improve the properties of bulk UHMWPE for many years, however, attempts to use radiation to treat UHMWPE fibers have
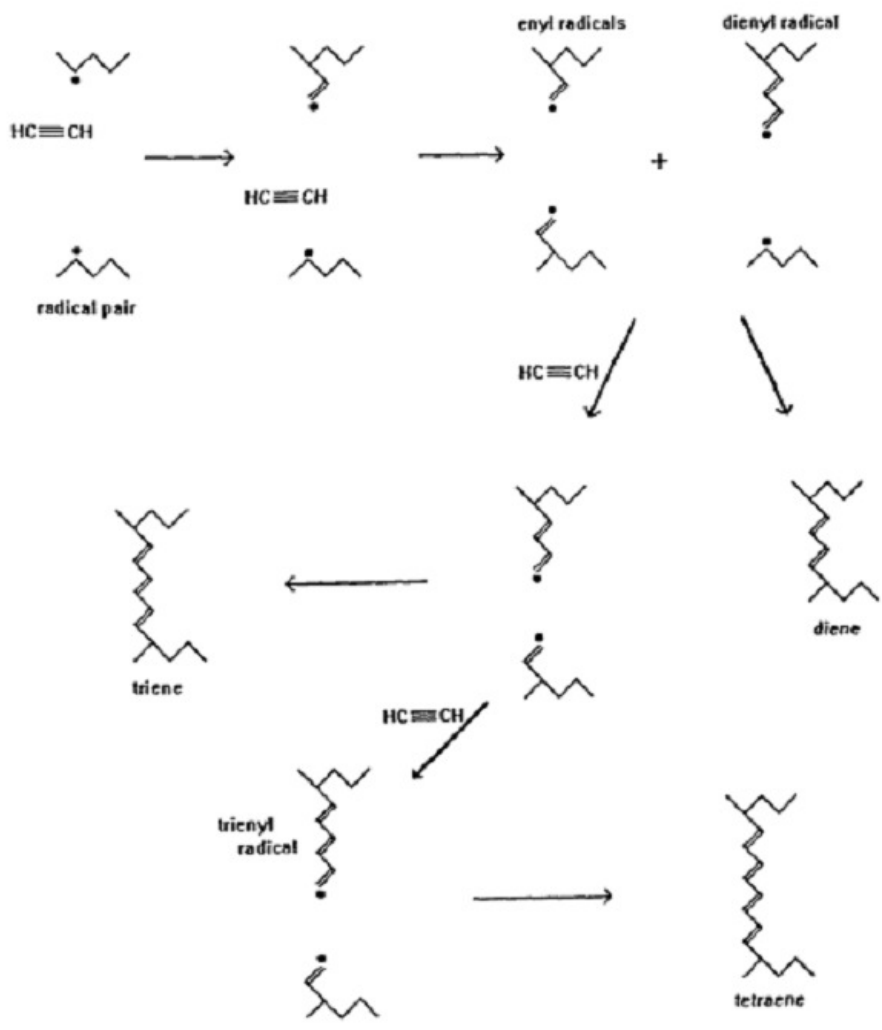
Figure 4.7: Mechanism for crosslinking polyethylene in the presence of acetylene [188]. This schematic shows how acetylene can enhance the formation of crosslinks between molecules by adding on to radical sites and bringing two radical sites closer together. Reducing the distance between molecules increasing the probability that they will combine.

been largely unsuccessful. However, the use of low dose (8-15 kGy), high dose rate radiation may allow for the formation of crosslinks without severing the essential taut-tie molecules. This section will focus on the use of radiation to improve the thermal properties of UHMWPE fibers without reducing their tensile strength.

4.5   Instrumentation and Analysis

A suite of instrumentation techniques have been established for use in characterizing various aspects of UHMWPE and UHMWPE fibers. The following is intended as a brief description of each technique and a demonstration of its application to UHMWPE.

The degree of crosslinking in the polymer is typically determined by a measurement of the residual gel content. This is done by dissolving the sample in a solvent in an inert environment to prevent oxidation, and measuring the residual solids after a set amount of time has passed. The solids represent the gelled portion of the material [189, 190, 191, 192].The addition of chains to the system is random [193]. This is valid for the polyethylene systems because polyethylene does not have any substituent groups, so the addition of chains is always random in this system. Crosslinking is classically determined from gel point using the Charlesby-Pinner equation, as shown in Equation 4.7.

$$s + s^{\frac{1}{2}} = \frac{\lambda}{2} + \frac{\left(2 - \frac{1}{2}\lambda\right) r_g}{r} \tag{4.7}$$

Where s is the soluble fraction of the polymer, λ is the ratio G(S)/G(X), which

refers to the number of broken and formed bonds per 100 eV, respectively, r is the dose, and r_g is the dose at the gel point [194]. Solubility obviously decreases with increased crosslinking.

Analysis of oxidation is typically performed by Fourier Transform Infrared Spectroscopy, or FTIR, as discussed in previous chapters. In this technique, a sample is placed in a beam of infrared radiation, which the sample absorbs at frequencies corresponding to molecular vibrations in the chemical structure of the sample. Identification of the chemical structure is possible because each material gives rise to unique vibrations and the resulting spectrum can serve as a "fingerprint" for that material [195]. Oxidation has been measured by several researchers [196, 131, 197, 198, 199] using this technique with great success by examining peaks in the range between 1689 and 1756 cm^{-1}, and typically focusing on the peak at 1740^{-1}, which has been shown to correspond to carbonyls, carboxylic acids, and alcohols generated during oxidation of polyethylene [198, 199]

Differential scanning calorimetry can be used to detect physical or chemical changes in a material that are accompanied by the absorption or liberation of heat by measuring the differential heat flow between the sample and a reference [195]. Measurement of crystallinity and melting point is traditionally performed for polymers using differential scanning calorimetry [200] and has been used extensively in the study of UHMWPE fibers [175, 184, 185, 186, 187].

Electron paramagnetic resonance spectroscopy (EPR) provides information about materials with unpaired electrons, such as organic free radicals. Most molecules have closed shells of valence electrons and no signal is observed from these samples

in the ESR. However, samples with unpaired electrons, or molecules containing an odd number of electrons in their normal oxidation state (NO, for example) are EPR-active. The unpaired electrons possess spin angular momentum and in the presence of an external electric field have a magnetic moment, which interacts with an external magnetic field. The basic principle behind EPR is that in an external magnetic field, B_0, unpaired spins will align parallel to the magnetic field. Simultaneously, microwave radiation is applied to the sample to drive the unpaired electron to change its alignment from parallel to antiparallel or vice versa, while sweeping the strength of the magnetic field. The unpaired electron will absorb energy to make this transition at the field for resonance, and this energy absorption is detected as the EPR signal. The energy is supplied by a photon which is generated by a microwave, and is given by Equation 4.8.

$$\Delta E = \hbar \nu = g\mu_0 B \tag{4.8}$$

Where ΔE is the energy required to flip the spin, $\hbar$ is Plank's constant, $1.055 \text{x} 10^{-34}$ J s, ν is the microwave frequency, g is the g-factor, approximately 2, μ_0 is the Bohr magneton, $9.264 \text{x} 10^{-24}$ J/T, and B is the total external magnetic field [201].

One can obtain information about the environment of surrounding the unpaired electron by examining the hyperfine structure of the unpaired electron, which arises from the nuclei of atoms surrounding the electron. These nuclei act as small bar magnets on the unpaired electron, splitting its absorption peak and providing

information about the radical's environment. The number of peaks and their relative intensities when n nuclei of spin 1/2 are equidistant from the unpaired electron are given by the number of terms in the Taylor expansion of $(1 + x)^n$.

The area of the EPR signal may be integrated to give an approximation of the amount of free radicals present in a sample. The total number of spins (or unpaired electrons) in a given sample can be calculated by measuring relative spin concentrations and comparing them against a standard with a known number of unpaired electrons. This technique is very useful for studying the free radicals formed during irradiation of any material, including UHMWPE [202, 203].

Breaking strength has long been used as a good method for characterizing the physical properties of yarns and fibers. In this type of test, the force required to break the material at a given rate of extension is determined and recorded as a material property [204]. This method has been used extensively for testing the physical properties of UHMWPE fibers and benchmarking the success of various crosslinking techniques [164, 172, 173, 175, 179, 174].

4.5.1 Determination of the Presence of Free Radicals in Unirradiated Fibers

A spool of gel-spun Dyneema SK-76 UHMWPE fiber filament yarn was supplied by DSM for use in all experiments. The first measurements made on this yarn were made using electron spin resonance (ESR) spectroscopy to determine if any radicals were present in the signal of the yarn prior to irradiation. Four
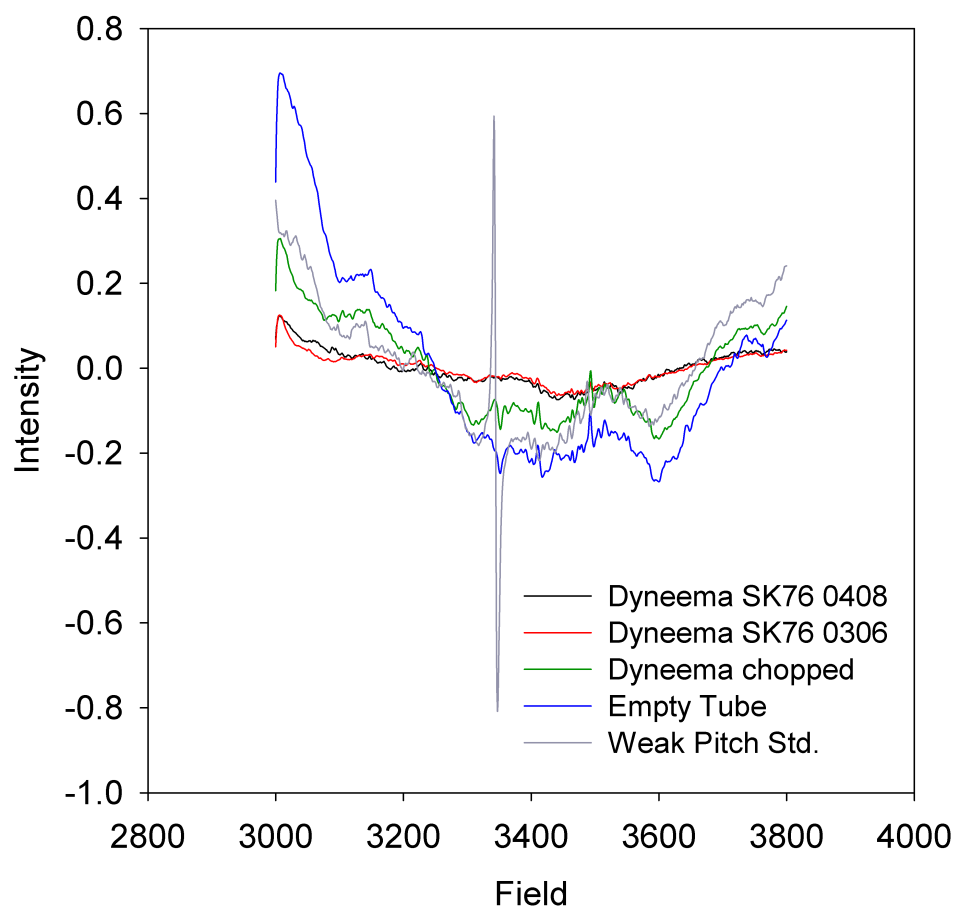
Figure 4.8: ESR spectra of unirradiated UHMWPE fibers, chopped fibers, an empty tube, and the Bruker weak pitch standard for reference.

samples were measured, UHMPWE fibers in a randomly oriented position, fibers which had been chopped with ceramic shears to find evidence of mechano-oxidative degradation [144], an empty tube, and a standard supplied with the instrument for comparison to a weak signal (Bruker weak pitch standard). The spectra of all of the samples measured (collected in Figure 4.8) indicates that no radicals were present in the samples measured (no radical signals observed), however this does not indicate that other batches of fiber from this producer or other producers would not contain any free radicals.

4.5.2 ^{60}Co Gamma Irradiation-Low Dose Exposure Experiments

In an experiment to assess the effect of radiation on this particular fiber (since previous experiments had been performed on other grades of UHMWPE fiber), fiber was wound onto glass cylinders and packaged in aluminized polyethylene. The packages were purged with argon for 30 minutes before heat sealing. The packaged samples were then placed in the ^{60}Co gamma source for irradiation. The dose rate obtained for the sample's position from MCMP simulation was 29 kGy/h. Radiochromic thin film dosimeters with a range from 0.5 to 200 kGy were placed on the samples and measured via ultraviolet visible spectroscopy. These films indicated that the dose rate was actually slightly lower than calculated. Based on the time the samples were irradiated, and the measured doses of the samples, the actual nominal dose rate is approximately 25.2 kGy/h. Doses ranged from 8.0 kGy to 86.8 kGy for samples in this experiment,and the intended range was 10 kGy to 100 kGy.

4.5.3 Measurement of Melting Points and Crystallinity of the Fibers

UHMWPE fiber samples were characterized by differential scanning calorimetry (DSC), Fourier transform infrared analysis (FTIR), and tensile testing. A Q2000 DSC (TA Instruments) with a refrigerated cooling system (RCS) was used to measure the crystalline melting temperatures and the percent crystallinity for all UHMWPE fiber samples. Samples ranging from 3 to 5 mg were cut and coiled in the bottom of a non-hermetically sealed aluminum sample pan. Experiments were performed in standard mode with a nitrogen purge. All samples were heated from 0

to 170 °C, then cooled to 0 °C, then heated back to 170 °C in a standard heat-cool-heat experiment. The heating and cooling rates were 5 °C/min. Percent crystallinity was calculated using the standard enthalpy of pure crystalline polyethylene as 291 J/g [202].

DSC thermograms are presented in Appendix B for all samples. All samples exhibited a reduction in crystallinity upon remelting, although crystallinity was difficult to calculate due to the broad nature of the melting peak in these samples. This broad peak may be due to a wide range of crystal sizes due to chain scission followed by melting and recrystallization, however this same phenomenon was observed in unirradiated UHMWPE, so it potentially is a feature of this polymer. All samples exhibited, to some varying degree, a dual melting peak on the first melt, which has previously been attributed to the core-sheath structure for gel-spun UHMWPE fibers. Previous work has shown that in systems in which oxidation did occur, a minor melting peak will then be followed by a major melting peak [175]. All irradiated samples studied showed a major, followed by a minor melting peak, which is another good indication that no oxidation occurred in the system.

4.5.4 Oxidation Measurements

4.5.4.1 Effect of Antioxidants

Commercial polyethylenes typically contain an antioxidant, commonly a type of hindered phenol marketed under the brand name Irganox [205]. Fourier transfer infrared spectroscopy can be a good method to look for the presences of antioxi-

dants in polyethylene [206]. Peaks of medium intensity associated with the aromatic phenol rings in Irganox would typically appear in the region between 1200 and 1000 cm^{-1}, and stronger peaks would appear between 950 and 750 cm^{-1} [51]. The presence of an Irganox-type hindered phenol antioxidant is strongly suspected due to peaks in these regions in the infrared spectra of all samples studied (Figure 4.9), and was also observed in the artificial aging work from Chapter 4. Antioxidants work by trapping and deactivating free radicals in the polymer, thus preventing oxidation reactions from occurring. This is a desirable effect in most applications, however, it can present problems during crosslinking with irradiation. In this case, free radicals are desirable in that they case the crosslinking to occur. If these radicals are trapped and deactivated by the antioxidant, there are fewer radicals available to participate in crosslinking, and the overall gelation content may be less than expected for a given dose. This is a factor that will be kept in mind as crosslinking experiments are undertaken.

4.6   Experimental Results

Infrared analysis was carried out using a Bruker Vertex 80 FTIR, equipped with a Smiths Detection Durascope ATR accessory. Nitrogen was used as the purge gas. Consistent pressure on the yarns was applied using the force monitor on the Durascope. FTIR spectra were recorded at a resolution of 4 cm^{-1} between 4000 cm^{-1} and 700 cm^{-1} and averaged over 128 scans. Three different locations on each yarn were analyzed. Spectral analysis and subtraction was carried out using a cus-
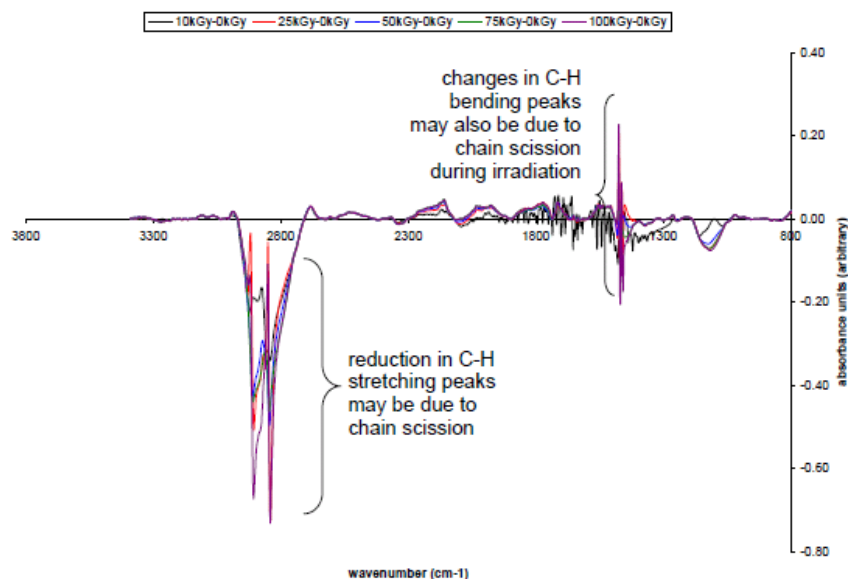
Figure 4.9: FTIR spectra for all irradiated UHMWPE fibers. Note that there is little discernible difference between the IR spectra of these fibers.

tom software program developed in the Building and Fire Research Laboratory's Polymeric Materials Group at NIST and used with that group's permission. There are four characteristic peaks for UHMWPE, identified as C-H stretching at 2914 cm^{-1} and 2846 cm^{-1}, and C-H bending at 1471 cm^{-1} and 1462 cm^{-1}. A broad peak of medium intensity at approximately 1131 cm^{-1} and two sharper peaks at 718 cm^{-1} may be attributed to the presence of hindered phenolic antioxidant, as discussed in the previous subsection. All spectra were baseline corrected and normalized to an absorbance of 1.00 using the C-H bending peak at 1462 cm^{-1}. Standard uncertainties associated with this measurement are typically 4 cm^{-1} in wavenumber and 1 % in peak intensity. Figure 4.9 shows FTIR spectra for all samples irradiated. Intended doses are used for clarity. A subtraction, or difference spectrum, is formed by normalizing all spectra to a given, unchanging peak, and then subtracting one

sample's spectrum from the spectra of all of the other samples. In this case, the unirradiated sample's spectrum was subtracted from the spectra of all of the irradiated samples. Negative peaks indicate loss of existing peaks, while positive peaks indicate formation of new peaks, or shifting of existing peaks. Only slight changes were seen in the spectra of the fiber after irradiation, as shown by the subtraction spectra presented in Figure 66, and no systematic trend in these changes can be discerned with increasing dose, although the sample with the highest dose shows the greatest changes. The reduction in the C-H stretching peaks at 2914 cm^{-1} and 2846 cm^{-1} may be due to chain scission in the polymer during irradiation, which migh also change the C-H bending observed at 1471 cm^{-1} and 1462 cm^{-1}, which showed both formation of new peaks and loss of existing ones. Oxidation is tyically measured for these systems from peaks in a range between 1689 and 1756 cm^{-1}, and typically focuses on a peak at 1740 cm^{-1} [198, 199]. To examine the samples for evidence of oxidation, the spectra of all samples in the region between 2000 and 1500 cm^{-1} was enlarged, see Figure 4.10. Other than noise in the spectra, no peaks can be seen in this region, indicating that if oxidation is present it is so minor as to be nearly undetectable, and also indicating that packaging in argon was a sufficient method to exclude oxygen from the system during irradiation.

4.6.1 Mechanical Properties Measurement

As in previous studies tensile testing of yarns was carried out in accordance with ASTM D2256-02, "Standard Test Method for Tensile Properties of Yarn by
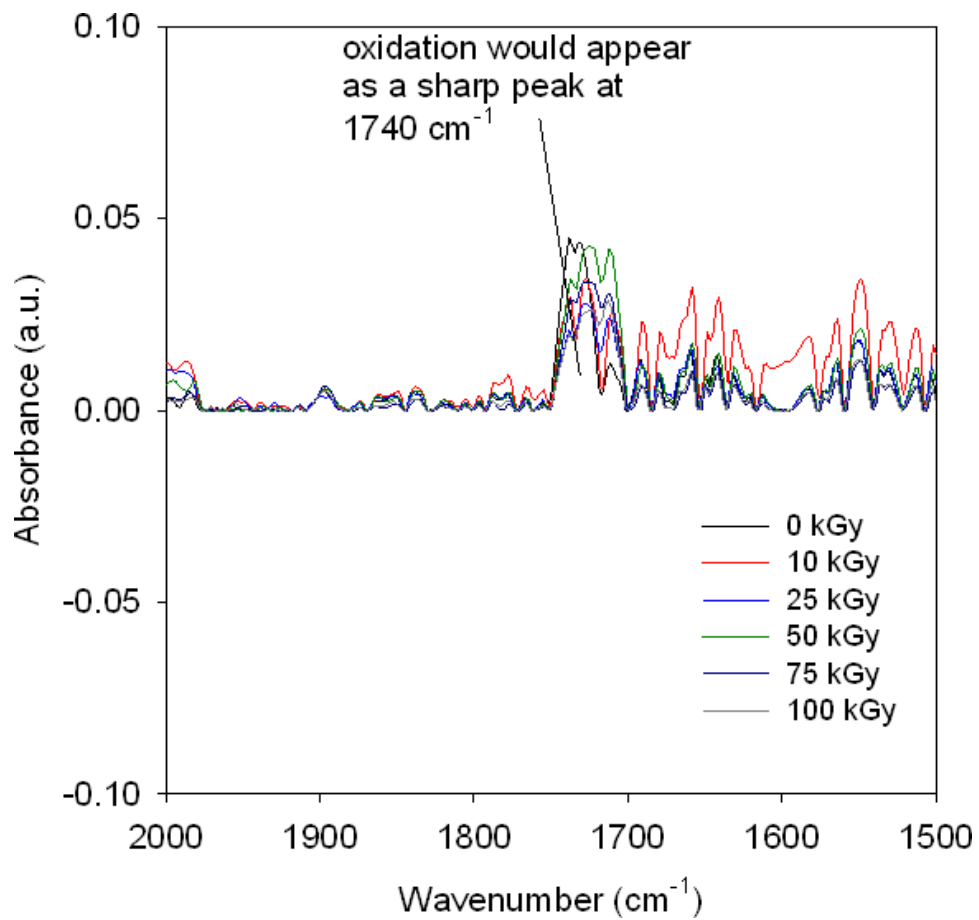
Figure 4.10: FTIR spectra for all irradiated UHMWPE fibers, enlarged to show the region in which oxidation would be expected.

the Single-Strand Method" [207], using an Instron Model 4482 test frame equipped with a 91 kg (200 lb) load cell, and pneumatic yarn and cord grips (Instron model 2714-006). The jaw separation was 25 cm (9.8 in) and the cross-head speed was 25 cm/min (9.8 in/min). In this study, yarns were nominally 58.4 cm (23 in) long, and given 23 twists on a custom designed yarn twisting device. This level of twist was maintained on the yarns as they were inserted into the pneumatic yarn and cord grips. Strain measurements were made with an Instron non-contacting Type 3 video extensometer in conjunction with black foam markers placed approximately 2.5 cm apart in the gage section of the yarn. Ten to twelve replicates from each sample set were tested to failure. The standard uncertainty of these measurements is typically 3 %. Figure 4.11 and 4.12 show the breaking load and breaking elongation for the fibers as a function of dose, respectively. (Intended dose is plotted for clarity). It is obvious that both breaking load and elongation are rapidly reduced as a result of the irradiation. This is due to the scission of taut-tie molecules as previously described in the fiber during irradation. At doses exceeding 50 kGy, the reduction is diminished, indicating that most of the available sites for scission have been exhausted. These preliminary experiments have shown that SK-76 fiber exhibits similar behavior when exposed to radiation as other types of gel-spun UHMWPE fibers- namely chain scission and a reduction in mechanical properties.
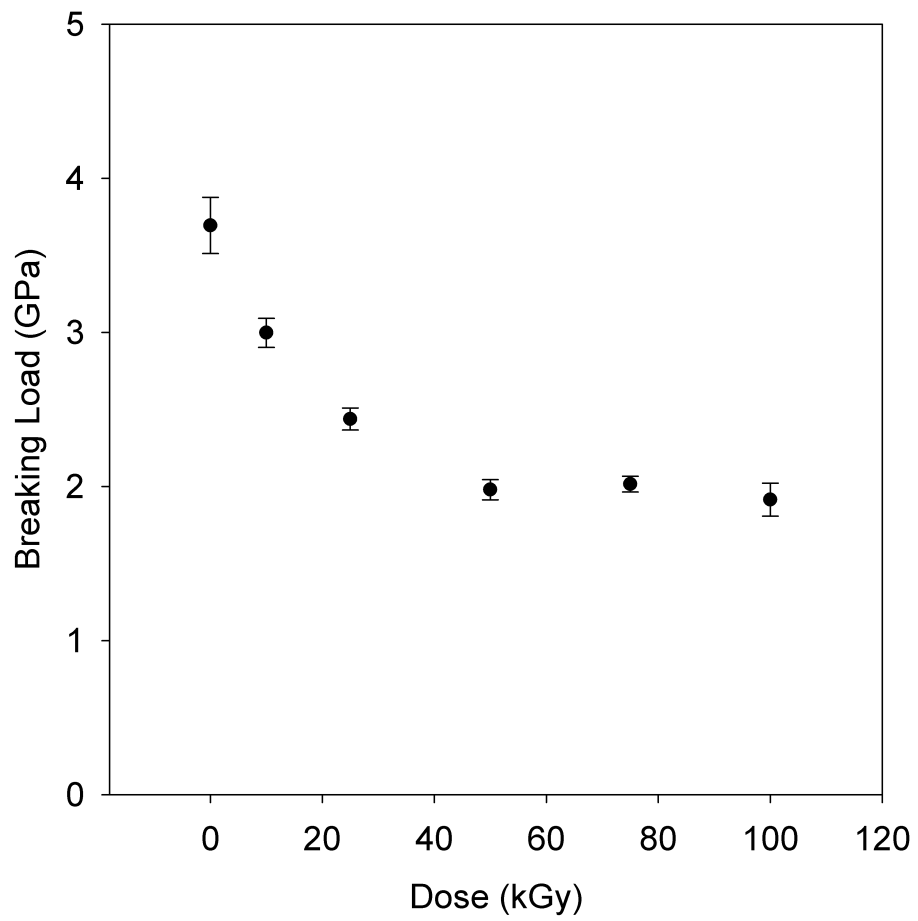
Figure 4.11: Breaking strength of irradiated UHMWPE fibers as a function of dose.
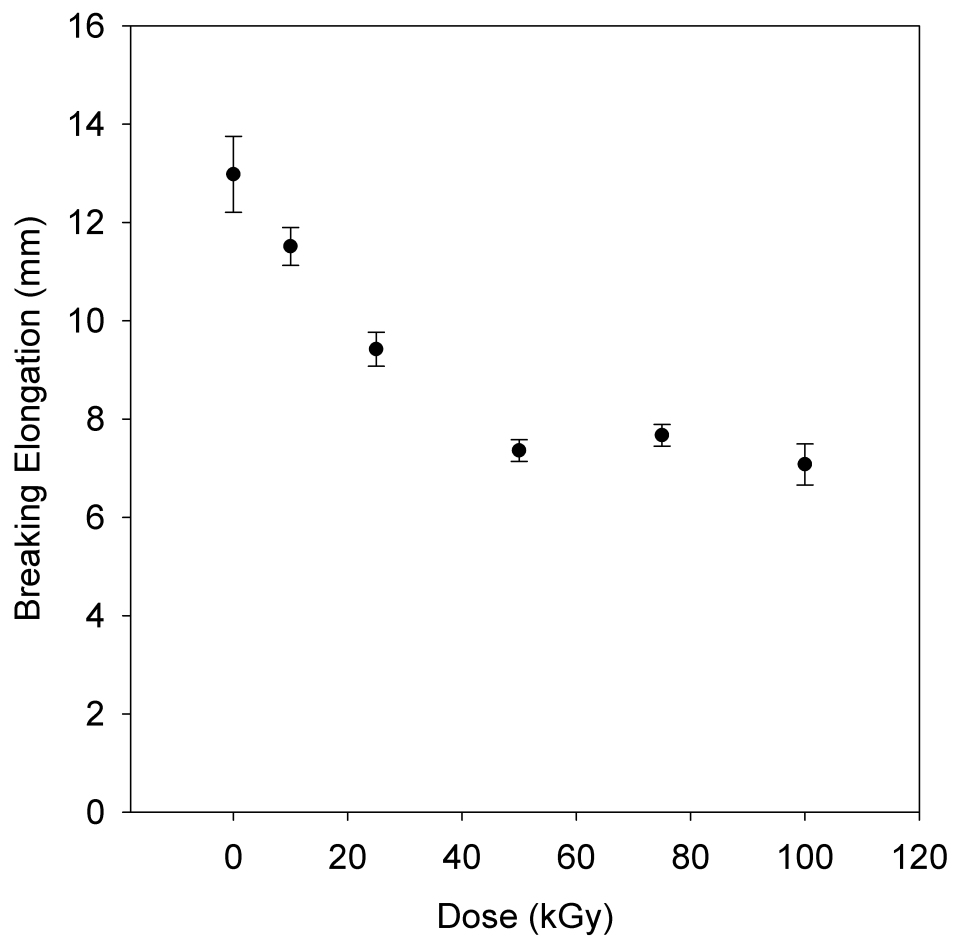
Figure 4.12: Breaking elongation of irradiated UHMWPE fibers as a function of dose.
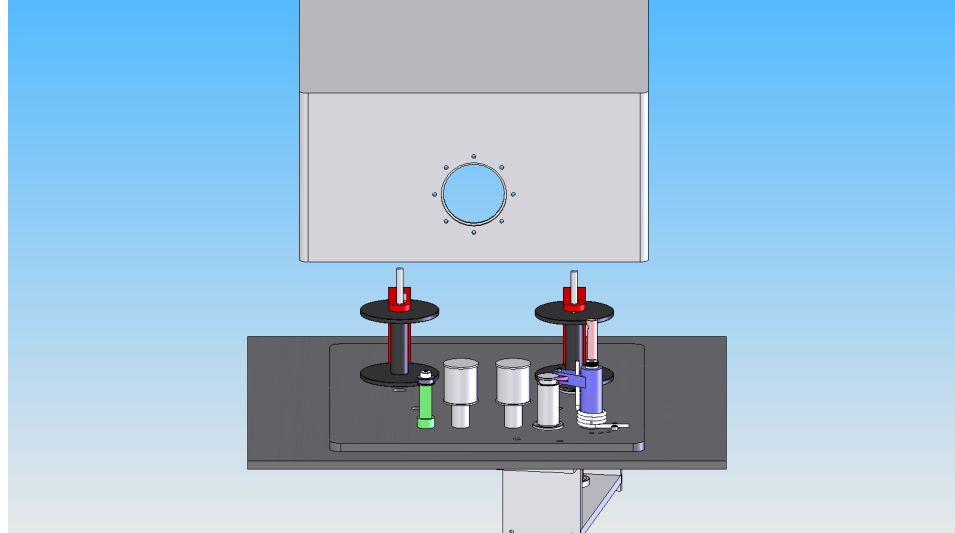
Figure 4.13: Continuous irradiation apparatus used to expose the fibers to the electron beam. Fibers are wound on the red and black roll in the back of the schematic, and fed over a series of rollers through the electron beam, which is centered between the two small gray spools in the center of the device. The fiber is then taken up by the other black and red roller in the back of the device.

4.7   High Dose Rate Irradiation Experiments

4.7.1   Irradiation Device Description

In order to irradiate the long, continuous samples necessary for yarn mechanical property measurements with the electron beam, a "fiber winder" had to be constructed to reliably feed a long continuous piece of UHMWPE yarn through the irradiation area, as shown in the schematic in Figure 4.13.

This apparatus has a variable speed controlled by a stepper motor, and used several guides and pinch rollers to smoothly and continuously feed the yarn through the irradiation window. The apparatus is controlled by a program in LabView to input a desired speed setting. This variable speed setting was used to control the dose received by the sample by controlling the time it remained in the electron beam,

while holding the electron beam energy (relatively) constant. The entire apparatus is enclosed in a large cover, which has a gas inlet for purging with argon. Argon was selected as the purge medium because it is heavier than air, and therefore should replace air more efficiently than nitrogen. Oxygen must be eliminated from the irradiation environment to prevent oxidation of the sample, which is a competing free radical reaction to the intended crosslinking, as discussed previously.

4.7.2 Medical and Industrial Radiation Facility

The Medical and Industrial Radiaton Facility (MIRF) is a pulsed electron beam with an energy range is continuously variable from 7 to 32 MeV. All experiments presented herein were performed with MIRF set to 10 MeV. The pulse width was 6 μs. The pulse repetition frequency is 120 pulses per second. The beam is assumed to be uniform and has a width of approximately 2 cm. Using the scan speed, and the measured dose values from the radiochromic film, the dose per second can be estimated. For example, for the 3 cm/s film the measured dose was 6 kGy. Using the beam size of 2 cm, and the pulse rate of 120 pps, this gives us the dose per pulse of 33 Gy/pulse.

Continuous irradiation experiments were performed using the medical and industrial radiation facility (MIRF) at NIST, depicted schematically in Figure 4.14.
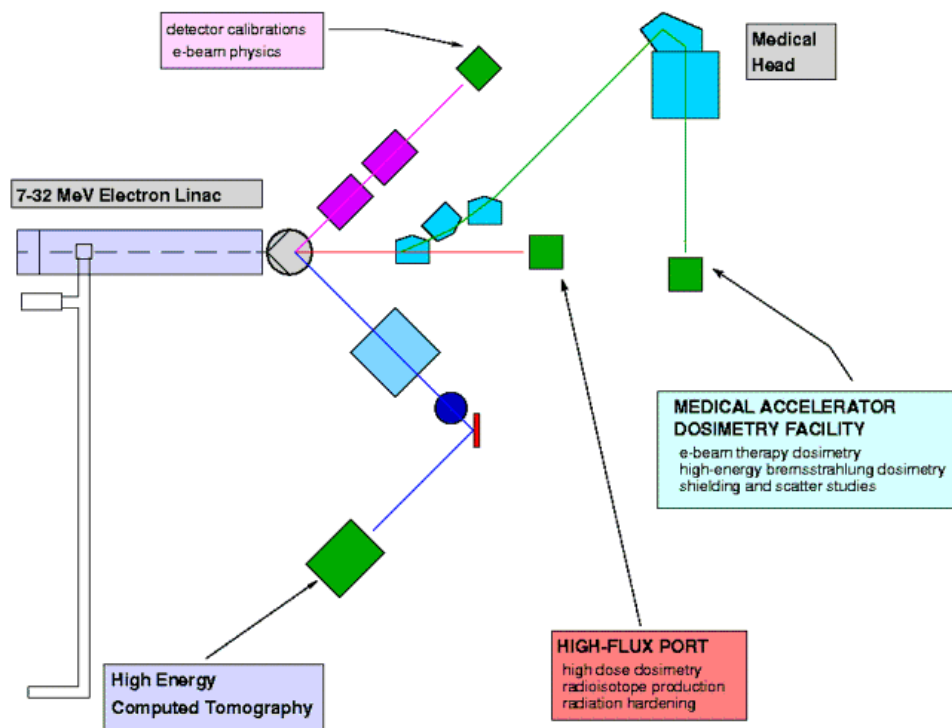
Figure 4.14: Schematic of the Medical and Industrial Radiation Facility (MIRF) at NIST. Continuous irradiation device was placed at the high flux port in the picture.

4.7.2.1 Dose Calibrations

In order to better understand the dose delivered by the electron beam at the various speeds, it was necessary to perform a calibration of the apparatus using a radiochromic dosimeter film. Since the film needed to be supplied in a continuous form, rolls of B3 WINdose radiochromic dosimeter film were purchased from GEX. This film undergoes a color change when exposed to ionizing radiation. The maximum color absorption peak is at approximately 554 nm, and it is not expected to be dose-rate dependent. The film is affected by both moisture and temperature, and it is recommended to be left sealed as long as possible prior to irradiation. It must be protected from UV radiation, and is recommended to be heat treated at 60-65 °C immediately after irradiation to prevent changes in color after irradiation [208].

Intended Dose (kGy)	Irradiation Time (min)
2	2.55
4	5.10
6	7.64
8	10.20
10	12.73
12	15.29
14	17.83
16	20.38
18	22.93
20	25.48

Table 4.1: Irradiation times and doses for radiochromic film calibration in the calibrated ^{60}Co Gamma Irradiation source with a dose rate of 47.1 kGy/h at 6 in from the centerline.

Prior to use in the fiber winder, these radiochromic films must be calibrated using a known source. Following the procedure outlined in ISO/ASTM Standard 51261:2002(E), 1 cm squares of the film were cut and irradiated using a calibrated ^{60}Co Gamma Irradiation source with a dose rate of 47.1 kGy/h at 6 in from the centerline. Three films were used at each dose, and the films were heat treated at 55 C after irradiation for one hour to fully develop the color. Table 4.1 shows each sample irradiated and the irradiation time necessary to achieve the intended dose.

Figure 4.15 shows the calibration curve (normalized by measured film thickness) generated by measuring the calibrated films. These data are best fitted using a quadratic polynomial function, which gives a correlation of 0.9961. It can also be fitted using a linear function, but the correlation is slightly worse at 0.9954. Traditionally, radiochromic film calibrations are fitted using a quadratic polynomial, so that function was used for the dose calculations. The equation for the fitting

function is given in Equation 4.9

$$y = -0.0018x^2 + 0.4021x + 2.409 \qquad (4.9)$$

This equation is rearranged and solved using the quadratic equation to find the dose of unknown films, given their thickness and absorbance at 554 nm.

4.7.3 Presence of Free Radicals in Irradiated Fibers

Samples of UHMWPE fiber irradiated at 1 cm/s using the fiber irradiation apparatus were examined using ESR, as described previously for unirradiated samples. There are three common radicals in irradiated polyethylene: the alkyl, the allyl, and the polyenyl free radicals. The alkyl free radical is commonly studied, and is depicted in Figure 4.16. This radical consists of a symmetrical sextet, and can be simulated using the hyperfine separation constants given in Figure 4.16. The alkyl radical is easy to detect because it has a very wide spectrum. Samples irradiated in the electron beam, shown in Figure 4.17, exhibits the characteristic alkyl sextet of peaks commonly observed in irradiated polyethylene [209].

4.7.4 Alpha-Relaxations in Polyethylene

The mechanical properties of polymers in the solid state are influenced strongly by molecular motions under the given thermodynamic condition and applied mechanical stress. The temperature at which a molecular motion stops or starts is known as a relaxation or transition temperature. Understanding these transitions
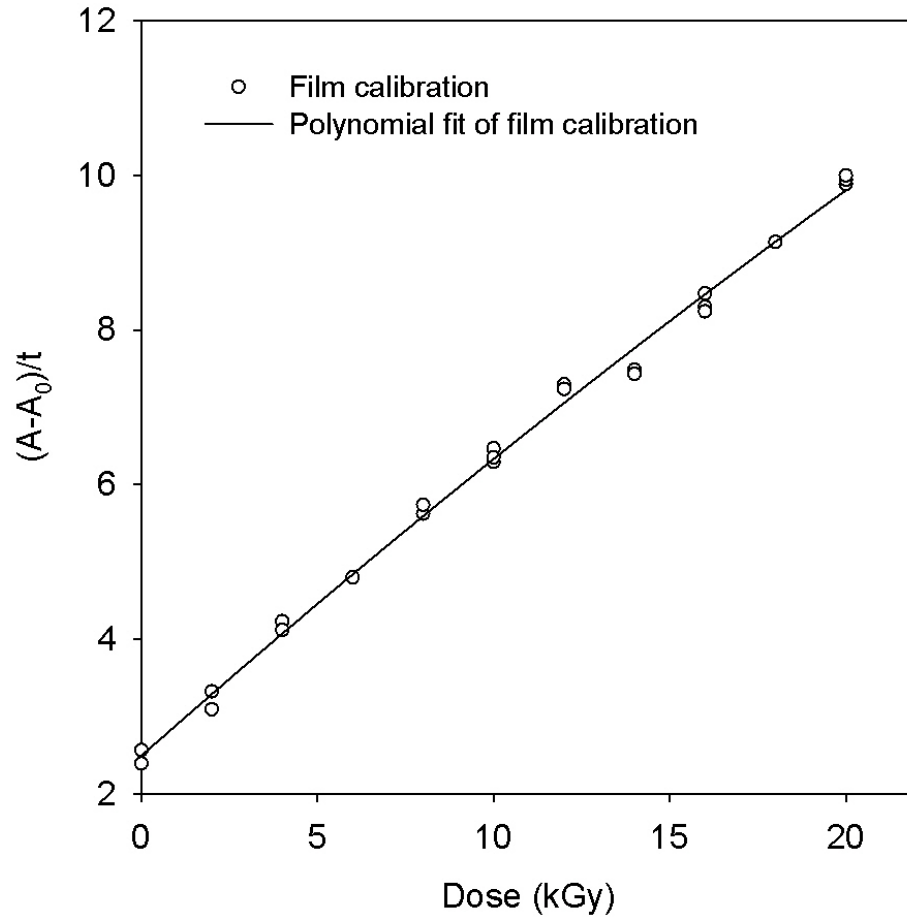
Figure 4.15: Calibration curve for B3 dosimeter film generated by exposing films to known doses on a calibrated ^{60}Co Gamma Irradiation source with a dose rate of 47.1 kGy/h at 6 in from the centerline. These data are best fitted with a quadratic polynomial fit. The correlation value is 0.9961. The $(A - A_0)/t$ term on the y-axis is used to denote the absorbance of the calibrated film minus the absorbance of unirradiated film normalized by the film thickness.

Figure 4.16: The structure, EPR spectra, and hyperfine splitting of the alkyl free radical [209]. Note the environment of hydrogens around the radical center giving rise to six characteristic peaks.
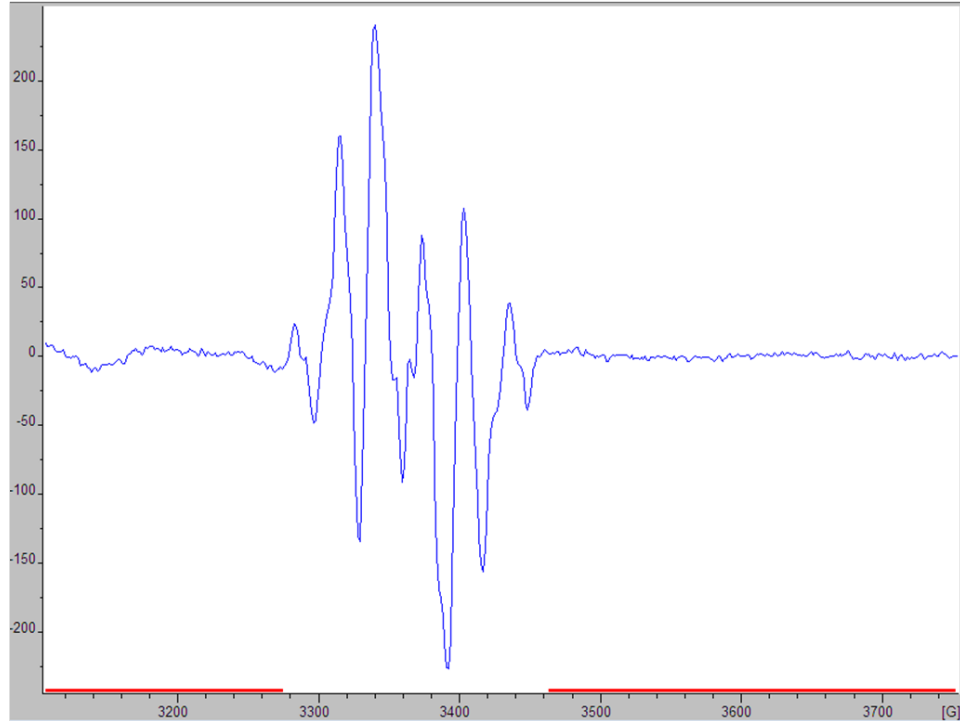
Figure 4.17: ESR spectra of UHMWPE fibers irradiated at 1 cm/s, for a dose greater than 20 kGy. Note the characteristic sextet peak of irradiated polyethylene.

is important for understanding the mechanical properties of a given polymer. The alpha transition is observed in all semi-crystalline polymers. This relaxation intensifies, meaning that the relative increase in tan delta is greater, with increasing crystallinity, so it usually assigned to the motion of chain units within the crystalline region [210]. Tan delta is the ratio of the loss modulus to the storage modulus of a material. In polyethylenes, this transition is split into two overlapping processes, both of which are related to the crystalline phase [211]. These two processes are described as the α and α' relaxations in order of increasing temperature. The α relaxation is attributed to either an intralamellar slip process (or grain boundary phenomenon), combined with motion in the intercrystalline region, and the α' relaxation is attributed to intracrystalline chain motion involving motion of chain

segments within the crystal lattice [210]. In polyethylene, the α transition is well known, and expected to occur in the region around 70 °C. The α' transition is less well-known and more difficult to detect. It occurs at a higher temperature, around 110 °C. Figure 4.18 shows typical examples of α relaxations in polyethylene. In this figure, α' is evident as a shoulder in the peak of the high density polyethylene (HDPE) sample, but is not apparent in data for the other samples. This is due to the greater crystallinity of the HDPE sample, and the fact that the α' transition partially coincides with the melting peak around 120 °C (above α') and with the α relaxation (below α') [211]. This relaxation is important for body armor because it is apparent as a loss in strength of the UHMWPE fiber, as shown in Chapter 1, and this relaxation falls within the potential use temperature for body armor, especially if the armor is stored in a car on a hot summer day. Previous work has shown that radiation crosslinking of polyethylene can reduce the magnitude of the alpha relaxation [212].

4.7.5   Effect of Radiation on Mechanical Properties of Fibers

Several experiments were conducted at different doses using the fiber irradiation apparatus in order to evaluate the effect of different doses on the fiber. In each experiment, the radiochromic film was irradiated first at the intended speed to determine the dose, and then the fibers were irradiated. Initial experiments were conducted at 0.5 cm/s, 0.75 cm/s, and 1.0 cm/s. Later analysis of the radiochromic films irradiated at these speeds indicated that the dose was out of the range of
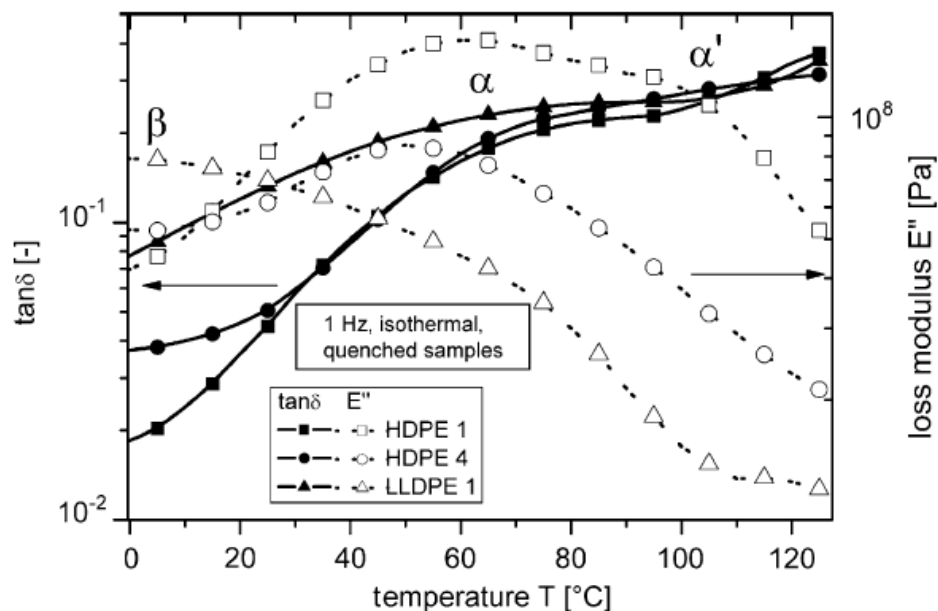
Figure 4.18: α relaxations in polyethylene, note the high temperature α' relaxation followed by the lower temperature α relaxation. In this figure, α' is evident as a shoulder in the peak of the high density polyethylene (HDPE) sample, but is not apparent in data for the other samples [211].

the film calibration- all of these samples received doses greater than 20 kGy. The electron beam power was reduced after these initial experiments, and films were calibrated at 2, 3, and 4 cm/s. The calibration curve generated previously was used to estimate the dose at these scan speeds, as shown in Table 4.2, and Figure 4.19, and were found to be approximately 12, 6, and 3 kGy, respectively. All film calibrations were performed in argon for the best approximation of the fiber irradiation environment.

The mechanical properties of these fibers were measured using the same techniques described previously. In all cases, the tensile strength was greatly reduced by the irradiation. The tensile strength results are presented in Table 4.3. The sample with a speed and dose of zero is the unirradiated control fiber. Experiments at the
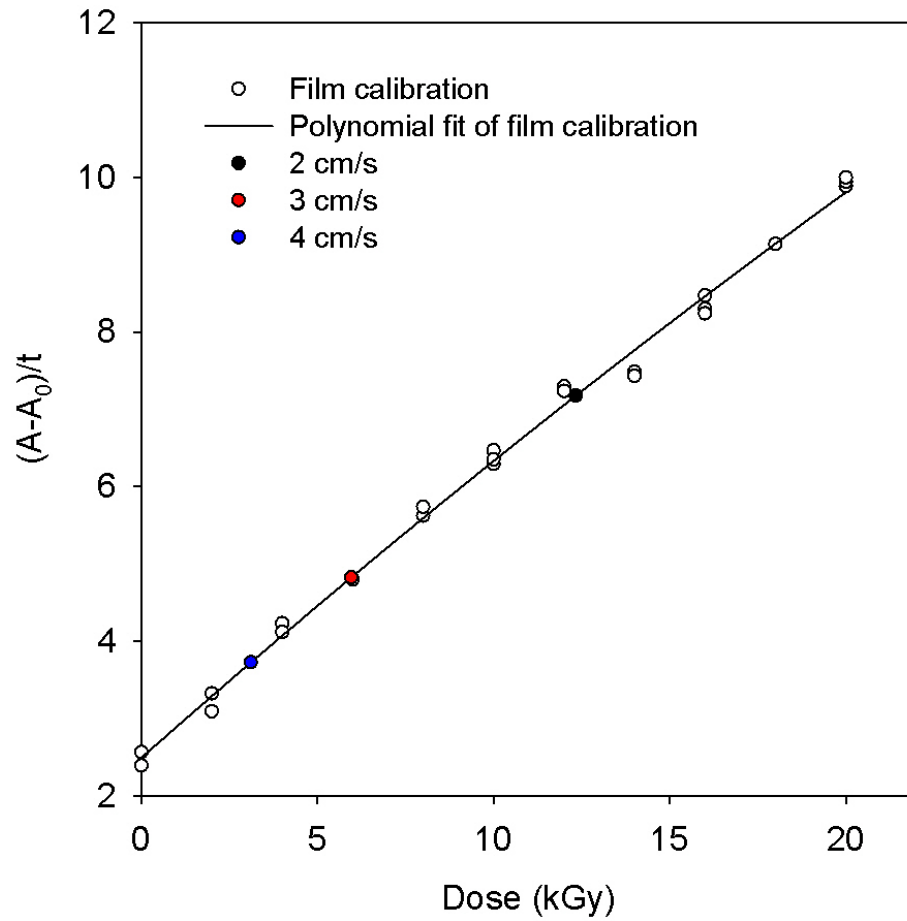
Figure 4.19: The estimation of the dose of films irradiated at different speeds using the calibration curve for B3 dosimeter film generated by exposing films to known doses on a calibrated ^{60}Co Gamma Irradiation source with a dose rate of 47.1 kGy/h at 6 in from the centerline. These data are best fitted by a quadratic polynomial fit. The absorbance of films calibrated at 2, 3, and 4 cm/s were used to estimate the dose according to this curve, as shown by the colored dots.

Programmed Speed (cm/s)	Estimated Dose (kGy)
0.5	>20
0.75	>20
1	>20
2	12
3	6
4	3

Table 4.2: Estimated doses for films irradiated using fiber irradiation apparatus at various programmed scan speeds in argon.

Programmed Speed (cm/s)	Estimated Dose (kGy)	Tensile Strength (GPa)	Standard Deviation (kGy)	Percent Reduction (%)
0	0	3.81	0.18	0
0.5	>20	2.81	0.29	27
0.5	>20	2.31	0.17	40
0.75	>20	2.37	0.26	38
1.0	>20	2.75	0.31	28
3.0	6	2.59	0.52	32

Table 4.3: Irradiation times and doses for radiochromic film calibration in the calibrated ^{60}Co Gamma Irradiation source with a dose rate of 47.1 kGy/h at 6 in from the centerline.

lower speeds were conducted using MIRF at its full power in order to maximize the dose per pulse. However, using the beam this way makes it difficult to control beam fluctuations over the course of the experiment. The later experiments conducted at speeds of 2, 3, and 4 cm/s were conducted at a lower power so that the counts could be tuned to the same value over the course of the experiment. This fluctuation may account for the differences in tensile strength of fibers irradiated at 0.5 cm/s.

There are several potential explanations for the reduced tensile strength of these irradiated samples. The localized heating of the electron beam may be enough

to melt the fibers or disrupt their highly ordered crystal structure and orientation. The experiment relies on the flow of purge gas to cool the fibers, but this may not be sufficient. The purge itself may also be insufficient, causing oxidation in the fibers instead of crosslinking. The fibers may also still be preferentially scissioning, as was observed previously in the gamma irradiation experiments, possibly due to an insufficient pulse rate for MIRF- radicals may not be generated fast enough to crosslink the taut tie molecules before they scission. Since even the very low dose sample exposed to 6 kGy showed a significant reduction in tensile strength (32 %), and tensile strength is so important to ballistic performance (as described in Chapter 3) it was determined that the use of the fiber irradiation apparatus and MIRF is not the best way to crosslink these fibers. Additional options will be discussed in the future work section.

4.7.5.1 Effect of Irradiation on Alpha-Relaxations

The samples irradiated at 3 cm/s were also analyzed using dynamic mechanical thermal analysis (DMTA) to repeat the experiment performed in Chapter 1 that illustrated the susceptibility of UHMWPE fibers to changes in their properties over their potential range of use temperatures for body armor due to their alpha relaxation. Single fiber samples were mounted using film and fiber grips, and measured using a temperature-frequency sweep from 30 °C to 110 °C, at a frequency of 1 Hz. All four replicates of the irradiated sample broke during the experiment. A representative plot for an unirradiated sample is shown overlaid with best avail-
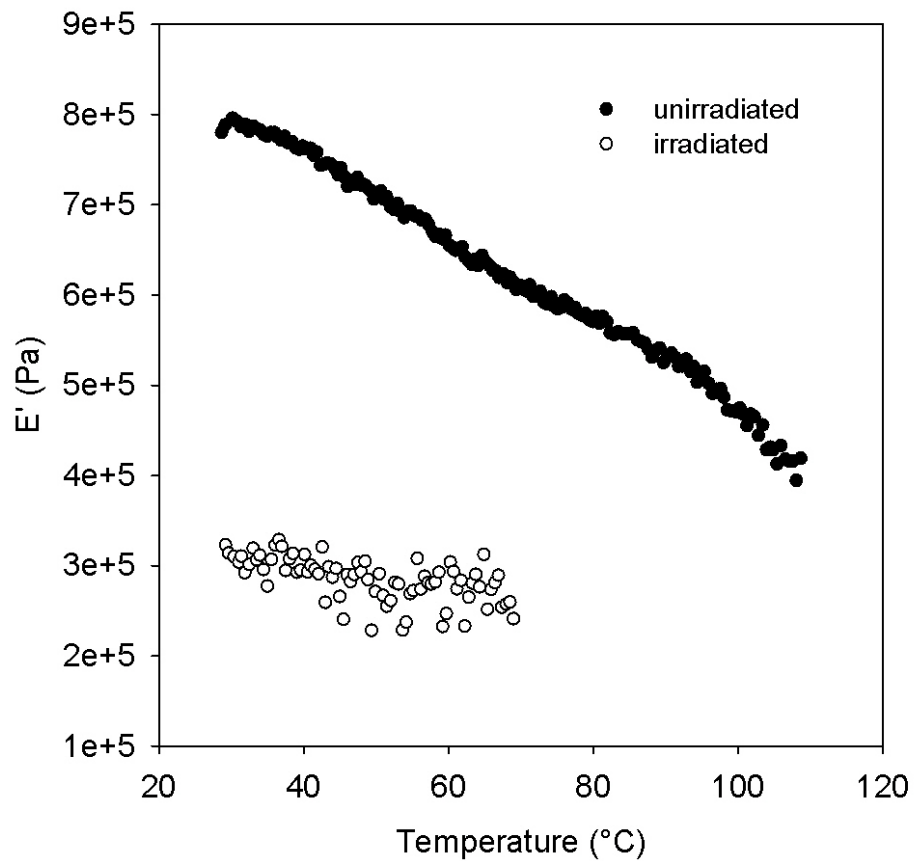
Figure 4.20: DMTA temperature-frequency sweep of irradiated and unirradiated UHMWPE fiber. While the storage modulus of the material is obviously deteriorated by the treatment, the irradiated material seems less sensitive to temperature than the unirradiated sample.

able data for the irradiated sample, which broke around 80 °C in Figure 4.20. The

weakening of the irradiated fiber by the treatment is apparent from this analysis,

however the thermal response of the sample appears to be much less sensitive than

the unirradiated sample, so perhaps the irradiation treatment did improve the ther-

mal properties of this sample.

Chapter 5

Conclusions and Future Work

5.1 Contributions to Science

In this course of this work, several important contributions to science were uncovered. The first, and possibly most important of these, is the elucidation of the mechanism of hydrolysis in PBO by which the benzoxazole ring opens between the double bond and the oxygen and that water adds across this bond when this material is exposed to a warm, humid environment. An extension of this contribution was the discovery that this reaction likely goes to complete, irreversible chain scission by breaking the bond between the carbonyl group and the adjacent phenyl ring of the next repeat unit of the polymer. The broader impact of this contribution will be discussed in the next section.

The next contribution is that aramid copolymer fibers release acids used during synthesis (these polymers are synthesized using an acid chloride polycondensation reaction) and processing (these fibers are spun from acid solutions) from within the fiber when exposed to water. This acid release does not reach equilibrium for several days, indicating that the acid continues to migrate to the surface from within the yarn over a period of time.

Another contribution to science is that binary (either the armor was or was not perforated by the shot) ballistic limit data for different materials in different aging

227

states can be described equally well by logistic, probit, and c-log-log generalized linear models. This issue has been debated within the ballistic testing community for the last decade, and this debate will continue as new models are examined.

Finally, the primary aging mechanisms in UHMWPE yarns were examined via studies relating oxidation index, tensile strength, and crystal structure to elevated temperature exposures. The activation energy for the oxidation of UHMWPE fibers was calculated and found to be 140 kJ/mol. It was also shown that the primary mechanism to which this material is susceptible is oxidation under aging and use conditions.

5.2 Broader Impacts

In addition to the scientific contributions of this work, these contributions were extended to several broader impacts for the body armor manufacturing community and law enforcement. The first, and possibly most important of these is the removal of PBO from use in NIJ-certified body armor due to concerns with the long-term stability and ballistic performance of this material due to its susceptibility to hydrolysis in wear conditions. This work has also led to a major lawsuit by the US Civil Division against manufacturers of PBO materials and body armor. To date, this effort has recovered $61M for the US Treasury through settlements, with at least 3 major cases still pending.

In an effort to find other armors with similar vulnerabilities during the initial certification testing program, the NIJ Ballistic Resistant Body Armor Standard was

revised to include an armor conditioning protocol as described in Chapter 1. This conditioning protocol has proven to be a useful tool, catching problematic armors and driving armor manufacturers to consider the wear environment when designing armor. The conditioning protocol has also recently been adopted by the US Army for use in major armor procurements. The US Army has also been interested in the work performed on aramid copolymer fibers, and is considering using these in some advanced armor designs, as they do not appear to have major vulnerabilities to environmental degradation.

The work to examine various generalized linear models for use in analysis of ballistic limit data has been employed by the NIJ Body Armor Compliance Testing Program to evaluate at least one armor model using the three different analysis methods. The US Army and several armor manufacturers have also expressed an interest in the analysis of ballistic limit data using these different models.

The analysis of the primary aging mechanism in UHMWPE yarn and the calculation of the activation energy of this reaction was presented to several UHMWPE fiber manufacturers at a recent international meeting. These manufacturers discussed the possibility of changing either the type or concentration of antioxidant in the fibers in an effort to make them more robust to this type of degradation.

5.3 Future Work

While the work described herein is quite broad, there remain many additional areas for future work. First, given the interest in the body armor community in bet-

ter understanding the expected lifetime of body armor, coupled with the increased use of aramid copolymers in both law enforcement and military armor designs, more work needs to be performed to understand the long-term stability of high strength fibers. This can be accomplished through additional temperature and humidity aging studies and a calculation of the activation energies of hydrolytic and thermo-oxidative degradation mechanisms in these materials. This information can be used along with measurements on fielded armor samples to develop models to predict the service life of body armor. Next, the scientific community would also benefit from fundamental studies on the structure of the aramid copolymer fibers. It is not known whether they have a structure more similar to the "broom straw bundle" structure of PBO or the "pleated sheet" structure of PPTA. One way to discern this might be to longitudinally section an fiber and perform atomic force microscopy and electron microscopy to examine the microstructure of these fibers. The role of acid release in the aramid copolymers is also not fully understood, as the chloride ion was not the appropriate counterion to explain the pH changes in these materials. Additional work should be performed to correctly identify the source of the acid release in these fibers.

Next, much work still remains to examine other types of ballistic limit test methodologies and models to understand how best to fit this binary response data and accurately estimate the probability of perforation for new and aged armors. It is also especially important to evaluate methods for predicting changes in ballistic performance for aged armors, in an effort to answer the question- How much degradation can an armor withstand before it loses its ability to protect the wearer?

Two remaining issues in the aging of UHMWPE fibers are to further the understanding of the change from orthorhombic to monoclinic crystal structure for the samples heated to 65 °C, and to repeat the WAXS measurements on fibers aged at all the different temperature in the study for the same amount of time, to determine if there is an effect due to aging temperature and not just aging time.

Finally, much work remains to examine the potential of using irradiation to crosslink UHMWPE fibers to improve their thermal resistance without destroying their strength. The use of an electron beam with a faster pulse rate, coupled with a cooling system to remove the heat building up in the fiber during the irradiation is a promising next step to achieving this goal.

In addition, processes for which many time scales exist are considered dispersive. The rate coefficient for a dispersive process depends on time. For example, in the case of chemical reactions, the most reactive species are the first to disappear from the system. This will disturb the reactivity distributions of reactants in a condensed medium, and the extent of this disturbance depends on the ratio of the rates of reactions to the rate of mixing in the system, which restores the initial distribution of reactants in the system. If rate of the chemical reaction exceeds that of the internal rearrangement, then these initial distributions of reactivity cannot be maintained and the specific reaction rate will depend on time. If the rate of internal rearrangement is faster than the rate of reaction, then the extent of this disturbance is negligible, and classical kinetics may adequately describe the system. EPR studies to look at radical decay should be performed to understand whether the decay processes of free radicals generated during the irradiation of UHMWPE

231

fibers undergo classical or dispersive kinetic decay.

Appendix A

Developing Links Between Fiber Properties and Ballistic Performance

A.1 Motivation

While it makes sense that changes in fiber strength affect ballistic performance, very limited work has been performed in this area to establish direct correlations between these parameters for the purposes of improving armor performance. This chapter will introduce different methods of estimating armor performance, the state of the art of using material properties to predict ballistic performance, and discuss strategies for developing improved armors in the future based on specific material properties.

A.2 Ballistic Testing of New and Conditioned Body Armor

NIJ Standard–0101.06 recommends estimating the performance of body armor by performing a statistical analysis on V_{50} ballistic limit testing data. During a V_{50} ballistic limit test, bullet velocity is varied to obtain mixed outcomes. Some shots are stopped by the armor, but other shots yield perforations. From these results, the ballistic performance of the armor can be estimated using a statistical regression model. The logistic regression model is commonly used in many binary response

systems, such as biomedical applications and was therefore targeted for use in the NIJ Standard. However, depending on the armor system and the amount of data collected, other regression models may be more appropriate.

The experimental conditions of ballistic limit testing are strictly controlled in the laboratory. All projectiles used in testing are prepared in the laboratory, rather than being purchased. The amount of propellant is selected by using previously established curves relating the mass of propellent (the charge weight) to a specific velocity of interest. The propellant is weighed on a microbalance and poured into a cartridge case using a funnel. Bullets from a single lot of a single manufacturer are mated with a press to the cartridge case and then used for testing. Projectiles are fired using a universal receiver, which is a fixed mount, single shot device rather than a typical handgun. Reinforced stainless steel barrels machined Sporting Arms and Ammunition Manufacturers' Institute, Inc. (SAAMI) specifications were used in the universal receiver to replicate the action of the handgun of interest (in this case 9 mm). The same shot locations, which had been selected so that no projectile should strike the same stitch line and all locations would be a minimum of 7.62 cm apart, were used for each test, however the order of the shots was randomly selected for each armor panel. All testing was performed using Roma Plastilina #1 clay for the behing-armor backing material. All clay was calibrated according to the procedures in NIJ Standard–0101.06.

A.2.1 The Logistic, Probit and Complementary Log-Log Regression Models

Once the ballistic limit testing has been completed, the test results are analyzed for each threat by performing a regression to estimate the performance of the armor over a range of velocities. During ballistic limit testing only a limited number of shots are taken. From those data the full performance of the body armor can be estimated. In particular, the analysis attempts to estimate the velocity where the probability of perforation becomes reasonably small. As previously mentioned, the shot outcome of the ballistic limit tests is a perforation or a stop, codified as 1 and 0, respectively. This type of outcome data is commonly called binary response data. A vast literature in statistics, biometrics, and econometrics is concerned with the analysis of binary response data and the classical approach fits a binomial regression model using maximum likelihood [213]. The binomial regression model is a special case of an important family of statistical models, namely Generalized Linear Models [214, 215, 216, 217] (originally due to Nelder and Wedderburn [218]). The acronym GLM is a shorthand for generalized linear model [219]. The binomial family is associated with several links; among the common binomial links there are the probit, the logit and the complementary log-log link functions. The probit model [220] was the first model of binary regression used. It was originally developed for analyzing dose-response data from bioassays [220, 221]. This model is still used by researchers for biological assay analysis, and often used to model other data situations. Logistic regression was developed later and not used much until

the 1970s, but it is now more popular than the probit model [219, 222]. Indeed, in recent decades, the logistic regression model has become the standard method of analysis for binary response data to model the relationship between the binary outcomes (shot outcome in this case) and the independent variable (the velocity of the bullet) in many fields, such as biomedical [223, 219, 224, 225, 226] and economical research [222, 227]. Alternatives to the traditional logistic approach using the probit and complementary log-log link functions were studied [228, 229, 230].

Current opinion regarding the selection of link function in binary response models is that the probit and logistic links give essentially similar results [223, 216, 219, 231, 232]. Long [233] wrote that the choice between the logistic and probit models is largely one of convenience and convention, since the substantive results are generally indistinguishable. Moreover, Gill [215] discussed link functions including the complementary log-log and indicated that any of these three link functions can be used and will provide identical substantive conclusions.

Conversely, other studies have shown that in many cases this most commonly used logistic regression model may be not always the most appropriate, and that alternative models can also provide good results in this context of binary response data [228, 97]. Many authors have examined the best way to discriminate the logit and probit models [233, 97, 234]. Logistic regression is usually preferred because of the wide variety of fit statistic associated to the model. However if normality is involved in the linear relationship, as it often is in bioassay, then probit may be the appropriate model. It may also be used when the researcher is not interested in odds but rather in prediction or classification [216]. Hahn and Soyer [235] found

clear evidence that model fit can be improved by the selection of the appropriate link even in small data sets, and that the probit and logit links do not always give similar results in binary data analysis. They showed that in certain cases, the probit model provides a better fit, while in others the logit model is more appropriate. Moreover, empirical support for the recommendations regarding both the similarities and differences between the probit and logit models can be traced back to results obtained by Chambers and Cox [234]. These researchers found that it was only possible to discriminate between the two models when sample sizes were large and certain extreme patterns were observed in the data [234]. Despite the similarities of these models, even minimal differences can lead to different estimations in some particular cases [234]. Thus, it is always recommended to attempt to apply more than one regression model to the data to better understand the abilities of other models to fit those data.

The use of regression models to analyze ballistic tests of armor systems have been suggested in different studies [236, 237]. NIJ Standard–0101.06 recommends the use of the logistic regression model for the analysis of ballistic limit data. However, other probability distributions and regression methods may be used when one can be shown to better estimate the performance of a particular armor model. In the field of analysis of perforation statistics of body armor, Van Es [238] studied the probit method versus the Kneubuhl method and showed that probit analysis was a robust tool to analyze ballistic limit data. Maldague [239] also studied the analysis of V_{50} using different methods and used successfully the probit method with ballistic results. For this reason, other alternative distributions able to fit these data will be

studied and compared in terms of quality of estimation of the armor performance.

A.2.2 Presentation of the Three GLMs

As previously mentioned, three different distribution models are considered in this study: the logistic, the probit and the complementary log-log (extreme value type I) response models. For the purposes of this paper, the logistic regression model will be called logit or logistic, and the complementary log-log regression model will be called c-log-log. The logit link function is a fairly simple transformation of the prediction curve so it is popular among researchers [231]. Logit models use the logistic probability distribution [231]. The probit models assume the standard normal distribution [220]; it has a mean of 0 and standard deviation of 1. The standard logistic distribution has a mean of 0 and standard deviation of 1.8. When both models fit well, parameter estimates in logistic regression models are approximately 1.8 times those in probit models [233]. The normal and logistic distributions are both symmetric [220, 231]. The logit and probit links are very similar; in particular, both approach 0 and 1 symmetrically and asymptotically. Because of this similarity, they usually lead to analogous results [220, 231]. The c-log-log analysis is an alternative to logit and probit analysis. The c-log-log model is based on the extreme value type I distribution, also referred to as the Gumbel distribution [240, 241], which is asymmetric in contrast to the logistic or standard normal distribution of the logit and probit models, respectively. All of the three model transforms produce a sigmoidal (or S-shaped) response curve. However, since the extreme value distribution
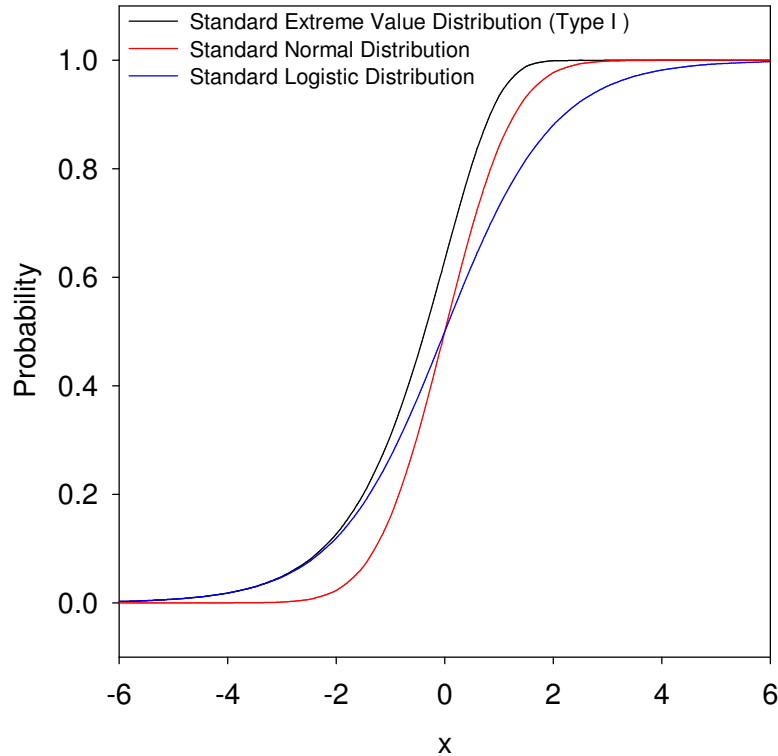
Figure A.1: Cumulative density functions for the three GLMs. The idealized models are plotted to show the differences in their tails in the low probability region. This is the region of interest in ballistic limit analysis because of the interest in the margin of safety designed into armor for lower velocity threats.

is asymmetric, the results are slightly different from those of the two other symmetrical models. To illustrate this difference, idealized curves for all three models are presented in Figures A.1 and A.2. The reason why Cumulative Distribution Functions (CDF) are used as link functions for binary data is because the CDF is always between 0 and 1.

The cumulative density function of the standard normal distribution is steeper in the middle than that of the standard logistic distribution and quickly approaches 0 on the left and 1 on the right. From Figure A.2 it can be noted that the logit link has heavier tails than the probit or c-log-log, i.e. this link assigns a greater probability to observations that fall outside the mean. The implication of this is that in the event
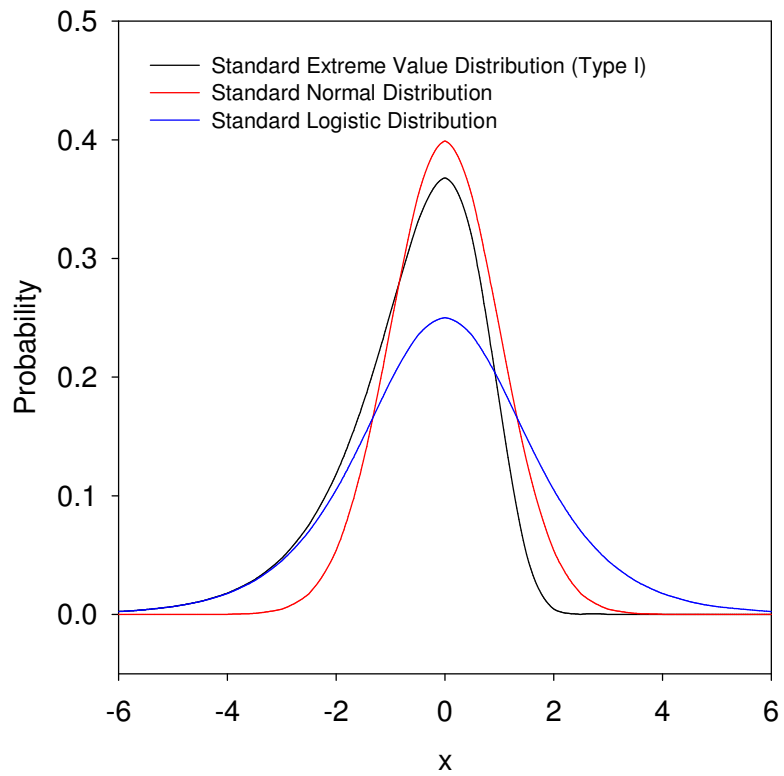
Figure A.2: Probability density functions for the three GLMs. The idealized models are plotted for reference to illustrate both sides of the distribution for comparison to the common standard normal distribution.

Link Name (distribution)	Probability of perforation $\pi(v)$	Velocity where probability of perforation is π, $\hat{V}_\pi$	Estimated V_{50}
Logit (Logistic)	$\dfrac{e^{\hat{\beta}_0+\hat{\beta}_1 v}}{1+e^{\hat{\beta}_0+\hat{\beta}_1 v}}$	$\dfrac{\ln\left(\dfrac{\pi}{1-\pi}\right)-\hat{\beta}_0}{\hat{\beta}_1}$	$\dfrac{-\hat{\beta}_0}{\hat{\beta}_1}$
Probit (Normal)	$\Phi\left(\hat{\beta}_0+\hat{\beta}_1 v\right)$	$\dfrac{\Phi^{-1}(\pi)-\hat{\beta}_0}{\hat{\beta}_1}$	$\dfrac{-\hat{\beta}_0}{\hat{\beta}_1}$
Complementary log-log (Extreme value)	$1-e^{-e^{(\hat{\beta}_0+\hat{\beta}_1 v)}}$	$\dfrac{\ln\left(-\ln(1-\pi)\right)-\hat{\beta}_0}{\hat{\beta}_1}$	$\dfrac{\ln\left(-\ln(0.5)\right)-\hat{\beta}_0}{\hat{\beta}_1}$

Table A.1: Comparison of distributions.

that there is variability in the measurements the parameter estimates using the logit link will capture this as a result of the heavier tails whereas the other distributions may not. From this observation one could assume that it is generally safer to use the logit link as it is less susceptible to outliers or to data with a lot of variability than the two other links. The three link functions and their corresponding distributions are summarized in Table A.1.

Table A.1 contains the probability of a complete perforation occurring at velocity v: $\pi(v)$; and also the velocity at which the probability of perforation is π %: $\hat{V}_\pi$. The calculation of V_{50} is determined from the estimated regression parameters $\hat{\beta}_0$ and $\hat{\beta}_1$, which are the estimated *constant* and the estimated *velocity coefficient*, respectively. The formula of this estimated V_{50} is also shown in Table A.1 for each model. The explanation and the calculation of the confidence intervals of the estimates can be found in Ref. [223, 242]. The different regressions are performed on the data using the method of maximum likelihood [223, 243] to estimate the logistic, the probit or the c-log-log parameters $\hat{\beta}_0$ and $\hat{\beta}_1$. The confidence intervals of the

estimates are calculated using the Wald test [223, 242]. Fieller's theorem [220] is used to estimate the confidence intervals of V_{50}.

A.3 Application of the Different Models to Fit V_{50}

A.3.1 R Software

The three regression models are performed on the ballistic limit data using the method of maximum likelihood to estimate the regression parameters. The R statistical software package [244] was used to execute the different regressions and estimate the regression coefficients. R is a free software environment for statistical computing. It provides a wide variety of statistical techniques, such as data analysis using regression models. The R statistical software allows computing and fitting each of the three different regression models (logistic, probit and c-log-log) to the data. The generalized linear model (GLM) procedure [245], with the parameters family=binomial and link=logit, probit, or cloglog, as appropriate, to specify the model is used to fit the different regression models to the binary response data using maximum likelihood estimation. After the regression computation, R outputs provide the regression coefficients estimates and their standard errors, as well as all the information needed to calculate the confidence interval (variance matrix), and also some useful statistics like deviance and Akaike's Information Criterion. Both statistics will be discussed further later in this work.
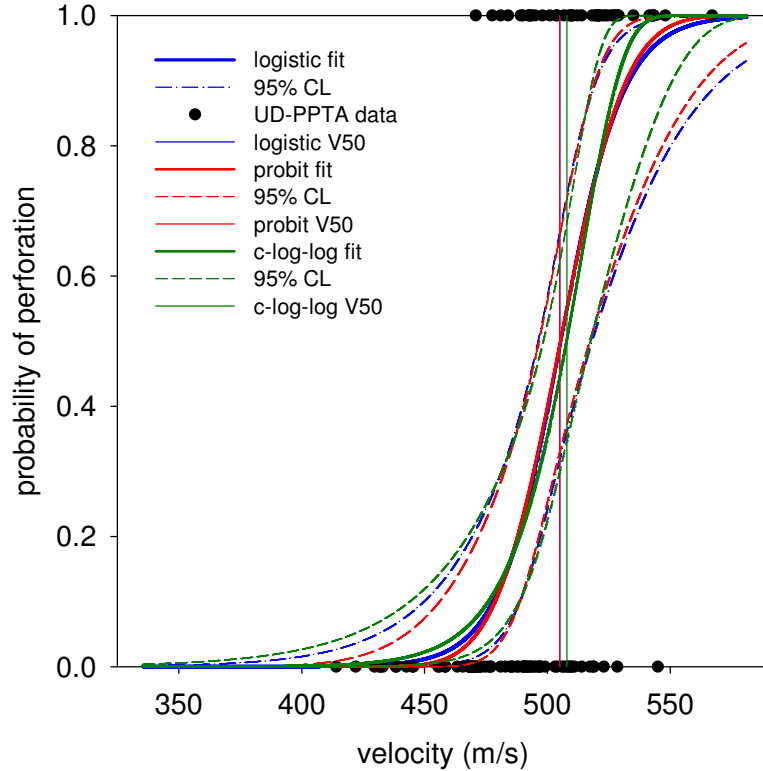
Figure A.3: Estimated response curves for a new UD-PPTA body armor given by the three GLMs. Experimental ballistic limit data are given by the black dots, with a 0 corresponding to a stop and a 1 corresponding to a perforation. The solid lines represent the best fit of the three different models to this data, and the dotted lines represent the upper and lower 95 % confidence intervals for the fit of the model.

A.3.2   Comparison of the GLM Estimates

To illustrate the application of the different regression analysis and their results in terms of estimations, a typical example is presented in Figure A.3: the analysis of the ballistic performance of a new UD-PPTA body armor which shows the estimated response curve of this body armor given by the three different models.

The estimated response curves of the logistic, probit and c-log-log regression models and their 95 % confidence intervals as presented in Figure A.3 are very similar. However, the confidence interval generated using the c-log-log model is not comparable with those obtained from logistic and probit models because of

the asymmetrical shape of the c-log-log distribution function. The three function curves are all S-shaped. As previously discussed, the logit and probit curves are very similar; in particular, both approach 0 and 1 symmetrically and asymptotically. However the c-log-log distribution is asymmetric, it approaches 1 much more rapidly than it approaches 0, accordingly, the results obtained with this model are different. The logistic and probit functions are almost linearly related over the interval of probabilities of perforation between 0.1 and 0.9. These two models perform similarly at the center (at V_{50}). The primary difference between the logit and probit response curves is that probit has slightly flatter lower and upper asymptotes, which means the probit curve approaches the axes more quickly than the logistic curve. Therefore, the two GLMs give different estimations of armor perforation for low and high bullet velocities, which are important in ballistic limit analysis. As expected, the asymmetrical c-log-log response curve approaches much more quickly the high probability of perforation (i.e., probability of 1) than either the logit or probit function. For small values of probability of perforation, the c-log-log function is close to the logistic. The preceding discussion of the differences and similarities between the response curves given by the three regression models considered herein are confirmed by further examining the V_{50} and V_{02} estimate values directly. This information is presented in Table A.2.

While the estimates of parameters differ in size due to the different scaling of the normal and logistic distributions, the substantive conclusions (and the predicted probabilities of perforation for the armor) are very similar. The estimated V_{50} value is the same for the logit and probit models. Because of its asymmetry, the

	Logit	Probit	C-log-log
V_{50} **(m/s)**	**505**	**505**	**508**
Upper 95 % CL on V_{50} (m/s)	518	517	518
Lower 95 % CL on V_{50} (m/s)	496	497	498
CI width (m/s)	22	21	19
Predicted prob. at 350 m/s	**0.0000044**	**5.63 E -14**	**0.0000653**
Upper 95 % CL at 350 m/s	0.002392	0.000034	0.005925
Lower 95 % CL at 350 m/s	0	0	0
CI width	0.002392	0.000034	0.005924
V_{02} **(m/s)**	**457**	**462**	**448**
Upper 95 % CL on V_{02} (m/s)	473	477	469
Lower 95 % CL on V_{02} (m/s)	406	426	390
CI width (m/s)	67	50	78

CI is confidence interval.
CL is confidence level.
350 m/s is the NIJ reference velocity.
V_{02} is the velocity at which a bullet has a 2 % chance of perforating the armor.

Table A.2: Summary of estimates for a new UD-PPTA body armor.

estimations of the high and low velocities related to the logistic and probit models are different from the ones obtained by the c-log-log model. Generally, the estimated V_{50} provided by the logit and probit regression models are similar but the V_{50} estimated by c-log-log is slightly higher. In the case of the V_{02} estimate, the c-log-log model provides the lowest value for V_{02}, while the probit provides the highest value. In most applications, results from the c-log-log model are not very different from logit and probit, however, occasionally the estimate results can suggest qualitatively different conclusions.

Even if differences and similarities between estimates given by the three regression models can be discerned, it is difficult to discriminate between these three models on the basis of the quality of the armor performance estimation. The three regression models lead to very similar results, especially for the estimation of V_{50}.
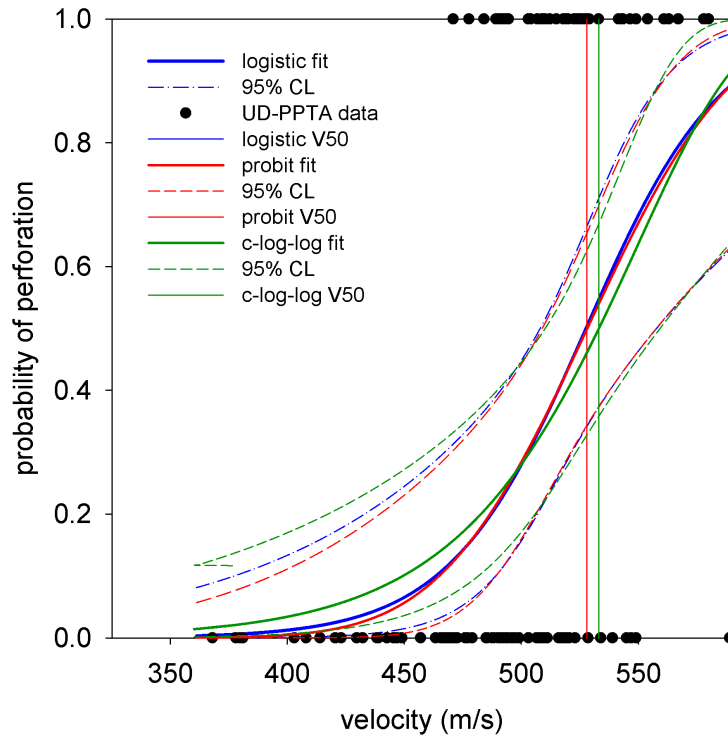
Figure A.4: Estimated response curve for an UHMWPE body armor given by the logistic model. Experimental ballistic limit data is given by the black dots, with a 0 corresponding to a stop and a 1 corresponding to a perforation. The solid line represent the best fit of the logistic model this data, and the dotted lines represent the upper and lower 95 % confidence intervals for the fit of the model.

For the estimation of V_{02} and the predicted probability of perforation at the NIJ reference velocity (350 m/s), the difference between the estimates given by the diverse models is larger, but they are still similar. Moreover, the binary nature of the analyzed data does not allow a visual comparison. From Figure A.3 it is not possible to identify the best model.

This same approach is used to examine the response curve of a UD-UHMWPE armor. Once again, the estimated response curves of the logistic, probit and c-log-log regression models and their 95 % confidence intervals as presented in Figure A.4, Figure A.5, and Figure A.6 are very similar.
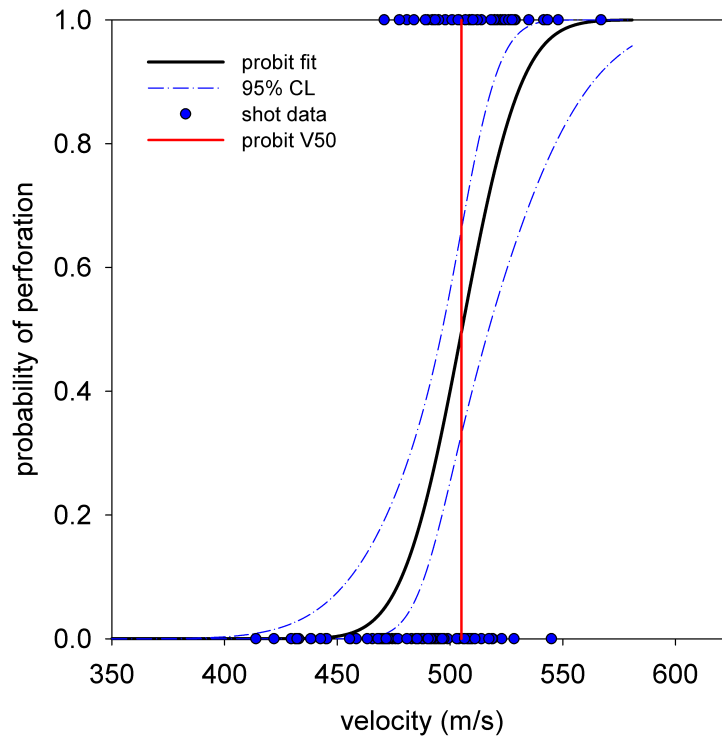
Figure A.5: Estimated response curve for a new UHMWPE body armor given by the probit model. Experimental ballistic limit data is given by the black dots, with a 0 corresponding to a stop and a 1 corresponding to a perforation. The solid line represent the best fit of the probit model this data, and the dotted lines represent the upper and lower 95 % confidence intervals for the fit of the model.
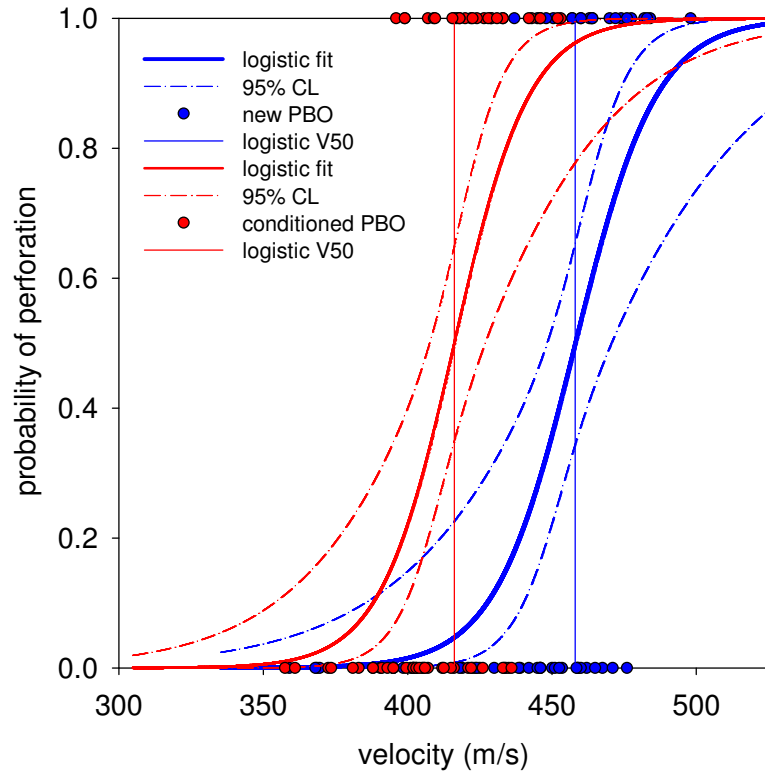
Figure A.6: Estimated response curve for a new UHMWPE body armor given by the c-log-log model. Experimental ballistic limit data is given by the black dots, with a 0 corresponding to a stop and a 1 corresponding to a perforation. The solid line represent the best fit of the c-log-log model this data, and the dotted lines represent the upper and lower 95 % confidence intervals for the fit of the model.

	Logit	Probit	C-log-log
V_{50} **(m/s)**	**507**	**507**	**510**
Upper 95 % CL on V_{50} (m/s)	522	522	523
Lower 95 % CL on V_{50} (m/s)	493	494	454
CI width (m/s)	29	28	69
Predicted prob. at 350 m/s	**0.00049**	**2.22 E -6**	**0.00347**
Upper 95 % CL at 350 m/s	0.0393	0.000000	0.0579
Lower 95 % CL at 350 m/s	0.00000589	0.0172	0.000203
V_{02} **(m/s)**	**440**	**449**	**421**
Upper 95 % CL on V_{02} (m/s)	466	471	453
Lower 95 % CL on V_{02} (m/s)	349	380	321
CI width (m/s)	67	50	78

CI is confidence interval.
CL is confidence level.
350 m/s is the NIJ reference velocity.
V_{02} is the velocity at which a bullet has a 2 % chance of perforating the armor.

Table A.3: Summary of estimates for a new UD-PPTA body armor.

The preceding discussion of the differences and similarities between the response curves given by the three regression models considered herein are confirmed by further examining the V_{50} and V_{02} estimate values directly. This information is presented in Table A.3.

As for the UD-PPTA armor, the estimates of parameters differ in size due to the different scaling of the normal and logistic distributions, the predictions are all very similar and it is not possible to determine which model best describes the armor.

Consequently, some criteria of goodness-of-fit are required to assist in the determination of which model could better estimate the armor performance from the available ballistic data. The next section will examine this issue.

A.4 Generalized Linear Model Estimation Evaluation

Different criteria for assessing the goodness-of-fit of each model will be applied to the ballistic limit data. The objective of this analysis is to identify criteria that can distinguish which regression method produces the best estimate of the performance of a particular armor model, since the estimations given by the three models were shown to be analogous.

A.4.1 Assessment Criteria

Once a model has been fitted to the observed values of a binary response variable, it is essential to check that the fitted model is actually valid. Goodness-of-fit statistics given by the R software can be used to compare fits using different link functions. The significance test of the regression coefficients is provided after every regression and allows one to verify the significance of each coefficient. The R outputs also indicate the estimates of the regression coefficients and are accompanied by the standard errors.

A.4.2 Akaike's Information Criterion

One way to choose between different specifications (e.g. between the probit, logit and c-log-log models) is to use a model selection criterion. Akaike [243] defined *an information criterion* commonly known as *Akaike's Information Criterion*, or AIC. This criterion is a measure of goodness-of-fit which takes into account the number of fitted parameters. The formula for calculation of AIC is given in Equa-

tion A.1.

$$AIC = -2 \log L + 2p \qquad \qquad \text{(A.1)}$$

where $\log L$ is the log-likelihood function evaluated of the model parameters and p is the number of model parameters. The AIC is a convenient metric for this analysis because it is given in R's ANOVA (analysis of variance) output. Smaller AIC values are associated with better fits. The AIC was calculated for all the GLMs considered, and the model with the smallest AIC is considered to be the closest to the unknown reality that generated the data.

A.4.3   Log-Likelihood

As a quick and simple way to compare the performance across the different models, one can simply look at the maximized log-likelihood of each specification, since the models contain an equal number of parameters. However, Akaike [243] showed that the maximized log-likelihood is biased upward as an estimator of the model selection criterion and then defined the AIC as a better criterion for measuring goodness-of-fit.

A.4.4   Deviance of the Model

Huettmann and Linke [230] presented two methods of assessing which link function performs best for inferences and for predictions. The first decision criterion is centered on the model deviance, e.g. relevant for inferences. A measure of

discrepancy between the observed and fitted values is the deviance statistic. In a perfect fit the deviance is zero. Thus, the most preferable model can be found on the basis of the minimum-deviance criterion for model selection. For example, if the deviance of a probit model is significantly lower than the one of the corresponding logit model, then the former is preferred. This postulate holds when comparing any of the links within the binomial family [216]. Conversely, the model that provides the least desirable fit to the data can also be found. The deviance criterion is also given in the R output as an indicator of goodness-of-fit.

A.4.5   Prediction Error Rate

The second criterion presented by Huettmann and Linke [230] is based on prediction errors. It uses the differences between expected and predicted values as an indication of the fit. Once the regression model analysis is performed, the resulting regression coefficients estimates are used to predict the data and provide predictive probabilities of perforation. If the probabilities of perforation are greater than 50 %, these probabilities are classified in the perforation group, if they are less than 50 %, they are classified in the non-perforation group. Then the observed and predicted responses can be cross-tabulated and the proportion of cases predicted correctly can be calculated. The lower the misclassification rate, the better the model fits the data. However, this misclassification rate is not independent of the model (since it is based on the data used to build the model) and therefore could underestimate the real error rate.

A.4.6 Cross-Validation Method

The cross-validation method avoids this problem of dependence; therefore, it gives a better calculated error rate than the usual prediction error rate. In k-fold cross-validation, one divides the data into k subsets of (approximately) equal size. One trains the net k times, each time leaving out one of the subsets from training, but using only the omitted subset to compute the error criterion of interest, in this case the prediction error rate. This way, it avoids the problem of dependence of the model observed previously. Cross-validation can be used simply for model selection by choosing the model that has the smallest estimated generalization error.

In this study, where the ballistic performance of an armor type is estimated by testing several armor panels and combining their ballistic results, this training/testing set method uses the ballistic data of *n-1* panels to estimate the model and uses the data of the nth panel to test the prediction of the model. Then the model is trained n times, each time leaving out one panel to calculate the error rate. Finally the average error rate of re-substitution is calculated and used as a model selection criterion.

Among all of the model selection criteria previously presented, the AIC and the average error rate calculated by cross-validation, also called average error rate of training/testing sets method, will be used as criteria to try to distinguish which regression method produces the best estimate of the performance of a particular armor model. However, in case of few differences between the model results, the optimal model could be at the end chosen by the user, regarding mostly its specifications,

	Logit	Probit	C-log-log
V_{50} **(m/s)**	**505**	**505**	**508**
Upper 95 % CL on V_{50} (m/s)	518	517	518
Lower 95 % CL on V_{50} (m/s)	496	497	498
AIC	51.94	**51.40**	52.07
Misclassified Data (%)	23.3	23.3	**21.7**
Error Rate by Cross-Validation (%)	23.3	23.3	**21.7**

Table A.4: V_{50} estimates and selection criteria for new UD-PPTA armor.

its estimations and its applications in a practical way.

A.5 Model Diagnostics Results

Some general observations about the results of these model diagnostics can be noted. First, the lack of fit tests given by the R software output do not indicate a significant lack of fit for any of the three models, for all the datasets tested, and the criteria values for all three models are similar. Furthermore, the prediction error rate is, as expected, lower when it is calculated from the whole set of data used to create the model, and the average error rate of cross-validation method is higher. These misclassification rate criteria have the same values for logit and probit. The comparison of the predicted values, previously made in Figure A.3 showing the predicted values given by the three models and the observed data, did not indicate strong evidence for distinguishing models on the basis of link. Therefore, the model selection criteria given in Table A.4 will be the focus of the rest of this work.

In Table A.4, the best criteria are shown in bold. Thus the AIC statistic for the probit model is lower than for the logistic and c-log-log models, suggesting

a slight, but probably insignificant, preference for the probit model. The criteria based on the two error rates show that the c-log-log model is better for prediction. However the difference between the error rates for the different models is small.

A.6   Results of Theoretical Analysis

A regression model can be fitted to the ballistic limit data to estimate the overall response of particular body armor. Different possible models were considered and compared in terms of quality of estimation of the body armor's performance. Comparisons were made only between models that have been applied to the same dataset, so with the same number of data points and the same number of parameters. The comparison was made at the level of estimation of the V_{50}. The estimation given by each model was evaluated on its confidence interval (CI) width, the percentage of misclassified data, the estimation of V_{50} and other parameters like AIC. The results show that the logistic analysis generally gives a good overall estimation of the body armor's performance, but other regression models could be better. For a particular armor, a model can be shown to better estimate its performance on the basis of a selection criteria. However, the difference between the three models examined herein is relatively small in terms of estimation. Additionally, the values of the different criteria studied are too close to make a meaningful determination among the various models. Even if some criteria indicate a slight preference for one model, the others cannot be necessarily considered bad models to fit the ballistic data. Thus, the commonly used logistic regression model specified in NIJ Standard–0101.06 can still

be considered an appropriate choice for V_{50} ballistic limit analysis.

A.7 Application to New and Conditioned Armor Analysis

Within the body armor community, many questions still remain regarding whether the initial distribution model deemed appropriate for new armor continues to describe the armor as it ages. Therefore, the analysis of new and environmentally conditioned armors is examined, with the objective of selecting an appropriate distribution model for both new and environmentally conditioned armor samples. Further details about the environmental conditioning of the body armor are discussed in Chapter 1. Using the three different regression models and their specificities in terms of data fitting presented previously, and the criteria able to help identify the best model for a particular armor, the focus is made on the aspect of body armor conditioning and the fitting of ballistic data from new and environmentally conditioned body armor. Data generated from the V_{50} ballistic limit testing of the new and conditioned samples of the same model of armor are considered.

To facilitate an understanding of the effects of conditioning on the ballistic performance of a particular armor, the estimates provided by the same regression model on new and environmentally conditioned armor data are compared.

A.7.1 Comparison of New and Conditioned Armors

If the results from the new armors are compared to the environmentally conditioned armors, the armor model's performance appears to decrease after condition-

ing. Whatever the regression model applied, the estimates for V_{50} and V_{02} decrease, while the size of their associated confidence intervals increase. This indicates a reduced confidence in the armor response curve and therefore an increase in the probability of perforation for these velocities. The probability of perforation at the NIJ reference velocity also increases, as well as its confidence interval. The observed shifts in values for V_{50} and V_{02} are of the same range, regardless of which regression model is used. To illustrate these observations, the observed data and the predicted probability of perforation given by the logistic regression for new and environmentally conditioned PBO armors are presented in Figure A.7. The new armor is represented in blue and the environmentally conditioned armor in red. The shape of the ballistic response curves of new and environmentally conditioned armors look similar, but as previously mentioned, it appears that the response curve has shifted to the left when the armor is environmentally conditioned.

Obviously the PPTA armor is made from a different material than the PBO armor, subsequently the ballistic performances of new and environmentally conditioned PPTA armors are different. The point estimates for V_{50} of conditioned PPTA armor are higher than those for new PPTA armor, though the size of the linked confidence intervals increases as well. However, the V_{02} decreases and the probability of perforation at NIJ reference velocity increases in the PPTA armor, as was seen in the PBO armor, and the confidence intervals associated with the analysis also increase. Figure A.7.1 illustrates these observations. Note the shape of estimated response curve changes between the new and the environmentally conditioned armors. The curve of environmentally conditioned armor is more elongated and its slope is less
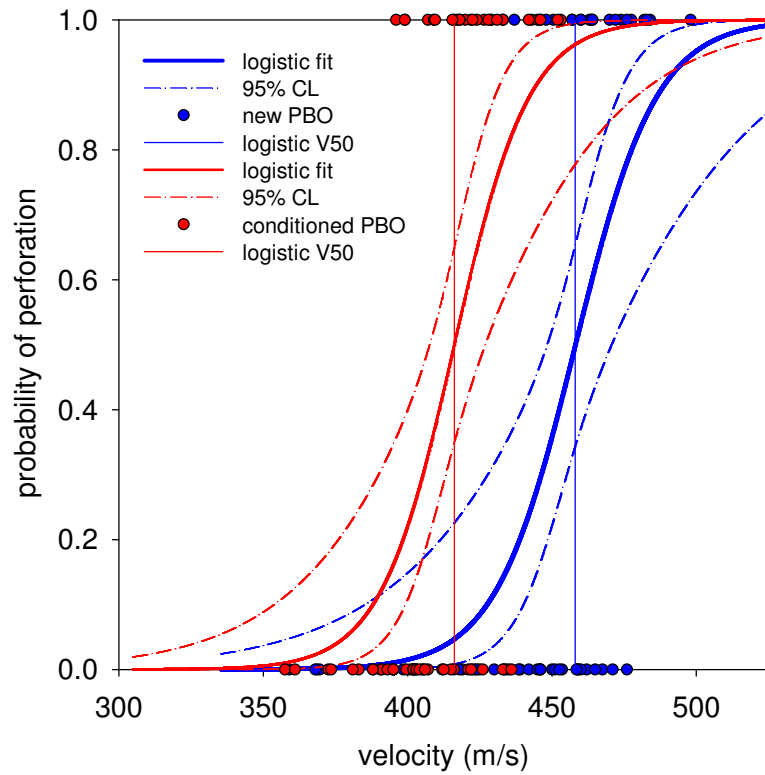
Figure A.7: Estimated response curve for new and conditioned PBO body armor given by the logistic model. Experimental ballistic limit data for the new armor is given by blue dots, and experimental ballistic limit data for the conditioned armor is given by red dots. As in the previous analysis, a 0 corresponds to a stop and a 1 corresponding to a perforation. The solid line represent the best fit of the logistic model this data, and the dotted lines represent the upper and lower 95 % confidence intervals for the fit of the model.

steep. The confidence interval of the environmentally conditioned armor response curve is much wider, so the uncertainty in the ballistic performance increases as the PPTA armor is conditioned.

Finally, the analysis was repeated for all three models for the UHMWPE armor discussed previously. These are presented in Figure A.9, Figure A.10, and Figure A.11.

A.8   Selection of an Appropriate Model for New and Environmentally Conditioned Body Armors

This study seeks to answer the question of whether or not the initial distribution model deemed appropriate for new armor continues to describe the armor as it ages, and the goal is to try to find an appropriate distribution model for both new and environmentally conditioned armor samples. Typical results of the selection model criteria for PBO new and environmentally conditioned armors are shown in Table A.5. Using the prediction performance as a criterion, the three models behave similarly. Using the model AIC as a decision criterion, the findings indicate that for the V_{50} ballistic data studied, the probit model would best fit the data. On the basis of the minimum AIC and the minimum average error rate criteria for model selection, the probit model could be slightly preferable to the others and is deemed appropriate for both new and environmentally conditioned armors. However, as previously noted, the difference between the models is minimal, especially between the probit and logistic models.
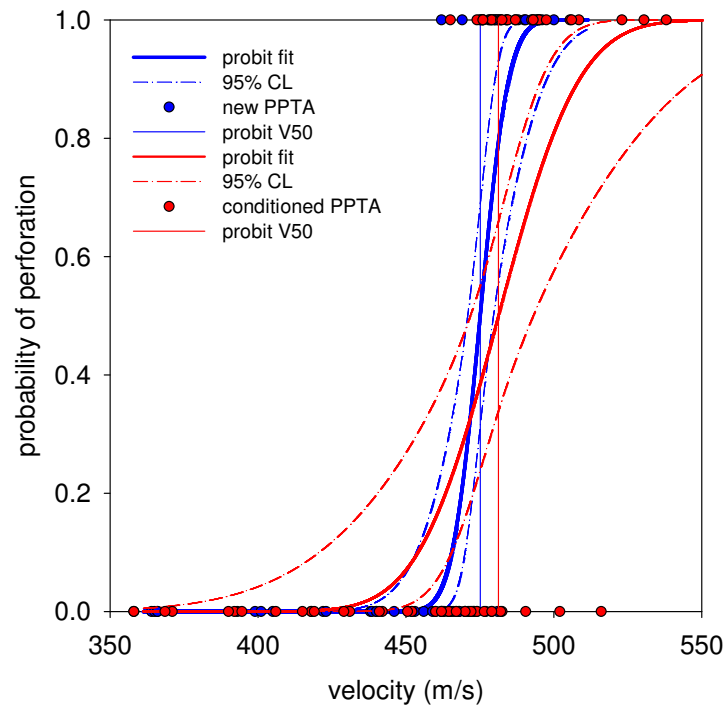
Figure A.8: Estimated response curve for new and conditioned PPTA body armor given by the probit model. Experimental ballistic limit data for the new armor is given by blue dots, and experimental ballistic limit data for the conditioned armor is given by red dots. As in the previous analysis, a 0 corresponds to a stop and a 1 corresponding to a perforation. The solid line represent the best fit of the probit model this data, and the dotted lines represent the upper and lower 95 % confidence intervals for the fit of the model.
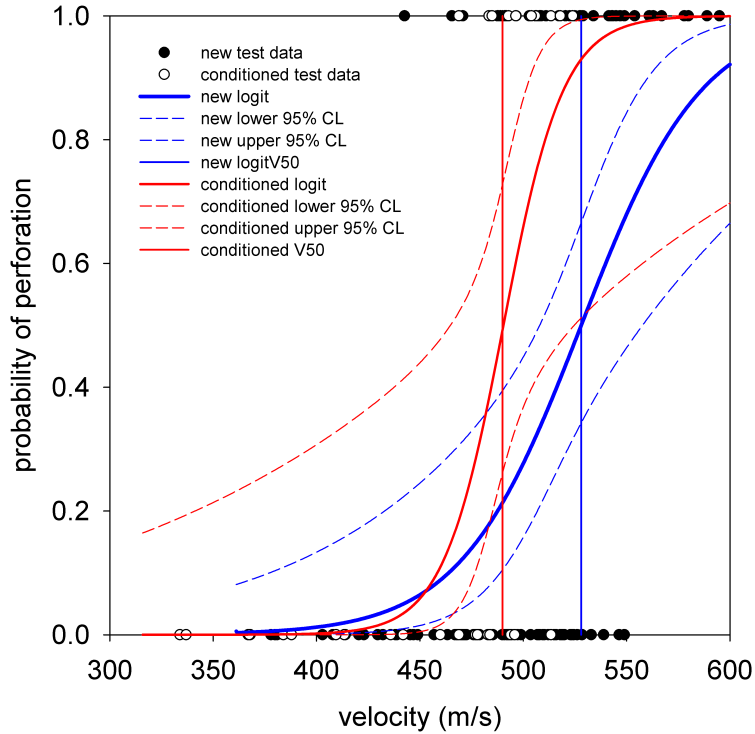
Figure A.9: Estimated response curve for new and conditioned UHMWPE body armor given by the logistic model. Experimental ballistic limit data for the new armor is given by black dots, and experimental ballistic limit data for the conditioned armor is given by white dots. As in the previous analysis, a 0 corresponds to a stop and a 1 corresponding to a perforation. The solid blue (new) and red (conditioned) lines represent the best fit of the logistic model this data, and the dotted lines represent the upper and lower 95 % confidence intervals for the fit of the model.

Armor Type	Minimum AIC	Minimum Misclassification (%)	Minimum average Error Rate by Cross-Validation
New	probit	c-log-log	tie
Conditioned	probit	logit/probit	tie

Table A.5: The best models for new and conditioned PBO armors.

261
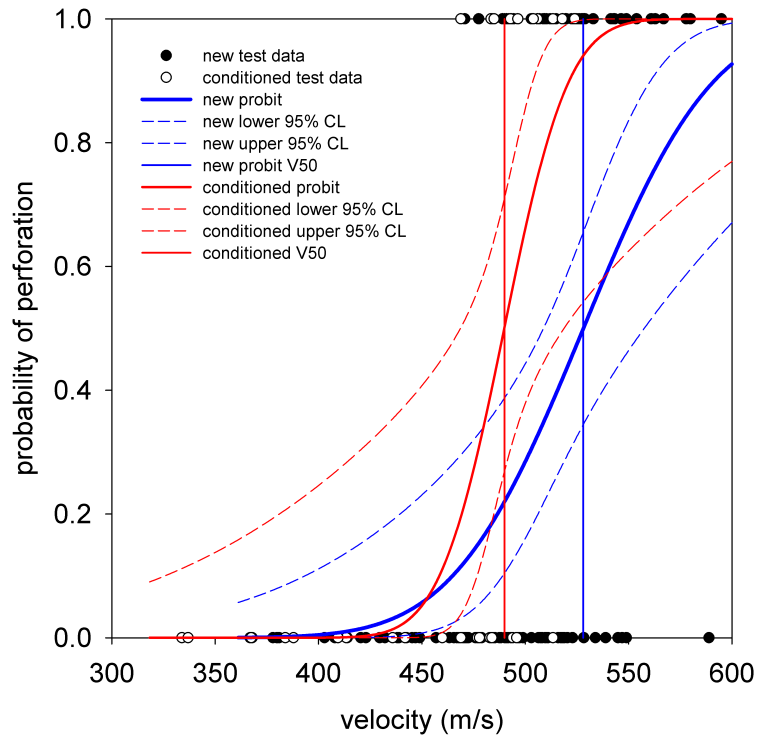
Figure A.10: Estimated response curve for new and conditioned UHMWPE body armor given by the probit model. Experimental ballistic limit data for the new armor is given by black dots, and experimental ballistic limit data for the conditioned armor is given by white dots. As in the previous analysis, a 0 corresponds to a stop and a 1 corresponding to a perforation. The solid blue (new) and red (conditioned) lines represent the best fit of the probit model this data, and the dotted lines represent the upper and lower 95 % confidence intervals for the fit of the model.
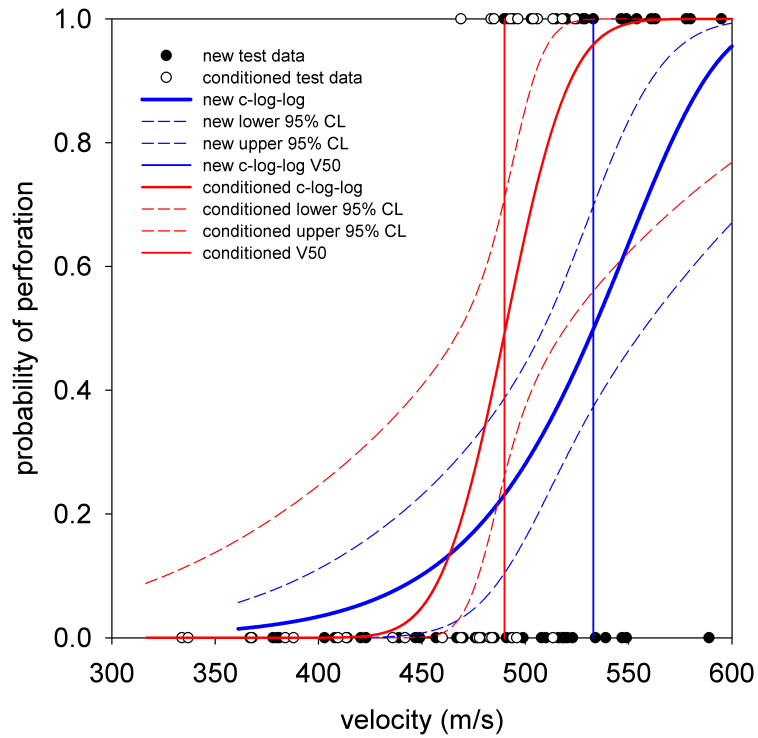
Figure A.11: Estimated response curve for new and conditioned UHMWPE body armor given by the c-log-log model. Experimental ballistic limit data for the new armor is given by black dots, and experimental ballistic limit data for the conditioned armor is given by white dots. As in the previous analysis, a 0 corresponds to a stop and a 1 corresponding to a perforation. The solid blue (new) and red (conditioned) lines represent the best fit of the c-log-log model this data, and the dotted lines represent the upper and lower 95 % confidence intervals for the fit of the model.

A.8.1 Summary

The results show that for a particular armor, one GLM can be shown to better estimate the performance of that specific armor. However, the difference between the GLMs is relatively small in terms of the quality of estimation, and the values of the different criteria studied are similar. Thus, even if some criteria prefer one GLM, the other GLMs could still be an appropriate choice to fit the ballistic data set. None of the three models examined herein can be generally considered to be the *best* model- that is, the model providing the best estimate of the performance of body armor, regardless of its condition.

The contingency table (also called confusion matrix) is a table presenting observed perforations and stops versus their predicted values (in this case predicted perforations or stops). In this matrix, the number of correctly and incorrectly predicted data points is presented. As far as the ballistic limit analysis is concerned, the amount of misclassified perforations is an important number because it represents the amount of real perforations that are not estimated well by the model. Considering that body armor is life safety equipment, one could assume the viewpoint that it is more serious to misclassify an observed perforation as a predicted stop than the opposite.

By examining the contingency table for all the different models applied to the ballistic limit data, it can be noted that the estimates of logit and probit models have the same amount of misclassified perforations, and that the c-log-log model estimates have the same or lightly more misclassified perforations. Consequently,

either the logit or the probit models may be slightly preferred over the c-log-log model, though the c-log-log model cannot be considered to be invalid based on this observation.

A.9 Application of the GLMs to an Unusual Data Set

In the previous sections, the analysis with the different regression models did not show much difference between the models. However, if an armor had an atypical ballistic limit response, then perhaps one of the GLMs could be shown to better describe that particular armor. To investigate this possibility, a dataset from an armor in which one panel had a high number of stops or perforations was of interest in determining if any of the three different models could be determined to be more appropriate than the others for such a system.

A.9.1 Global Analysis of the Armor

Data from a new hybrid armor model with a large number of high velocity stops on one panel were selected for this analysis. The estimated response curves for all three regression models are presented in Figures A.12, A.13, and A.14. As in the previous analysis, the estimated response curves of the logistic, probit and c-log-log regression models and their 95 % confidence intervals presented in Figures A.12 through A.14 are very similar. However, the confidence interval generated using the c-log-log model is not comparable with those obtained from logistic and probit models because of the asymmetrical shape of the c-log-log distribution function.
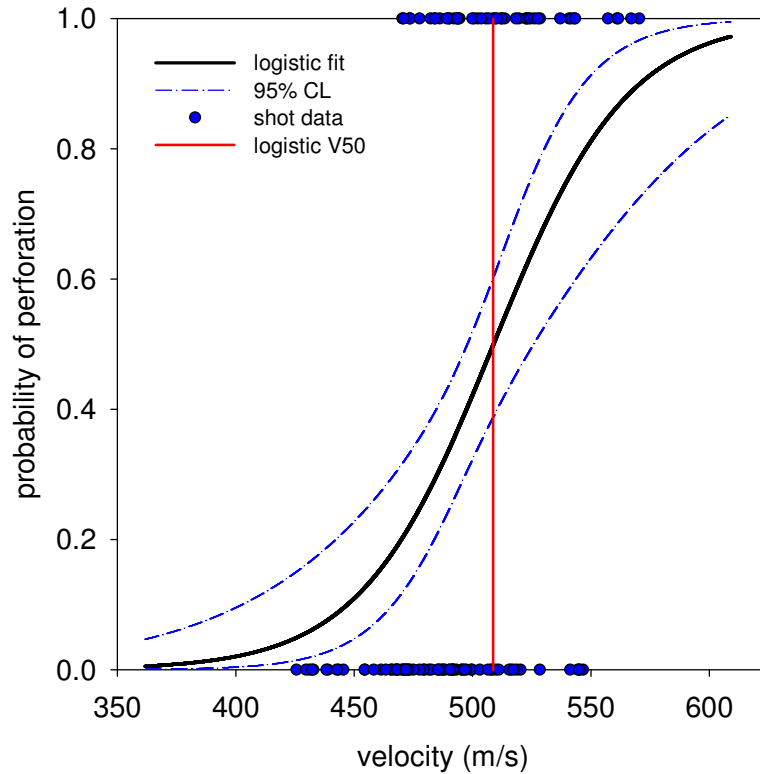
Figure A.12: Logit estimated response curves for a new hybrid armor. Experimental ballistic limit data for the new armor is given by black dots. As in the previous analysis, a 0 corresponds to a stop and a 1 corresponding to a perforation. The solid blue line represents the best fit of the logistic model this data, and the dotted lines represent the upper and lower 95 % confidence intervals for the fit of the model. The estimated v_{50} is indicated by the vertical red line in the graph.

As previously discussed, the logit and probit curves are very similar; in particular, both approach 0 and 1 symmetrically and asymptotically. However the c-log-log is asymmetric, meaning that it approaches 1 much more rapidly than it approaches 0.

It is important to note that this particular armor model has a very large zone of mixed results (ZMR) of 76.2 m/s (250 ft/s). This is due to a large number of stops on one particular armor panel at high velocities. This large zone of mixed results makes it difficult for any model to accurately predict the armor performance at low velocities by reducing the slope of the curve. These results are presented in
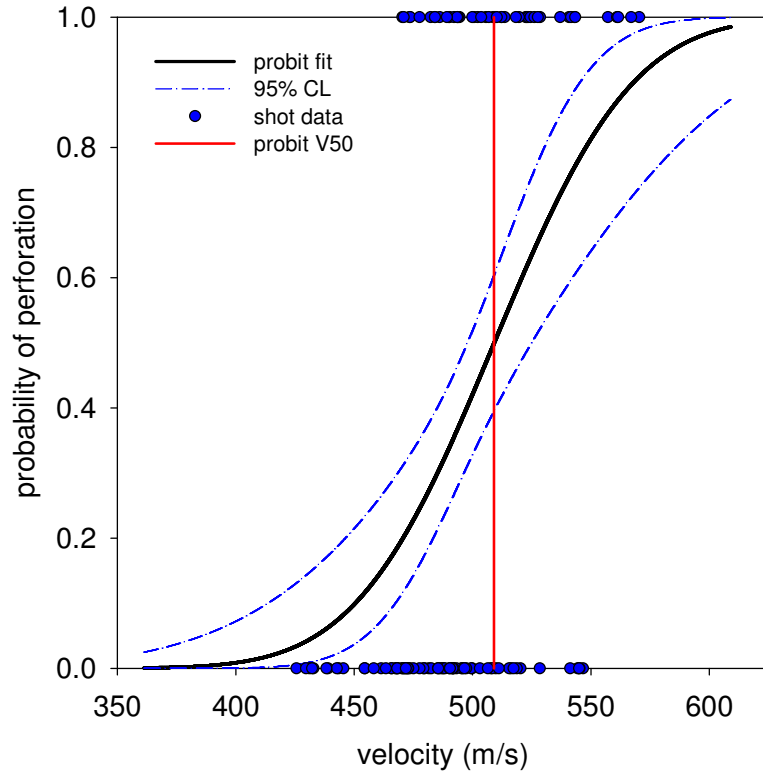
Figure A.13: Probit estimated response curves for a new hybrid armor. Experimental ballistic limit data for the new armor is given by black dots. As in the previous analysis, a 0 corresponds to a stop and a 1 corresponding to a perforation. The solid blue line represents the best fit of the probit model this data, and the dotted lines represent the upper and lower 95 % confidence intervals for the fit of the model. The estimated v_{50} is indicated by the vertical red line in the graph.
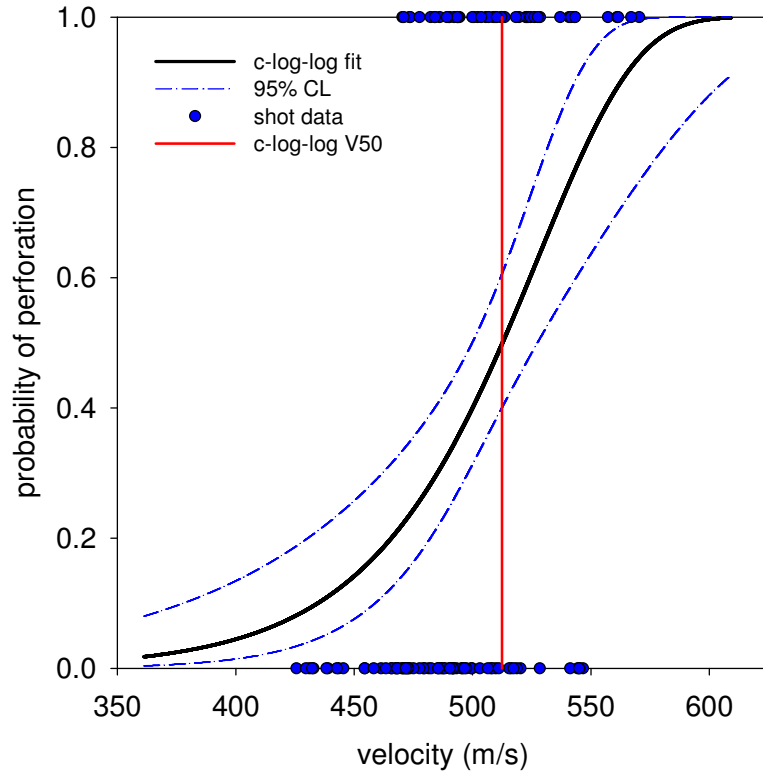
Figure A.14: C-log-log estimated response curves for a new hybrid armor. Experimental ballistic limit data for the new armor is given by black dots. As in the previous analysis, a 0 corresponds to a stop and a 1 corresponding to a perforation. The solid blue line represents the best fit of the c-log-log model this data, and the dotted lines represent the upper and lower 95 % confidence intervals for the fit of the model. The estimated v_{50} is indicated by the vertical red line in the graph.

	Logit	Probit	C-log-log
V_{50} **(m/s)**	**509**	**509**	**513**
Upper 95 % CL on V_{50} (m/s)	525	525	527
Lower 95 % CL on V_{50} (m/s)	497	498	500
CI width (m/s)	28	27	28
Predicted probability at 436 m/s	**0.069745**	**0.055381**	**0.103460**
Upper 95 % CL at 436 m/s	0.181378	0.163059	0.214941
Lower 95 % CL at 436 m/s	0.024743	0.013636	0.048092
CI width	0.156636	0.149423	0.166848
V_{05} **(m/s)**	**426**	**434**	**405**
Upper 95 % CL on V_{05} (m/s)	450	455	437
Lower 95 % CL on V_{05} (m/s)	365	386	326
CI width (m/s)	86	69	111

Table A.6: Summary of estimates for a new hybrid body armor.

Table A.6.

While the estimates of parameters differ in size due to different scaling of the normal and logistic distributions, the estimated V_{50} values predicted by all three models are very similar (Figure A.15). The calculation of the error bars of the V_{50} estimates are based on the Fieller's theorem [220].

However, the probabilities of perforation at the NIJ reference velocity (436 m/s) predicted by the three different models are very different (Figure A.16). Note that the estimates shown in Figure A.16 are different and that the error bars (indicating the range of the estimate), calculated using the Wald test [223, 242], are large. This means that, when the error of the estimate is taken into account, all three estimates are probably within the same range. This phenomenon is attributed to the large ZMR for this sample.

Analysis with the c-log-log asymmetric model indicated that the probability of perforation at the NIJ reference velocity was approximately 10 % for this armor.
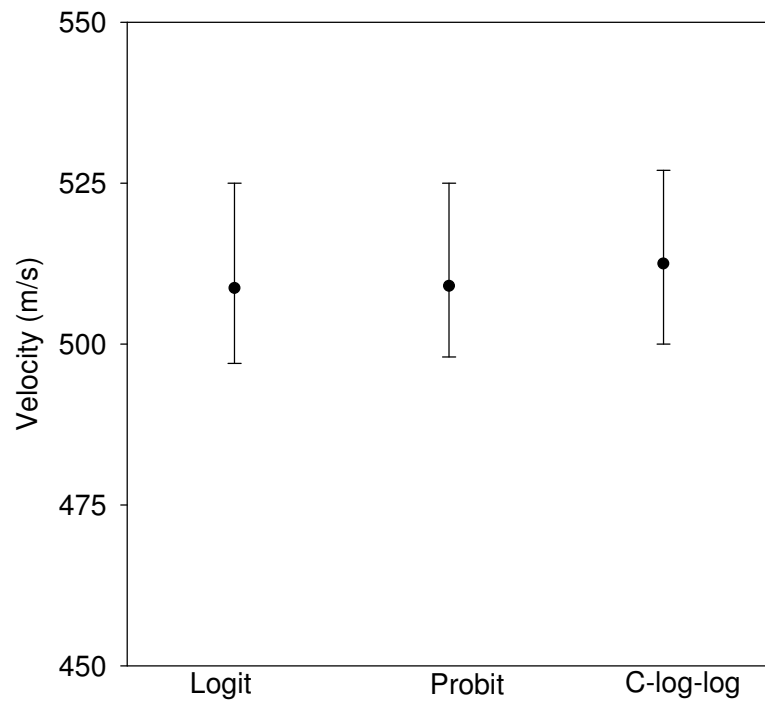
Figure A.15: Estimates of V_{50} using the three different models. Note that the estimates are similar. The large error bars are attributed to the inherent variability of ballistic testing, which requires very large sample sizes for increased confidence. This is impractical due to the time and expense of ballistic limit testing.
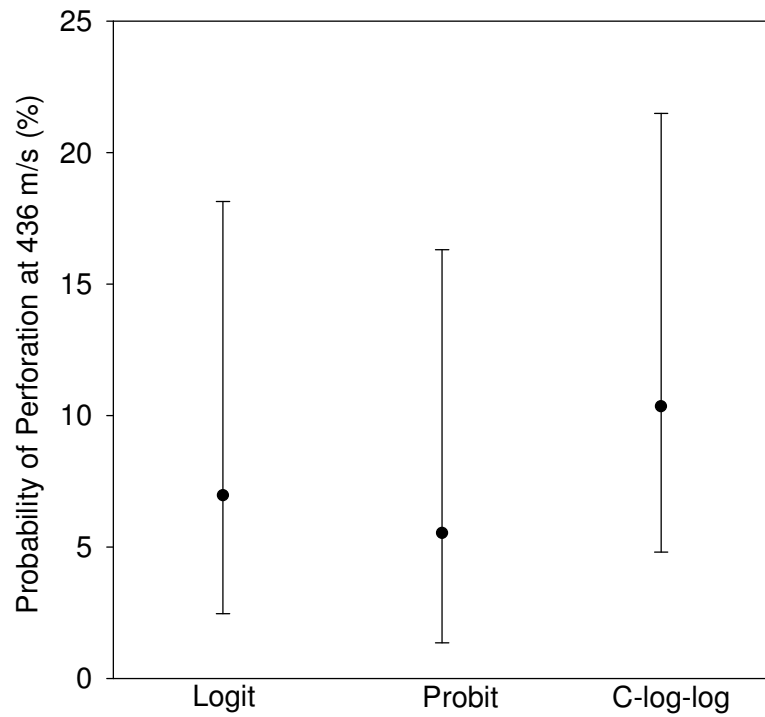
Figure A.16: Estimates of probability of perforation at the NIJ reference velocity (436 m/s). The large error bars are attributed to the inherent variability of ballistic testing, which requires very large sample sizes for increased confidence. This is impractical due to the time and expense of ballistic limit testing.

	Logit	Probit	C-log-log
AIC	139.61	**139.15**	141.06
Misclassified Data (%)	**30.0**	30.8	32.5
Error Rate by Cross-Validation (%)	31.7	31.7	31.7

Table A.7: Summary of selection criteria for a new hybrid body armor.

This is higher than the 7 % that was predicted by the logistical model used in the NIJ Standard–0101.06 ballistic limit calculation, and much higher than the 5.5 % that was predicted by the probit model.

Table A.7 shows the values of the different goodness-of-fit criteria for each model. As in the previous analysis, an assessment of how well the different link functions fit the data using the AIC does not indicate one GLM is a better fit than the others. While there is a slight preference for the probit model, the difference is not so large as to be significant. This same conclusion can be drawn from an analysis of the misclassification percentage or the average error rate as statistical measures for comparison. The values of these criteria are similar for all three GLMs, however, the c-log-log model has the worst criteria values, so perhaps either the logit or the probit models would be slightly preferred.

A.9.2 Examination of the Armor Data by Panel

A.9.2.1 Estimation of Individual Panel V_{50}s

In an effort to better understand the wide ZMR of this armor model, especially the large number of stops on one panel, the individual V_{50} of each armor panel was computed. The estimates were determined using the logistic model. It is important

Armor Panel	V_{50} (ft/s)	V_{50} (m/s)
A Front [*]	1583.56	482.7
A Back [*]	1584.04	482.8
B Front [*]	1577.24	480.7
B Back [**]	**1810.75**	**551.9**
C Front [**]	1689.61	515.0
C Back [**]	1689.21	514.9
D Front [**]	1614.10	492.0
D Back [**]	1708.64	520.8
E Front [**]	1646.14	501.7
E Back [**]	1681.76	512.6

[*] indicates test was conducted on Day 1.
[**]indicates test was performed on Day 2.

Table A.8: Logistic V_{50} estimates for each armor panel.

to note that due to the small number of shots on each armor panel, these individual V_{50} estimates are uncertain, but still useful for comparison purposes and for the detection of any anomalies in the armor testing.

From Table A.8, one can note that Panel B Back had a much higher V_{50} than any of the other panels tested. Additional analysis will further examine this observation.

A.9.2.2 Bullet Fragmentation Phenomenon

Another possible explanation for the high V_{50} for Panel B Back may be the unique combination of bullet and target leading to unusual bullet behavior. When this phenomenon occurs, the bullet behavior changes as a function of velocity. For example, at lower velocities, the bullet may deform in a predictable manner as we typically see in armor testing; while at higher velocities, the bullet may fragment

upon impact before significant deformation, or perhaps components of the bullet may not remain intact [246, 247]. Because the bullet behavior is different, its penetrative characteristics may be different. This behavior is more typically encountered when testing hard plate armors, but may be possible to encounter when testing at high bullet velocities. Due to the two different competing mechanisms that dominate penetration mechanics, bullet fragmentation effectively leads to more than one ballistic penetration curve for a particular armor-bullet system. In one case, bullet properties dominate (when the bullet breaks up instead of deforming); in another, armor properties dominate (typical armor testing). The armor community typically focuses on finding the lowest V_{50} of the armor system, since that is the one of most practical importance to the person wearing the armor, which is what the test methods in NIJ Standard–0101.06 are intended to do. Note that very high velocities resulted in *stops*, leading one to suspect that the bullets may either fracturing or losing their copper jackets at these very high velocities. To examine this possibility, the armor panel was de-constructed, and bullets were recovered from the armor and examined. These bullets (Figures A.17 and A.18) show evidence of bullet failure due to bullet fragmentation. Therefore, additional analysis was performed to examine the effect of this panel on the large ZMR and the outcome of this analysis is the subject of the next section.

Figure A.17: Photograph of de-constructed armor with shattered bullet inside.

Figure A.18: Photograph of shattered bullet removed from armor.

	Logit	Probit	C-log-log
V_{50} **(m/s)**	**502**	**502**	**505**
Upper 95 % CL on V_{50} (m/s)	514	514	516
Lower 95 % CL on V_{50} (m/s)	492	493	494
CI width (m/s)	22	21	22
Predicted probability at 436 m/s	**0.042333**	**0.029177**	**0.073777**
Upper 95 % CL at 436 m/s	0.143464	0.124872	0.182044
Lower 95 % CL at 436 m/s	0.011532	0.004206	0.028807
CI width	0.131932	0.120666	0.153237
V_{05} **(m/s)**	**440**	**445**	**423**
Upper 95 % CL on V_{05} (m/s)	458	461	448
Lower 95 % CL on V_{05} (m/s)	393	408	363
CI width (m/s)	65	54	85

Table A.9: Results of analysis with all three models, excluding Panel B Back.

A.10 Effect of Alternative Data Sampling

A.10.1 Effect of Panel B Back

Since it was confirmed that Panel B Back exhibited anomalous behavior during the test series, the analysis was repeated, excluding the data from Panel B to determine the effect of this panel on the outcome of the analysis. These data are summarized in Table A.9.

Removing this panel does affect the outcome of this analysis. The logit predicts a 4.23 % probability of perforation at the NIJ reference velocity and the probit predicts a 2.92 % probability of perforation. Both of these results would meet the criteria required by the NIJ standard. The c-log-log model predicts a 7.38 % probability of perforation, but there is no information to indicate that this armor model is best described by an asymmetric distribution.

	Logit	Probit	C-log-log
V_{50} **(m/s)**	**502**	**502**	**504**
Upper 95 % CL on V_{50} (m/s)	515	515	515
Lower 95 % CL on V_{50} (m/s)	493	493	495
CI width (m/s)	22	21	20
Predicted probability at 436 m/s	**0.035811**	**0.022165**	**0.053903**
Upper 95 % CL at 436 m/s	0.132794	0.111885	0.152016
Lower 95 % CL at 436 m/s	0.008928	0.002513	0.018448
CI width	0.123867	0.109372	0.133568
V_{05} **(m/s)**	**443**	**448**	**434**
Upper 95 % CL on V_{05} (m/s)	461	463	455
Lower 95 % CL on V_{05} (m/s)	397	412	381
CI width (m/s)	64	51	74

Table A.10: Results of analysis with all three models, excluding shots above 541 m/s.

A.10.2 Effect of Shots with Velocities above 541 m/s

All shots above 541 m/s (1775 ft/s) were arbitrarily excluded (resulting in the exclusion of 13 data points) and the analysis was repeated (Table A.10).

The examination of the armor, which indicated that the bullet behavior may have changed dramatically as a function of velocity (due to bullet fragmentation) can be used to justify this approach. Again, the logistic regression analysis indicated that the probability of perforation at the NIJ reference velocity is less than 5 %. The logit predicts a 3.58 % probability of perforation at the NIJ reference velocity and the probit predicts a 2.22 % probability of perforation. The c-log-log model predicts a 5.39 % probability of perforation, but again, there is no information to indicate that this armor model is best described by an asymmetric distribution.

A.11   Summary

This work shows that the choice of link function, between the logit, the probit and the complementary log-log link functions, is not the most important issue in V_{50} ballistic limit performance estimation, since the different GLMs examined all gave similar results. The three regression models have been applied to the ballistic data and then evaluated, but none of them distinguished itself from the others in terms of armor performance estimation. Findings indicate that for all the ballistic data studied, all three link functions behave similarly, even if the model selection criteria prefer a particular regression model. The diverse criteria calculated for all three models were of the same magnitude; therefore, even if one model has a lower value for a criterion, the two other models' criterion values are close. Overall, it can be concluded that for the ballistic data sets examined herein, the logit and probit link functions performed well and seemed to give more accurate estimation of the ballistic performances than the c-log-log function.

The primary objective of this study was to analyze the three regression models to determine which model produces a good estimate of the performance of a body armor model, and to understand how an armor model's performance changes with environmental conditioning. Slight preference can be assigned to the probit and logistic models for new armor, because they gave consistently good results. The comparison of V_{50} ballistic performance results of new and environmentally conditioned armors shows that in general the armor's model performance decreases as it is conditioned. Moreover, all three regression models are appropriate distribution

models for both new and aged armor samples. If an initial distribution model is deemed appropriate for new armor, it will continue to describe well the armor as it ages.

The second objective of this study was to examine the usefulness of applying different models to ballistic limit data analysis of a new armor with ballistic limit test results that may indicate that the logistic model is not the appropriate model for this armor. The detailed analysis of V_{50} data from a new hybrid armor, to examine the effect of symmetric and asymmetric regression models (logit, probit, c-log-log) on the predicted performance of the armor at the NIJ reference velocity, showed no effect on the test outcome. Furthermore, there is no evidence to indicate that this armor model is better described by an asymmetric regression model than a symmetric one. However, in the course of completing this analysis, one panel, Armor Panel B back, appeared to have a high number of high velocity stops. Possible explanations of this observation were discussed, including a bullet fragmentation phenomenon, or test anomalies occurring during the test in the laboratory. The high velocity stops observed on this panel contribute to a wide ZMR in the ballistic limit calculations, causing the probability of perforation at the NIJ reference velocity to be higher than the acceptable (5 %) criteria. In an effort to better understand the effect of this panel on the test outcome, analysis was repeated with all three models in two different ways: excluding Panel B back from the calculation, and excluding shots above 541 m/s from the calculation. However, the exclusion of either data set is justifiable only if it can be shown that the tests or test conditions were different from what is specified in the NIJ standard.

A.12 Link to Mechanical Properties

A.12.1 Overview

Mechanical and ballistic property data were collected from PBO and PPTA armor panels of the same model during the conditioning protocol development described in Chapter 1. These data are leveraged here to investigate the relationship between mechanical properties, specifically load at break, and the ballistic property of V_{50}. The relationship will be investigated separately for each armor material: PBO and PPTA.

A.12.2 Sample description

The laboratory aging study took place over several phases, as previously described. The data included in this study are from Phases III and IV, plus a 3rd study, phase V. In each phase a group of armor panels were exposed to various accelerated aging conditions. As previously discussed, these conditions were not all the same across all groups of armor panels. After a period of time the mechanical properties of the group were tested by extracting yarns from several panels and subjecting them to relevant test protocols, including tensile testing. If the observed mechanical property values had dropped below a target value, then the study was deemed to have reached its conclusion, and V_{50} testing was performed. To investigate the relation between mechanical properties and V_{50} values, it is most simple to examine data pairs of tensile strength and V_{50}. To accomplish this, lots have been defined as described in Table A.11 for which tensile strength and V_{50} values pairs

will be developed.

A.12.3   Analytical Approach

A.12.3.1   Overview

A simulation approach will be taken in this analysis. A population of tensile strength and V_{50} data pairs will be developed using the data from to each defined lot. From each lot's tensile strength and V_{50} data pair population, a data pair will be randomly selected. A linear regression model will be developed for this data pair relating the independent variable, tensile strength to the dependent variable, V_{50}. This process will be repeated numerous times. The resulting distribution of the slope parameter, β_1 from the numerous regression models will be explored. A β_1 distribution that largely encompasses the value of zero will indicate that no relation between the variables exists.

A.12.3.2   Data Pair Development

For any given vest panel in the study there only exists either material property data or V_{50} data, since both tests are destructive. To study the relationship between material properties and V_{50} values, data pairs of tensile strength and V_{50} are needed. Therefore, an assumption must be made that each lot of panels as defined above form a homogeneous population, even though they came from different actual physical samples. Thus, a load value sampled from within a lot may be paired with a V_{50} value sampled from within the same lot. A method to developing populations of

Lot Designation	Armor Material	Source	Aging Condition	Conditioning Duration (days)
A1	PPTA	New Armor	none	0
A2	PPTA	Phase 3	tumble	13
A3	PPTA	Phase 3	all	13
A4	PPTA	Phase 4	all	10
A5	PPTA	Phase 5	all	10
B1	PBO	New Armor	none	0
B2	PBO	Phase 3	tumble	13
B3	PBO	Phase 4	all	10
B4	PBO	Phase 5	all	10

Table A.11: Lot designations for PBO and PPTA armors for the bootstrap simulations to evaluate links between tensile strength and ballistic limit.

data pairs is described below.

A.12.3.3 Lot Bootstrap

Within a lot, the population of data pairs will be developed by considering a complete exploration of the tensile strength data and the V_{50} data. For example, the A1 lot which consists of 72 tensile strength values and 4 V_{50} values, will result in a population of data pairs of all 72 x 4 = 288 possible combinations. A single point from each lot population of data pairs will be randomly selected to be included in the regression analysis.

A.12.4 Results and Discussion

The linear regression results for ten simulations for PPTA are shown in Figure A.19. Similar results for PBO are displayed in Figure A.20. This sampling and linear regression modeling procedure was repeated 10,000 times. Summary statis-
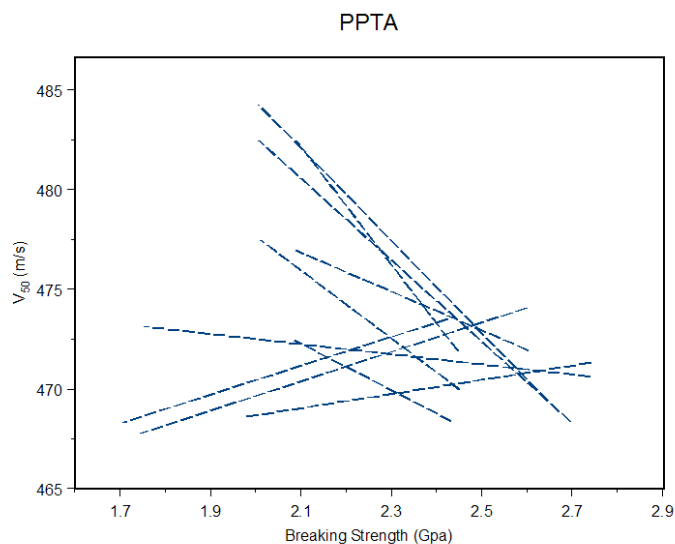
Figure A.19: Linear regression results of 10 bootstrap simulations for PPTA armors. Note that the lines have both positive and negative slopes.

tics for the resulting regression slope parameters are displayed in Table A.12. The distribution of the resulting regression slope parameters are displayed by means of a histogram in Figure A.21.

The reason for this effort was to examine the hypothesis that changes in the material properties of yarn extracted from body armor can indicate changes in the ballistic performance of that body armor. Thus, a body armor whose yarns become weaker might be expected to display a lessened ballistic resistance. If one assumes that the relationship between tensile strength and ballistic performance is positive (increased tensile strength relates to increased ballistic resistance), then the slope parameter from a linear regression model relating tensile strength to V_{50} is to be greater than zero.

Figure A.21 shows the distribution of 10,000 slope parameter resulting from the re-sampling efforts for PPTA and PBO body armor. The distribution of slope

283
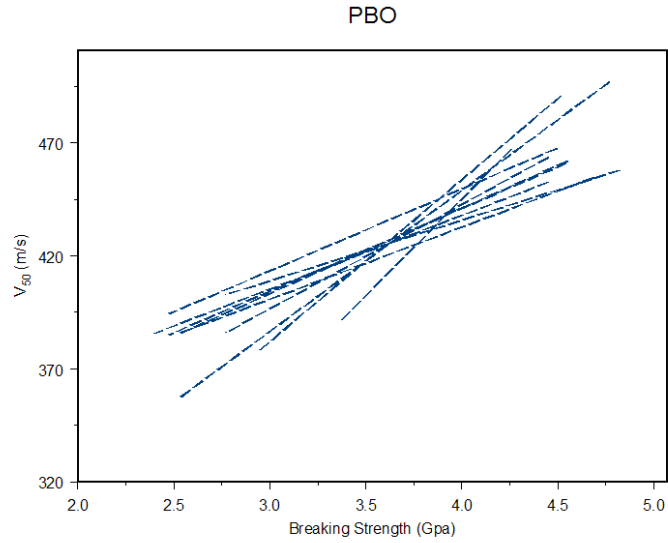
Figure A.20: Linear regression results of 10 bootstrap simulations for PBO armors. Note that the lines all have positive slopes.
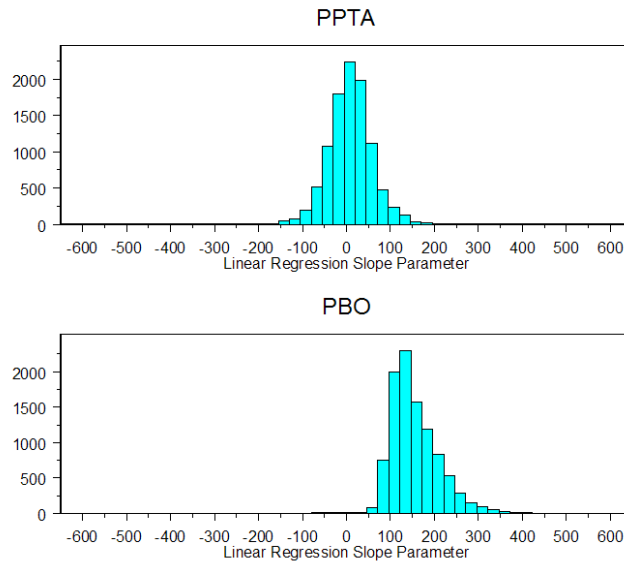
Figure A.21: A histogram depicting the results of 10,000 simulations of the linear regression slope parameters for PPTA and PBO body armors.

Armor Material	No. of Simulations	Average	Standard Deviation	2.5th Percentile	97.5th Percentile	No. of Simulations	No. of Simulations
PPTA	10,000	9.6	51.0	-87.9	115.8	4144	5856
PBO	10,000	152.2	69.2	75.2	286.7	99	9901

Table A.12: Simulation results for the linear regression slope parameter from bootstrap simulations to evaluate links between tensile strength and ballistic limit.

parameters from PPTA contains zero, while the distribution of slope parameters pertaining to PBO lies primarily to the right of zero. This observation indicates that the regression slope parameter for PPTA armor does not likely differ from zero, meaning there is neither a positive, nor a negative relationship between tensile strength and ballistic resistance. However, the regression slope parameter for PBO armor is likely greater than zero, indicating a positive relationship between tensile strength and ballistic resistance.

An examination of the confidence intervals association with the previous analysis further supports this conclusion. The 95 % bootstrap percentile confidence interval [ref] for the PPTA armor slope parameter is *(-120.5, 96.3)*, and for the PBO armor it is *(74.7, 354.7)* (see Table A.12), again indicating the slope parameter for PPTA does not differ from zero, and therefore no relationship exists between load and V_{50}, whereas this relationship is indicated to be positive for the PBO armor. This is further underscored by an examination of the regression lines from Figure A.20 and Figure A.21. The ten sample regression lines for PBO are rather clustered and show a positive slope. The ten regression lines for PPTA are very sporadic with both positive and negative slopes. It was also noted that the range

of tensile strength values is much greater for the PBO samples as opposed to the PPTA samples. This point was further investigated in the next section.

A.12.4.1   Material Properties of Used PPTA Body Armor

From previous work, it was known that the targeted reduction in tensile strength for PBO was based upon the reduction in tensile strength that had been observed in PBO armor that had failed in the field. However, it was not known if the strengths for the PPTA body armor were realistic for field-worn armors. An existing data set was used to answer this question. Measurements of extracted yarn tensile strength that were collected in conjunction with the efforts of the Canadian government to examine used body armor were utilized in this investigation of the tensile strengths seen in PPTA-based body armor to determine if they were reasonable. This Canadian effort examined surplus armor that had been worn in the field, removed from service, and placed in storage.

Forty-one armor panels of interest from the Canadian work were subject to material properties testing. These armor panels were all manufactured by the same parent company and were comprised entirely of PPTA yarns. The manufacturing date of the panels span the ten year time period: October 1992 - October 2002. Approximately 14 yarns were extracted from each armor panel and subjected to material properties testing. A summary of the tensile results obtained are displayed in Table A.13. A histogram of the observed tensile strength of these 577 total samples is displayed in Figure A.22.

No. of Samples	Minimum	Average	Maximum	Standard Deviation
577	2.148	2.841	3.435	0.234

Table A.13: Tensile strength results for PPTA yarns extracted from field-worn armors.
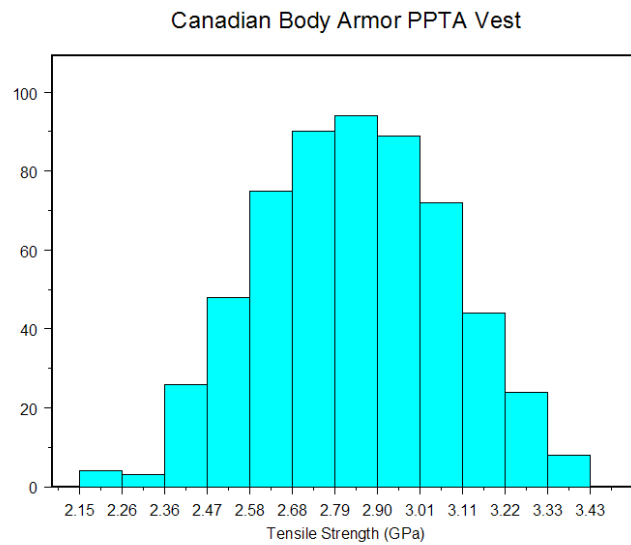
Figure A.22: A histogram depicting the tensile strength results for field-worn Canadian PPTA body armors.

While this data is limited to PPTA armor from one manufacturer during the time period: October 1992 - October 2002, it indicates that the tensile strength of the extracted PPTA yarns found in such used vests is normally centered around 2.84 GPa. Furthermore, no sample was seen to display a tensile strength lower than 2.14 GPa. Thus, the analysis of the relationship between mechanical properties and V_{50} values, which examined vests made of PPTA with tensile strengths ranging from 1.706 GPa to 2.918 GPa adequately captures the lower tail of this distribution. And hence, the results of the investigation between tensile strength and V_{50} may be considered applicable to used armor found in service.

In a similar effort, data from field-worn PBO body armor was also examined to ensure that the reduction in tensile strength targeted by the conditioning protocol development was reasonable and had been observed in other fielded armors. This data was collected in 2004 and 2005 and was not as readily processed as the newer data examined for PPTA armors. Therefore, only the average tensile strength, comprised of the breaking strengths of at least 10 different yarns extracted from each armor was used to prepare the histogram in Figure A.23. The armor in this population represented a wide variety of different models, ages, manufacturers, and protection levels. The average tensile strength of extracted PBO yarns is normally distributed around 2.64 GPa, with average extracted yarn tensile strengths from each armor ranging from 1.41 to 3.93 GPa. The conditioned PBO armor samples used in this analysis had average extracted yarn tensile strengths ranging from 2.33 GPa to 2.94 GPa, which are reasonable when compared to field worn PBO-containing armor.

Fielded PBO Body Armor
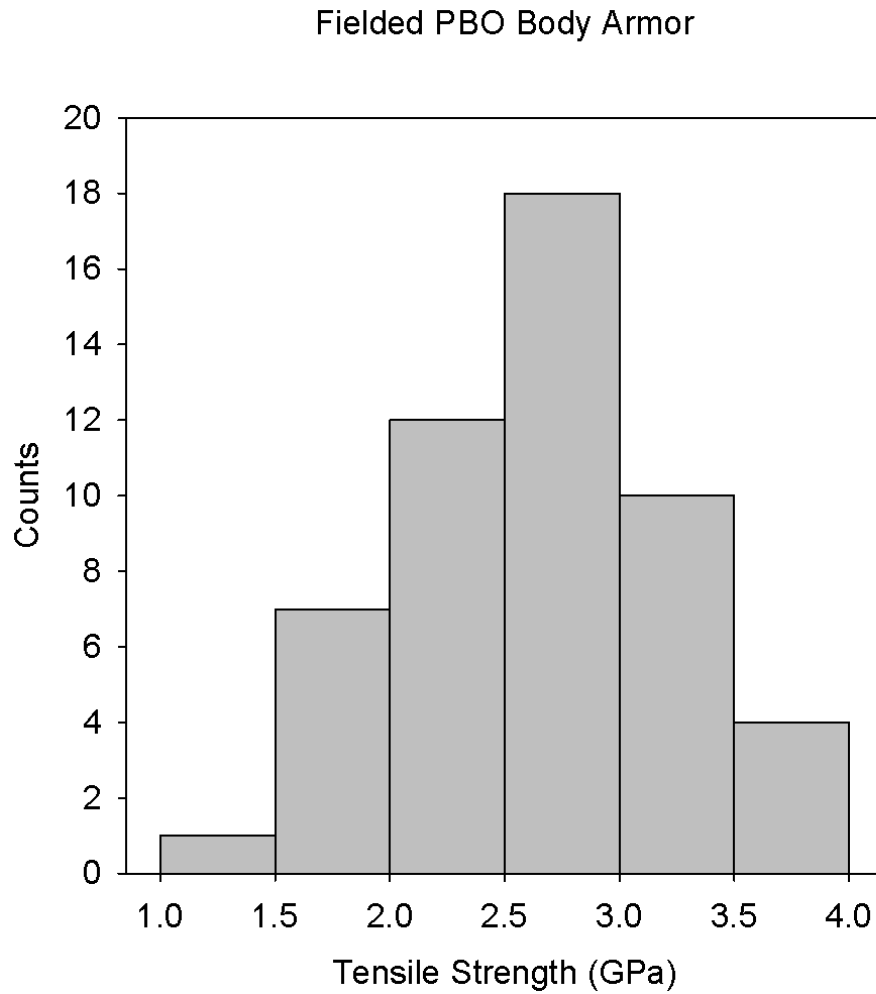
Figure A.23: A histogram depicting the average tensile strength results for field-worn PBO body armors from a previous study conducted in 2004-2005. The body armor from this study was gathered from different areas of the country, and represents different models, different ages, and different wear conditions. Thus, it should be fairly representative of the distribution of tensile strengths of PBO yarns in fielded body armor from this time.

A.13 The Dimensional Ratio for the Estimation of Ballistic Performance, U*

In addition to the analysis presented here, there are other methodologies for considering the influence of mechanical properties on ballistic performance. One such approach was outlined in a landmark paper by Cuniff in 1999 [248]. In this paper, Cuniff introduces the concept of the dimensionless parameter in the optimization of textile-based body armor systems. The objective of his analysis is to relate the system and projectile characteristics to the ballistic limit of a model armor system with a specific areal density. The physical quantities for this system are shown in Equation A.2, adapted from [248],

$$\Phi \left(\frac{\sigma \varepsilon}{2 \rho}, \sqrt{\frac{E}{\rho}}, \frac{A_p}{m_p}, v_{50}, A_d \right) \tag{A.2}$$

in which σ is the fiber ultimate tensile strength, ε is the fiber ultimate tensile strain, ρ is the fiber density, E is the fiber modulus (all fibers are assumed to be linearly elastic), A_p is the projectile presented area (relative to the fiber), m_p is the projectile mass, V_{50} is the ballistic limit, and A_d is the system areal density, or mass per unit area [248].

The dimensional ratios for the system presented in Equation A.2 are presented in Equation A.3 below, adapted from [248]:

$$\Phi \left(\frac{v_{50}}{U^{*\frac{1}{3}}}, \frac{A_d A_p}{m_p} \right) \tag{A.3}$$

Where U* is given in Equation A.4 below as the product of fiber specific

toughness and strain wave velocity, adapted from [248].

$$U^* = \frac{\sigma \varepsilon}{2\rho} \sqrt{\frac{E}{\rho}} \tag{A.4}$$

U^* has been used since its inception to estimate the theoretical effect of improvements in fiber properties on ballistic performance, but it does have some limitations that are not always well-appreciated, for example, it assumes that all projectiles are nondeforming fragment simulators, however most armor is designed to be used against deforming projectiles with lead cores, adapted from [248]. Several other researchers have extended this idea to develop complex, multilayer textile armor computational models [249, 250, 251]. These models will not be discussed further in this work.

A.13.1 Application of U* to environmentally conditioned armor analysis

One might surmise that the concept of U* might be a useful tool in predicting the general effect of a change in quasi-static fiber properties on the ballistic performance of an armor system. It could help determine when a change in the material properties measured from an armor sample might translate into a loss in performance in the case of field and artificial degradation studies, or an increase in performance in the case of new fibers or improved fibers.

Sometimes, only very limited data or samples are available from a fielded or laboratory-aged armor, and it is not practical to conduct extensive V_{50} testing.

In order to develop a V_{50} with reasonable confidence, multiple panels should be tested, but large sample sizes might not be available. Additionally, the idea of incorporating coupon samples that could be routinely tested in an armor package has been proposed.

The data sets presented herein are quite limited and are insufficient to make confident statements about theoretical V_{50}. However, one can make a relative comparison of V_{50} retention and how it relates to tensile strength. Data sets from two phases of the conditioning protocol development were examined to compare measured and theoretical V_{50} retention with tensile strength retention for PBO and PPTA body armor. Figure A.24 and Figure A.25 show tensile strength retention, U* retention, and measured V_{50} retention for conditioned PPTA samples. The armor in Figure A.24 was conditioned at 70 °C and 90 % RH while being tumbled for 10 days, and the armor in Figure A.25 was conditioned at 65 °C and 80 % RH while being tumbled for 10 days.

Yarns extracted from the PPTA armor exposed at 70 °C and 90 % RH had an average initial tensile strength of approximately 2.54 GPa, which dropped to 1.97 GPa after 10 days of exposure and tumbling, and the armor exposed to 65 °C and 80 % RH while being tumbled had an initial tensile strength of approximately 2.78 GPa which dropped to approximately 2.36 GPa after 10 days of exposure. In both cases, the actual measured V_{50} of the PPTA armor was relatively unchanged by the conditioning protocol. The predicted V_{50}, U*, did show a theoretical decline of approximately 16 % for 10 days of the 70 °C and 90 % RH while tumbling exposure, and a thoeretical decline of approximately 9 % for 10 days of the 65 °C and 80
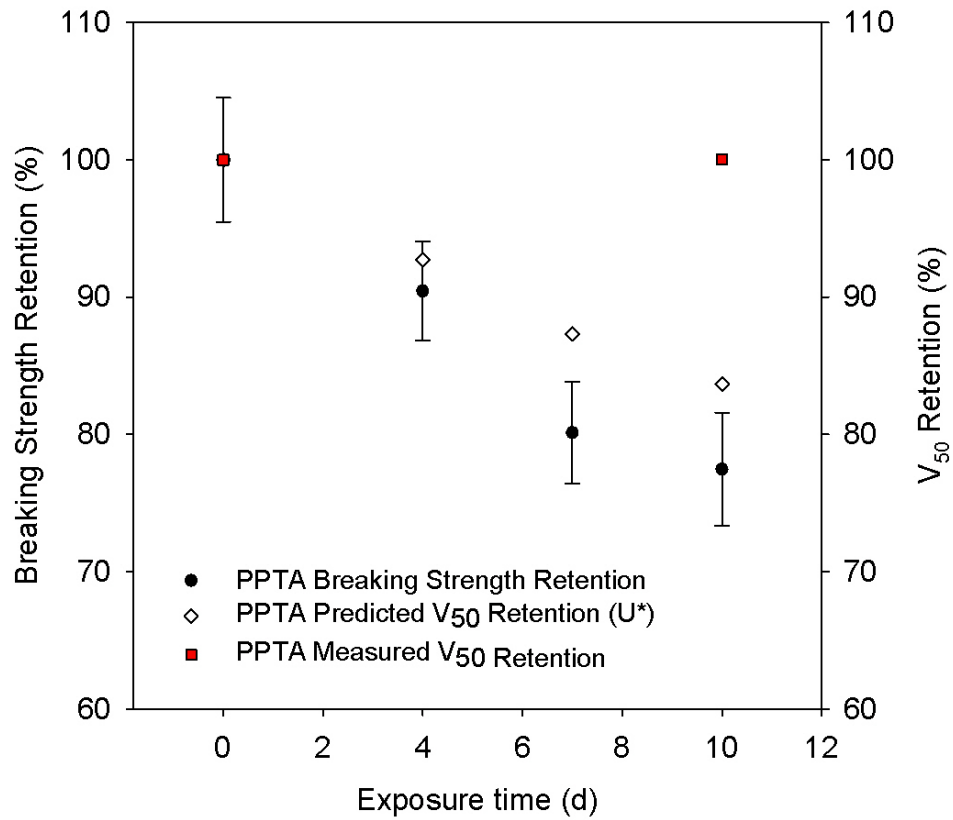
Figure A.24: Tensile strength retention, U* retention, and actual V_{50} retention for PPTA armor conditioned at 70 °C and 90 % RH while being tumbled for 10 days. Note that the actual V_{50} retention was essentially unchanged, while U* retention did predict a change in V_{50} to correspond with the change in tensile strength.
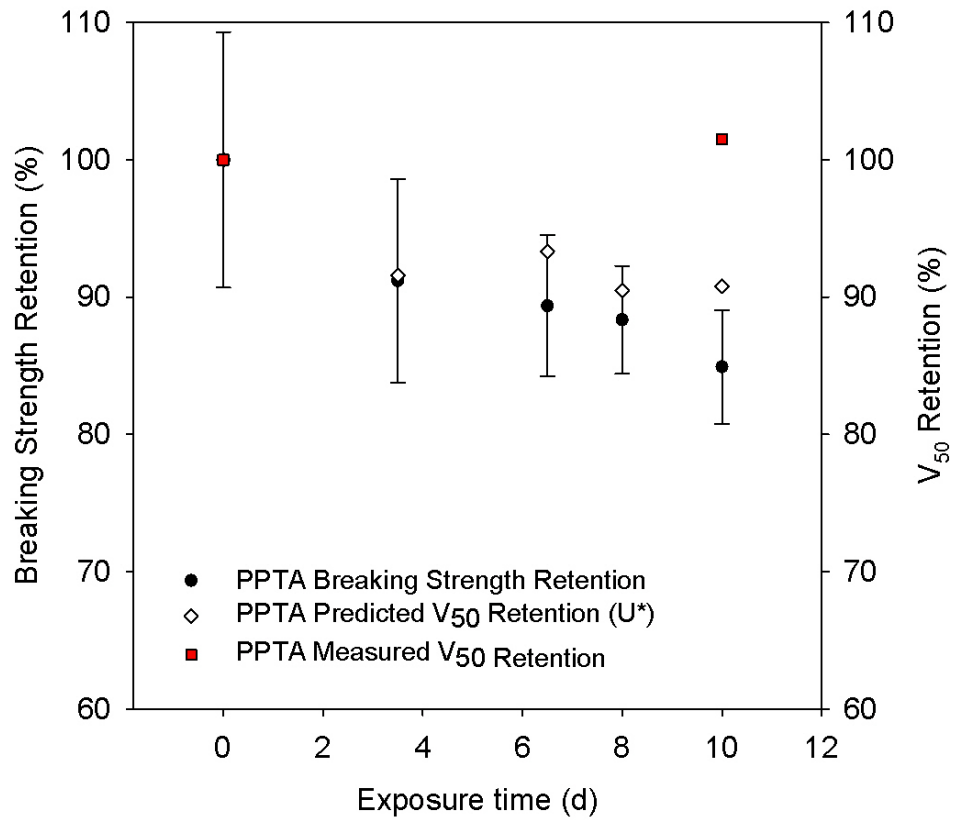
Figure A.25: Tensile strength retention, U* retention, and actual V_{50} retention for PPTA armor conditioned at 65 °C and 80 % RH while being tumbled for 10 days. Note that the actual V_{50} retention was essentially unchanged, while U* retention did predict a change in V_{50} to correspond with the change in tensile strength.

% RH while tumbling exposure. It is interesting to note that the predicted V_{50}, U*, consistently provides a conservative estimate of the V_{50} for the degraded PPTA system, and that it appears to be more sensitive to changes in tensile strength for this system. With the analysis of additional data sets, perhaps the predicted V_{50}, U*, could serve as a warning to indicate when a particular armor should be removed from service.

This same analysis was also applied to similar data sets for a PBO armor that is expected to exhibit a decline in V_{50} after conditioning. Figure A.26 and Figure A.27 show tensile strength retention, U* retention, and measured V_{50} retention for conditioned PBO samples. The armor in Figure A.26 was conditioned at 70 °C and 90 % RH while being tumbled for 10 days, and the armor in Figure A.27 was conditioned at 65 °C and 80 % RH while being tumbled for 10 days.

Yarns extracted from the PBO armor exposed at 70 °C and 90 % RH had an average initial tensile strength of approximately 4.47 GPa, which dropped to 2.72 GPa after 10 days of exposure and tumbling, and the armor exposed to 65 °C and 80 % RH while being tumbled had an initial tensile strength of approximately 3.72 GPa which dropped to approximately 2.94 GPa after 10 days of exposure. (These experiments were conducted with samples originally purchased in 2006, and the first study was performed in 2007, the second in 2011. It is possible that the material properties of the PBO in these samples changed during the four year lapse between the two experiments. The initial tensile strength was verified by additional tensile strength measurements to ensure that it was not an erroneous result.) In both cases, the actual measured V_{50} of the PBO armor was reduced by 15-18 % by
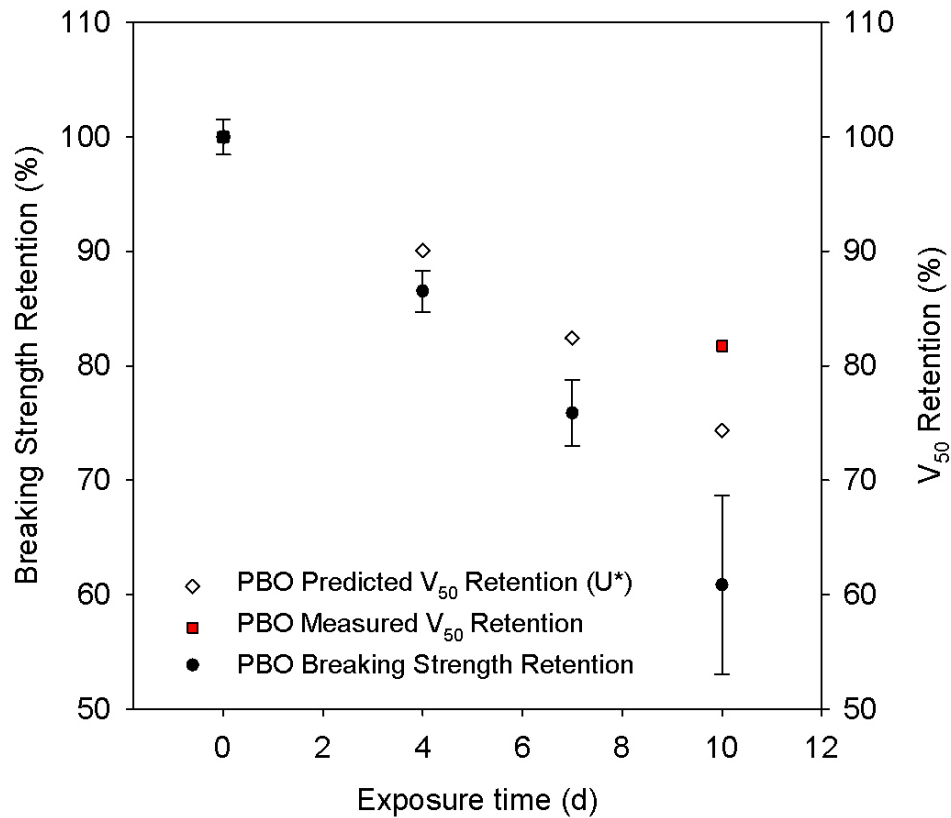
Figure A.26: Tensile strength retention, U* retention, and actual V_{50} retention for PBO armor conditioned at 70 °C and 90 % RH while being tumbled for 10 days. The actual V_{50} retention was reduced by the protocol, and U* retention did predict a change in V_{50} to correspond with the change in tensile strength, although U* prediction of V_{50} retention was greater than that actually measured.
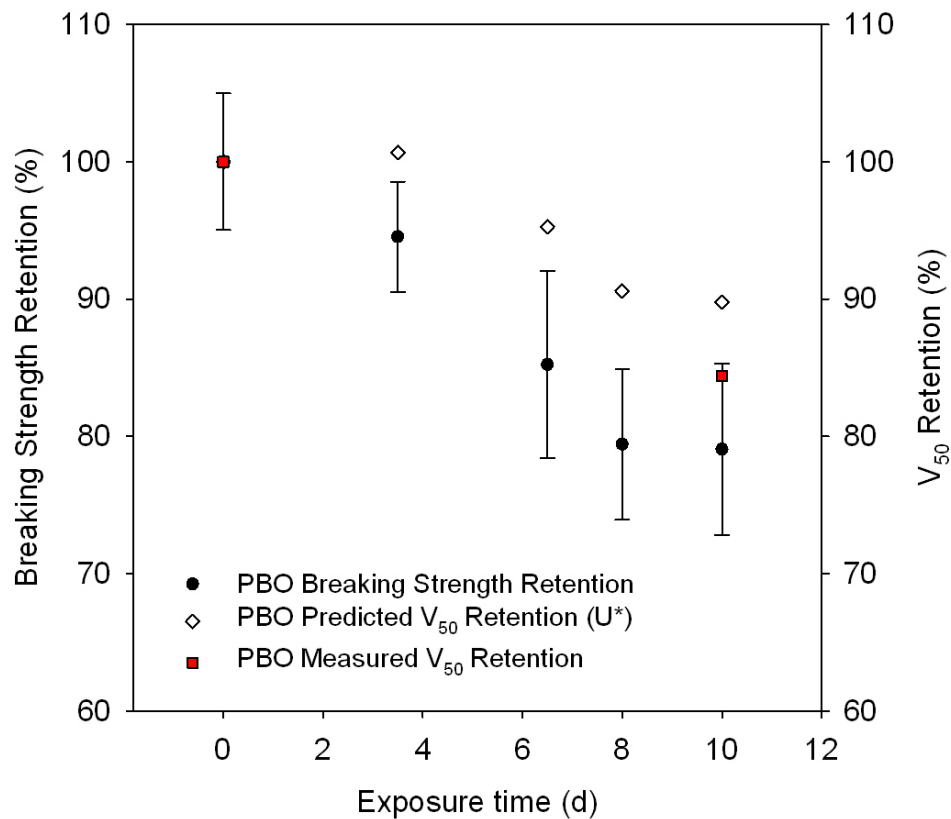
Figure A.27: Tensile strength retention, U* retention, and actual V_{50} retention for PBO armor conditioned at 65 °C and 80 % RH while being tumbled for 10 days. The actual V_{50} retention was reduced by approximately 15 % by the protocol, and U* predicted a thoeretical decline of approximately 10 % for 10 days of the 65 °C and 80 % RH while tumbling exposure. It is interesting to note that the predicted V_{50}, U*, provides a conservative estimate of the V_{50} for the PBO system exposed at 70 °C and 90 % RH while tumbling, and that it appears to underestimate the change V_{50} for the system exposed at 65 °C and 80 % RH while tumbling.

the conditioning protocol. The predicted V_{50}, U*, did show a theoretical decline of approximately 25 % for 10 days of the 70 °C and 90 % RH while tumbling exposure, and a thoeretical decline of approximately 10 % for 10 days of the 65 °C and 80 % RH while tumbling exposure. It is interesting to note that the predicted V_{50}, U*, provides a conservative estimate of the V_{50} for the PBO system exposed at 70 °C and 90 % RH while tumbling, and that it appears to underestimate the change V_{50} for the system exposed at 65 °C and 80 % RH while tumbling. The strain to failure in the samples conditioned and tested in 2011 was higher than in the samples conditioned and tested in 2007, which is responsible for the calculation of a higher predicted U* for these samples. This observation will be the subject of a future investigation.

A.14   Conclusions and Future Work

In conclusion, the first part of this study shows that there appears to be a relationship between changes in mechanical properties and changes in ballistic performance for PBO armor, but that there was not a relationship for PPTA armor. Although the decrease in material properties of the PBO vests were seen to have an impact on the ballistic performance, had the safety margin been larger (e.g. additional layers of material) when the vest was new, might this impact had not been observed? Similarly, while the relative decrease in material properties of PPTA is seen to be much less dramatic, had the original safety margin been less (e.g. fewer layers of material) perhaps an impact on ballistic performance would have been

observed. However it is possible that the backface signature requirement mandated by the NIJ Body Armor Standard does not allow for a PPTA vest to approach a safety margin that would provide such results. A future study involving simplified PPTA armors with a varying number of layers subjected to several aging conditions may address some of these questions.

In the second part of this study, the well known parameter of U* was also calculated to understand the theoretical change in ballistic performance of new and conditioned armor as compared to its actual change in ballistic performance. A puzzling result was found for one PBO sample, which had a lower actual than expected change in V_{50} as calculated by U*. Yarns extracted from armor that exhibited this result had a lower than expected initial tensile strength and a higher than expected conditioned strain to failure. For all other samples investigated, U* appeared to provide a conservative estimate of the change in ballistic performance, and might be a useful tool for fielded armor performance surveillance programs relying upon testing of armor coupon samples. Additional analysis of the armor with a lower than expected change in U* may provide for a better understanding of why this armor had a lower than expected initial tensile strength and a higher than expected strain to failure.

Appendix B

Supplementary Material

B.1   Specifications for the tumbler used in many aging experiments.

In the course of the development of the conditioning protocol for NIJ Standard–0101.06, significant exploration of existing methods of performing accelerated wear testing were examined, however, no commercial apparatus met all of the criteria necessary for this test. Therefore, a tumbling apparatus was designed with some assistance from DuPont at NIST. This device is now specified in NIJ Standard–0101.06 and has also been adopted by the US Army for some of their armor procurement acceptance criteria.

The tumbler is depicted in the two engineering drawings immediately following this section.

Sheets in Drawing	
SHEET #	SHEET TITLE
I	TITLE SHEET
2	NOTES AND COMMENTS
	3D VIEWS OF ASSEMBLED TUMBLER
3	3D VIEW: FRONT AND RIGHT SIDE
4	3D VIEW: FRONT AND LEFT SIDE
5	3D VIEW: REAR AND RIGHT SIDE
6	3D VIEW: REAR AND LEFT SIDE
	SUPPORT FRAME BASE
7	3D VIEW OF SUPPORT FRAME BASE
8	TOP VIEW OF SUPPORT FRAME BASE
9	BOTTOM VIEW OF SUPPORT FRAME BASE
I0	SIDE VIEW OF SUPPORT FRAME BASE
	SUPPORT FRAME TOP
II	3D VIEW OF SUPPORT FRAME TOP
I2	TOP VIEW OF SUPPORT FRAME TOP
I3	BOTTOM VIEW OF SUPPORT FRAME TOP
I4	SIDE VIEW OF SUPPORT FRAME TOP
	SUPPORT FRAME SIDES
I5	FRONT VIEW OF SUPPORT FRAME SIDES
I6	RIGHT SIDE VIEW OF SUPPORT FRAME SIDES
I7	LEFT SIDE VIEW OF SUPPORT FRAME SIDES
I8	BACK VIEW OF SUPPORT FRAME SIDES
	REAR DRUM SUPPORT ASSEMBLY
I9	3D VIEW OF REAR DRUM SUPPORT ASSEMBLY
20	FRONT VIEW OF REAR DRUM SUPPORT ASSEMBLY
2I	SIDE VIEW OF REAR DRUM SUPPORT ASSEMBLY
22	TOP VIEW OF REAR DRUM SUPPORT ASSEMBLY
	MOTOR SUPPORT ASSEMBLY & MOTOR DIMENSIONS
23	3D VIEW OF MOTOR SUPPORT ASSEMBLY
24	TOP VIEW OF MOTOR SUPPORT ASSEMBLY
25	SIDE VIEW OF MOTOR SUPPORT ASSEMBLY
26	TOP VIEW OF MOTOR
27	END VIEW OF MOTOR
	FORWARD DRUM SUPPORT ASSEMBLY
28	3D VIEW OF FORWARD DRUM SUPPORT AND BASE
29	TOP VIEW OF FORWARD DRUM SUPPORT AND BASE
30	FRONT VIEW OF FORWARD DRUM SUPPORT
	DRUM, DRIVE ASSEMBLY, AND MOTOR
3I	3D VIEW OF DRUM, DRIVE ASSEMBLY, AND MOTOR
32	REAR VIEW OF DRUM, DRIVE ASSEMBLY, & MOTOR
33	TOP VIEW OF DRUM AND SHAFT
34	FRONT VIEW OF DRUM
	DRUM DOOR ASSEMBLY
35	3D VIEW OF DRUM DOOR WITH SUPPORT FRAME
36	FRONT VIEW OF DOOR ASSEMBLY
37	REAR VIEW OF DOOR ASSEMBLY
	ADDITIONAL INFORMATION
38	BILL OF MATERIALS - PART I OF 2
39	BILL OF MATERIALS - PART 2 OF 2

Revisions		
REV	DESCRIPTION	DATE
0.I	DRAFT FOR REVIEW AND PROTOTYPE CONSTRUCTION	2007-08-20
0.2	DRAFT BASED ON REVISED DIMENSIONS	2007-09-04
I.0	AS BUILT AT NIST/OLES WITH REVISED DRIVE PULLEY	2007-I2-II
I.I	AS MODIFIED WITH DRUM REINFORCEMENT AND REVISED CASTERS	2008-08-I5
I.2	ADDED LETTER SIZED SHEETS AND NOTES & COMMENTS. REVISED THE BOM.	2008-08-27

NIST
National Institute of
Standards and Technology
U.S. Department of Commerce

Office of Law Enforcement Standards

ENVIROMENTAL CONDITIONING TUMBLER - REFERENCE DESIGN

TITLE SHEET

SIZE	LETTER (8.5" X II")	DWG NO.	OLES-ECTUMBLER	REV	I.2
SCALE	NOT TO SCALE	DRAWN BY	M. A. RILEY	SHEET	I OF 39

Figure B.1: Schematic of NIJ Standard–0101.06 tumbling apparatus designed at NIST.

Figure B.2: Schematic of NIJ Standard–0101.06 tumbling apparatus designed at

NIST.

B.2   Ziegler-catalyzed polymerization of polyethylene, for reference.
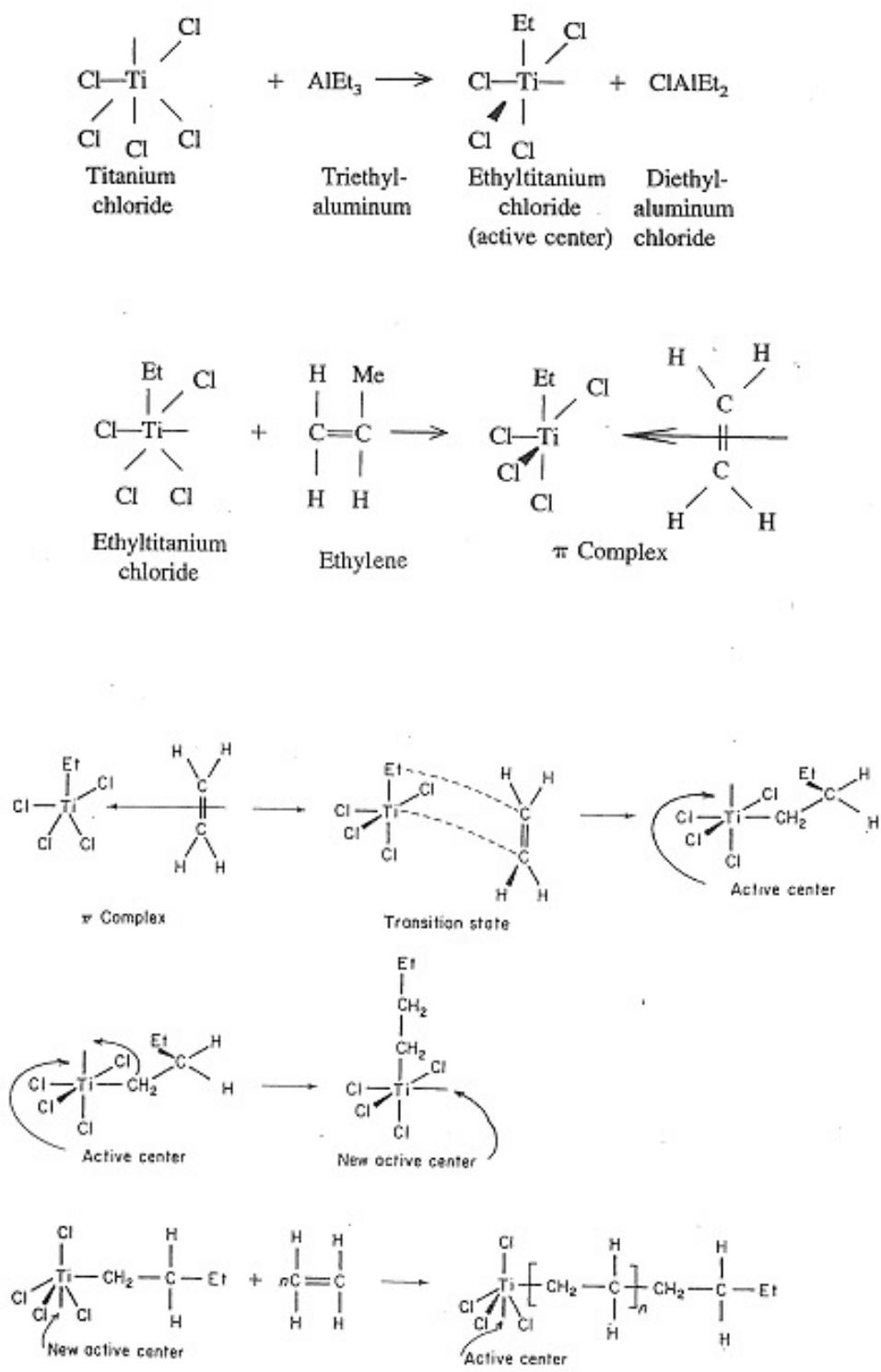
Figure B.3: Ziegler catalyzed polymerization of polyethylene.

304

B.3 FTIR spectra for aged polyethylene.
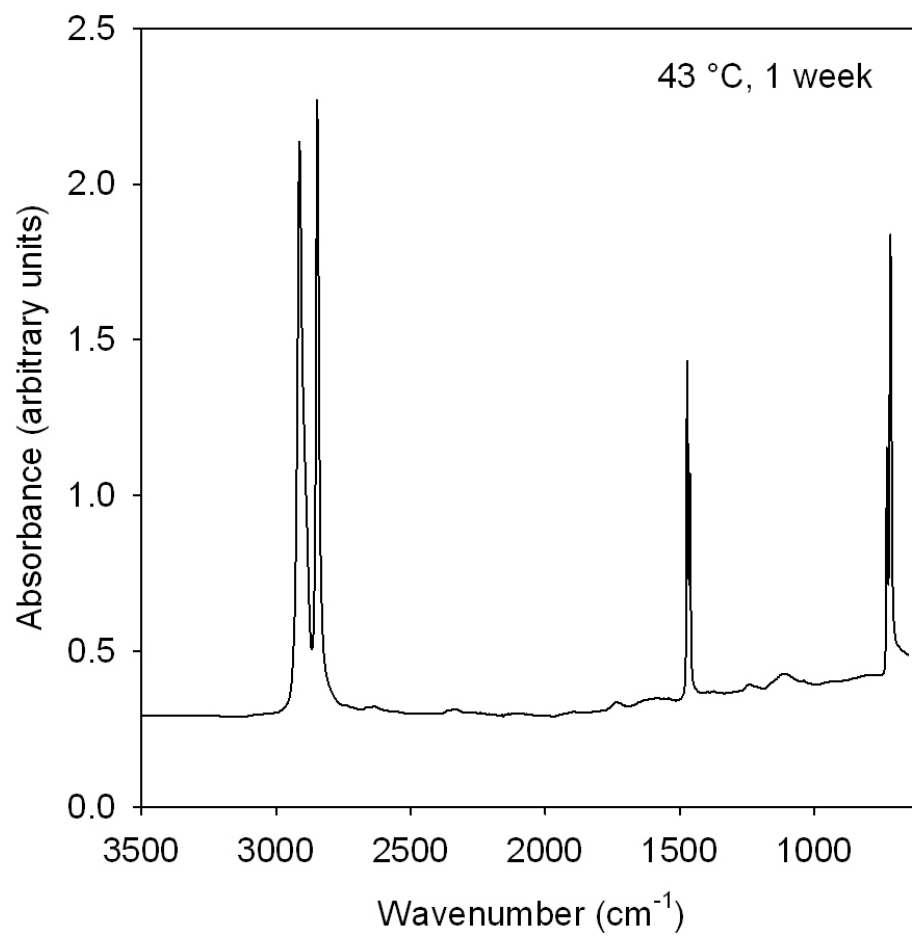
Figure B.4: FTIR Spectrum of UHMWPE fiber aged at 43 °C for 1 week.
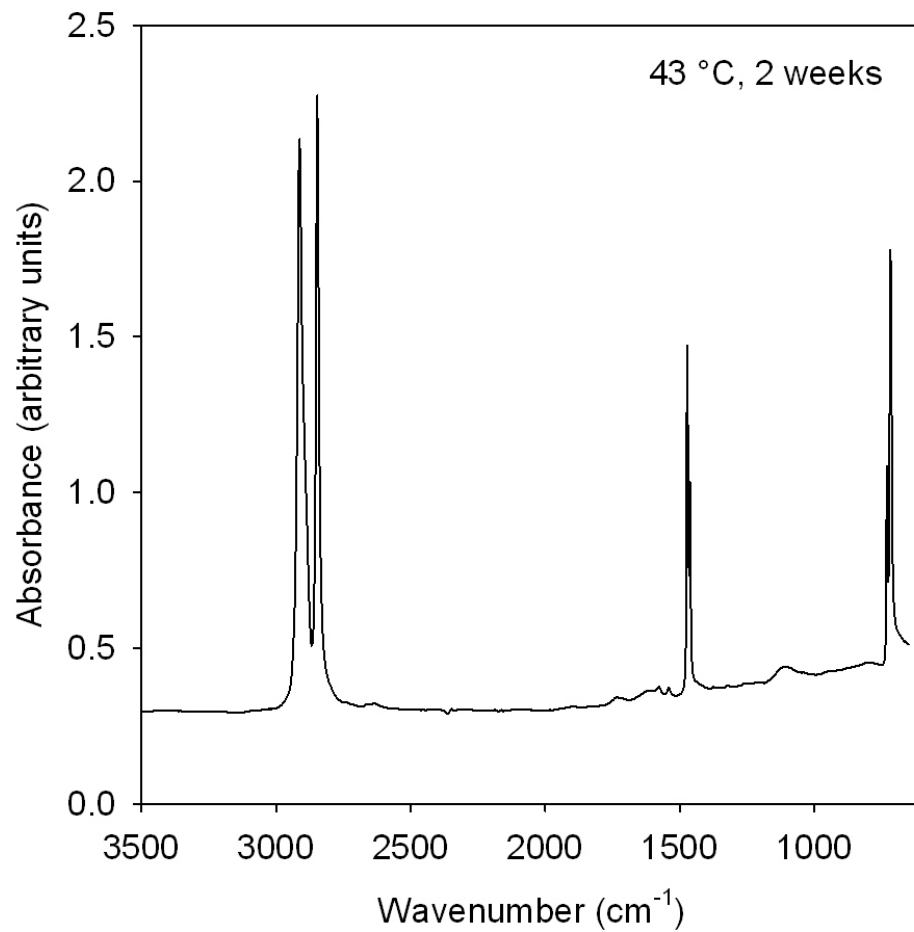
Figure B.5: FTIR Spectrum of UHMWPE fiber aged at 43 °C for 2 weeks.
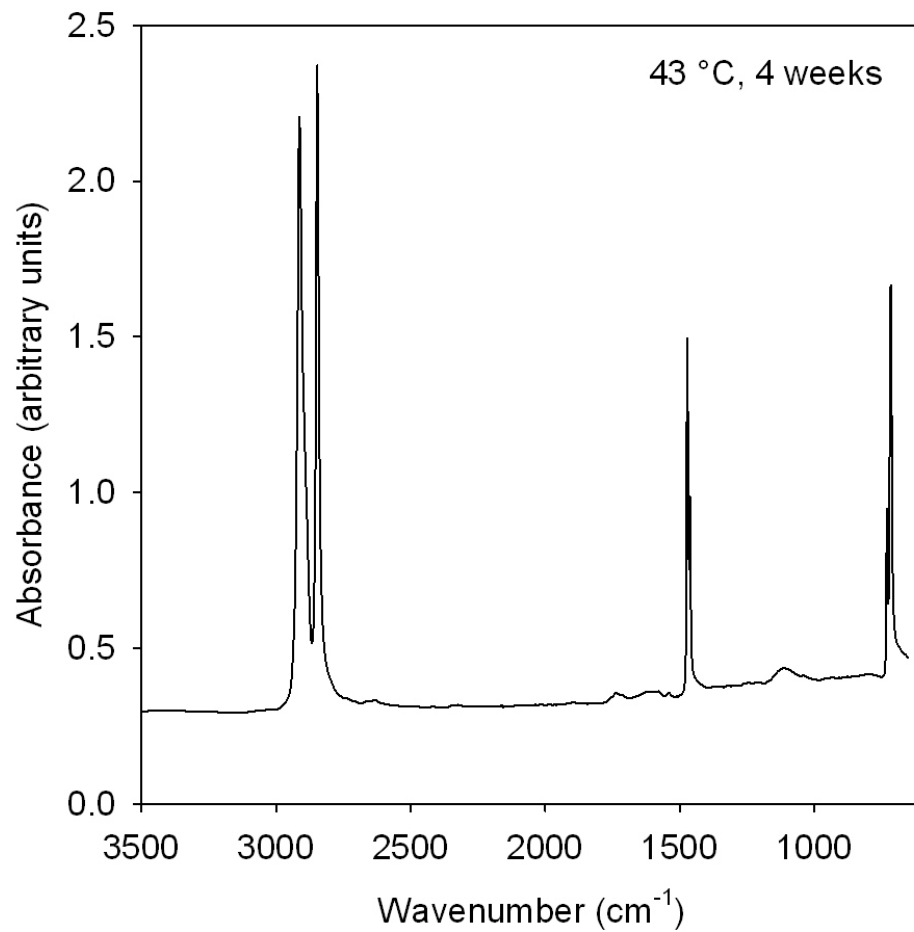
Figure B.6: FTIR Spectrum of UHMWPE fiber aged at 43 °C for 4 weeks.
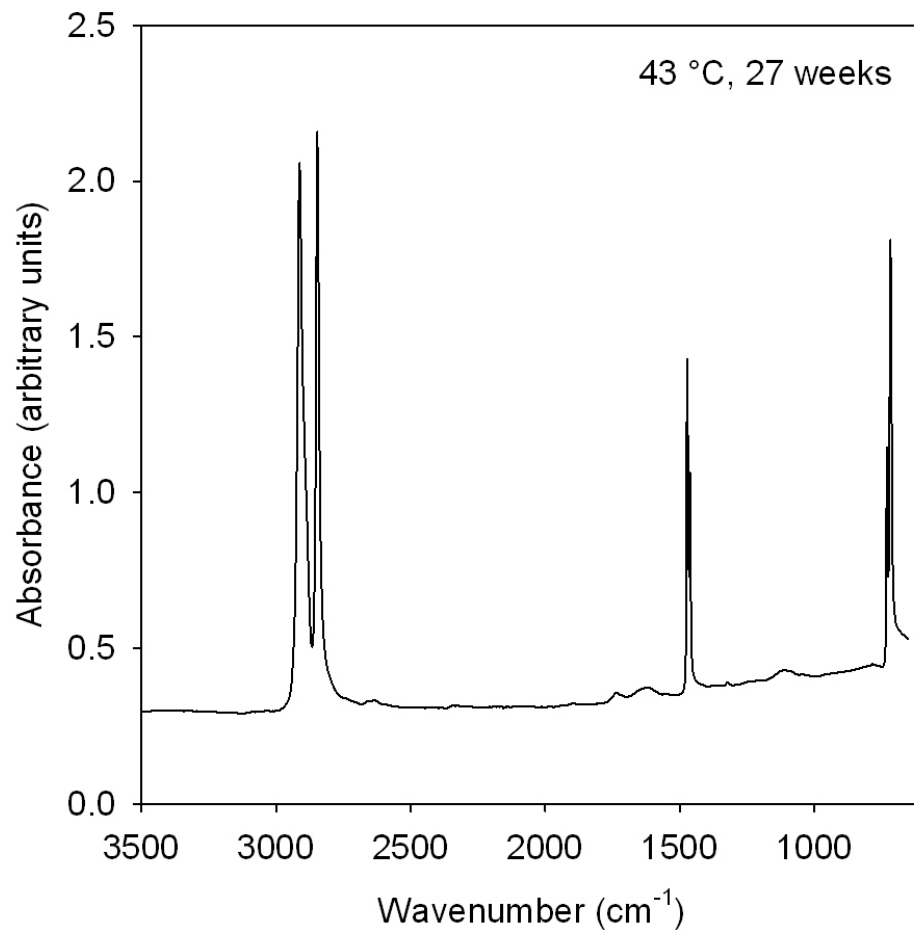
Figure B.7: FTIR Spectrum of UHMWPE fiber aged at 43 °C for 27 weeks.
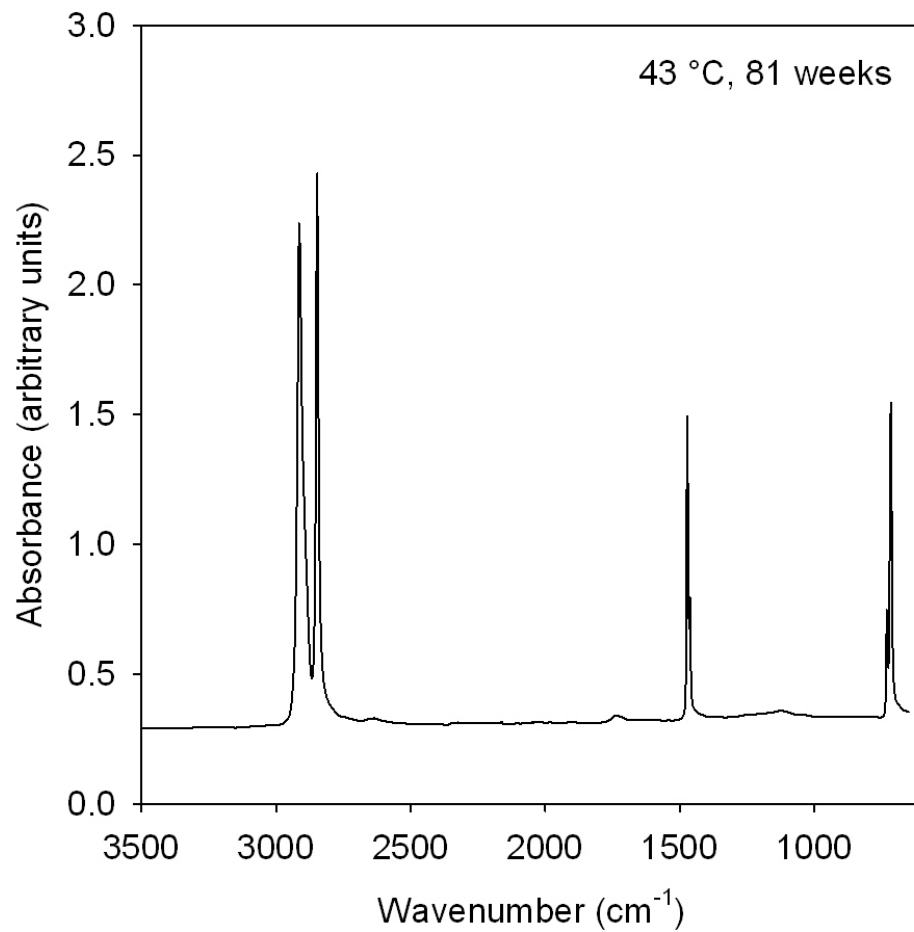
Figure B.8: FTIR Spectrum of UHMWPE fiber aged at 43 °C for 81 weeks.
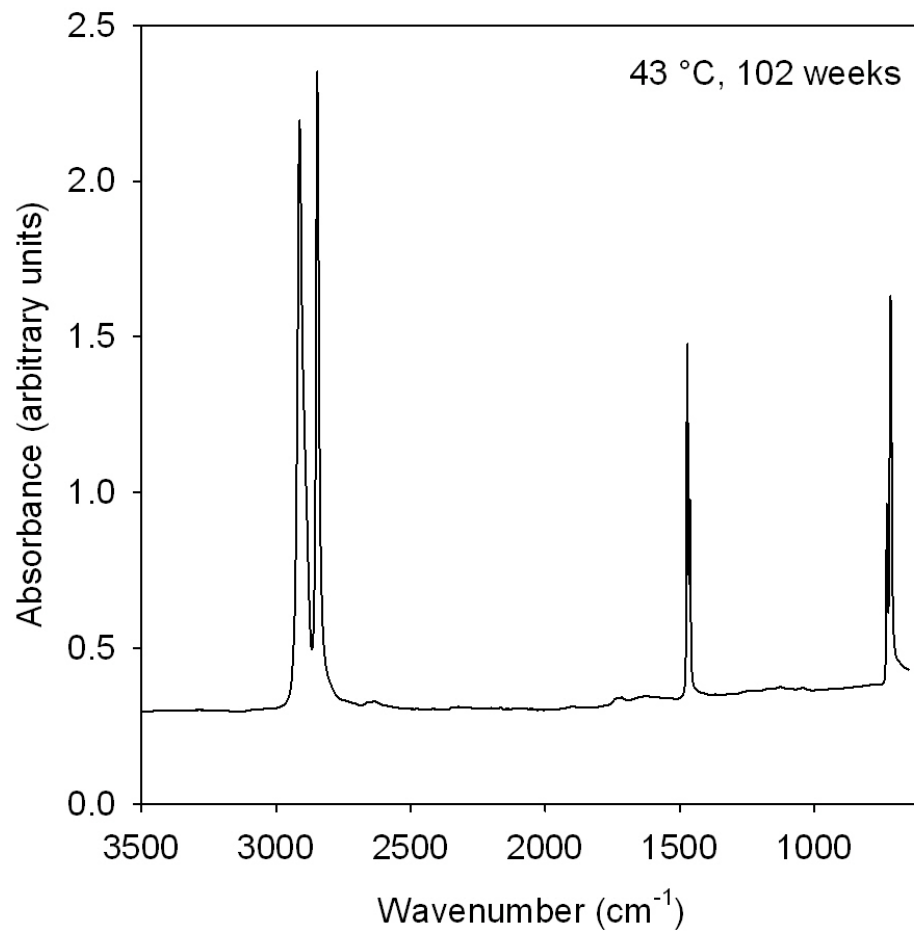
Figure B.9: FTIR Spectrum of UHMWPE fiber aged at 43 °C for 102 weeks.
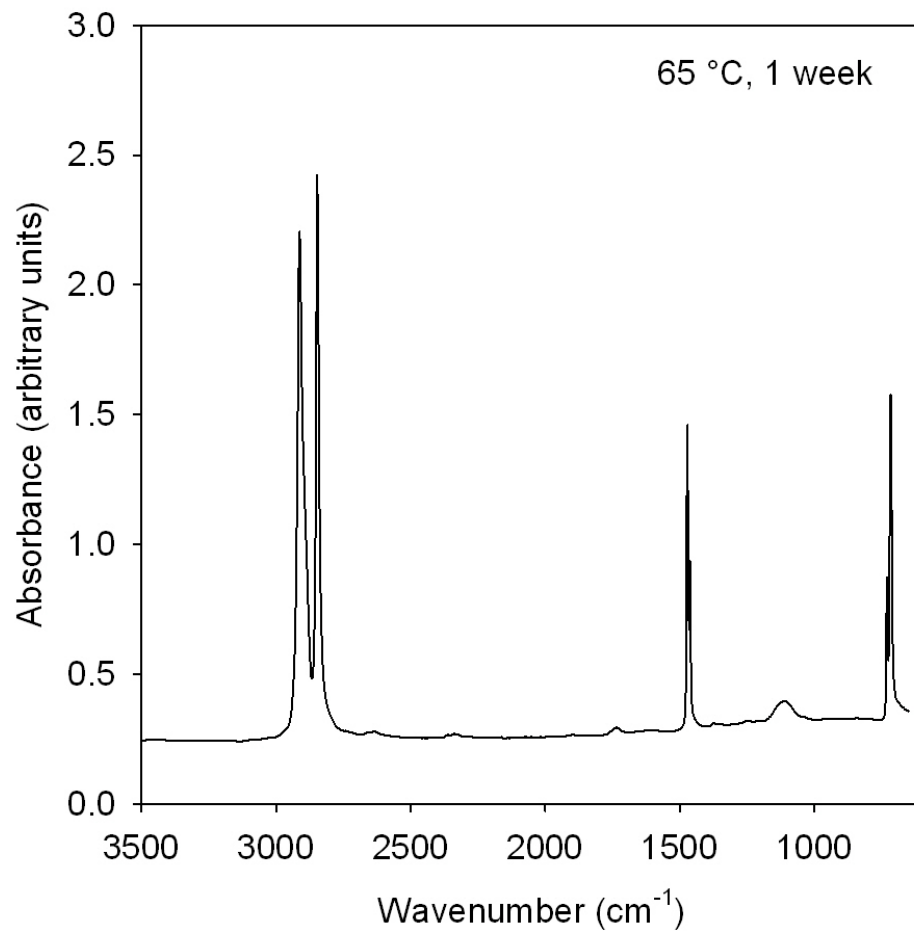
Figure B.10: FTIR Spectrum of UHMWPE fiber aged at 65 °C for 1 week.
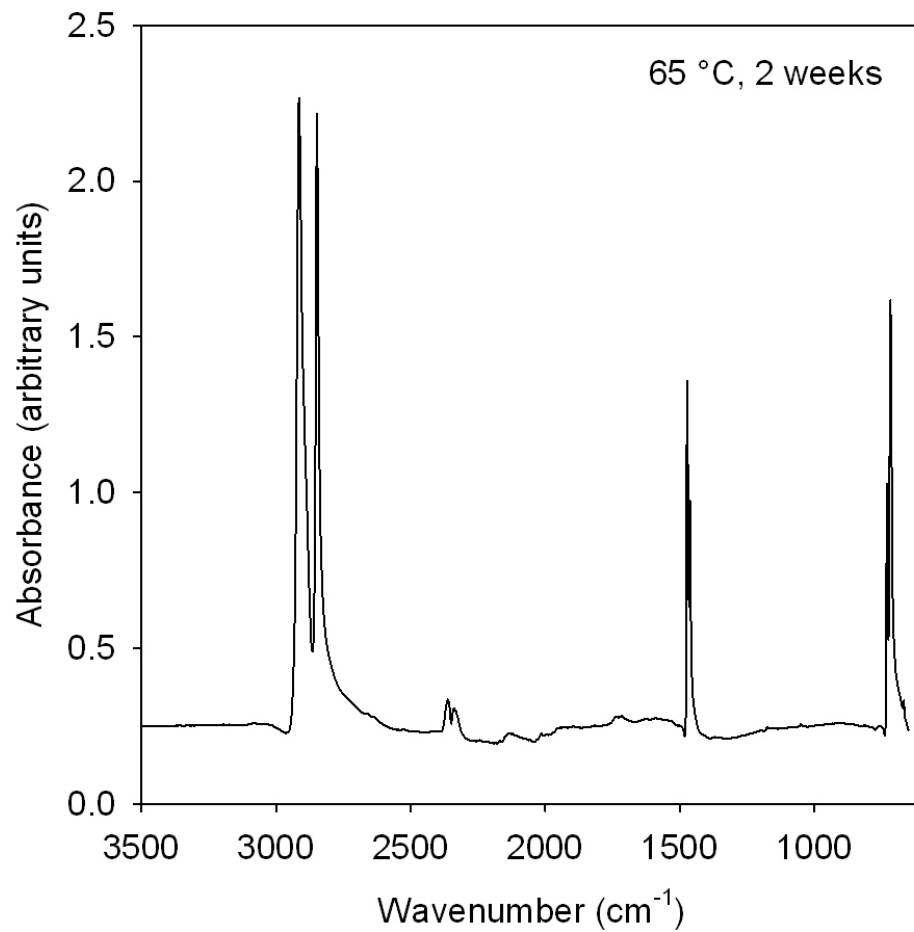
Figure B.11: FTIR Spectrum of UHMWPE fiber aged at 65 °C for 2 weeks.
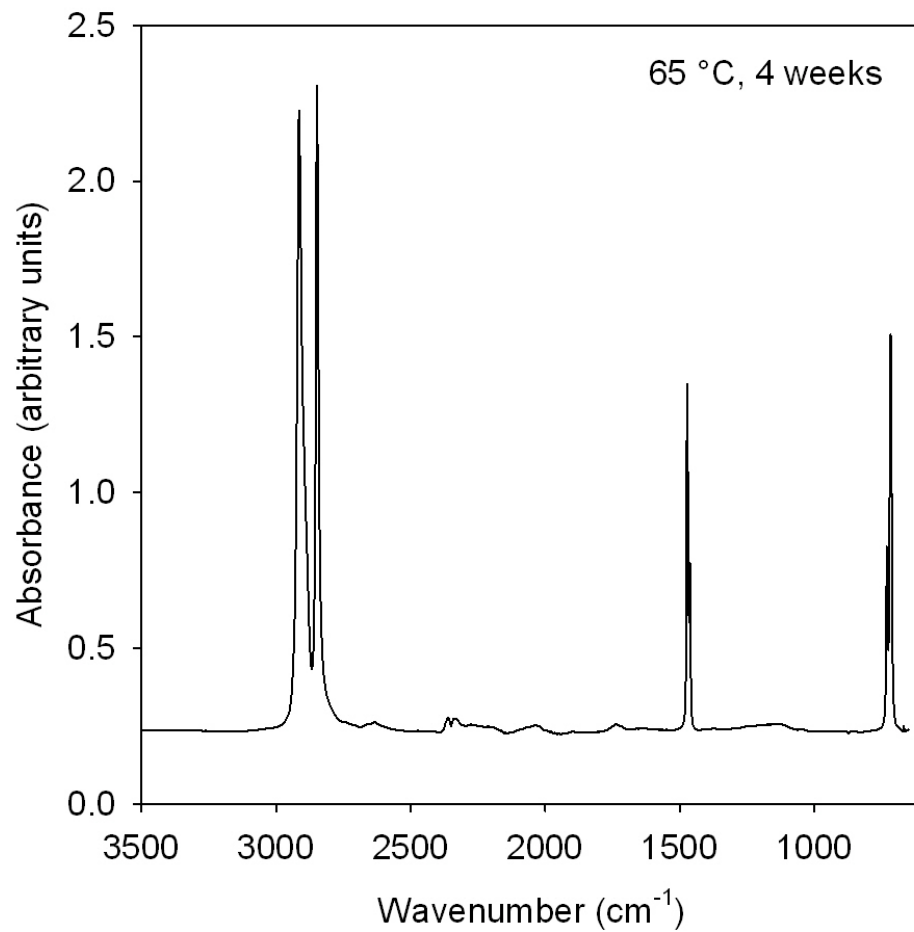
Figure B.12: FTIR Spectrum of UHMWPE fiber aged at 65 °C for 4 weeks.
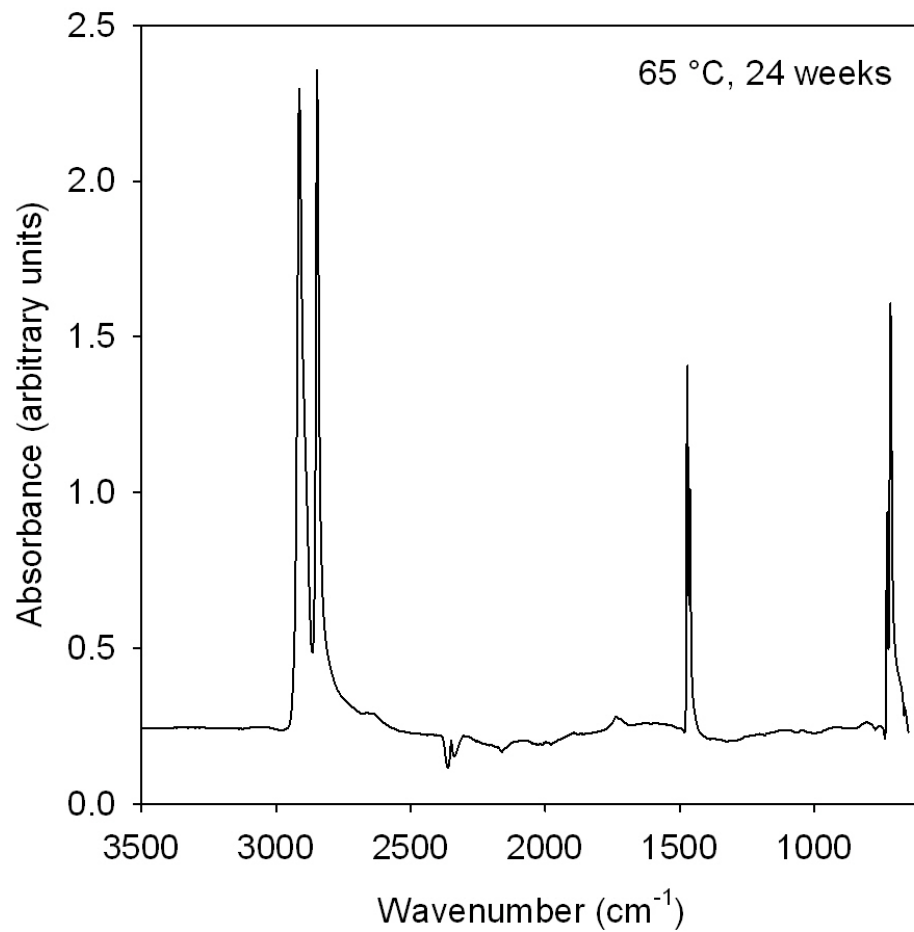
Figure B.13: FTIR Spectrum of UHMWPE fiber aged at 65 °C for 24 weeks.
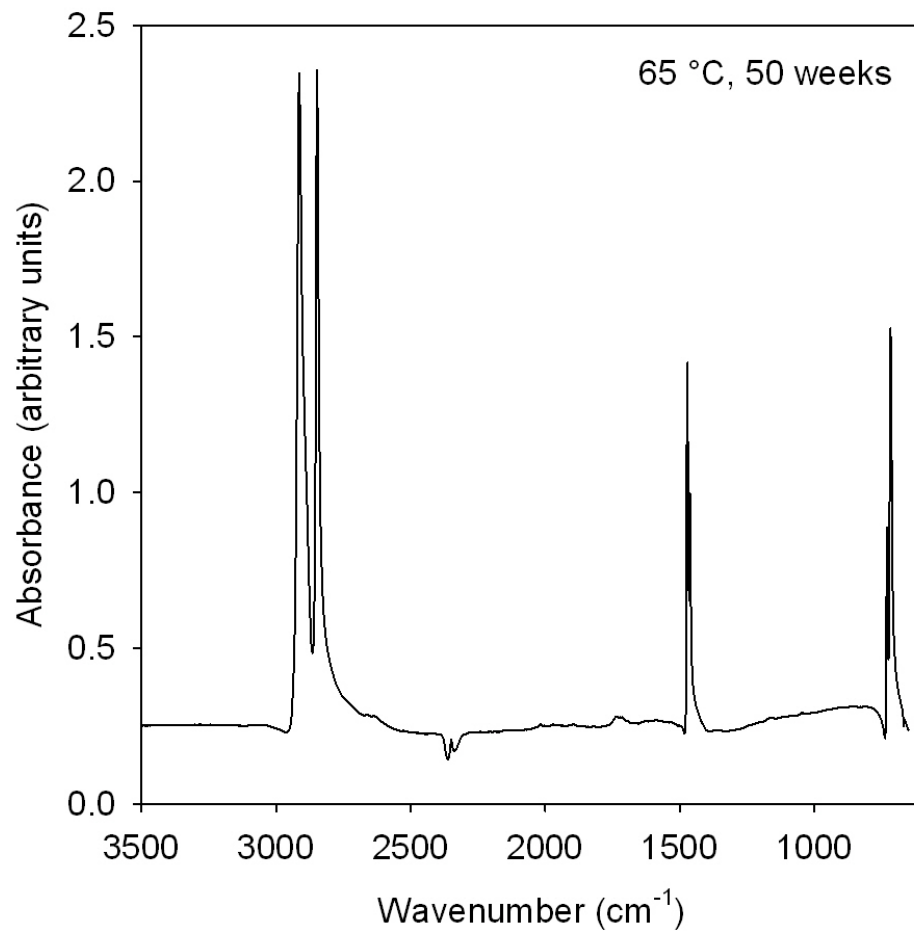
Figure B.14: FTIR Spectrum of UHMWPE fiber aged at 65 °C for 50 weeks.
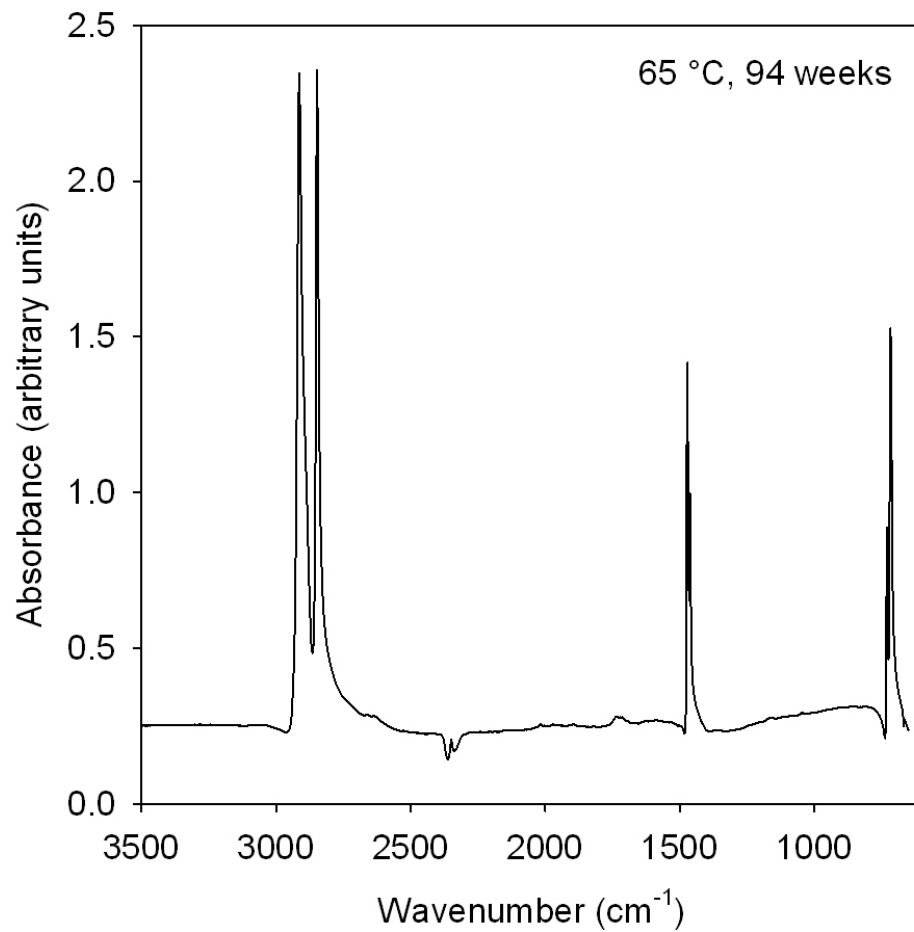
Figure B.15: FTIR Spectrum of UHMWPE fiber aged at 65 °C for 94 weeks.
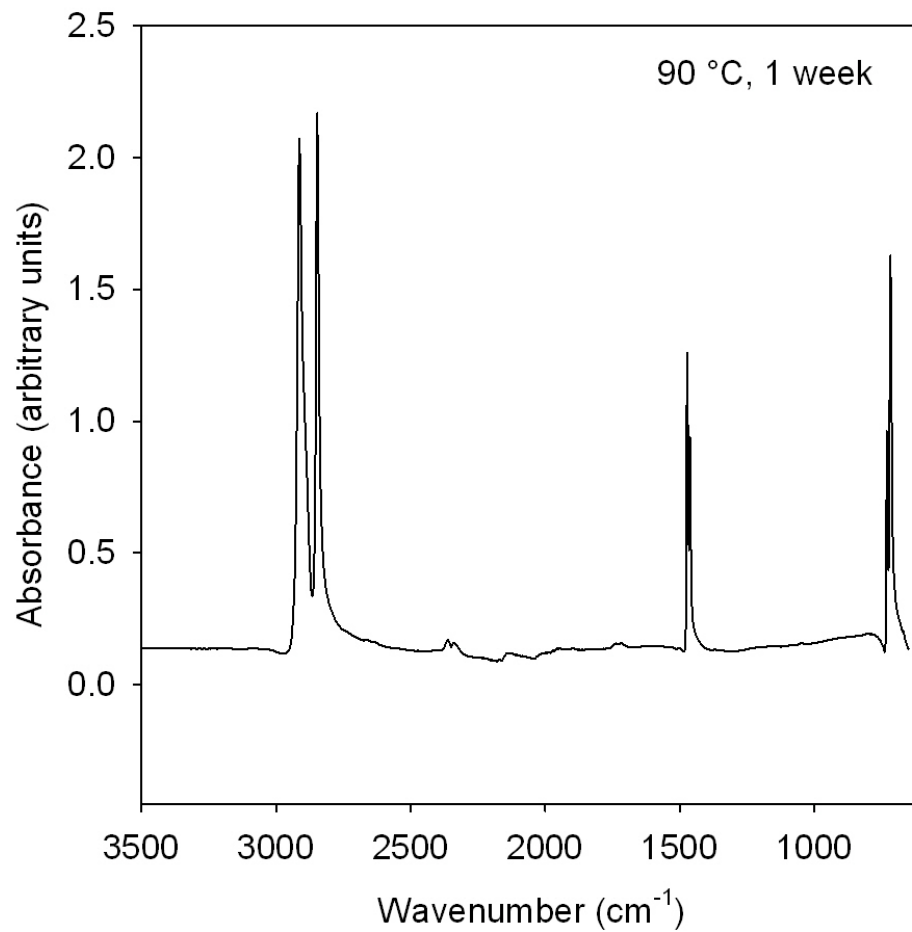
Figure B.16: FTIR Spectrum of UHMWPE fiber aged at 90 °C for 1 week.
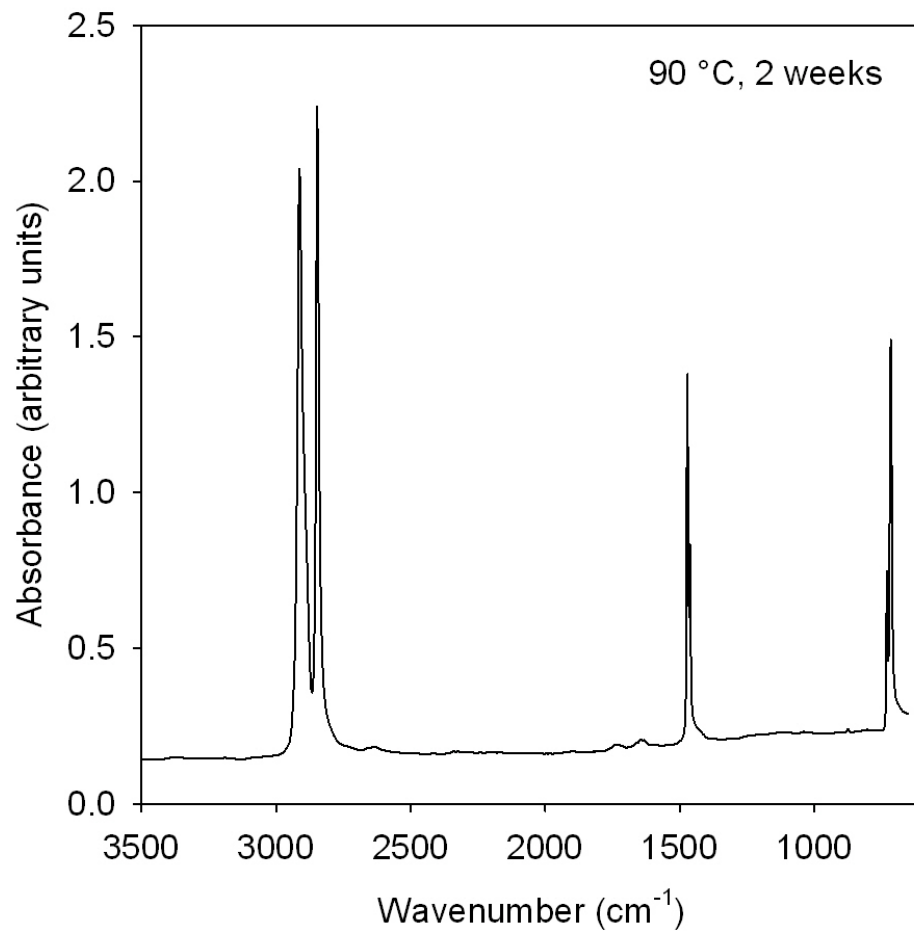
Figure B.17: FTIR Spectrum of UHMWPE fiber aged at 90 °C for 2 weeks.
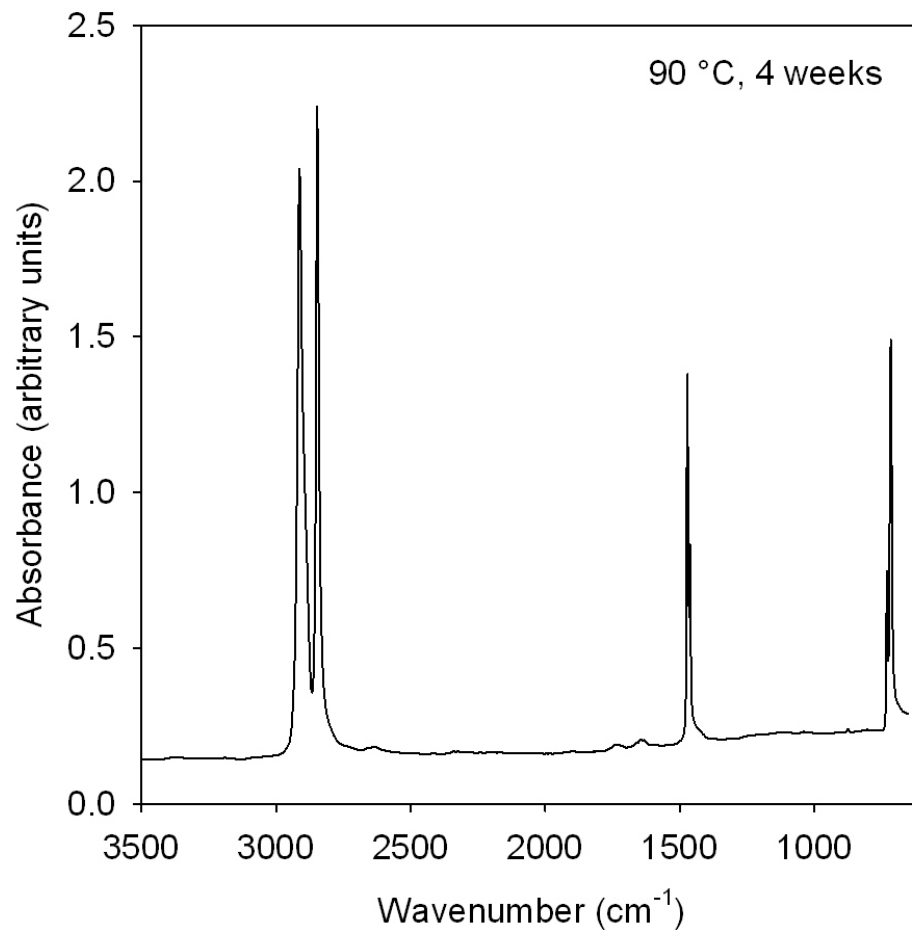
Figure B.18: FTIR Spectrum of UHMWPE fiber aged at 90 °C for 4 weeks.
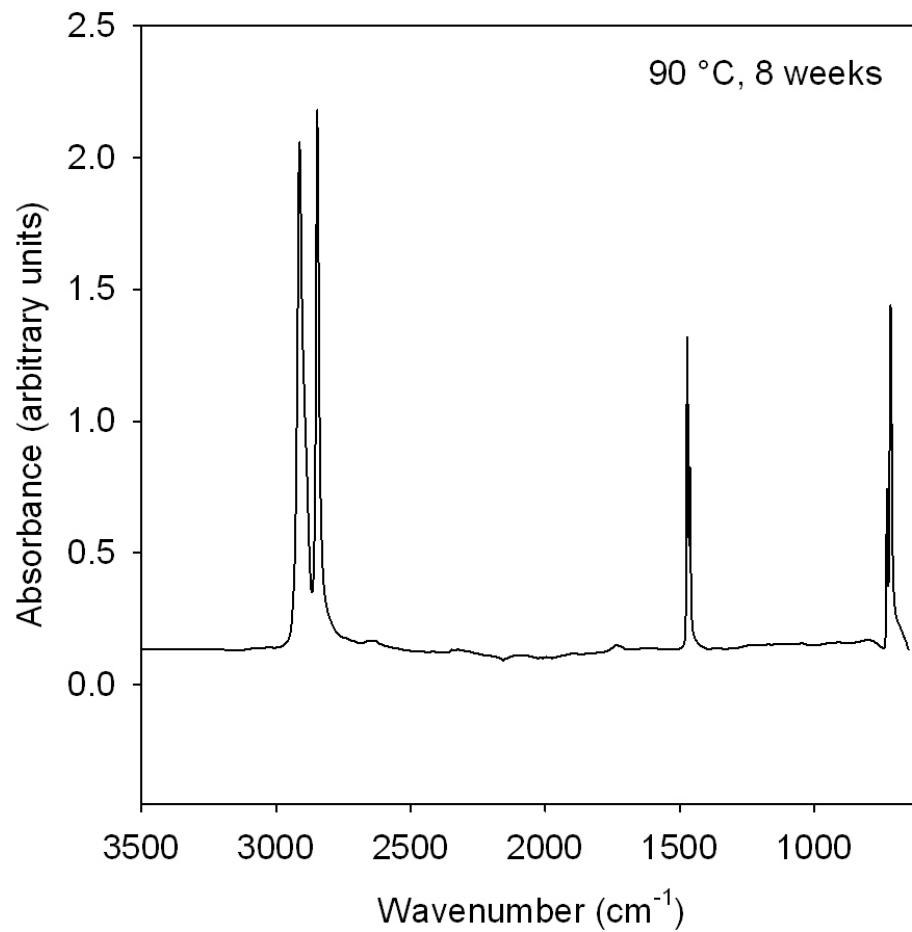
Figure B.19: FTIR Spectrum of UHMWPE fiber aged at 90 °C for 8 weeks.
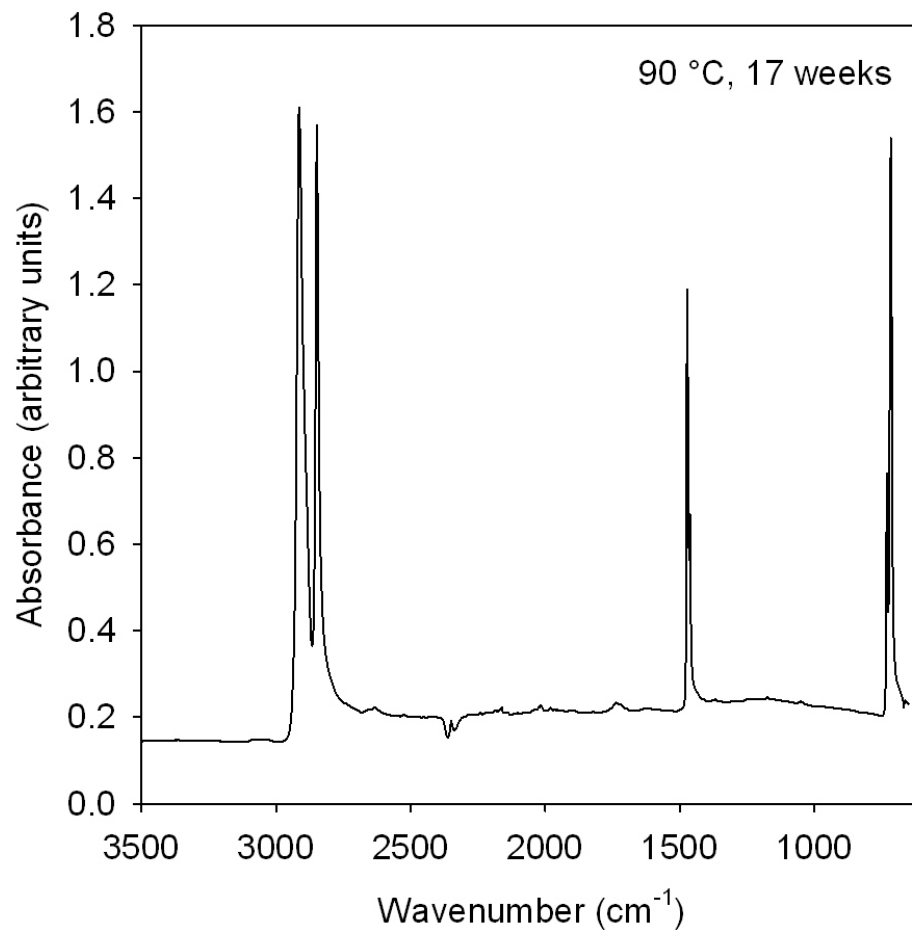
Figure B.20: FTIR Spectrum of UHMWPE fiber aged at 90 °C for 17 weeks.
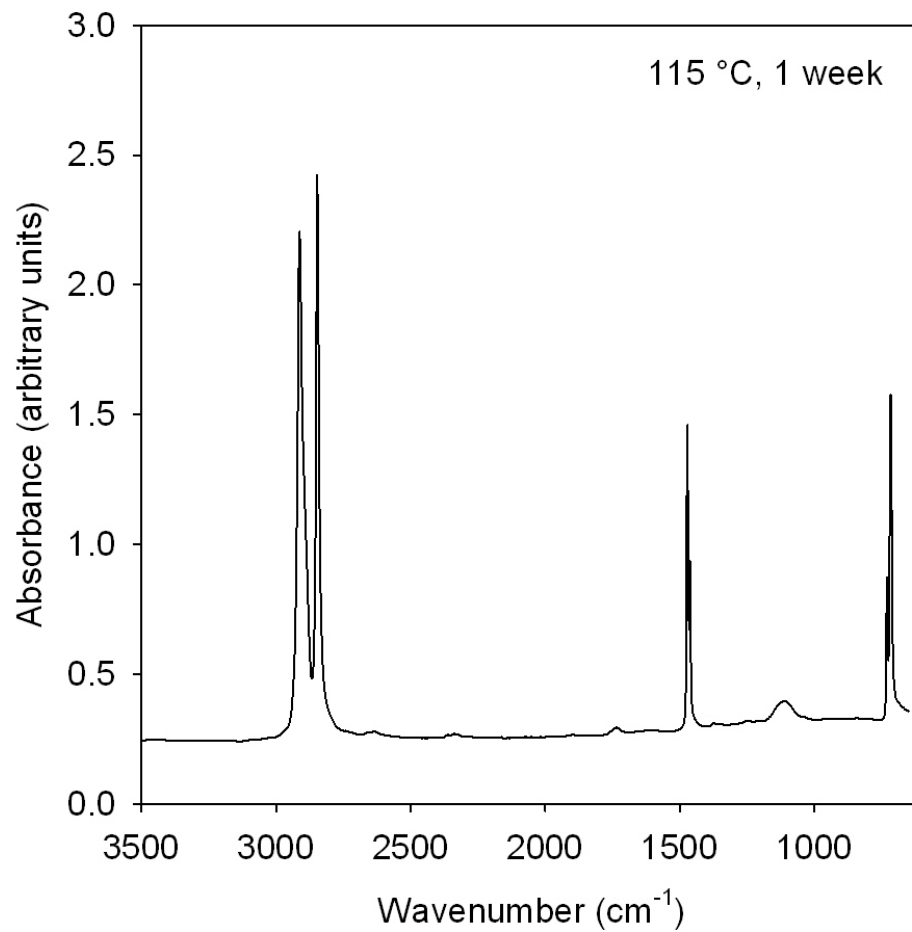
Figure B.21: FTIR Spectrum of UHMWPE fiber aged at 115 °C for 1 week.
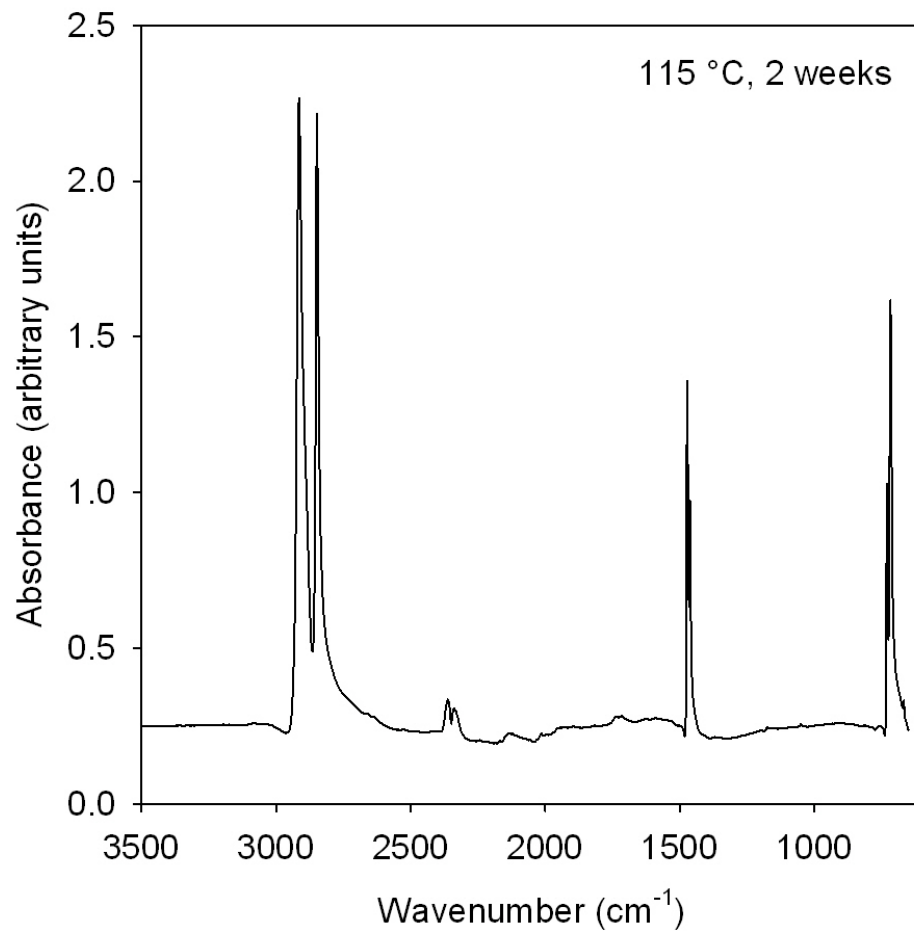
Figure B.22: FTIR Spectrum of UHMWPE fiber aged at 115 °C for 2 weeks.
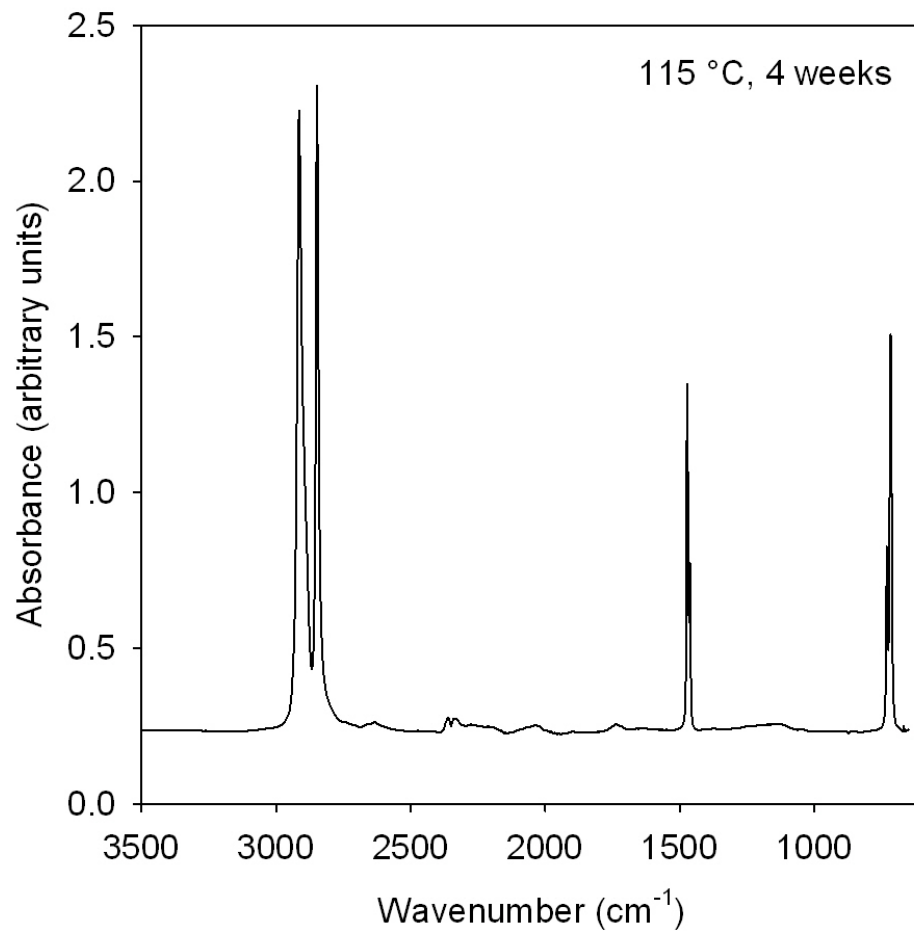
Figure B.23: FTIR Spectrum of UHMWPE fiber aged at 115 °C for 4 weeks.
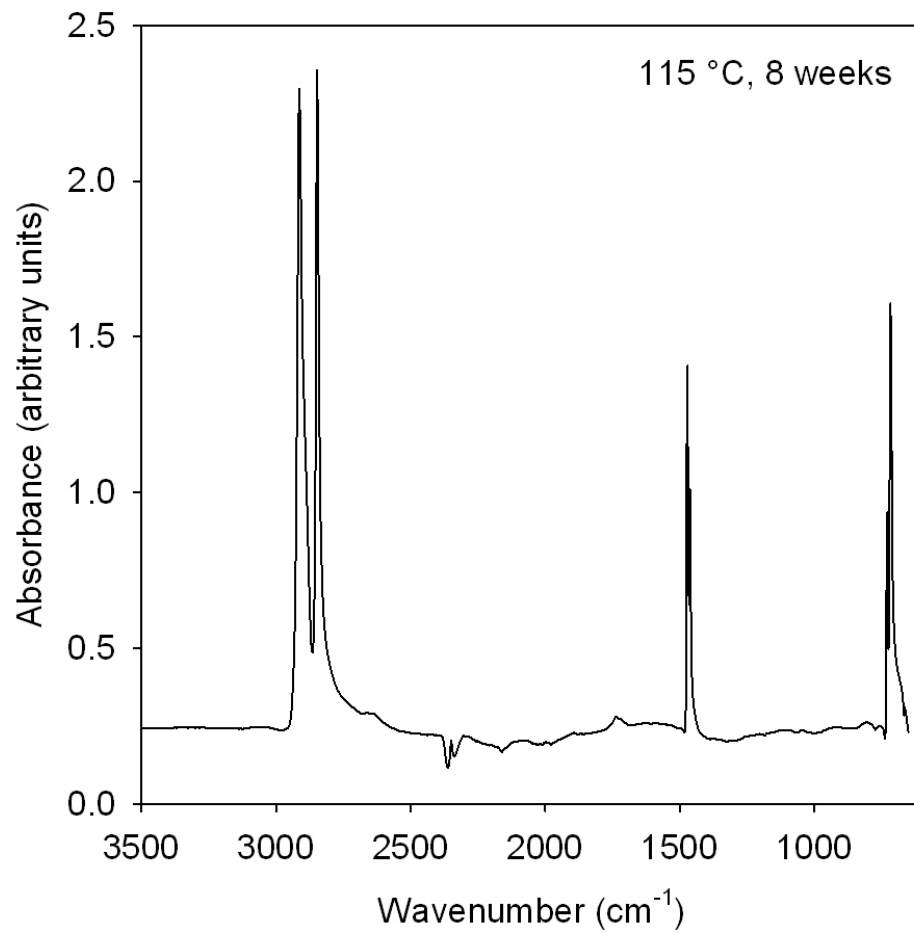
Figure B.24: FTIR Spectrum of UHMWPE fiber aged at 115 °C for 8 weeks.
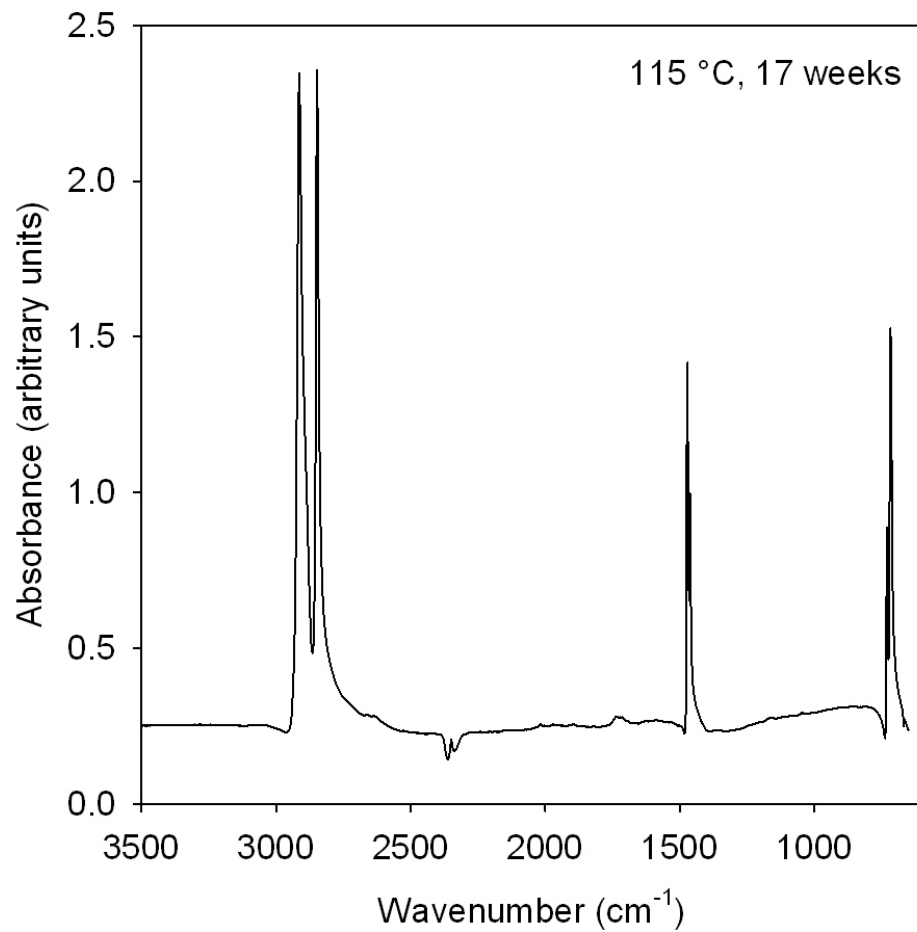
Figure B.25: FTIR Spectrum of UHMWPE fiber aged at 115 °C for 17 weeks.
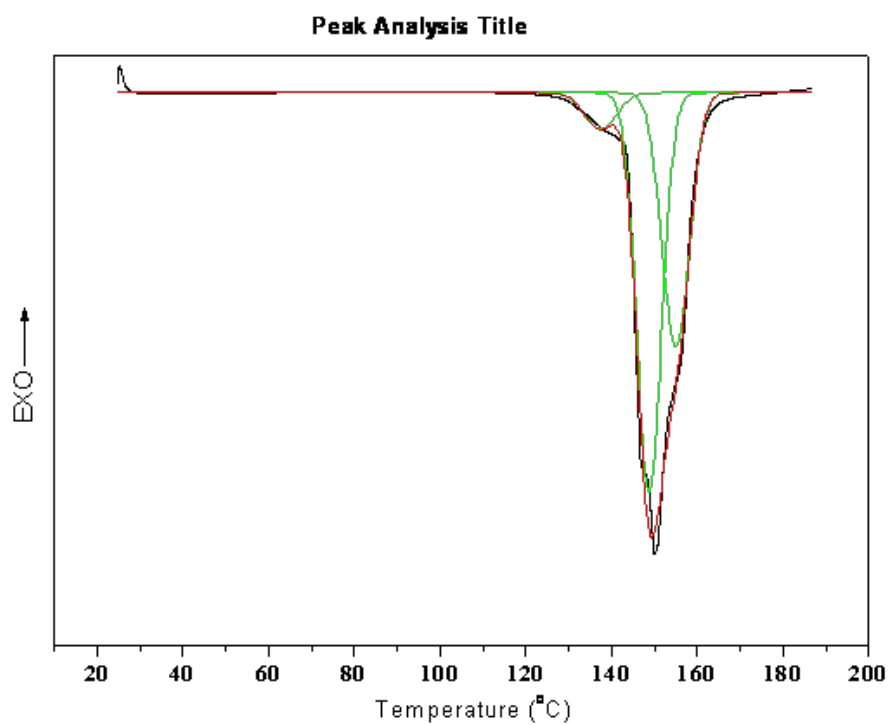
Figure B.26: Deconvolution of UHMWPE melting endotherm into 4 separate peaks.

B.4 DSC Thermograms for first and second melt for gamma-irradiated polyethylene.
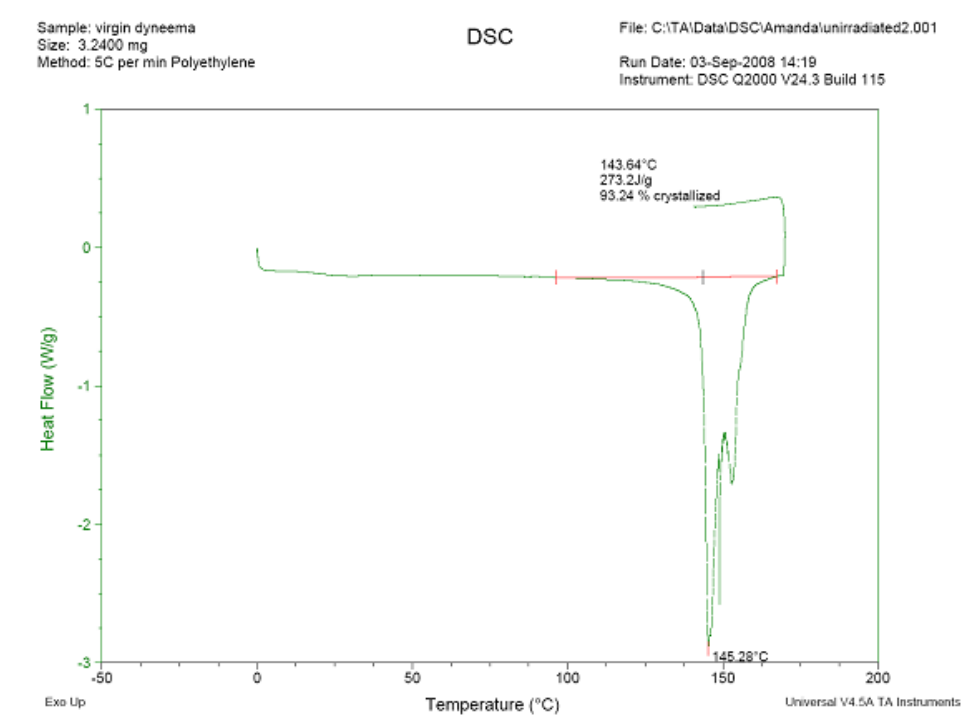
Figure B.27: DSC Thermogram for Gamma Irradiated Polyethylene, 1st melt.
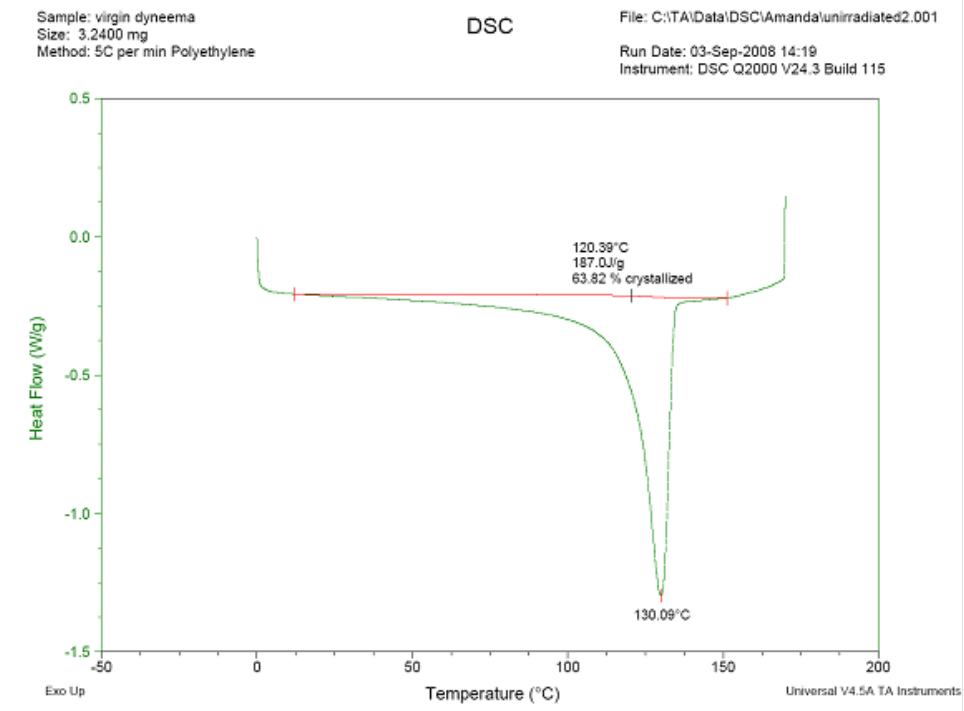
Figure B.28: DSC Thermogram for Gamma Irradiated Polyethylene, 2nd melt.
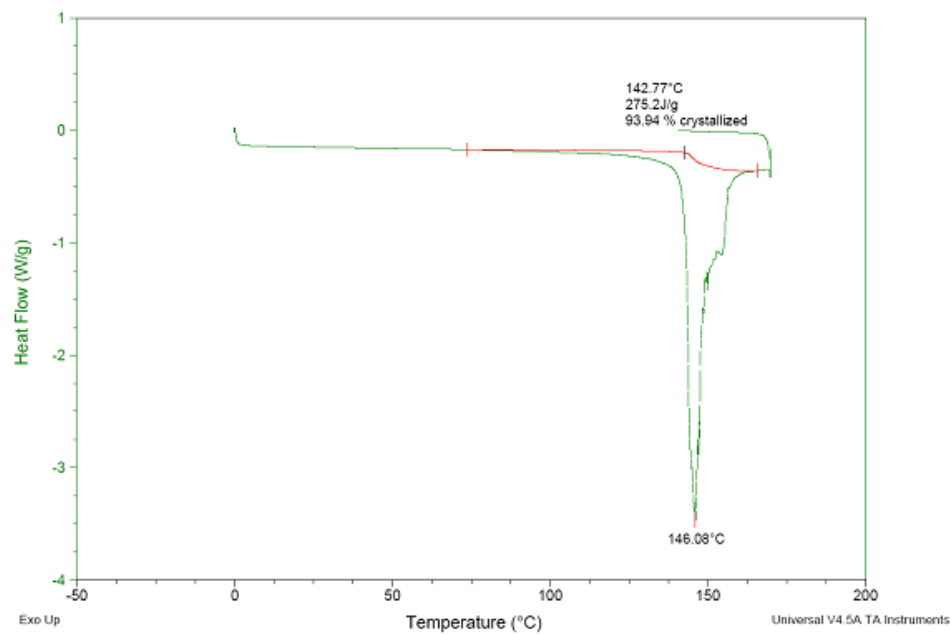
Figure B.29: DSC Thermogram for Gamma Irradiated Polyethylene, 1st melt.
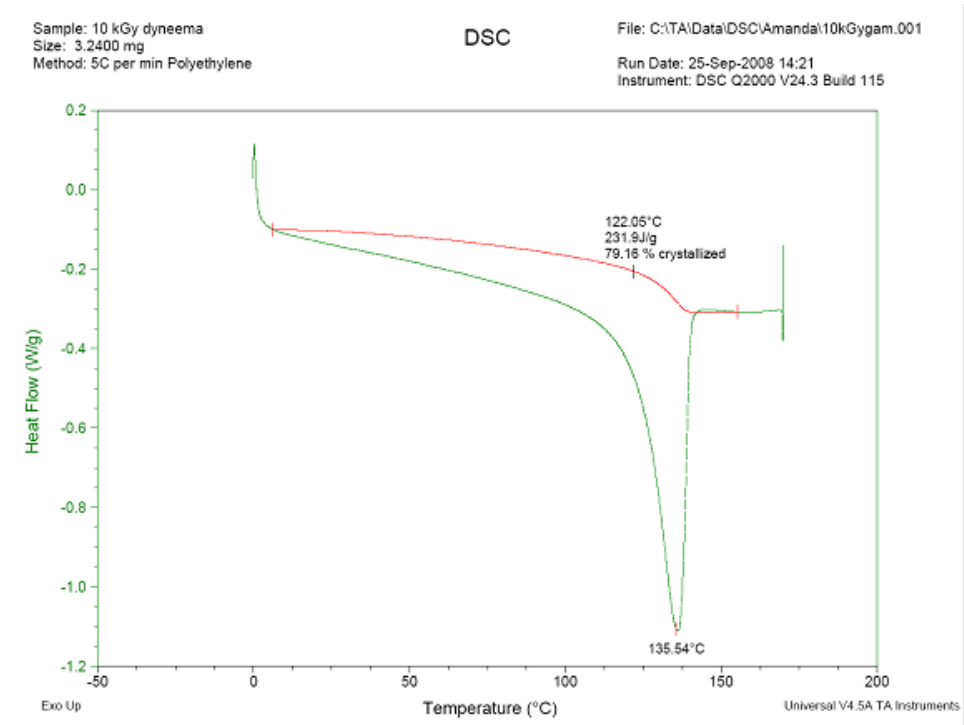
Figure B.30: DSC Thermogram for Gamma Irradiated Polyethylene, 2nd melt.
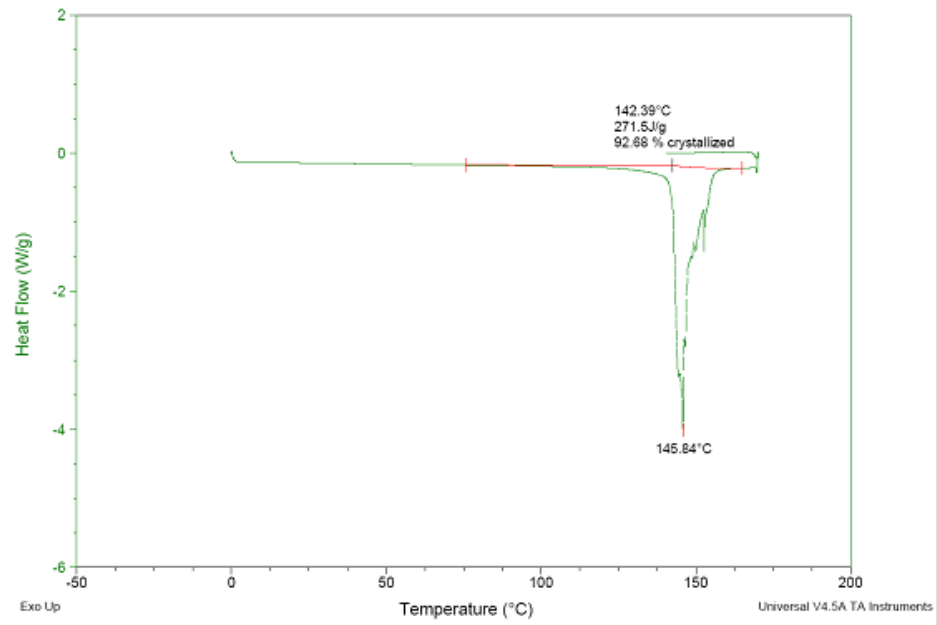
Figure B.31: DSC Thermogram for Gamma Irradiated Polyethylene, 1st melt.
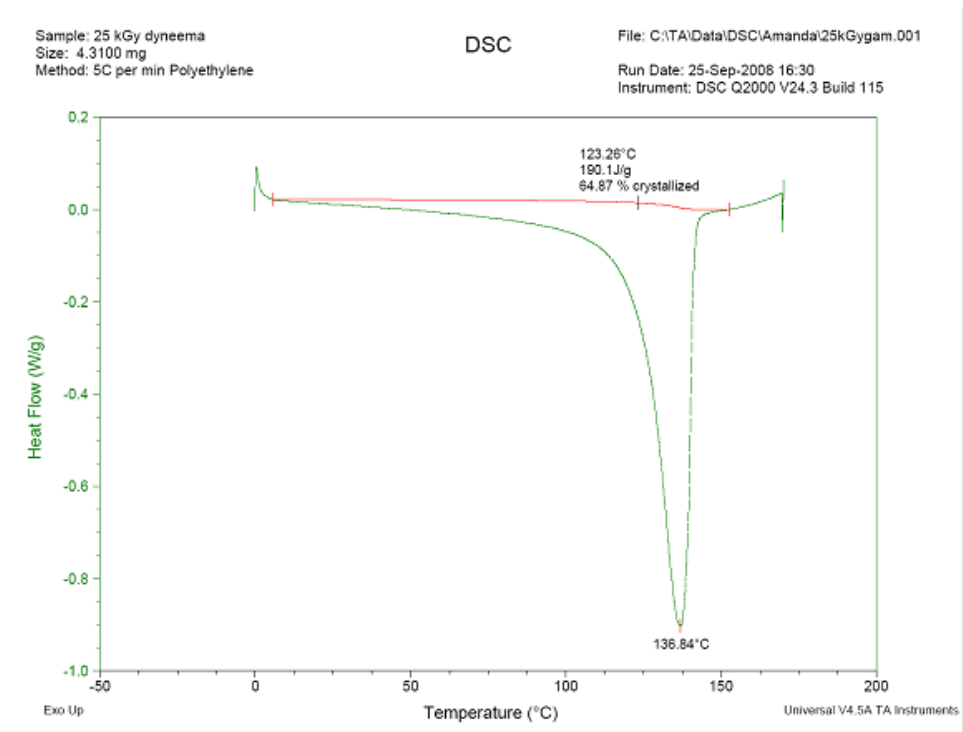
Figure B.32: DSC Thermogram for Gamma Irradiated Polyethylene, 2nd melt.
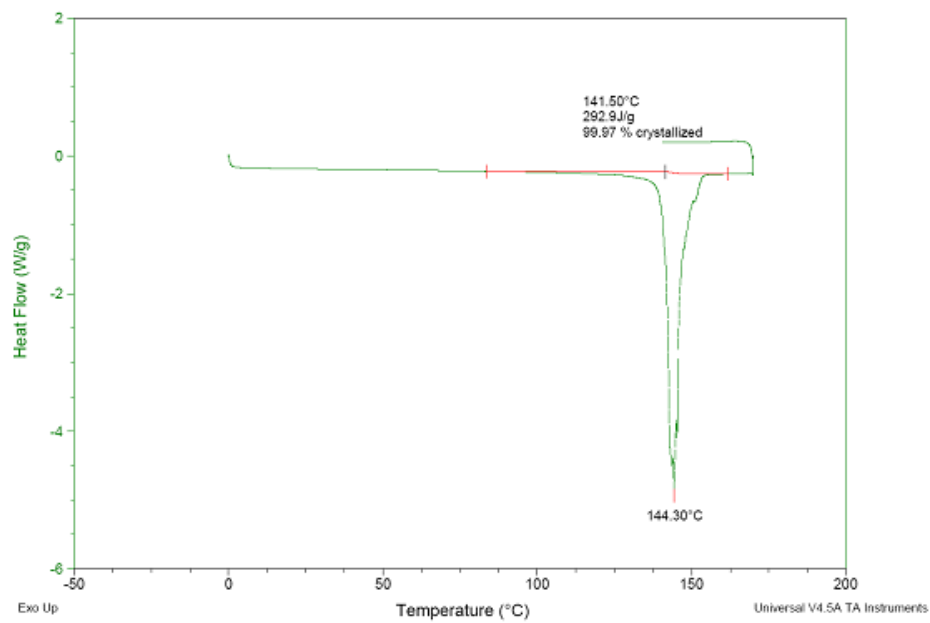
Figure B.33: DSC Thermogram for Gamma Irradiated Polyethylene, 1st melt.
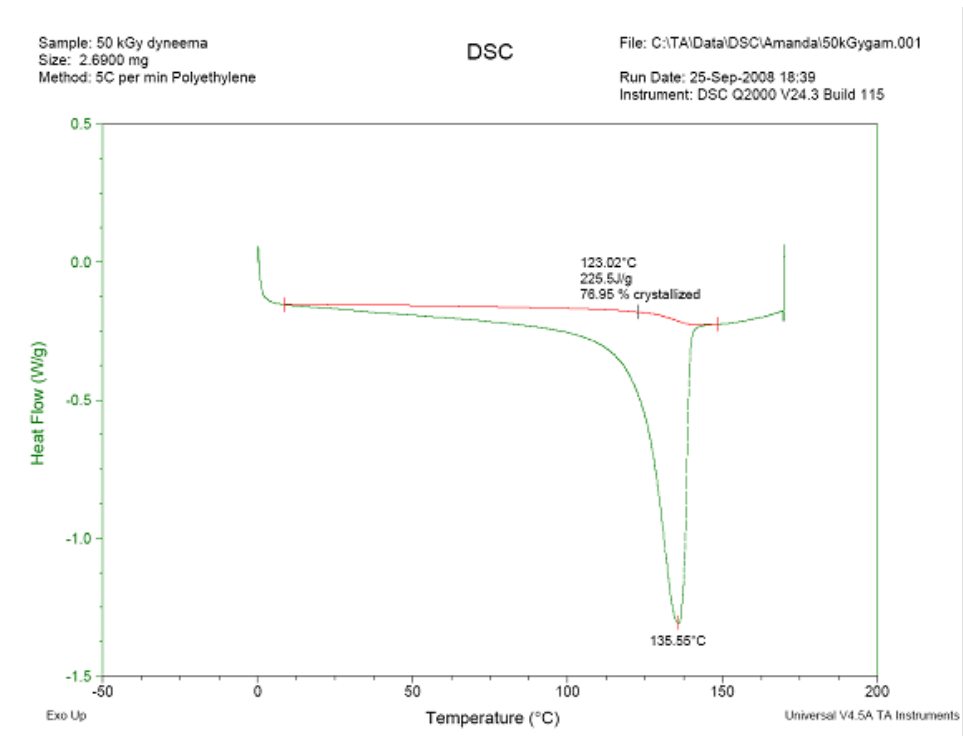
Figure B.34: DSC Thermogram for Gamma Irradiated Polyethylene, 2nd melt.
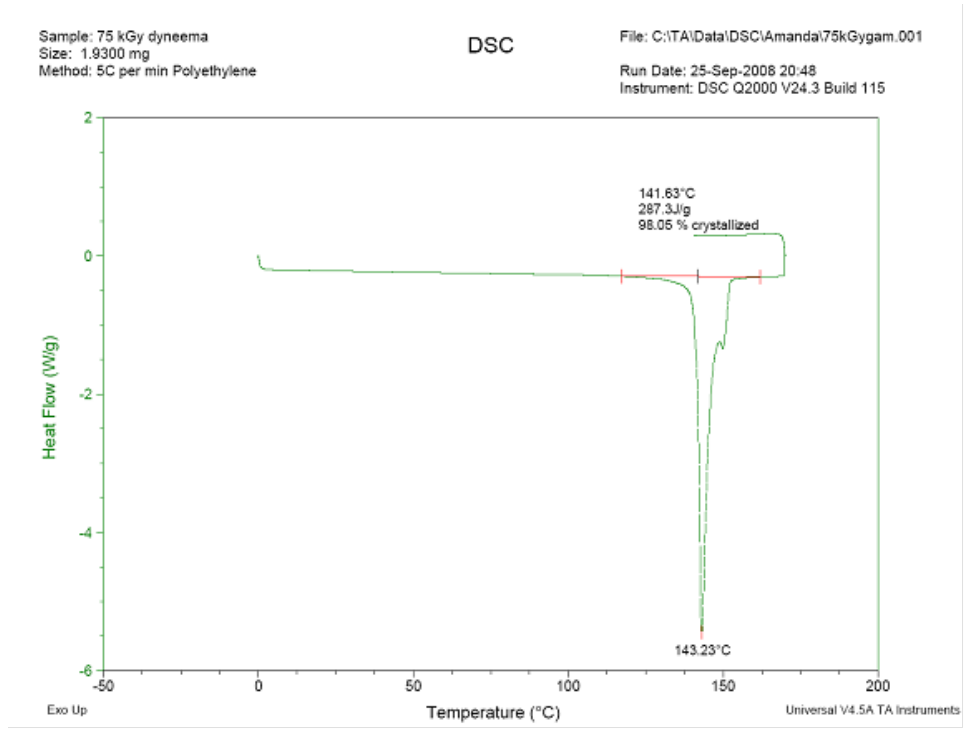
Figure B.35: DSC Thermogram for Gamma Irradiated Polyethylene, 1st melt.
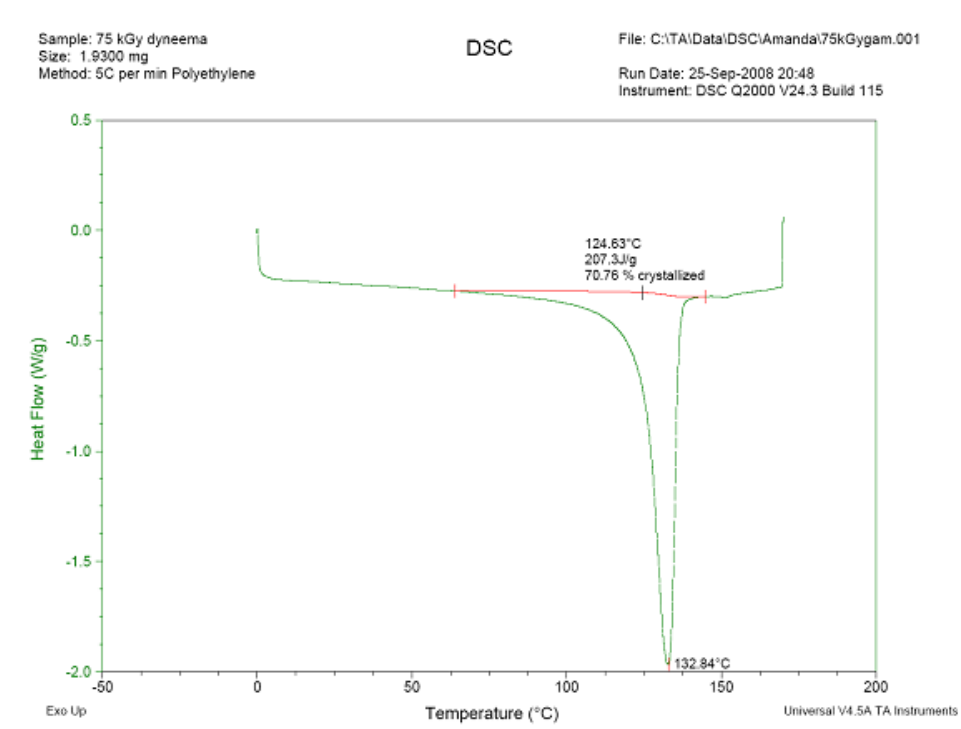
Figure B.36: DSC Thermogram for Gamma Irradiated Polyethylene, 2nd melt.
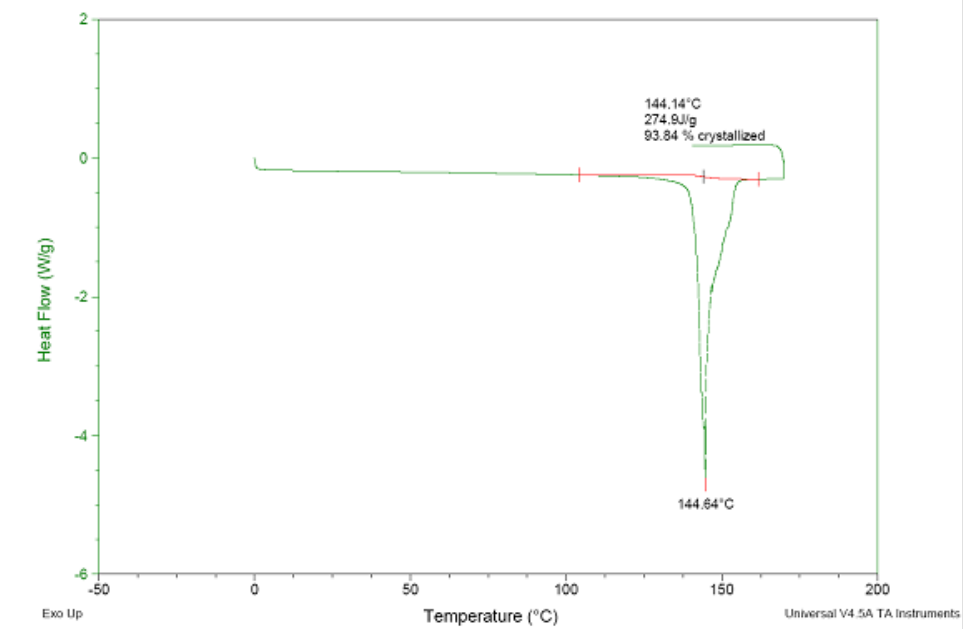
Figure B.37: DSC Thermogram for Gamma Irradiated Polyethylene, 1st melt.
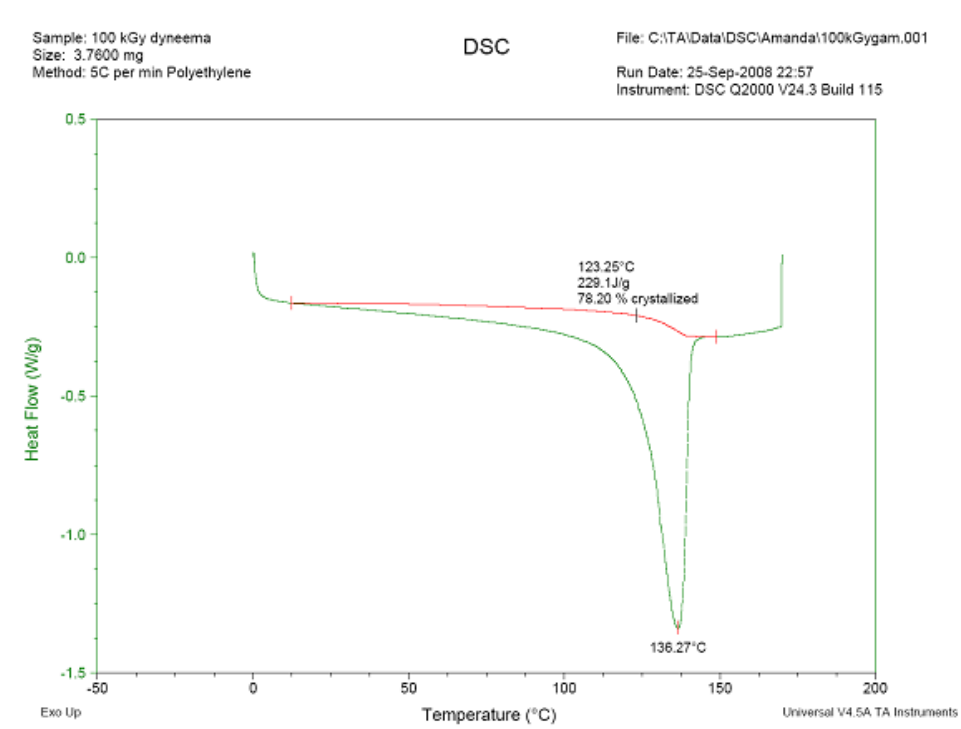
Figure B.38: DSC Thermogram for Gamma Irradiated Polyethylene, 2nd melt.

Bibliography

[1] H. Yang. *Kevlar Aramid Fiber.* John, 1993.

[2] P. Collins. *Liquid crystals.* Princeton University Press, Princeton, NJ, 2002.

[3] P. Collins. *Introduction to liquid crystals: chemistry and physics.* Taylor and Francis, Philadelphia, 2004.

[4] G. Odian. *Principles of Polymerization.* Wiley-Interscience, New York, 3rd edition, 1991.

[5] M. Shahnin. Optical Microscopy Study on Poly(p-phenylene terephthalamide) Fibers. *Journal of Applied Polymer Science*, 90:360–369, 2003.

[6] A. Leal, J. Deitzel, and J. Gillespie. Compressive strength analysis for high performance fibers with different modulus in tension and compression. *Journal of Composite Materials*, 43:661–674, 2009.

[7] X. Hu, S. Jenkins, B. Min, M. Polk, and S. Kumar. Rigid-Rod Polymers: Synthesis, Processing, Simulation, Structure, and Properties. *Macromolecular Materials Engineering*, 288:823–843, 2003.

[8] T. Kitagawa, H. Murase, and K. Yabuki. *Journal of Polymer Science Part B-Polymer Physics*, 36:39–48, 1998.

[9] N. Montanarelli, C. Hawkins, and L. Shubin. Body armor: Lightweight body armor for law enforcement officers. Technical report, National Institute of Law Enforcement and Criminal Justice, 1976.

[10] Ballistic resistance of personal body armor. *NIJ Standard–0101.06*, 2008.

[11] D. Tompkins. Body armor safety initiative: To protect and serve... better. *NIJ Journal*, 254, 2006.

[12] IACP. Survivor's club recognizes 3000th law enforcement officer saved by a protective vest, March 2006.

[13] J. Ashcroft. Attorney general ashcroft announces bulletproof vest safety initiative, November 2003.

[14] NIJ. Status report to the Attorney General of body armor safety initiative testing and activities. *NIJ Special Report*, 2004.

[15] NIJ. Supplement I: Status report to the Attorney General of body armor safety initiative testing and activities. *NIJ Special Report*, 2004.

[16] NIJ. Third status report to the Attorney General on body armor safety initiative testing and activities. *NIJ Special Report*, 2005.

[17] J. Chin, E. Byrd, A. Forster, X. Gu, T. Nguyen, S. Scierka, L. Sung, P. Stutzman, J. Sieber, and K. Rice. Chemical and Physical Characterization of Poly (p-phenylene-2,6-benzobisoxazole) Fibers Used in Body Armor. *NISTIR 7237*, 2006.

[18] J. Chin, E. Byrd, C. Clerici, M. Oudina, L. Sung, A. Forster, and K. Rice. Chemical and Physical Characterization of Poly (p-phenylene-2,6-benzobisoxazole) Fibers Used in Body Armor: Temperature and Humidity Aging. *NISTIR 7373*, 2007.

[19] A. Forster., J. Chin, and M. Gundlach. Effect of bending and mechanical damage on the physical properties of poly(p-phenylene-2,6-benzobisoxazole)(PBO) fiber. *Abstracts of Papers of the American Chemical Society*, 231:274–POLY, 2006.

[20] G. Holmes, J. Kim, D. Ho, and W. McDonough. The Role of Folding in the Degradation of Ballistic Fibers. *Polymer Composites*, in press, 2009.

[21] T. Bachner. Rational Replacement Policy–A Recommendation to the Law Enforcement Community, October 1985.

[22] D. Frank. Ballistic Tests of Used Soft Body Armor. *NBSIR 86-3444*, 1986.

[23] National Institute of Justice. Response to DuPont's Rational Replacement Policy, 1985.

[24] DuPont Kevlar Survivor's Club. Personal body armor facts book. Technical report, DuPont, 1989.

[25] OTA. Police body armor standards and testing Volume I: Report. *Congress of the United States Office of Technology Assessment*, 1992.

[26] OTA. Police body armor standards and testing Volume II: Appendixes. *Congress of the United States Office of Technology Assessment*, 1992.

[27] E. Hoffman. Soft Body Armor. *Police Product News*, 1986.

[28] Armor Holdings. Interim report on body armor testing: Investigations and actions. Technical report, Armor Holdings, 2004.

[29] DHB Armor Group. Dhb armor group armor safety report. Technical report, DHB, 2004.

[30] Z. Frund. Response to Request for Information: Artificial Aging of Armor, November 2005.

[31] H. Fogler. *Elements of Chemical Reaction Engineering*. Prentice Hall International Series in the Physical and Chemical Engineering Sciences. Prentice Hall, Englewood Cliffs, New Jersey, 2nd edition, 1992.

[32] F. Stadler, J. Kaschta, and H. Munstedt. Dynamic-mechanical behavior of polyethylenes and ethene-/alpha-olefin-co-polymers. Part I. alpha'-relaxation. *Polymer*, 46:10311–10320, 2005.

[33] S. Chabba, M. van Es, E. van Klinken, M. Jongedijk, D. Vanek, P. Gijsman, and A. van der Waals. Accelerated aging study of ultra high molecular weight polyethylene yarn and unidirectional composites for ballistic applications. *Journal of Materials Science*, 42:2891–2893, 2007.

[34] TA Instruments. *Rheometrics Series User Manual*. RSA III Manufacturer's Specifications. New Castle, DE, pn902-30027 edition, 2003.

[35] Ballistic resistance of personal body armor. *NIJ Standard–0101.04*, 2000.

[36] Ballistic resistance of personal body armor. *NIJ Standard–0101.04 Interim Requirements*, 2005.

[37] R. Wiley. The chemistry of the oxazoles. *Chemical Reviews*, 37(3):401–442, 1945.

[38] J. Cornforth. *Five-Membered Heterocycles Containing Two Hetero Atoms and Their Benzo Derivatives*, volume 5 of *Heterocyclic Compounds*. John Wiley and Sons, New York, 1957.

[39] I. Turchi. *Oxazoles*. John Wiley and Sons, New York, 1986.

[40] D. Palmer and S. Venkataraman. *Chemistry of Heterocyclic Compounds, Oxazoles: Synthesis, Reactions, and Spectroscopy, Part A*. Wiley-Interscience, Hoboken, NJ, 2003.

[41] A. Albert. *Heterocyclic Chemistry: An Introduction*. Essential Books, Fair Lawn, NJ, 1959.

[42] A. Albert. *Heterocyclic Chemistry: An Introduction*. The Athlone Press: University of London, London, 2nd edition, 1968.

[43] G. Badger. *The Chemistry of Heterocyclic Compounds*. Academic Press, New York, 1961.

[44] R. Acheson. *An Introduction to the Chemistry of Heterocyclic Compounds*. Interscience Publishers, New York, 1967.

[45] G. Boyd. *Comprehensive Heterocyclic Chemistry: The Structure, Reactions, Synthesis and Uses of Heterocyclic Compounds*. Pergamon Press, Oxford, 1984.

[46] P. Jackson, K. Morgan, and A. Turner. Studies in heterocyclic chemistry. part iv. kinetics and mechanisms for the hydrolysis of benzoxazoles. *Journal of the Chemical Society, Perkin transactions 2: Physical Organic Chemistry*, pages 1582–1587, 1972.

[47] J. Goetz. Hydrolysis of 2-methylbenzoxazole to 2-hydroxyacetanilide. *Texas Journal of Science*, 24(2):261, 1972.

[48] L. Hegedus, R. Odle, P. Winton, and P. Weider. Synthesis of 2,5-disubstituted 3,6-diamino1,4-benzoquinones. *Journal of Organic Chemistry*, 47(13):2607–2613, 1982.

[49] F. Carey. *Organic chemistry*. McGraw Hill, 1993.

[50] L. Wade. *Organic chemistry*. Prentice Hall, Englewood Cliffs, NJ, 1991.

[51] R. Silverstein, G. Bassler, and T. Morrill. *Spectrometric Identification of Organic Compounds*. John Wiley and Sons, New York, 5th edition, 1991.

[52] J. Martin, T. Nguyen, E. Byrd, and E. Embree. Relating laboratory and outdoor exposure of coatings: I. cumulative damage model and laboratory experiment apparatus. *Polym Deg Stab*, 75:193–210, 2002.

[53] T. Nguyen, J. Martin, E. Byrd, and N. Embree. Relating laboratory and outdoor exposure of coatings: Ii. *Journal of Coatings Technology*, 74:65–80, 2002. 10.1007/BF02697976.

[54] T. Nguyen, J. Martin, E. Byrd, and N. Embree. Relating laboratory and outdoor exposure of coatingsiii. effect of relative humidity on moisture-enhanced photolysis of acrylic-melamine coatings. *Polymer Degradation and Stability*, 77(1):1 – 16, 2002.

[55] R. Morgan and N. Butler. Hydrolytic degradation mechanism of kevlar 49 fibers when dissolved in sulfuric acid. *Polymer Bulletin*, 27:689–696, 1992.

[56] M. Riley. Environmental conditioning tumbler reference design, ftp://ftp.nist.gov/pub/bfrl/riley/nij_010106/tumbler/, 2009.

[57] E. Chatzi, S. Tidrick, and J. Koenig. Characterization of the surface hydrolysis of kevlar-49 fibers by diffuse reflectance ftir spectroscopy. *Journal of Polymer Science Part B: Polymer Physics*, 26:1585–1593, 1988.

[58] D. Roitman R. Wessling and J. McAlister. Characterization of Poly(p-phenylene-cis-benzobisoxazole) in Methanesulfonic Acid. *Macromolecules*, 26:5174–5184, 1993.

[59] W. Shanfeng, B. Gaobin, W. Pingping, and H. Zhewen. Viscometric study on the interactions of polymers of the poly(banzazole) family with nylon 66. *European Polymer Journal*, 36:1843–1852, 2000.

[60] D. Cotts and G. Berry. Polymerization kinetics of rigid rodlike molecules: Polycondensation of poly ([benzo(1,2-d:5,4,-d')bisoxazole-2,6-diyl]-1,4-phenylene). *Macromolecules*, 14:930–934, 1981.

[61] A. Gupta. *Improving UV Resistance of High Strength Fibers.* PhD thesis, North Carolina State University, 2005.

[62] C. Wong, H. Ohnuma, and G. Berry. Properties of some rodlike polymers in solution. *J Polym Sci Polym Symp*, 65:173–192, 1978.

[63] M. Arpin and C. Strazielle. Study of aromatic polyamides of poly[imino-1,4-phenyleneiminoterephtaloyl]-type by gel permeation chromotography. *Makromolekulare chemie-Macromolecular Chemistry and Physics*, 177:293–298, 1976.

[64] C. Carraher. *Polymer Chemistry.* Marcel Dekker, New York, 1996.

[65] M. Rubenstein and R. Colby. *Polymer physics.* Oxford University Press, New York, 2003.

[66] F. Billmeyer. *Textbook of polymer science.* John Wiley and Sons, New York, 3rd ed edition, 1984.

[67] M. Doi. *Introduction to polymer physics.* Oxford University Press, Oxford, 1996.

[68] V. Gabara. Dilute solution viscometry of ppta. *Personal Communication*, 2008.

[69] A. Forster, K. Rice, M. Riley, G. Messin, S. Petit, C. Clerici, M. Vigoroux, P. Pintus, G. Holmes, and J. Chin. Development of Soft Armor Conditioning Protocols for NIJ Standard–0101.06: Analytical Results. *NISTIR 7627*, 2009.

[70] J. Chin, S. Petit, A. Forster, M. Riley, and K. Rice. Effect of artificial perspiration and cleaning chemicals on the mechanical and chemical properties of ballistic materials. *Journal of Applied Polymer Science*, 113(1):567–584, 2009.

[71] J. Hearle. *High Performance Fibers.* Woodhead Publishing, Cambridge, 2001.

[72] A. Leal, J. Deitzel, and J. Gillespie. Assessment of compressive properties of high performance organic fibers. *Composites Science and Technology*, 67(13):2786–2794, 2007.

[73] ProsystemsSPA. Artec fiber vs rusar fiber technical differences. As per yarn manufacturer communication, 2006.

[74] Unpublished communication with dupont de nemours. March 2011.

[75] I. Slugin, G. Sklyarova, A. Kashirin, and L. Tkacheva. Rusar para-aramid fibres for composite materials for construction applications. *Fibre Chemistry*, 38(1):25–26, 2006.

[76] D. Hand. Hybrid vests made from twaron fibers and co-polymer aramid yarns containing 5-amino-2-(p-aminophenyl)-benzimidazole or related monomers, January 2006.

[77] N. Machalaba, N. Kuryleva, L. Okhlobystina, P. Matytsyn, and I. Andriyuk. Tver' fibres of the armos type: Manufacture and properties. *Fibre Chemistry*, 32(5):319–324, 2000.

[78] K. Perepelkin, N. Machalaba, and V. Kvaratskheliya. Properties of armos para-aramid fibres in conditions of use. comparison with other para-aramids. *Fibre Chemistry*, 33(2):105–114, 2001.

[79] S. Kotomin, A. Basharov, V. Bova, and E. Sapozhnikov. Realization of the strength of armos fibres with different acidity in epoxy plastics. *Fibre Chemistry*, 28(1):48–49, 1996.

[80] S. Grebennikov, T. Smotrina, N. Lebedeva, and K. Perepelkin. Molecular mobility in the superstrong para-aramid fibre-water system. *Fibre Chemistry*, 40(3):206–207, 2008.

[81] K. Perepelkin, S. Grebennikov, and N. Lebedeva. Sorption of water vapors by high-strength para-aramid fibres. *Fibre Chemistry*, 39(5):420–423, 2007.

[82] K. Perepelkin, I. Andreeva, G. Meshchervakova, and I. Morgoeva. Change in the mechanical properties of para-aramid fibres in thermal aging. *Fibre Chemistry*, 38(5):400–405, 2006.

[83] K. Perepelkin, I. Andreeva, E. Pakshver, and I. Morgoeva. Thermal characteristics of para-aramid fibres. *Fibre Chemistry*, 35(4):265–269, 2003.

[84] K. Perepelkin, O. Malan'ina, E. Pakshver, and R. Makarova. Comparative evaluation of the thermal properties of aromatic fibres (polyoxazole, polyimide, and polyaramid). *Fibre Chemistry*, 36(5):365–369, 2004.

[85] V. Platonov, G. Frenkel, and A. Shchetinin. X-ray study of the effect of heat on the structural parameters of armos fibres. *Fibre Chemistry*, 35(4):283–286, 2003.

[86] I. Slugin, G. Sklyarova, A. Kashirin, L. Tkacheva, and S. Komissarov. Rusar microfilament yarn for ballistic protection. *Fibre Chemistry*, 38(1):22–24, 2006.

[87] P. Cuniff. Dimensionless Parameters for Optimization of Textile-Based Armor Systems. In *18th International Symposium on Ballistics*, pages 1302–1310, San Antonio, TX, 1999.

[88] V. Shchetinin, I. Tikhonov, and A. Tokarev. The pseudoeffect of the hydrogen chloride contained in the aramid fibres svm, armos, and rusar on their properties during prolonged storage and use. *Fibre Chemistry*, 38(6):450–452, 2006.

[89] Fisher Scientific. *Accumet Excel XL Series Meters User Manual.*

[90] Bruker Optics, Ettlingen, Germany. *Vertex 80 User Manua*, 1st edition, 2006.

[91] L. Nollet. *Handbook of Water Analysis.* CRC Press, New York, 1st edition, 2000.

[92] H. Elias. *Macromolecules: Synthesis, Materials, and Technology.* Plenum Press, New York, 1984.

[93] L. Penn. and F. Larsen. Physicochemical properties of kevlar 49 fiber. *Journal of Applied Polymer Science*, 23:59–73, 1979.

[94] A. Tiefenthaler and M. Urban. Surface studies of polymer films and fibers by circle atr ft-ir. *Applied Spectroscopy*, 42(1):163–166, 1988.

[95] R. Gupta. *Physical Methods in Heterocyclic Chemistry.* General Heterocyclic Chemistry Series. John Wiley, New York, 1984.

[96] G. Socrates. *Infrared Characteristic Group Frequencies.* John Wiley, Chichester, 1980.

[97] C. Cameron. *Enhanced Rates of Electron Transport in Conjugated-Redox Polymer Hybrids.* PhD thesis, Memorial University of Newfoundland, 2000.

[98] A. Suwaiyan, R. Zwarich, and N. Baig. Infrared and raman spectra of benzimidazole. *Journal of Raman Spectroscopy*, 21:243–249, 1990.

[99] A.L. Forster. Study of acid generation from copolymer fibers based on 5-amino-2-(*p*-aminophenyl)-benzimidazole. *NISTIR 7592*, 2009.

[100] *Sigma-Aldrich Chemical Catalog.* Sigma-Aldrich, 2010.

[101] J. Chin, E. Byrd, A. Forster, X. Gu, T. Nguyen, S. Scierka, L. Sung, P. Stutzman, J. Sieber, and K. Rice. Chemical and Physical Characterization of Poly (p-phenylene-2,6-benzobisoxazole) Fibers Used in Body Armor. *NISTIR 7237*, 2006.

[102] J. Chin, E. Byrd, C. Clerici, M. Oudina, L. Sung, A. Forster, and K. Rice. Chemical and Physical Characterization of Poly (p-phenylene-2,6-benzobisoxazole) Fibers Used in Body Armor: Temperature and Humidity Aging. *NISTIR 7373*, 2007.

[103] A. Forster. Development of soft armor conditioning protocols for nij standard-0101.06: Analytical results. *NISTIR 7627*, 2003.

[104] E. Howard and S. Nemser. Ultrahigh molecular weight polyethylene and lightly-filled composites thereof. 5,292,584, 1991.

[105] C. Yang, H. Chang, and W. Lee. Catalyst for producing an ultrahigh molecular weight polyethylene (uhwmp) and method for producing an uhwmp using the same. 6,559,249, 2003.

[106] S. Kurtz. *The UHMWPE Handbook.* Elsevier Academic Press, New York, 2004.

[107] K. Jacobs. *Creep of Gel-Spun Polyethylene Fibers: Improvements by Impregnation and Crosslinking.* PhD thesis, Eindhoven: Technische Universiteit, 1999 1999.

[108] P. Lemstra, N. Van Aerle, and C. Bastiaansen. Chain-extended polyethylene. *Polymer Journal*, 19(1):85–98, 1987.

[109] P. Smith, P. Lemstra, and H. Booij. Ultradrawing of high-molecular-weight polyethylene cast from solution. ii. influence of initial polymer concentration. *Journal of Polymer Science Part B: Polymer Physics*, 19(5):877–888, 1981.

[110] L. Berger, H. Kausch, and C. Plummer. Structure and deformation mechanisms in uhmwpe-fibres. *Polymer*, 44(19):5877–5884, 2003. 0032-3861 doi: DOI: 10.1016/S0032-3861(03)00536-6.

[111] K. Prasad and D. Grubb. Direct observation of taut tie molecules in high-strength polyethylene fibers by raman spectroscopy. *Journal of Polymer Science Part B: Polymer Physics*, 27(2):381–403, 1989.

[112] Y. Fu, W. Chen, M. Pyda, D. Londono, B. Annis, A. Boller, A. Habenschuss, J. Cheng, and B. Wunderlich. Structure-property analysis for gel-spun, ultrahigh molecular mass polyethylene fibers. *Journal of Macromolecular Science, Part B*, 35(1):37 – 87, 1996.

[113] X. Hu and Y. Hsieh. Crystallite sizes and lattice distortions of gel-spun ultrahigh molecular weight polyethylene fibers. *Polymer Journal*, 30(10):771–774, 1998.

[114] Y. Takahashi and T. Furusaka. Monoclinic-to-orthorhombic transformation in polyethylene. *Journal of Polymer Science Part B: Polymer Physics*, 26(11):2267–2277, 1988.

[115] D. Dijkstra and A. Pennings. The role of taut tie molecules on the mechanical properties of gel-spun uhmwpe fibers. *Polymer Bulletin*, 19:73–80, 1988.

[116] L. Treloar. Calculations of elastic moduli of polymer crystals: I. polyethylene and nylon 66. *Polymer*, 1:95–103, 1960. 0032-3861 doi: DOI: 10.1016/0032-3861(60)90012-4.

[117] K. Tashiro, M. Kobayashi, and H. Tadokoro. Calculation of three-dimensional elastic constants of polymer crystals. 2. application to orthorhombic polyethylene and poly(vinyl alcohol). *Macromolecules*, 11(5):914–918, 1978.

[118] T. He. An estimate of the strength of polymers. *Polymer*, 27(2):253–255, 1986. 0032-3861 doi: DOI: 10.1016/0032-3861(86)90335-6.

[119] I. Ward and D. Hadley. *An Introduction to the Mechanical Properties of Solid Polymers*. John Wiley & Sons, New York, 1993.

[120] V. Jain and S. Badhur. Material transfer in polymer-polymer sliding. *Wear*, 46:177–188, 1978.

[121] I. Ward. Creep and yield behaviour of polyethylene. *Macromol. Symp.*, 98:1029–1041, 1995 1995.

[122] J. Ferry. *Viscoelastic Properties of Polymers*. John Wiley & Sons, New York, 1980.

[123] H. Kausch. *Polymer Fracture*. Springer, Heidelberg, 2nd edition, 1987.

[124] V. Kuksenko and V. Tamuzs. *Fracture Micromechanics of Polymer Materials*. Martinus Nijhof, Hague, 1981.

[125] J. Rasburn, P. Klein, and I. Ward. The influence of short chain branching on the creep behavior of oriented polyethylene, and its effect on the efficiency of crosslinking by electron irradiation. *Journal of Polymer Science Part B: Polymer Physics*, 32:1329–1338, 1994.

[126] H. Kausch and B. Von Schmeling. The role of chain length and conformation in stress-transmission and fracture of thermoplastic polymers. *Physics of the Solid State*, 47(5):934–941, 2005. 10.1134/1.1924858.

[127] L. Govaert, C. Bastiaansen, and P. Leblans. *Polymer*, 34:534–540, 1993.

[128] S. Walley, D. Chapman, D. Williamson, M. Morley, T. Fairhead, and W. Proud. 9th international conference on the mechanical and physical. In *Dymat 2009*, 2009.

[129] I. Karacan. *Fibers and Textiles in Eastern Europe*, 13:15–21, 2005.

[130] J. Greenwood and P. Rose. *J. Mater Sci*, 9:1809–1814, 1974.

[131] P. Taddei, S. Affatato, C. Fagnano, and A. Toni. Oxidation in ultrahigh molecular weight polyethylene and cross-linked polyethylene acetabular cups tested against roughened femoral heads in a hip joint simulator. *Biomacromolecules*, 7:1912–1920, 2006.

[132] M. Aryafar and F. Zaera. Kinetic study of the catalytic oxidation of alkanes over nickel, palladium, and platnium foils. *Catalysis Letters*, 48:173–183, 1997.

[133] J. H. Chan and S. T. Balke. The thermal degradation kinetics of polypropylene: Part i: Molecular weight distribution. *Polymer Degradation and Stability*, 57:113–125, 1997.

[134] M. Iring, F. Tudos, Zs. Fodor, and T. Kelen. The thermo-oxidative degradation of polyolefins- part 10. correlation between the formation of carbonyl groups and scission in the oxidation of polyethylene in the melt phase. *Polymer Degradation and Stability*, 2:143–153, 1980.

[135] Textiles- yarns from packages: Determination of single-end breaking force and elongation at break.

[136] S. Li and A. Burstein. *J. Bone Surg Am*, 76:1080–1090, 1994.

[137] E. del Prever, M.Crova, L. Costa, A. Dallera, G. Camino, and P. Gallinaro. *Biomaterials*, 17:873–878, 1996.

[138] K. Tashiro an d S. Sasaki and M. Kobayashi. *Macromolecules*, 29:7460–7469, 1996.

[139] D. Dijkstra and A. Pennings. Shrinkage of highly oriented gel-spun polymeric fibers. *Polymer Bulletin*, 19:65–72, 1988.

[140] L. Goavert and P. Lemestra. Deformation behavior of oriented uhmwpe fibers. *Colloid & Polymer Science*, 270:455–464, 1992.

[141] J. Menczel and R. Prime. *Thermal Analysis of Polymers: Fundamentals and Applications*. Wiley Interscience, 2009.

[142] S. Cooper and A. Tobolsky. *J. Appl. Polym. Sci.*, 10:1837–1844, 1966.

[143] J. Cowie. *Polymers: Chemistry and Physics of Modern Materials*. CRC Press, 1991.

[144] L. Costa, M. Luda, and L. Trossarelli. Ultra-high molecular weight polyethylene: I. mechano-oxidative degradation. *Polymer Degradation and Stability*, 55:329–338, 1997.

[145] X. Hu, S. Jenkins, B. Min, M. Polk, and S. Kumar. Rigid-Rod Polymers: Synthesis, Processing, Simulation, Structure, and Properties. *Macromolecular Materials Engineering*, 288:823–843, 2003.

[146] J. Pak. *Thermochimica Acta*, 421:203–209, 2004.

[147] R. Roe. *Methods of X-Ray and Neutron Scattering in Polymer Science*. Oxford University Press, 2000.

[148] A. Peacock. *Handbook of Polyethylene: Structures, Properties, and Applications*. Marcel Dekker, 2000.

[149] S. Rastogi, L. Kurelec, and P. Lemestra. Chain moibility in polymer systems: On the borderline between solid and melt 2. crystal size influence in phase transition and sintering of ultrahigh molecular weight polyethylene via the mobile hexagonal phase. *Macromolecules*, 31:5022–5031, 1998.

[150] W. Callister and D. Rethwisch. *Fundamentals of Materials Science and Engineering An Integrated Approach.* John Wiley and Sons, 2007.

[151] C. Stephens, H. Yang, M. Islam, S. Chum, S. Rowan, A. Hiltner, and E. Baer. *J. Polymer Sci B Polym Phys*, 41:2062–2070, 2003.

[152] L. Fontana, D. Vinh, M. Santoro, S. Scandolo, F. Gorelli, R. Bini, and M. Hanfland. High-pressure crystalline polyethylene studied by x-ray diffraction and ab initio simulations. *Physical Review B*, 75:174112, 2007.

[153] C. Riekel and R. Davies. Applications of synchrotron radiation micro-focus techniques to the study of polymer and biopolymer films. *Current Opinion in Colloid and Interface Science*, 9:396–403, 2005.

[154] D. Yakusheva, R. Yakushev, T. Oschepkova, and V. Strelnikov. Properties of ultra high molecular weight polyethylene fibers after ion beam treatment. *Journal of Applied Polymer Science*, 122:1628–1633, 2011.

[155] A. Singh. *Radiation Physics and Chemistry*, 56:375–380, 1999.

[156] S. Bhateja, R. Duerst, J. Martens, and E. Andrews. *Polymer Reviews*, 35:581–659, 1995.

[157] M. Ormerod. *Polymer*, 1963:451–457, 4.

[158] D. Bodily and M. Dole. *The Journal of Physical Chemistry*, 4:1433–1439, 1963.

[159] D. Waterman and M. Dole. *Journal of Physical Chemistry*, 74:1913–1922, 1970.

[160] T. Fujimura, N. Hayakawa, and I. Kuriyama. *J. Polymer Sci. Polym Phys*, 9:1173, 1971.

[161] M. Dole, C. Gupta, and N. Gvozdic. *Radiation Physics and Chemistry*, 14:711–720, 1979.

[162] R. Woods and A. Pikaev. *Applied Radiation Chemistry: Radiation Properties.* John Wiley and Sons, Inc., New York, 1994.

[163] P. Alexander and D. Toms. The effect of oxygen on the changes produced by ionizing radiations in polymers. *Journal of Polymer Science*, 22:343, 1956.

[164] W. Perkins, V. Stannett, and R. Porter. Effect of gamma radiation and annealing on ultra-oriented polyethylene. *Polymer Engineering and Science*, 18(6):527, 1978.

[165] C. Jun. Uv and thermal oxidation of polyethylene compounded with photosensitizer. *Korea Polymer Journal*, 3:7–11, 1994.

[166] R. Clough. Isotopic exchange in gamma-irradiated mixtures of c24h50 and c24d50: Evidence of free radical migration in the solid state. *J Chem Phys*, 87:1588–1595, 1987.

[167] A. Yamanaka, Y. Izumi, T. Kitagawa, T. Terada, H. Hirahata, K. Ema, H. Fujishiro, and S. Nishijima. The effect of gamma-irradiation on thermal strain of high strength polyethylene fiber at low temperature. *Journal of Applied Polymer Science*, 102(1):204–209, 2006.

[168] S. Bhateja, R. Duerst, J. Martens, and E. Andrews. Radiation-induced enhancement of crystallinity in polymers. *Polymer Reviews*, 35(4):581–659, 1995.

[169] J. DeBoer and A. Pennings. Crosslinking of ultra-high strength polyethylene fibers by means of gamma-radiation. *Polymer Bulletin*, 7:309–316, 1982.

[170] D. Dijkstra and A. Pennings. Cross-linking of ultra-high strength polyethylene fibers by means of electron beam irradiation. *Polymer Bulletin*, 17:507–513, 1987.

[171] R. Hikmet, P. Lemstra, and A. Keller. X-linked ultra high strength polyethylene fibers. *Colloid and Polymer Science*, 265:185–193, 1987.

[172] P. Klein, D. Woods, and I. Ward. The effect of electron irradiation on the structure and mechanical properties of highly drawn polyethylene fibers. *Journal of Polymer Science Part B: Polymer Physics*, 25:1359–1379, 1987.

[173] P. Klein, J. Gonzalez-Orozco, and I. Ward. Effect of draw ratio on the structure and properties of electron beam crosslinked polyethylene. *Polymer*, 35(10):2044–2048, 1994.

[174] M. Wilding and I. Ward. Routes to improved creep behaviour in drawn linear polyethylene. *Plastics and Rubber Processing and Applications*, 1:167–172, 1981.

[175] M. Deng, R. Latour, M. Drews, and S. Shalaby. Effects of gamma irradiation, irradiation environment, and postirradiation aging on thermal and tensile properties of ultrahigh molecular weight polyethylene fibers. *Journal of Applied Polymer Science*, 61:2075–2084, 1996.

[176] J. DeBoer and A. Pennings. Crosslinking of ultra-high strength polyethylene fibers by means of gamma radiation. *Polymer Bulletin*, 5:317–324, 1981.

[177] I. Chodak. High modulus polyethylene fibres: Preparation, properties and modification by crosslinking. *Progress in Polymer Science*, 23(8):1409–1442, 1998. Times Cited: 34.

[178] J. DeBoer, H. VanDenBerg, and A. Pennings. Crosslinking of ultra-high molecular weight polyethylene in the oriented state with dicumylperoxide. *Polymer*, 25:513–519, 1984.

[179] M. Jacobs, N. Heijnen, C. Bastiaansen, and P. Lemstra. A novel, efficient route for the crosslinking and creep improvement of high modulus and high strength polyethylene fibres. *Macromol. Mater. Eng.*, 283(1):120–125, 2000.

[180] J. Penning, H. Pras, and A. Pennings. Influence of chemical crosslinking on the creep behavior of ultra-high molecular weight polyethylene fibers. *Colloid & Polymer Science*, 272(6):664–676, 1994. 10.1007/BF00659280.

[181] Z. Zheng, X. Tang, M. Shi, and G. Zhou. Surface modification of ultrahigh-molecular-weight polyethylene fibers. *Journal of Polymer Science Part B-Polymer Physics*, 42(3):463–472, Feb 2004. Times Cited: 10.

[182] J. Yu, Z. Chen, J. Zhu, Z. Liu, and Q. Wang. Crosslinking modification of uhmwpe fibers by ultra-violet irradiation. *International Polymer Processing*, 14(4):331–335, Dec 1999. Times Cited: 2.

[183] L. Woo and C. Sandford. Comparison of electron beam iradiation with gamma processing for medical packaging materials. *Radiation Physics and Chemistry*, 63:845–850, 2002.

[184] K. Patel. Crystallinity and the effect of ionizing radiation in polyethylene. i. crosslinking and the crystal core. *Journal of Polymer Science Part B: Polymer Physics*, 13(2):303–321, 1975.

[185] G. Patel and A. Keller. Crystallinity and the effect of ionizing radiation in polyethylene. ii. crosslinking in chain-folded single crystals. *Journal of Polymer Science Part B-Polymer Physics*, 13(2):323–331, 1975.

[186] G. Patel. Crystallinity and the effect of ionizing radiation in polyethylene. iv. effect of segregation of low molecular weight chains on determination of main-chain scission in linear polyethylene. *Journal of Polymer Science Part B: Polymer Physics*, 13(2):339–350, 1975.

[187] G. Patel. Crystallinity and the effect of ionizing radiation in polyethylene. v. distribution of trans-vinylene and trans, trans conjugated double bonds in linear polyethylene. *Journal of Polymer Science Part B: Polymer Physics*, 13(2):351–359, 1975.

[188] R. Jones, G. Salmon, and I. Ward. Radiation-induced crosslinking of polyethylene in the presence of acetylene: A gel fraction, uv-visible, and esr spectroscopy study. *Journal of Polymer Science Part B: Polymer Physics*, 31(7):807–819, 1993.

[189] P. Eyerer, M. Kurth, H. McKellup, and T. Mittlmeier. Characterization of uhmwpe hip cups run on joint simulators. *Journal of Biomedical Materials Research*, 21:275–291, 1987.

[190] H. Kang, O. Saito, and M. Dole. The radiation chemistry of polyethylene. ix. temperature coefficient of cross-linking and other effects. *Journal of the American Chemical Society*, 89(9):1980–1986, 1967.

[191] M. Parth, N. Aust, and K. Lederer. Studies on the effect of electron beam radiation on the molecular structure of ultra-high molecular weight polyethylene under the influence of alpha-tocopherol with respect to its application in medical implants. *Journal of materials Science: Materials in Medicine*, 13:917–921, 2002.

[192] M. Parth, N. Aust, and K. Lederer. Molecular characterization of ultrahigh molar mass and soluble fractions of partially cross-linked polyethylenes. *International Journal of Polymer Analytical Characterization*, 8:175–186, 2003.

[193] M. Dole, M. Fallgatter, and K. Katsuura. The mechanism of decay of vinyl unsaturation during the radiolysis of marlex-50 polyethylene. *The Journal of Physical Chemistry*, 70(1):62–70, 1966.

[194] A. Charlesby and S. Pinner. Analysis of the solubility behaviour of irradiatied polyethylene and other polymers. *Proceedings of the Royal Society of London, Series A, Mathematical and Physical Sciences*, 249(1258):367–386, January 13, 1959 1959.

[195] J. Sibilia, editor. *A Guide to Materials Characterization and Chemical Analysis*. VCH Publishers, New York, 2nd edition, 1996.

[196] S. Kurtz, O. Muratoglu, M. Evans, and A. Edidin. Advances in the processing, sterilization, and crosslinking of ultra-high molecular weight polyethylene for total joint arthroplasty. *Biomaterials*, 20:1659–1688, 1999.

[197] B. Daly and J. Yin. Subsurface oxidation of polyethylene. *J. Biomed. Mater. Res.*, 42:523–529, 1998.

[198] M. Goldman, R. Gronsky, R. Ranganathan, and L. Pruitt. The effects fo gamma radiation sterilization and ageing on the structure and morphology of medical grade ultra high molecular weight polyethylene. *Polymer*, 37(14):2909–2913, 1996.

[199] M. Goldman, M. Lee, R. Gronsky, and L. Pruitt. Oxidation of ultrahigh molecular weight polyethylene characterized by fourier transform infrared spectroscopy. *Journal of Biomedical Materials Research*, 37(1):43–50, 1997.

[200] E. Turi, editor. *Thermal Characterization of Polymeric Materials*. Academic Press, 1997.

[201] M. Kasser. User guide to umd bruker esp 300, 2008.

[202] E. Oral, A. Malhi, and O. Muratoglu. Mechanisms of decrease in fatigue crack propagation resistance in irradiated and melted uhmpwe. *Biomaterials*, 27:917–925, 2006.

[203] M. Kuzuya, J. Niwa, and H. Ito. Nature of plasma-induced surface radicals of powdered polyethylene studied by electron spin resonance. *Macromolecules*, 26:1990–1995, 1993.

[204] J. Booth. *Principles of Textile Testing*. Chemical Publishing Co, Inc., New York, 1961.

[205] D. Allen, D. Leathard, and C. Smith. The effects of gamma irradiation on the fate of hindered phenol antioxidants in food contact polymers. analytical and 14-c labelling studies. *Radiation Physics and Chemistry*, 38(5):461–465, 1991.

[206] M. Uhniat, M. Sudol, and S. Kudla. Stabilization of ldpe cross-linked in the presence of peroxides ii. ftir study of chemical changes taking place in the ldpe-dicumyl peroxide-irganox 1081 system. *Polymer Degradation and Stability*, 71:75–82, 2001.

[207] Standard test method for tensile properties of yarn by the single-strand method. ASTM D2256-02.

[208] M. Butson, P. Yu, T. Cheung, and P. Metcalfe. Radiochromic film for medical radiation dosimetry. *Materials Science and Engineering R*, 41:61–120, 2003.

[209] D. Waterman and M. Dole. *Journal of Physical Chemistry*, 74:9, 1970.

[210] K. Nitta and A. Tanaka. Dynamic mechanical properties of metallocene catalyzed linear polyethylenes. *Polymer*, 42:1219–1226, 2001.

[211] F. Stadler, J. Kaschta, and H. Munstedt. Dynamic-mechanical behavior of polyethylenes and ethene-/alpha-olefin-co-polymers. part i. alpha'-relaxation. *Polymer*, 46:10311–10320, 2005.

[212] K. Sinnott. Mechanical relaxations in single crystals of polyethylene. *Journal of Applied Physics*, 37:3385, 1966.

[213] J. Albert and S. Chib. Bayesian analysis of binary and polychotomous response data. *Journal of the American Statistical Association*, 88(422):669–679, 1993.

[214] A. Dobson. *An Introduction to Generalized Linear Models*. Chapman & Hall, Boca Raton, FL, 2nd edition, 2001.

[215] J. Gill. Generalized linear models: a unified approach. In *Sage University Papers Series Volume 134*, Thousand Oaks, CA, 2001.

[216] J. Hardin and J. Hilbe. *Generalized Linear Models and Extensions*. Stat Press Publication, College Station, TX, 2nd edition, 2007.

[217] P. McCullagh and J. Nelder. *Generalized Linear Models.* Chapman & Hall, London, 2nd edition, 1989.

[218] J. Nelder and R. Wedderburn. Generalized linear models. *Journal of The Royal Statistical Society. Series A (General)*, 135(3):370–384, 1972.

[219] A. Agresti. *Introduction to Categorical Data Analysis.* John Wiley & Sons, 2nd edition, 2007.

[220] D. Finney. *Probit Analysis.* Cambridge University Press, Cambridge, UK, 3rd edition, 1971.

[221] B. Greenberg. Chester I. Bliss, 1899-1979. *International Statistical Review*, 8(1):135–136, 1980.

[222] J. Cramer. *Logit Models from Economics and Other Fields, Chapter 9: Origin and Development of the Probit and Logit Models.* Cambridge University Press, Cambridge, UK, 1971.

[223] D. Hosmer and S. Lemeshow. *Applied Logistic Regression.* John Wiley & Sons, NY, 2nd edition, 2000.

[224] D. Altman. *Practical Statistics for Medical Research.* Chapman & Hall, 1991.

[225] P. Armitage, G. Berry, and J.N.S. Matthews. *Statistical Methods in Medical Research.* Blackwell, Oxford, 4th edition, 2002.

[226] F. Harrell. *Regression Modeling Strategies: with Applications to Linear Models, Logistic Regression, and Survival Analysis.* Springer, 2001.

[227] J. Horowitz. and N. Savin. Binary response models: Logits, probits and semi-parametrics. *Journal of Economic Perspectives, American Economic Association*, 15(4):43–56, Fall 2001.

[228] A. Agresti. *Categorical Data Analysis, chapter 6: Building and Applying Logistic Regression Models.* John Wiley & Sons, Hoboken, NJ, 2nd edition, 2002.

[229] D. Collett. *Modelling Binary Data.* Chapman & Hall, Boca Raton, FL, 2nd edition, 2003.

[230] F. Huettmann and J. Linke. *Assessment of Different Link Functions for Modeling Binary Data to Derive Sound Inferences and Predictions.* Springer, Berlin, 2003.

[231] D. Cox and E. Snell. *Analysis of Binary Data.* Chapman & Hall, NY, 2nd edition, 1989.

[232] W. Greene. *Econometric Analysis.* Prentice Hall, Upper Saddle River, NJ, 3rd edition, 1997.

[233] S. Long. *Regression Models for Categorical and Limited Dependent Variables (Advanced Quantitative Techniques in the Social Sciences)*. Sage Publications, Thousand Oaks, CA, 1997.

[234] E. Chambers and D. Cox. Discrimination between alternative binary response models. *Biometrika*, 54:573–578, 1967.

[235] E. Hahn and R. Soyer. Probit and logit models: Differences in a multivariate realm. *The Journal of the Royal Statistical Society, Series B*, 2005. Working Paper.

[236] B. Kneubuhl. Improved test procedures for body armour. In *Proceedings of the Personal Armour Systems Symposium*, Colchester, UK, 1996.

[237] P. Gotts, P. Fenne, and D. Leeming. The application of critical performance analysis to UK military and police personal armour. In *Proceedings of the Personal Armour Systems Symposium*, The Hague, Netherlands, 2004.

[238] M. Van Es. Improved method to determine the stop velocity of armour. In *Proceedings of the Personal Armour Systems Symposium*, Leeds, UK, 2006.

[239] M. Maldague. Evaluation of some methods in order to determine v50. In *Proceedings of the Personal Armour Systems Symposium*, Brussels, Belgiums, 2008.

[240] E. Gumbel. *Statistical Theory of Extreme Values and Some Practical Applications*. National Bureau of Standards Applied Mathematics Series 33, Washington, DC, 1954.

[241] NIST/SEMATECH e-Handbook of Statistical Methods, 2010.

[242] D. Leber. Assessment of body armor characteristics. National Institute of Standards and Technology internal communication, March 2006.

[243] H. Akaike. Information theory and an extension of the maximum likelihood principle. In *Proceedings of the Second International Symposium on Information Theory*, pages 610–624, New York, 1973.

[244] R Development Core Team. *R: A Language and Environment for Statistical Computing*. R Foundation for Statistical Computing, Vienna, Austria, 2009.

[245] W. Venables and B. Ripley. *Modern Applied Statistics with S*. Springer, 4th edition, 2002.

[246] Department of Defense. *Test Method Standard for Performance Requirements and Testing of Body Armor*. MIL-STD-3027. U.S. Department of Defense, Washington, DC, January 2007.

[247] NATO Standardization Agency. *Procedures for Evaluating the Protection Levels of Logistic and Light Armoured Vehicles.* AEP-55. NATO/PFP Unclassified, 1st edition, January 2004.

[248] P. Cuniff. Dimensionless Parameters for Optimization of Textile-Based Armor Systems. In *18th International Symposium on Ballistics*, pages 1302–1310, San Antonio, TX, 1999.

[249] S. Phoenix and P. Porwal. A new membrane model for the ballistic impact response and v_{50} performance fo multi-ply fibrous systems. *International Journal of Solids and Structures*, 40:6723–6765, 2003.

[250] P. Porwal and S. Phoenix. Modeling system effects in ballistic impact into multi-layered fibrous materials for soft body armor. *International Journal of Fracture*, 135:217–249, 2005.

[251] P. Porwal and S.L. Phoenix. Effects of layer stacking order on the v_{50} velocity of a two-layered hybrid armor system. *Journal of Mechanics of Materials and Structures*, 3:627, 2008.